Title

Structure and Property Relationships in Zintl Phases

Author

He, Allan

Publication Date

2021

Peer reviewed|Thesis/dissertation

Structure and Property Relationships in Zintl Phases

By

ALLAN HE

DISSERTATION

Submitted in partial satisfaction of the requirements for the degree of

DOCTOR OF PHILOSOPHY

in

Chemistry

in the

OFFICE OF GRADUATE STUDIES

of the

UNIVERSITY OF CALIFORNIA

DAVIS

Approved:

_____

Professor Susan M. Kauzlarich, Chair

_____

Professor Valentin Taufour

_____

Professor Davide Donadio

Committee in Charge

2021

Dedicated to my beautiful wife, Annie, and my Mom and Dad

TABLE OF CONTENTS

LIST OF FIGURES

LIST OF TABLES

LIST OF EQUATIONS

ABSTRACT

Structure and Property Relationships in Zintl Phases

Zintl phases are an extremely broad class of compounds that are charge balanced semiconductors. They follow simple assumptions where the more electropositive atoms donate their electrons (cations) to the more electronegative atoms (anions) which may or may not form additional bonding networks to satisfy their valence. Given the large scope of this category, this naturally brings about a huge number of possible structures and range of physical phenomenon. The understanding of how the atomic structure relates to the physical properties is fundamental in the design and optimization of new materials.

Thermoelectric materials are a unique type of material that can convert heat directly into electricity in a reversible fashion. These materials can be used in power generators to recycle and convert waste heat into usable electricity. Given that there are no moving parts in these thermoelectric generators and are only based on the solid-state materials, they are an extremely reliable source of power and commonly used on long term space missions where other power sources are not realistic or robust enough. Their widespread application is however, currently being held back by their conversion efficiencies. The efficiency of a thermoelectric material is dependent on $zT = \frac{\alpha^2 T}{\rho\kappa}$, the figure of merit, where α is the Seebeck coefficient, ρ is the electrical resistivity, and κ is the thermal conductivity. To maximize zT, a compound would need to have low electrical resistivity, low thermal conductivity and a high Seebeck coefficient. The optimization of these parameters is non-trivial due to their interconnected nature with carrier concentration. Optimization schemes such as a single parabolic band model can provide directions to probe experimentally. The viability of this method will be visited in this work.

The first part of this dissertation will focus on the structure and properties of the $Yb_{21}Mn_4Sb_{18}$ phase. This material was predicted to have a promising starting value of zT because of its complex structure. The intrinsic phase was successfully synthesized in both bulk powder and single crystal form and indeed has a high zT prior to optimization. A systematic study was done to explore the effects on the electronic structure through isovalent substitution on all three sites where Yb was replaced with Ca, Mn with Cd, and Sb with Bi site. The carrier concentration was also tuned explicitly through aliovalent doping by introducing Na on the Yb site. An increase in the figure of merit was observed when the carrier concentration of the system increased showing large improvements in the case of Na doping and Cd substitution. The structure was analyzed through synchrotron x-ray diffraction and pair distribution function analysis revealing both long range and local disorder.

While the aforementioned studies focused on the high temperature physical properties, the structure-property relationship in the low temperature regime was also visited in two compounds: the new $Eu_5Al_3Sb_6$ phase and the $Yb_{14}MSb_{11}$ (M = Zn, Mg, Mn) series. The $Eu_5Al_3Sb_6$ phase represents a new structure type that features Al_4 tetrahedra in the solid state. These kinds of triel clusters are rarely seen with only a few examples in the literature making it a great case study for examining the emergent properties of this unique structure. This compound features antiferromagnetic ordering and metallic-like resistivity. Single crystal x-ray diffraction suggests the possibility of a supercell or modulated structure. From electronic band structure calculations, band crossing has been observed indicating that there is potential for this material to exhibit topological behavior. Careful defect tuning can shift the Fermi level to the appropriate energy to induce this behavior.

The intermediate valent nature of the $Yb_{14}MSb_{11}$ (M = Zn, Mg, Mn) compounds have been confirmed through XANES, heat capacity and magnetic susceptibility measurements showing that they are not strictly valence precise compounds as predicted from a Zintl formalism. The three substitutions provide

a systematic study on the effect of d electrons within the system where Mg^{2+} is d^0, Mn^{2+} is d^5 and $Zn^{2+}$is d^{10}. In all cases, there is a small amount of intermediate valency. The amount of intermediate valency is constant for the Mn and Mg compounds while the Zn compound was found to exhibit temperature dependent behavior.

This dissertation contains works that are to be published in the future. Some of the work presented here has already been published in part, or full in the following articles:

- He, A.; Bux, S. K.; Hu, Y.; Uhl, D.; Li, L.; Donadio, D.; Kauzlarich, S. M. Structural Complexity and High Thermoelectric Performance of the Zintl Phase: $Yb_{21}Mn_4Sb_{18}$. *Chem. Mater.* 2019, **31**, 8076 – 8086.
- He, A.; Cerretti, G.; Kauzlarich, S. M. The impact of site selectivity and disorder on the thermoelectric properties of $Yb_{21}Mn_4Sb_{18}$ solid solutions: $Yb_{21}Mn_{4-x}Cd_xSb_{18}$ and $Yb_{21-y}Ca_yMn_4Sb_{18}$. *Mater. Adv.,* 2021, **2**, 5764 – 5776.
- He, A.; Wille, E. L. K; Moreau, L. M.; Thomas, S. M.; Lawrence, J. M.; Bauer, E. D.; Booth, C. H.; Kauzlarich, S. M. Intermediate Yb valence in the Zintl phases $Yb_{14}MSb_{11}$ (M = Zn, Mn, Mg): XANES, magnetism, and heat capacity. *Phys. Rev. Mater.*, 2020, **4**, 114407.

Below are other published manuscripts that I have worked on but are not included in this dissertation:

- Shang, R.; Nguyen, A. T.; He, A.; Kauzlarich, S. M. Crystal structure characterization and electronic structure of a rare-earth-containing Zintl phase in the Yb-Al-Sb family: Yb_3AlSb_3. *Acta Cryst. C.* 2021, **C77**, 281 – 285.

ACKNOWLEDGEMENTS

I would like to thank my PhD advisor, Professor Susan Kauzlarich. She was the best advisor a graduate student could ask for and I am privileged to have the opportunity to work in her group. She was generous with her time and willing to listen, provided incredible wisdom and feedback about life and science. Her scientific curiosity was infectious and her guidance was invaluable to my growth as an individual. She taught me to be confident in my own ideas. I would also like to thank her for the countless workshops and conferences she allowed me to attend where I was able to meet world class scientists from around the world, enriching the PhD experience and allowing me to learn as much as I could. The lessons I have learned will stay with me forever. I would also like to thank the rest of my committee members, Professor Valentin Taufour and Professor Davide Donadio for their help, guidance, insightful conversations and unique perspectives where the work presented here would not be possible without them.

Thank you to all past and present group members for making these years full of excitement. Special thanks to: Katayoun Tabatabaei, Elizabeth Kunz Wille, Chris Perez, Zheng Ju, Andy Justl, Ashlee Hauble, Tanner Kimberly, and Luis Garay.

I would like to thank my wife, Annie, who has given me love and support for many years and steered me in the right direction and my family who have always been there for me. Thank you to my mother and father who understood the value of education and pushed me to go as far as I could.

Chapter 1 Introduction

1.1 Zintl Phases and Thermoelectric Materials

Zintl phases are a subgroup within intermetallic compounds that are usually charge balanced semiconductors. They follow the Zintl-Klemm concept, a basic rule that assumes complete electron transfer from the electropositive element to the electronegative one. The number of electrons transferred is not necessarily an amount that satisfies octet for each atom and when this happens, additional covalent bonds are formed between said atoms to compensate. The large scope of the Zintl phase categorization brings diversity. Both simple and structurally complex materials can arise from the Zintl rules due to the covalent bonding frameworks. A few examples are $CaZn_2Sb_2$,[1] $Eu_5Al_2Sb_6$,[2] $Yb_{11}GaSb_9$,[3] $Yb_{14}MnSb_{11}$[4] which are visualized below in **Figure 1.1**.

These compounds are easily tuned through chemical substitution with atoms that are similar in size and bonding (can be both aliovalent or isovalent) giving the chemist a huge composition space to explore for property optimization.

For thermoelectric materials, one strives to produce the so-called "electron-crystal phonon-glass" material[5] meaning that the material should be a good electrical conductor while simultaneously being a poor thermal conductor. This desirable and unique set of properties stems from the equation that defines how good a thermoelectric material is, the figure of merit, zT:

$$zT = \frac{\alpha^2 T}{\rho\kappa}$$

Equation 1.1: The thermoelectric figure of merit, zT.

Here, α is the Seebeck coefficient (a measure of how well a material can convert heat into electricity, units of V/K), ρ is the electrical resistivity, κ is the thermal conductivity of the material and T is temperature.

Therefore, to maximize zT, we need low electrical resistivity ("electron-crystal") and low thermal conductivity ("phonon-glass"). The figure of merit is a good metric and predictor of the efficiency of a thermoelectric material.

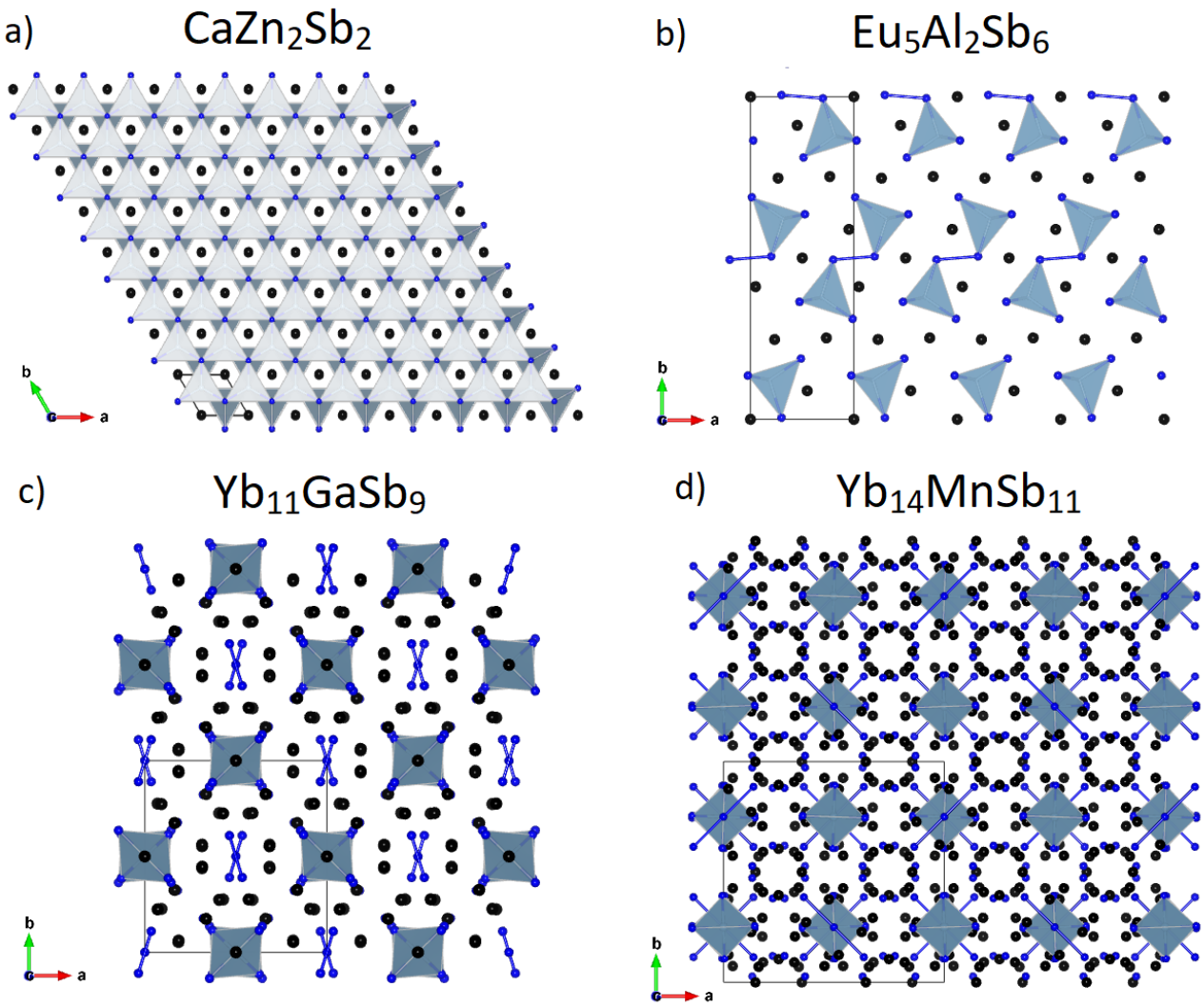

Figure 1.1: Examples of Zintl phases showing the diversity in structure types, arranged in increasing complexity. A) $CaZn_2Sb_2$, b) $Eu_5Al_2Sb_6$, c) $Yb_{11}GaSb_9$, d) $Yb_{14}MnSb_{11}$. For ease of structure type comparison, all the cations are shown in black, transition metal or triel atom in light blue, and pnictogen in blue.

Although chemical substitutions can be made and properties can be tuned, the optimization of zT is a non-trivial task due to the interconnected relationship of all the aforementioned variables to carrier concentration (n). This is shown explicitly below in **Figure 1.2**.

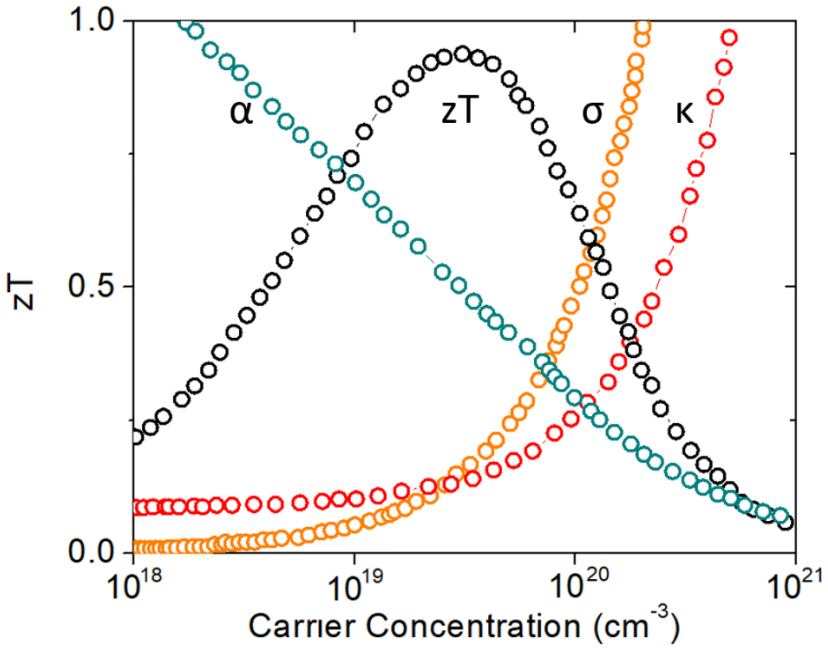

Figure 1.2: Relationship of the figure of merit zT with respect to α (Seebeck coefficient), σ (electrical conductivity) and κ (thermal conductivity) showing the interconnected relationship of all the different variables with carrier concentration. Data for the figure was taken from Ref. 6.

Assuming that the material has electrical transport governed by a single parabolic band model (SPB model, discussed more in detail in **Chapter 2** and **Chapter 3**), then the Seebeck coefficient can be written as:

$$\alpha = \frac{8\pi^2 k_b^2}{3eh^2} m^* T \left(\frac{\pi}{3n}\right)^{\frac{2}{3}}$$

Equation 1.2: Seebeck coefficient under the assumption of a single parabolic band model. Note that it is inversely proportional to carrier concentration.

where m^* is the effective mass of the single parabolic band and n is the carrier concentration. The electrical resistivity can be written as:

$$\rho = \frac{1}{\sigma} = \frac{1}{ne\mu}$$

Equation 1.3: Electrical resistivity written in terms of carrier concentration.

where σ is the electrical conductivity, n is the carrier concentration, and μ is the carrier mobility. Finally, the thermal conductivity can be split up and written in terms of its lattice and electronic component:

$$\kappa = \kappa_{lat} + \kappa_e = \kappa_{lat} + L\sigma T = \kappa_{lat} + Ln e\mu T$$

Equation 1.4: Thermal conductivity written in terms of its lattice and electronic contributions using the Wiedemann-Franz law.

where κ_{lat} is the lattice component of the thermal conductivity (phonon contribution), κ_e is the electrical component of the thermal conductivity and L is the Lorenz number. From all these equations, one can see that the carrier concentration (n) is present in α, ρ, κ_e. Therefore, any change in the carrier concentration will affect all three parameters simultaneously in different magnitudes where, for example, n is inversely proportional to Seebeck coefficient and directly proportional to electrical conductivity.

Any chemical substitutions made to a compound will (obviously) affect the atomic orbitals that contribute to its electrical transport, change the electronic band structure, the Fermi level, and overall change the carrier concentration of the compound. Other effects such as defects or non-stoichiometry will also have a strong effect on the carrier concentration, however, putting this and other secondary effects to the side and focusing only on an idealized system, for any compound under a SPB model, there will be an optimal carrier concentration for that compound that can be calculated. The SPB assumption does not often hold true for many compounds and instead electronic transport is often mediated by multiple bands at the Fermi level. In these cases, accurate analysis of transport optimization requires much more sophisticated

methodology. Despite this, in the majority of cases, the SPB is still a very powerful method for thermoelectric property optimization and will be shown in detail in **Chapters 2** and **Chapter 3**.

Although α, ρ, and κ_e are all linked through carrier concentration, the lattice contribution (κ_{lat}) to the thermal conductivity is decoupled to the electrical properties of the material and thus gives an additional pathway for experimentalists to explore and optimize. There has been much research going into the reduction of κ_{lat} through methods such as nanocompositing and/or texturing where large improvements in zT have been realized.[7,8] Intense efforts have also been put into material discovery of very complicated structure types for intrinsically low κ_{lat} serving as a great starting point for thermoelectric property optimization such as the $Yb_{14}MnSb_{11}$ compound and $Yb_{21}Mn_4Sb_{18}$ structure type (discussed below).

1.2 The $A_{21}M_4Pn_{18}$ (21-4-18) Structure Type

Particularly interesting are the Zintl phases with $A_{21}M_4Pn_{18}$ (referred to as 21-4-18) stoichiometry where A is a rare-earth or alkali earth atom, M is a transition metal atom, and Pn is a pnictogen atom. These compounds have very large unit cells and are expected to have a very low starting thermal conductivity. Currently in the literature, there have been many compounds isolated with the 21-4-18 stoichiometry. Most of these studies have focused on the magnetic and structural properties, but given the complexity of the structure, these compounds are predicted to be good thermoelectric materials. The 21-4-18 phases can be classified into three different structure types: orthorhombic C*mce*, monoclinic C*2/m*, and monoclinic C*2/c*. For a complete list, see below:

Table 1.1: Review of Existing Compounds of the 21-4-18 Structure and Magnetic Properties Arranged by Space Group

Phase	Space Group	Lattice Parameters	Magnetism	Band Gap (eV)	Reference
$Ba_{21}Cd_4Sb_{18}$	C*mce*	*a* = 18.191(6) Å *b* = 19.103(6) Å *c* = 37.062(10) Å V = 12879(7) Å^3	N/A	~0.5 (T)	[9]
$Ba_{21}Cd_4Bi_{18}$	C*mce*	*a* = 18.438(7) Å *b* = 19.303(7) Å *c* = 37.66(1) Å V = 13404(14) Å^3	N/A	N/A	[9]
$Eu_{21}Zn_4Sb_{18}$	C*mce*	*a* = 17.1256(11) Å *b* = 17.9312(12) Å *c* = 34.996(2) Å V = 10746.7(12) Å^3	Paramagnetic (10K – 300K), AFM ordering ~8K, polycrystalline, 7.88 μ_B/mol Eu	~0.2 (ρ)	[10]
$Sr_{21}Cd_4Bi_{18}$	C*2/m*	*a* = 18.510(4) Å *b* = 17.685(4) Å *c* = 18.213(4) Å β = 92.064(4)° V = 5958(2) Å^3	N/A	~0.5 (T)	[9]
$Eu_{21}Cd_4Bi_{18}$	C*2/m*	*a* =18.3298(13) Å *b* = 17.4929(12) Å *c* = 17.9504(13) Å β = 92.073(1)° V = 5751.9(7) Å^3	Curie-Weiss behavior >50K, single crystals, 7.87 μ_B/mol Eu	N/A	[9]
$Ca_{21}Zn_4As_{18}$	C*2/m*	*a* = 16.3736(16) Å *b* = 15.5944(15) Å *c* = 16.1638(16) Å β = 92.190(2)° V = 4124.2(7) Å^3	N/A	N/A	[10]
$Ca_{21}Zn_4Sb_{18}$	C*2/m*	*a* = 17.3717(13) Å *b* = 16.5723(13) Å *c* = 17.0540(13) Å β = 91.913(1)° V = 4906.9(6) Å^3	N/A	N/A	[10]
$Eu_{21}Zn_4As_{18}$	C*2/m*	*a* = 16.958(6) Å *b* = 16.166(6) Å	N/A	N/A	[10]

		c = 16.668(6) Å β = 92.008(6)° V = 4567(3) Å^3			
β-$Ca_{21}Mn_4Sb_{18}$	C*2/m*	*a* = 17.415(6) Å *b* = 16.567(6) Å *c* = 17.047(6) Å β = 92.068(4)° V = 4915(3) Å^3	N/A	N/A	[11]
$Sr_{21}Mn_4Sb_{18}$	C*2/m*	*a* = 18.1981(6) Å *b* = 17.3589(6) Å *c* = 17.8391(6) Å β = 91.957(1)° V = 5632.1(3) Å^3	Sharp upturn <12K, Pauli paramagnet >80K, Possible spin fluctuation	N/A	[12]
$Sr_{13}Eu_8Cd_3MnSb_{18}$	C*2/m*	*a* = 18.1522(11) Å *b* = 17.3096(10) Å *c* = 17.7691(10) Å β = 91.9638(8)° V = 5579.9(6) Å^3	Paramagnetic (high T), AFM ordering (T_N = 3.5K), 19.3 μ_B/f.u.	N/A	[13]
$Eu_{21}Cd_4Sb_{18}$	C*2/m*	*a* = 18.068(4) Å *b* = 17.228(4) Å *c* = 17.651(4) Å β = 91.942(4)° V = 5491(2) Å^3	Paramagnetic (high T), AFM ordering (T_N = 10K), 36.4 μ_B/f.u.	~0.26 (ρ)	[14]
$Eu_{21}Mn_4Sb_{18}$	C*2/m*	*a* = 18.0227(10) Å *b* = 17.1988(9) Å *c* = 17.5981(9) Å β = 91.876(1)° V = 5451.9(5) Å^3	Paramagnetic (high T), AFM ordering (T_N = 7K), 38.8 μ_B/f.u.	~0.08(ρ)	[14]
α-$Ca_{21}Mn_4Sb_{18}$	C*2/c*	*a* = 17.1001(15) Å *b* = 16.567(15) Å *c* = 17.047(6) Å β = 92.068(4)° V = 4914.9(8) Å^3	Ferrimagnetic (T_c = 48K), single crystal, ~4 μ_B/f.u.	~0.16 (ρ)	[15]
$Ca_{21}Mn_4Bi_{18}$	C*2/c*	*a* = 17.470(2) Å *b* = 17.392(2) Å *c* = 17.208(2) Å β = 93.253(2)° V = 5219.9(11) Å^3	Ferromagnetic (T_c = 55K), single crystal, ~4 μ_B/f.u.	~0.2 (T)	[11]
$Yb_{21}Mn_4Sb_{18}$	C*2/c*	*a* = 16.930(3) Å *b* = 17.029(3) Å *c* = 16.693(3) Å	Paramagnetic, single crystal, ~11.8 μ_B/f.u.	~0.4 (ρ) ~0.3 (T)	[14,16,17]

		β = 92.61(3)° V = 4807.7(4) Å^3			

AFM indicates antiferromagnetic ordering. T stands for theoretical where the band gap value was derived from DFT calculations and ρ indicates that the band gap value was derived from temperature dependent resistivity measurements.

An overarching feature among all the $A_{21}M_4Pn_{18}$ (where *A* is an alkaline earth or rare-earth element, *M* is a transition metal, and *Pn* is a pnictogen) phases are the MPn_4 tetrahedral units. The way in which that these tetrahedra are interconnected can be used to identify the structure type. For the following figures, the A site cations will be represented in black, M site cations will be in pink, and Pn site anions will be in red for ease of comparison between the three structure types.

1.2.1 C*mce* structure type

For the orthorhombic C*mce* structure type (**Figure 1.3**), there are a total of 29 crystallographic sites: 12 *A* sites, 3 *M* sites and 14 *Pn* sites. In a single unit cell, there contains 168 A^{2+} cations, 32 isolated Pn^{3-} anions, 8 $[Pn_2]^{4-}$ "dumbbell"-shaped units, and 8 $[M_4Pn_{12}]^{26-}$ clusters to make an overall charge balanced compound. The M transition metal atom forms tetrahedra with the Pn atoms. In this structure type, two tetrahedra are linked in diborane-like $[M_2Pn_6]$ units and are further attached to another perpendicular $[M_2Pn_6]$ unit through a corner shared Pn atom to make the $[M_4Pn_{12}]^{26-}$ cluster. These clusters can be seen in polyhedral view below in **Figure 1.3**.

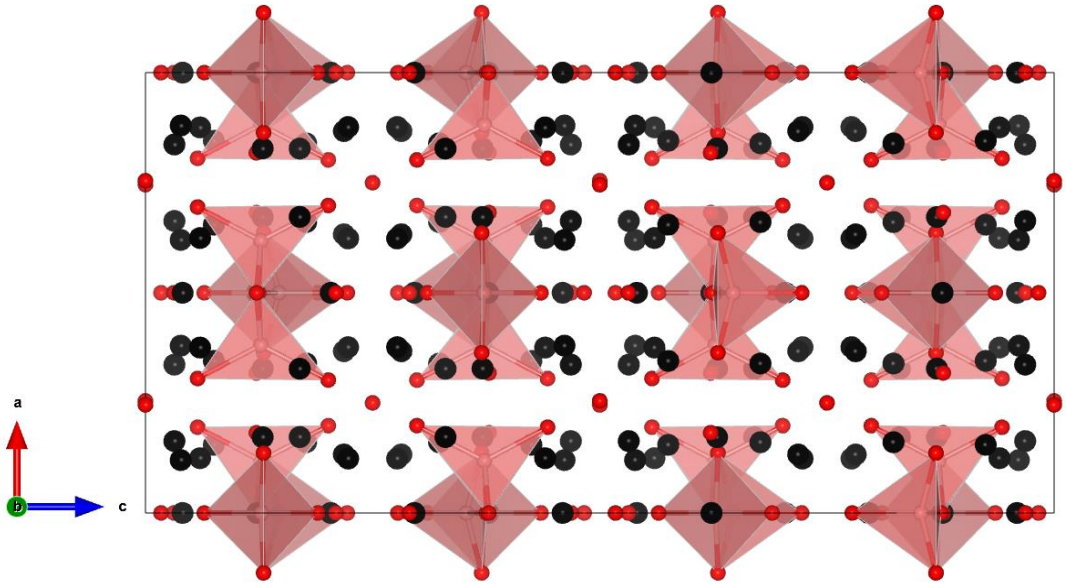

Figure 1.3: Orthorhombic (C*mce*) 21-4-18 unit cell ($Eu_{21}Zn_4Sb_{18}$) with *a* = 17.1256(11) Å, *b* = 17.9312(12) Å, *c* = 34.996(2) Å. Eu atoms are in black, Zn atoms are in pink, and Sb atoms are in red.

There are a total of 3 different compounds that crystallize in the *Cmce* space group which are $Ba_{21}Cd_4Sb_{18}$,[9] $Ba_{21}Cd_4Bi_{18}$,[9] and $Eu_{21}Zn_4Sb_{18}$.[10] The Ba-containing compounds were synthesized on stoichiometry in sealed Nb tubes and jacketed in fused silica ampoules for annealing.[9] Density of states calculations for $Ba_{21}Cd_4Sb_{18}$ show that the compound is expected to be a semiconductor with a band gap of ~0.5 eV.[9] The majority of states in the conduction band are made up of the Ba-6d orbitals while the valence band is made up mostly of Sb-5p states.[9] Physical property measurements for the Ba phases are yet to be reported.

The $Eu_{21}Zn_4Sb_{18}$ compound was synthesized using Pb flux methods where Eu:Zn:Sb:Pb were loaded in 21:4:18:100 stoichiometry.[10] Magnetic susceptibility measurements on the compound followed a Curie-Weiss law with an effective moment of 7.88 μ_B/mol Eu close to the expected value of 7.94 μ_B for a free Eu^{2+} ion.[10] There is an antiferromagnetic transition at ~8 K where the susceptibility reaches a maximum.[10]

Electrical resistivity on single crystals reveals a room temperature value around 0.02 Ω·m and Arrhenius fitting yields a band gap of around 0.2 eV.[10]

1.2.2 C2/*m* structure type

The second structure type of the family, the monoclinic C2/*m* (**Figure 1.4**) features again 29 crystallographic sites: 12 *A* sites, 3 *M* sites and 14 *Pn* sites. The Zintl formalism for this compound contains 84 A^{2+} cations, 16 Pn^{3-} anions, 6 $[Pn_2]^{4-}$ "dumbbell" shaped units, and 2 $[Mn_8Sb_{22}]^{48-}$ units. The $[Mn_8Sb_{22}]^{48-}$ units can be considered as 2 $[Mn_4Sb_{11}]^{25-}$ entities connected through a Sb-Sb bond. These $[Mn_4Sb_{11}]^{25-}$ entities are extremely similar to the $[M_4Pn_{12}]^{26-}$ clusters seen in the orthorhombic structure type, except here the clusters are connected together to form the $[Mn_8Sb_{22}]^{48-}$ unit and can be seen in polyhedral view below in **Figure 1.4**.

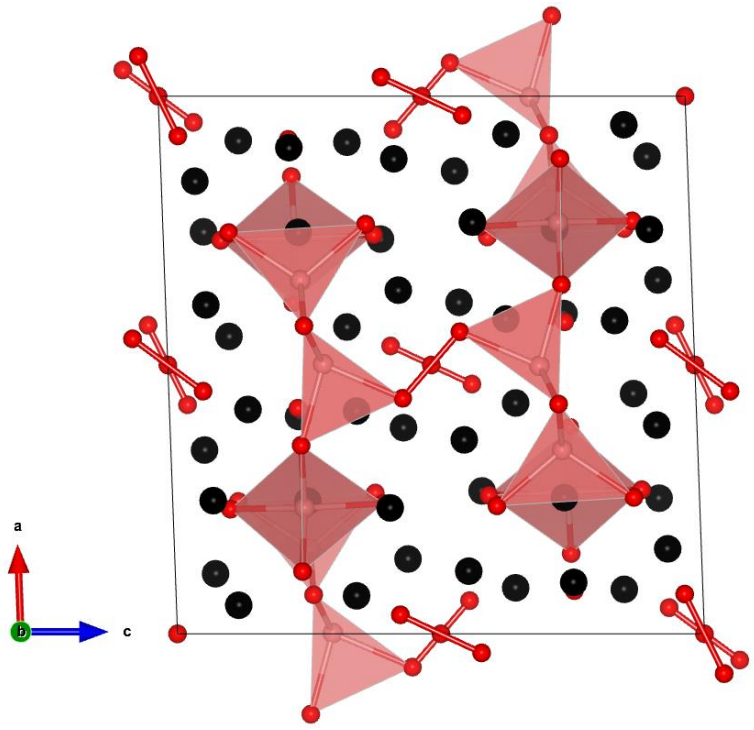

Figure 1.4: Monoclinic (C2/*m*) 21-4-18 unit cell (β-$Ca_{21}Mn_4Sb_{18}$) with *a* = 17.415(6) Å, *b* = 16.567(6) Å, *c* = 17.047(6) Å, β = 92.068(4)°. Ca atoms are in black, Mn atoms are in pink, and Sb atoms are in red.

There are 10 compounds in the C2/*m* structure type for 21-4-18 phases: $Sr_{21}Cd_4Bi_{18}$,[9] $Eu_{21}Cd_4Bi_{18}$,[9] $Ca_{21}Zn_4As_{18}$,[10] $Ca_{21}Zn_4Sb_{18}$,[10] $Eu_{21}Zn_4As_{18}$,[10] β-$Ca_{21}Mn_4Sb_{18}$,[11] $Sr_{21}Mn_4Sb_{18}$,[12] $Sr_{13}Eu_8Cd_3MnSb_{18}$,[13] $Eu_{21}Cd_4Sb_{18}$,[14] $Eu_{21}Mn_4Sb_{18}$.[14]

The $Sr_{21}Cd_4Bi_{18}$ and $Eu_{21}Cd_4Bi_{18}$ phases could not be synthesized on stoichiometry and were instead isolated from cadmium flux reactions with ratios of 22:150:18 of Sr(Eu):Cd:Bi.[9] Excess amounts of cation were included to mitigate formation of impurity phases. DFT calculations on the density of states show that the $Sr_{21}Cd_4Bi_{18}$ compound is a semiconductor with a band gap of approximately 0.5 eV.[9] The majority of states in the conduction band are made up of the Sr-6d orbitals while the valence band is made up mostly of Bi-6p states.[9] The related $Sr_{13}Eu_8Cd_3MnSb_{18}$ phase has also been synthesized through Sn flux where the elements Eu:Sr:Cd:Mn:Sb:Sn were loaded in 5:6:5:1:12:30 molar ratio.[13] Magnetic susceptibility measurements on the $Sr_{13}Eu_8Cd_3MnSb_{18}$ compound yielded a moment of 19.3 μ_B/mol f.u. and shows paramagnetic behavior down to 3.5 K where an antiferromagnetic type transition is observed.[13] Susceptibility measurements for the $Eu_{21}Cd_4Bi_{18}$ compound show Curie-Weiss behavior above 50 K with a calculated magnetic effective moment of 7.87 μ_B/mol Eu with an antiferromagnetic ordering around 8 K, similar to the $Eu_{21}Zn_4Sb_{18}$ phase.[9]

The $Ca_{21}Zn_4As_{18}$, $Ca_{21}Zn_4Sb_{18}$, and $Eu_{21}Zn_4As_{18}$ compounds were made in a similar fashion to the *Cmce* $Eu_{21}Zn_4Sb_{18}$ where Pb flux methods were used and the elements (Ca,Eu):Zn:(As,Sb):Pb were loaded in 21:4:18:100 stoichiometry.[10] The authors note that the flux reactions did not yield phase pure products but pre-reacting Zn-Pn into binary phases helped the phase purity of the crystals.[10] Physical properties have yet to be reported for these compounds.

The β-$Ca_{21}Mn_4Sb_{18}$ phase was discovered serendipitously as a minor product after loading Ca, Mn, and Sb in a welded Nb tube and annealing.[11] Attempts at isolating the compound on stoichiometry and through flux methods ended up yielding majority phase $Ca_{14}MnSb_{11}$.[11]

For $Sr_{21}Mn_4Sb_{18}$, the phase was synthesized from Sn flux where the elements Sr:Mn:Sb:Sn were loaded in 21:7:8:64 stoichiometry.[12] Magnetization measurements show very weak temperature dependence from 80K – 300K.[12] As the temperature drops below 80 K, magnetization decreases to a minimum before sharply increasing where this anomaly is reminiscent of spin-fluctuating systems.[12]

The last two compounds in the C2/*m* family are the $Eu_{21}Cd_4Sb_{18}$ and $Eu_{21}Mn_4Sb_{18}$ phases. These were synthesized from Pb flux where Eu:(Mn,Cd):Sb:Pb were loaded in 21:10:18:100 ratio. The large excess of Mn was necessary due to the low solubility in the flux. Both $Eu_{21}Cd_4Sb_{18}$ and $Eu_{21}Mn_4Sb_{18}$ show very similar magnetism behavior and follow Curie-Weiss behavior. The calculated moments from the fitting are 36.4 μ_B/mol f.u and 38.8 μ_B/mol f.u with antiferromagnetic transitions at 10K and 7K respectively. Electrical resistivity measurements for the two compounds both show semiconducting behavior where band gaps of 0.26 eV and 0.08 eV were obtained from Arrhenius fitting respectively. Room temperature resistivity values show orders of magnitude higher resistivity for the Cd analog (~6 Ω·m) compared to the Mn analog (~1.4×10^{-3} Ω·m).

1.2.3 C2/*c* Structure type

Finally, the last structure type of the 21-4-18 composition crystallizes in the monoclinic C2/*c* space group (**Figure 1.5**). This structure has 11 *A* sites, 4 *M* sites and 9 *Pn* sites. The structure contains 21 A^{2+} cations, 4 Pn^{3-} anions, 2 $[Pn_2]^{4-}$ anions and a $[M_4Pn_{10}]^{22-}$ polyanion. The $[Mn_4Sb_{10}]^{22-}$ unit can be described as 4 edge-sharing $MnSb_4$ tetrahedra, which will be referred to as a tetramer unit. These tetramer units extend along the b-axis and a polyhedral view of the structure can be seen below in **Figure 1.5**.

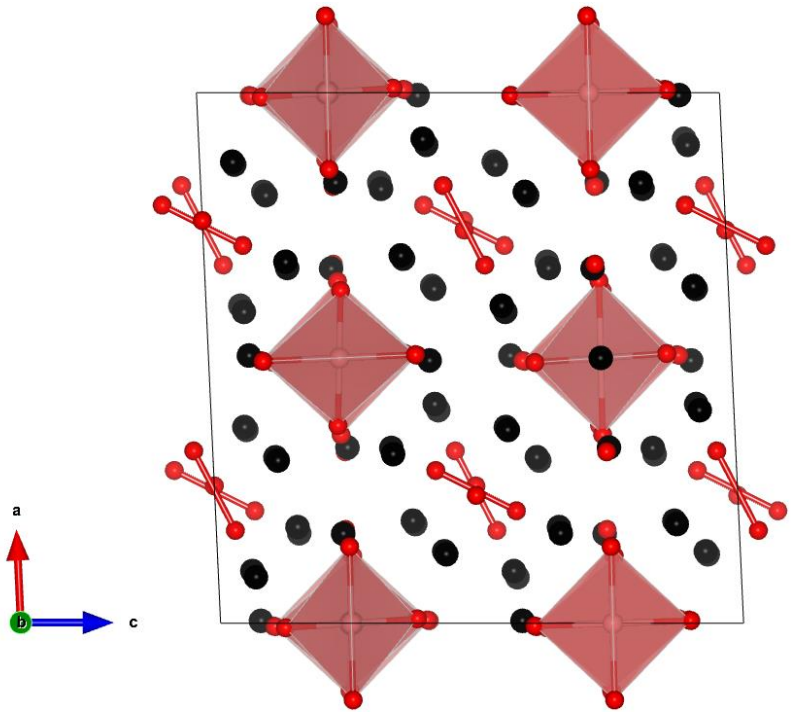

Figure 1.5: Monoclinic (C2/*c*) 21-4-18 unit cell ($Yb_{21}Mn_4Sb_{18}$) with *a* = 16.930(3) Å, *b* = 17.029(3) Å, *c* = 16.693(3) Å, β = 92.61(3)°. Yb atoms are in black, Mn atoms are in pink, and Sb atoms are in red.

There are a total of three compounds in the C*2/c* family of 21-4-18: α-$Ca_{21}Mn_4Sb_{18}$,[15] $Ca_{21}Mn_4Bi_{18}$,[11] and $Yb_{21}Mn_4Sb_{18}$.[14,16]

The α polymorph of $Ca_{21}Mn_4Sb_{18}$, α-$Ca_{21}Mn_4Sb_{18}$, has been synthesized through Sn flux methods where the elements Ca:Mn:Sb:Sn are loaded in 21:7:18:64 ratio into alumina crucibles.[15] The authors completed systematic synthetic studies where they report pure phase product with the aforementioned composition heating slowly (3°C/h) to 950°C, 1h dwell, and cooling to 800°C (3°C/h), followed by 1 week dwell before centrifugation.[15] Magnetization measurements suggest long range coupling ordering between the linear $[Mn_4Sb_{10}]^{22-}$ entities. The magnetic moment for the $[Mn_4Sb_{10}]^{22-}$ cluster is predicted to be 11.8 μ_B where $\mu_{eff}^2 = 4\mu_{Mn2+}^2$ but a magnetic moment of 4.04 μ_B is observed.[15] This suggests that there is long range ordering between the $[Mn_4Sb_{10}]^{22-}$ clusters that result in partial spin cancellation.[15] Electrical resistivity measurements reveal a band gap of 0.16 eV and semiconducting behavior.[15]

The $Ca_{21}Mn_4Bi_{18}$ phase was synthesized by sealing the elements in Nb tubes with a 3-fold excess of Mn and annealing. Reactions yielded multiple products and attempts to isolate the 21-4-18 phase were unsuccessful. Density functional theory calculations were done that show the system prefers an antiferromagnetic arrangement of the Mn atoms in the cluster as opposed to a ferromagnetic configuration. The density of states calculations also show that the band gap is approximately 0.2 eV and is predicted to be a semiconductor. Magnetic susceptibility measurements yield a similar moment to the α-$Ca_{21}Mn_4Sb_{18}$ compound (~4 μ_B).

Finally, the $Yb_{21}Mn_4Sb_{18}$ structure was first reported by Wang et al.[14] This compound is studied extensively in this dissertation and is explored in **Chapter 2** (He et al., Ref. 16), **Chapter 3** (He et al., Ref. 18) and **Chapter 4**. The synthesis was reported to be successful using Pb flux where the elements Yb:Mn:Sb:Pb were loaded in 21:4:18:80 ratio.[16] Loading reactions in Nb tubes on stoichiometry also yields pure phase product.[16] Thermoelectric properties were measured and show that the intrinsic phase without any doping yields a maximum zT of ~0.8 at 800 K. Single crystal x-ray diffraction, pair distribution function and synchrotron x-ray powder diffraction analysis show that the $Yb_{21}Mn_4Sb_{18}$ phase is extremely disordered on both an average and local scale. Density functional theory calculations on the band structure and density of states show that the material is half-metallic at low temperatures with Sb contributing most of the states in the valence band and Mn contributing most of the states in the conduction band.[16]

Given the complexity of all the different structure types, the 21-4-18 compounds are all expected to have very low starting thermal conductivities making this family a good space to explore for thermoelectric property optimization. This has been proven to be the case in the $Yb_{21}Mn_4Sb_{18}$ system, the first 21-4-18 compound measured for its thermoelectric properties.[16,18] The thermal conductivity of $Yb_{21}Mn_4Sb_{18}$ reaches a minimum value of ~0.4 $Wm^{-1}K^{-1}$ and has a maximum zT value of ~0.8 at 800 K.[16] In depth studies on the structure of this 21-4-18 system show that it is full of point defects and vacancies which contribute

to the extremely low thermal conductivity.[16,18] This class of compounds has promise to become one of the top materials in this temperature range after optimization.

1.3 Intermediate Valency

Intermediate valence compounds contain atoms that have a fluctuating valence state where the electron configuration can be found in state n or n-1 (where n is the number of electrons) at any given moment in time. Because of the fluctuation, there is an average valence of the intermediate valent atom that is a non-integer value that can be defined. This effect has been well documented in a number of compounds such as $YbAl_3$,[19] $Yb_3(Rh_{1-x}Co_x)_4Ge_{13}$,[20] $CePd_3$[21] and is studied in-depth for $Yb_{14}MnSb_{11}$ in **Chapter 6** (He et al., Ref. 22).

These effects are mostly found (but not necessarily) in compounds that contain Ce, Eu, Yb where for these rare-earth metals, the energy difference between E_n and E_{n-1} is smallest.[23] The physical origin of the energy fluctuation occurs from the interaction of the conduction electrons within the compound with the local 4*f* shell where only energies on the order of 0.02 eV are enough to induce the transition.[24] At temperatures much higher than the spin fluctuation temperature ($T >> T_{sf}$), the transitions between the two states can be induced by thermal energy. It is only at low temperatures ($T << T_{sf}$) where the quantum mechanical fluctuations dominate and present themselves. This can be probed through electrical resistivity measurements where the intermediate valency typically show up as minima and in magnetic susceptibility measurements typically seen as a broad hump.

The magnetic susceptibility of an intermediate valent compound can be described with the following equations:

$$\chi_{ICF} = \frac{N\left(\mu_n^2 \nu(T) + \mu_{n-1}^2\left(1-\nu(T)\right)\right)}{3k_B(T+T_{sf})}$$

Equation 1.5: Intermediate valence susceptibility.

$$\nu(T) = \frac{2J_n + 1}{(2J_n + 1) + (2J_{n-1} + 1)e^{-E_{ex}/k_B(T+T_{sf})}}$$

Equation 1.6 Fractional valence calculation.

where $\nu(T)$ is the fractional occupation of the E_n state, μ_n and μ_{n-1} are the effective magnetic moments of the two states, $2J_n + 1$ and $2J_{n-1} + 1$ are the degeneracies of the two energy levels E_n and E_{n-1}, E_{ex} is the energy required for excitation i.e. $E_{ex} = E_n - E_{n-1}$.

In the case for Yb, then the fluctuation of energy states would be between $4f^{13}$ (Yb^{3+}) and $4f^{14}$ (Yb^{2+}). Since the $4f^{14}$ is non-magnetic, it will have a $\mu_{eff} = 0$ and $J = 0$ while $4f^{13}$ has $\mu_{eff} = 4.54\ \mu_B$ and $J = \frac{7}{2}$. This simplifies the above equations into:

$$\chi_{ICF} = \frac{N\left(4.54\mu_B^2\left(1 - \nu(T)\right)\right)}{3k_B(T + T_{sf})}$$

Equation 1.7: Intermediate valence susceptibility for Yb case.

$$\nu(T) = \frac{1}{1 + 8e^{-E_{ex}/k_B(T+T_{sf})}}$$

Equation 1.8: Fractional valence calculation for Yb case.

Although these equations cover the intermediate valence portion of the magnetic susceptibility, it is often necessary to include them in conjunction with a Curie-Weiss law (χ_{CW}) and χ_0 component to describe the behavior over the whole temperature range (see **Figure 1.6**) as follows:

$$\chi(T) = \chi_{ICF}(T) + \chi_{CW}(T) + \chi_0$$

Equation 1.9: Total magnetic susceptibility including a Curie-Weiss component and background.

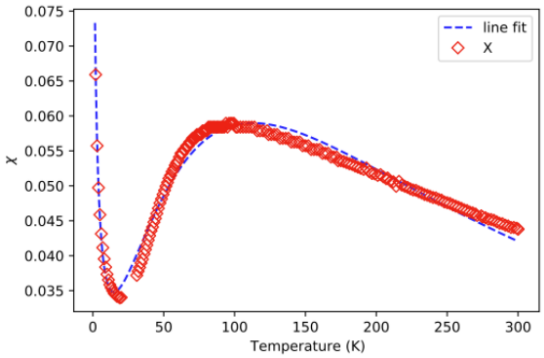

Figure 1.6: Intermediate valence fitting of the magnetic susceptibility (plotted in units of emu/mol Yb) using **Equation 1.9**.

In the context of thermoelectric materials, understanding the intermediate valent nature of the atoms can help in the optimization of the electrical resistivity, Seebeck, and thermal conductivity of the system. The degree of intermediate valence in the material will change the effective carrier concentration within the material. For example, in the case of Yb, substitutions or dopants that result in an increase in unit cell volume would be expected to shift the overall valence state lower since Yb^{2+} is larger than Yb^{3+}. Proper control of the valence can in theory be exploited to enhance the Seebeck coefficient especially since the 4*f* states of Yb fall close to the Fermi level and through the Mott relation, the large density of states contributed form the 4*f* states have a direct impact on the magnitude of Seebeck coefficient. In addition, the difference in local environments that arise from the valence fluctuation would also lead to lower thermal conductivity due to the non-periodicity and larger phonon scattering. The idea of using the intermediate valent nature of elements has been visited previously in some systems. [25,26]

Chapter 2

Structural Complexity and High Thermoelectric Performance of the Zintl Phase: $Yb_{21}Mn_4Sb_{18}$

Allan He[1], Sabah, K. Bux[2], Yufei Hu[1], David Uhl[2], Li Li[1,3], Davide Donadio[1] and Susan M. Kauzlarich[1*]

[1]Department of Chemistry, One Shields Ave, University of California, Davis, California 95616, USA

[2]Jet Propulsion Laboratory, California Institute of Technology, 4800 Oak Grove Drive, MS 277-207, Pasadena, California 91125, USA

[3]State Key Laboratory of Coordination Chemistry, School of Chemistry and Chemical Engineering, Collaborative Innovation Center of Advanced Microstructures, Nanjing University, Nanjing 210023, P. R. China

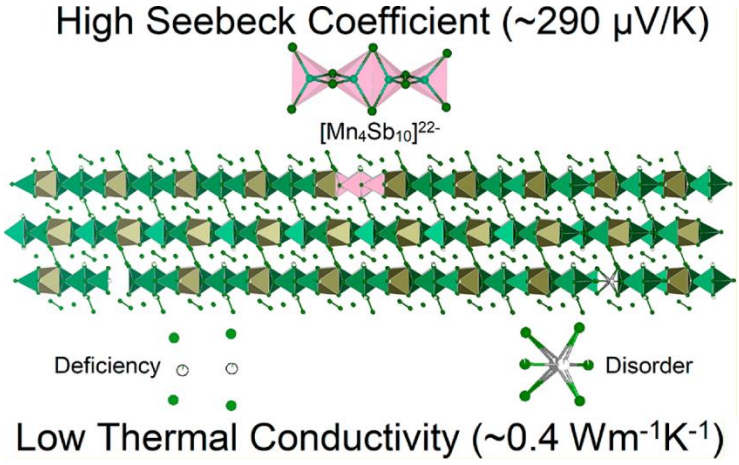

Published in *Chemistry of Materials*, **2019**, 31, 8076 – 8086.

Allan He conducted all of the synthesis and characterization of the compounds. Sabah K. Bux and David Uhl contributed to initial synthetic conditions and thermoelectric properties, interpretation of thermoelectric properties. Yufei Hu and Li Li helped with isolation of $Yb_{21}Mn_4Sb_{18}$ crystals and initial structural solution. Davide Donadio provided the density functional theory calculations and interpretation of the electronic structure.

This chapter was adapted with permission from:

He, A.; Bux, S. K.; Hu, Y.; Uhl, D.; Li, L.; Donadio, D.; Kauzlarich, S. M. Structural Complexity and High Thermoelectric Performance of the Zintl Phase: $Yb_{21}Mn_4Sb_{18}$. *Chemistry of Materials*. **2019**, *31(19)*, 8076-8086.

2.1 Abstract

Thermoelectric materials are a unique class of compounds that can recycle energy through conversion of heat into electrical energy. A new 21−4−18 Zintl phase has been discovered in the Yb−Mn−Sb system with high performance in the mid-to-high temperature regime. The efficiency of the $Yb_{21}Mn_4Sb_{18}$ results mainly from its large Seebeck coefficient (∼290 μVK^{-1} at 650 K) and extremely low thermal conductivity (∼0.4 $Wm^{-1}K^{-1}$). The complex crystal structure has been studied through single crystal X-ray diffraction, synchrotron powder X-ray diffraction, and pair distribution function (PDF) analysis using time-of-flight neutron diffraction revealing positional disorder on several sites. Electronic structure calculations of the band structure and the partial spin-density of states reveal that states near the Fermi level are contributed mostly by the Mn and Sb atoms that participate in the $[Mn_4Sb_{10}]^{22-}$ motif of the structure. The band structure confirms the p-type semiconducting nature of this material. The optimization of the hole carrier concentration was tuned according to a single parabolic band model through Na doping on the Yb site ($Yb_{21-x}Na_xMn_4Sb_{18}$, x = 0, 0.2, 0.4) showing an improvement in zT over the whole temperature range. A maximum zT ≈ 0.8 at 800 K is obtained for the x = 0.4 sample and increases the ZT_{avg} from 0.34 to 0.49 (over the entire temperature range) compared to the undoped sample

2.2 Introduction

Thermoelectric materials are a class of materials that can harvest energy by converting heat into electricity. Their unique ability has found many applications in industry, including the use of Peltier coolers to replace gas-based refrigeration technology thereby eliminating the use of chlorofluorocarbons and waste heat recovery in automobiles to increase fuel efficiency, as well as in deep-space missions where long-term, reliable power generation is necessary for on-board instruments. In order to deploy its full potential and to make thermoelectric technology more widespread, materials with higher thermoelectric

efficiency must be discovered. The performance of a material is based on its figure of merit, zT (**Equation 2.1**):

$$zT = \frac{\alpha^2 T}{\rho(\kappa_l + \kappa_e)}$$

Equation 2.1: The figure of merit, zT, shown with electrical and lattice thermal conductivity where α, T, ρ, κ_l, and κ_e are the Seebeck coefficient, temperature, resistivity, lattice, and electrical components of the thermal conductivity, respectively.

Zintl phases have been shown to be a very fruitful category for thermoelectric material discovery. [27,28] Typically, they are defined as semiconducting, charge balanced compounds with complete electron transfer between the more electropositive donor and the electronegative acceptor.[29,30] The electrons provided by the electropositive elements are sometimes not enough to compensate the more electronegative counterpart, thus leading to the formation of covalent bonding frameworks between anions. This combination of ionic and covalent bonding can lead to complex structure types (e.g., $Yb_{14}MnSb_{11}$,[4,31–33] $Zn_{13}Sb_{10}$,[34–36] $Ba_8Ga_{16}Ge_{30}$,[37,38] and $CeFe_4Sb_{12}$[39] to name a few) with intrinsically low thermal conductivity, making these materials a great starting point for optimization. Currently in the literature, Zintl phase structures with composition $A_{21}M_4Pn_{18}$ (referred to as 21−4−18) have been reported, such as $A_{21}Cd_4Pn_{18}$ (A = Eu, Sr, Ba; Pn = Sb, Bi),[9] $A_{21}Zn_4Pn_{18}$ (A = Ca, Eu; Pn = As, Sb),[10] and $Ca_{21}Mn_4(Sb,Bi)_{18}$.[11,15] There are several different structure types within this class of compounds, which crystallize in space groups C2/*c*, C2/*m*, and C*mce*. The structures all contain MPn_4 tetrahedral units linked in various manners. Attention has been paid mainly to the structural and magnetic properties of these complex phases; however, their thermoelectric properties have yet to be characterized.

Here, we report the structural and thermoelectric properties for a new member of the 21−4−18 family: $Yb_{21}Mn_4Sb_{18}$, with a high figure of merit in the mid-to-high temperature regime. $Yb_{21}Mn_4Sb_{18}$ adds a new composition to this class of Zintl phases, crystallizing in the α-$Ca_{21}Mn_4Sb_{18}$ structure type (monoclinic,

space group C2/*c*). The C2/*c* structure can be described as containing 4 discrete units per formula unit: 1 linear $[Mn_4Sb_{10}]^{22-}$ anion, 2 dumbbell-shaped $[Sb_2]^{4-}$ anions, 4 individual Sb^{3-} anions, and 21 Yb^{2+} cations (see **Figure A1.1**, in the **Appendix 1**). The expected low thermal conductivity, due to the large primitive cell, and potentially high Seebeck coefficient, because of the high density of states close to the Fermi level,[11] make this phase a good starting point for optimization of thermal and electrical transport properties. Optimization of $Yb_{21}Mn_4Sb_{18}$ was pursued through shifting of the Fermi level by changing the carrier concentration. The single parabolic band model was used to approximate the optimum carrier concentration and was accomplished through Na doping on the Yb site ($Yb_{21-x}Na_xMn_4Sb_{18}$, x = 0, 0.2, 0.4).

2.3 Experimental

2.3.1 Synthesis of $Yb_{21}Mn_4Sb_{18}$

Bulk powder samples were synthesized through mechanical milling for homogenization and spark plasma sintering for densification. Stoichiometric amounts of Yb filings (Metall Rare Earth Limited, 99.99%), Mn pieces (Alfa Aesar, 99.95%), and Sb shots (Alfa Aesar, 99.999%) were placed inside a stainless steel ball mill with total sample mass of 10 g. The ball mill was heat sealed inside a Mylar bag, and the materials were homogenized for one hour in a SPEX 8000 M High-Energy ball mill. The resultant mixture was ground thoroughly with an agate mortar and pestle inside an Ar atmosphere drybox (<1 ppm H_2O) and milled for an additional hour, as described above. The powder was transferred into 8 cm long Nb tubes inside the glovebox and sealed in an arc welder under partial Ar pressure. The Nb tubes were further encapsulated inside evacuated fused silica tubes. The reaction vessel was heated at 100 °C/h to 650 °C, sintered for 7 days, and allowed to slowly cool down to room temperature in the furnace. The reaction vessel was then transferred and opened in a drybox and ground finely, and the sintered powder was filtered through a 200 mesh sieve. Approximately 3 g of material was put into a 12.7 mm graphite die with graphite spacers and transferred into the chamber of a Dr. Sinter SPS-2050 spark plasma sintering (SPS) system for

densification. Prior to starting the heating profile, the chamber was evacuated until ~10 Pa, and a pressure of 6 kN was applied onto the die. To prevent overshooting, the temperature was first increased to 525 °C in 15 min, followed by an increase to 575 °C in 1 min where it stayed for 30 min. The displacement of the die was monitored closely, and upon compression of the material (~430 °C), the pressure was adjusted monotonically to 11 kN. Single crystal growth was successful using Pb flux. Elemental Yb metal filings (Metall Rare Earth Limited, 99.99%), Mn pieces (Alfa Aesar, 99.95%), Sb shots (Alfa Aesar, 99.999%), and Pb shots (Alfa Aesar, 99.99%) were loaded into Al_2O_3 crucibles[40] in a 21:4:18:80 ratio. Generous amounts of quartz wool were placed on both the top and the bottom of the crucible, and the reaction was sealed into evacuated quartz ampoules. The sample was heated to 500°C at 120 °C/h (2 h dwell) and afterward brought to 700°C at 120°C/h before cooling down to 400°C at 2°C/h. The sample was quickly heated to 500°C, and the molten flux was removed through centrifugation. Small single crystals were obtained which appeared irregularly shaped, black, and reflective (see **Figure A1.2**).

2.3.2 Single Crystal X-ray Diffraction

Single crystal diffraction data were obtained on $Yb_{21}Mn_4Sb_{18}$ at 100 K using a Bruker APEX II diffractometer with Mo Kα (λ = 0.71073 Å) radiation. Crystals were chosen under mineral oil and mounted on MiTeGen microloops. Space group determination was done using XPREP, and structural solutions were completed through direct methods with SHELXS and refined using the SHELXL software.[41]

2.3.3 Synchrotron X-ray Powder Diffraction

Synchrotron data were collected at the 11-BM-B beamline of the Advanced Photon Source (APS) at Argonne National Laboratory (ANL) with λ = 0.412736 Å at room temperature. The sample was placed into Kapton capillaries, and the scattering data were collected in transmission mode. The large absorption

coefficient of this material (51.279 mm^{-1}) required dilution of the sample with SiO_2 (approximately 1:80 ratio of $Yb_{21}Mn_4Sb_{18}$:SiO_2) to mitigate problems during Rietveld analysis.

2.3.4 Compositional Analysis

Samples were mounted in discs of epoxy resin and polished to a 0.05 μm finish. Elemental analysis was characterized through energy dispersive spectroscopy (EDS) using a FEI Scios DualBeam SEM/FIB with a window-less Oxford Instruments X-max50, 50 mm^2 silicon drift detector. Secondary electron images were collected with an accelerating voltage of 20 kV using an Everhart-Thornley detector. Elemental mapping was performed on the pelletized samples to check homogeneity. Samples were cross-checked with electron microprobe analysis (EMPA) to verify the composition of the $Yb_{21}Mn_4Sb_{18}$ phase. Quantitative elemental analysis was performed using a Cameca SX-100 electron probe microanalyzer with wavelength dispersive spectrometers using 15 kV accelerating potential. Compositions of samples were characterized with respect to calibrated standards of $Yb_{14}MnSb_{11}$, Sb metal, and Mn metal.

2.3.5 Time-of-Flight Neutron Powder Diffraction

Time-of-flight neutron scattering data were collected on the NOMAD powder diffraction beamline at the Spallation Neutron Source (SNS) of Oak Ridge National Laboratory (ORNL) at room temperature. The polycrystalline sample was placed inside 3 mm diameter quartz capillaries for the total scattering experiment. NOMAD data were reduced using beamline software[42] to be used for Rietveld refinement and pair distribution function (PDF) analysis. The reduced pair distribution function (G(r), **Equation 2.2**) was obtained through a sine Fourier transformation of S(Q) according to:

$$G(r) = 4\pi r[\rho(r) - \rho_0] = \frac{2}{\pi}\int_0^\infty Q[S(Q) - 1]\sin(Qr)\,dQ$$

Equation 2.2: The reduced pair distribution function, G(r).

where ρ(r) represents the atomic pair density and ρ_0 is the average atomic number density. Neutron diffraction data and PDF refinement were performed with TOPAS software v5 and PDFgui.[43]

2.3.6 Thermoelectric Property Measurements

A Linseis LSR-3 instrument was used to measure resistivity and Seebeck coefficient employing the four-probe method from 350 K to 800 K under He atmosphere. The sample measured was bar-shaped (~10 mm × 2 mm × 2 mm) using 8 mm probes and polished prior to measurement. Multiple samples were measured to ensure reproducibility, and the data was cross-checked by measurements at JPL. There, the Seebeck coefficient was measured using a light pulse technique as described in the following reference using W/Nb thermocouples.[44] Electrical resistivity (ρ) was measured using the van der Pauw (VDP) technique with a current of 100 mA, and the Hall coefficient was measured with a 0.75 T field and tungsten pressure contacts under high vacuum.[45] A Netzsch LFA 457 was used to measure thermal diffusivity under vacuum up to 800 K on sample disks, polished flat, and coated with graphite. Heat capacity was estimated using the Dulong–Petit method to calculate thermal conductivity.

2.3.7 Electronic Structure Theory

Spin-polarized total energy and electronic band structure calculations were carried out using density functional theory (DFT) with a semilocal exchange and correlation functional in the generalized gradient approximation.[46] The Kohn− Sham orbitals for the valence electrons are expanded on a plane wave basis set with a cutoff energy of 45 Ry, and the core electrons, including the f-electrons of Yb, are taken into account by Project Augmented Wave pseudopotentials. The first Brillouin zone of the 86-atom primitive cell is integrated over a uniform 4 × 4 × 3 k-points mesh[47] in the geometry optimization run and over a

thicker 6 × 6 × 4 k-point mesh for the subsequent self-consistent electronic structure calculations. All the calculations are carried out using the open-source Quantum-Espresso package v6.3.[48]

2.4 Results and Discussion

2.4.1 Yb-Mn-Sb Systems

An extensive amount of work has already been reported for the Yb−Mn−Sb system on the $YbMn_2Sb_2$ phase,[49] the $Yb_9Mn_{4+x}Sb_9$ phase,[50–52] and the $Yb_{14}MnSb_{11}$ phase.[5–8] The composition for $Yb_{21}Mn_4Sb_{18}$ is indicated by a star in **Figure 2.1**. An overarching structural theme among these phases is the $MnSb_4$ tetrahedra that are either isolated or linked in various manners. The progression of the structure and bonding of these tetrahedra with the stoichiometry change is shown in **Figure 2.1**. The $YbMn_2Sb_2$ structure consists of covalently bonded Mn−Sb tetrahedra layers with Yb^{2+} occupying the interplanar spacings. Very similar to the $YbMn_2Sb_2$ structure is the $YbMnSb_2$ phase where the structure is basically the same but in addition have Sb planes that separate the cationic Yb^{2+} and layers of Mn-Sb tetrahedral layers. As we move to the more Mn deficient $Yb_9Mn_{4+x}Sb_9$ phase, the crystal structure changes to form interconnected ribbons of the Mn−Sb tetrahedra. More Mn deficient still is the 21−4−18 phase, where the infinitely connected chains of Mn−Sb tetrahedra start to become disconnected entities. The signature 21−4−18 structural motifs are the $[Mn_4Sb_{10}]^{22-}$, edge-sharing tetramer units that extend along the b-axis, indicated by the green polyhedra. The $Yb_{10}MnSb_9$ phase features 2-unit edge-sharing $MnSb_4$ tetrahedra along with several disordered point defects. Finally, in the most Mn deficient phase so far in the Yb−Mn−Sb system, the $Yb_{14}MnSb_{11}$ phase, the large number of Sb atoms to Mn brings about the appearance of $[Sb_3]^{7-}$ trimers and isolated $[MnSb_4]^{9-}$ tetrahedra. It has been demonstrated that $Yb_{14}MnSb_{11}$ is one of the best p-type thermoelectric materials in the high temperature region (800−1200 K) because of its low electrical resistivity and thermal conductivity.[7]

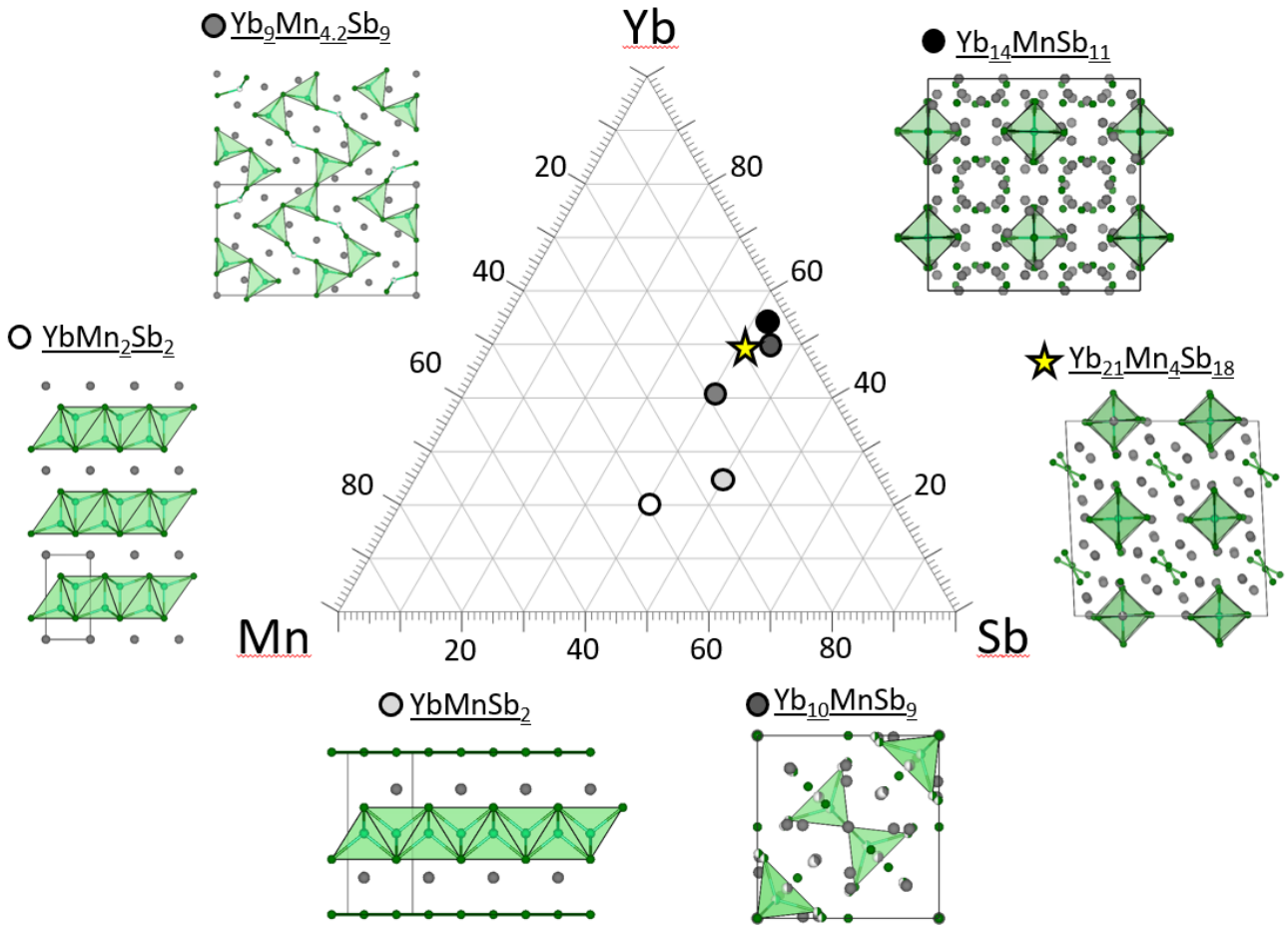

Figure 2.1: Phase diagram of current existing compounds in the Yb−Mn−Sb ternary system. The $YbMn_2Sb_2$, $Yb_9Mn_{4.2}Sb_9$, $Yb_{21}Mn_4Sb_{18}$, and $Yb_{14}MnSb_{11}$ phases are indicated with open circle, gray circle, star, and black circle respectively.

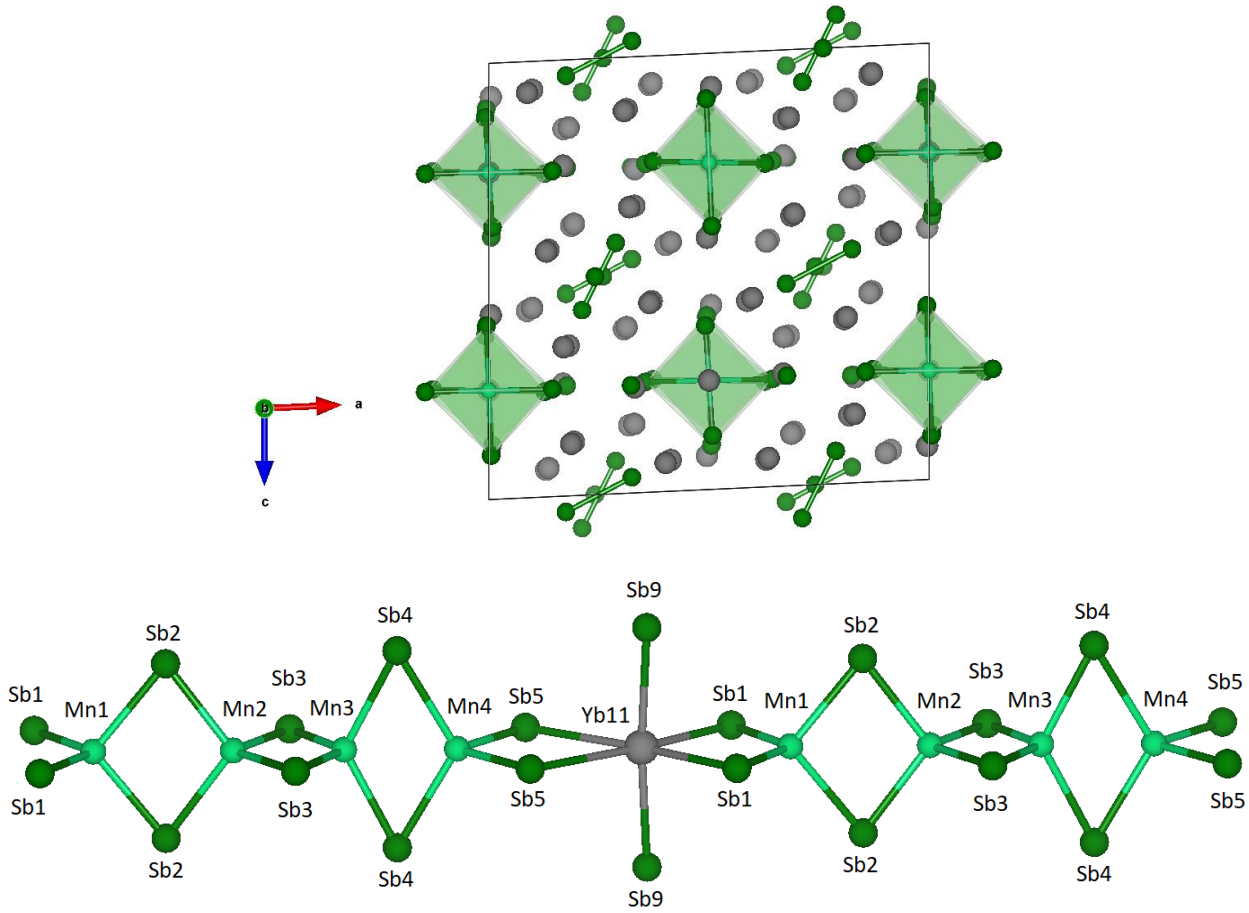

Figure 2.2: View of the $Yb_{21}Mn_4Sb_{18}$ structure highlighting the $[Mn_4Sb_{10}]^{22-}$ units and $[Sb_2]^{4-}$ dimers projected down the b-axis, shown without disorder for clarity (top). A view of the overarching 21−4−18 motif of $[Mn_4Sb_{10}]^{22-}$ tetramer units linked through an octahedrally coordinated Yb atom (bottom).

2.4.2 Crystal Structure

Structural solution and refinement of single crystal data (results summarized in the **Appendix 1**, **Table A1.1**) show that $Yb_{21}Mn_4Sb_{18}$ (**Figure 2.2**) crystallizes with monoclinic symmetry (space group C2/c). In the ordered structure, there are a total of 24 crystallographic sites (11 Yb sites, 9 Sb sites, and 4 Mn sites). Included in the unit cell are 1 $[Mn_4Sb_{10}]^{22-}$ unit (two tetramer units shown linked through the octahedral Yb11 atom), 2 $[Sb_2]^{4-}$ dimers, 4 isolated Sb^{3-} anions, and 21 Yb^{2+}, satisfying the Zintl−Klemm formalism of being a charge balanced compound. The $[Mn_4Sb_{10}]^{22-}$ subunits are composed of edge-shared $MnSb_4$

tetrahedra, are an overarching motif of the α-$Ca_{21}Mn_4Sb_{18}$ structure type and play a large role in the good transport properties of this compound. The valence band states near the Fermi level are largely composed from atoms in this motif. The stability of this structure is confirmed by DFT calculations, which also shows that the structure is sustained by the magnetic ordering of the d-electrons of Mn. A geometry optimization imposing no magnetization leads to the dimerization of Mn atoms and to a substantial distortion of the crystal.

The final structural solution determined experimentally indicated positional disorder and deficiencies on several sites, and the intrinsic nature of these disorder and deficiencies was verified with several independent high-quality crystals. Initially, a perfectly ordered model of the crystal structure was assumed; however, residual electron density was found to gather close to the Yb11 site, between the Mn2/Mn3 sites, the Sb3 site, and the Sb9 site (shown in **Figure 2.2**). The magnitude of these residual densities was too large to ignore as noise (∼6−8 e−/$Å^3$), and due to their close proximity to existing sites (∼1 Å), were modeled as site disorder (Yb12, Mn5, Sb11, Sb10). **Table A1.2** (**Appendix 1**) provides the atomic positions and atomic displacement parameters for all of the sites. Starting with the Yb site disorder, analysis of all Yb− Sb polyhedral volumes shows that the Yb11 site has the largest polyhedral volume out of all of the Yb sites which allows for rattling of the Yb atom between the extremum positions of the Yb11 site and Yb12 site. The occupancies of these two sites were allowed to refine freely and converged to be 91.6(2)% and 2.5(1)%, respectively, making the overall Yb site slightly deficient. When the Yb11 or Yb12 sites are not occupied, the Sb9 atoms are able to relax closer to the center of the octahedron to the Sb10 position, causing the Sb site to be disordered as well. The Sb site is disordered only when there is a Yb deficiency, and therefore, the Sb9/Sb10 site were refined to be occupied (91.6(2)% + 2.5(1)% = 94.2(2)%) 94.2(2)%/5.8(2)% respectively. The SI displays a close-up of the Yb11/Yb12 and Sb9/Sb10 disorder (**Figure A1.3**) and the second region of disorder (**Figure A1.4**), which occurs in the middle of the tetramer chain.

Residual electron density was observed to gather near the middle of the Mn2/Mn3 atoms and the Sb3 site from the refinement. In the case that the Mn5 site is occupied, it is not possible for any of the Mn2 and Mn3 sites to be occupied, for the resultant bond distance would be too small (Mn3−Mn5: 1.138(2) Å, Mn2−Mn5: 1.587(2) Å). During the refinement, the Mn2/Mn3 atoms were assumed to contribute equally to the Mn5 site and were constrained to have the same site occupancy. Therefore, the refined occupancies of the Mn2/Mn3/Mn5 sites are 92.3(3)%/92.3(3)%/7.7(3)% respectively. Upon occupation of the Mn5 site, the rigidity of the tetramer chain falls apart because of the disconnect (see SI), and the Sb3 atoms are able to relax further out to occupy the Sb11 position. The Sb11 position was restrained to have the same occupancy as the Mn5 atom resulting in the Sb3/Sb11 position being occupied 92.3(3)%/ 7.7(3)%, respectively.

2.4.3 Elemental Composition

Ball-milling of the elemental reagents followed by spark plasma sintering resulted in >95% dense pellets. Secondary electron imaging confirms the high density of the sample, and elemental mapping reveals a homogeneous distribution of elements after processing (**Figure 2.3**). Compositions of the pelletized samples were found to be within ~ 1 at. % of nominal stoichiometry (see **Appendix 1**, **Table A1.3**) according to EDS and WDS studies for all samples.

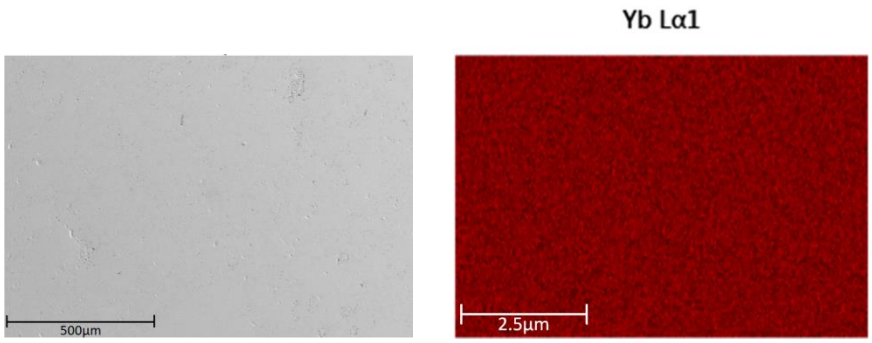

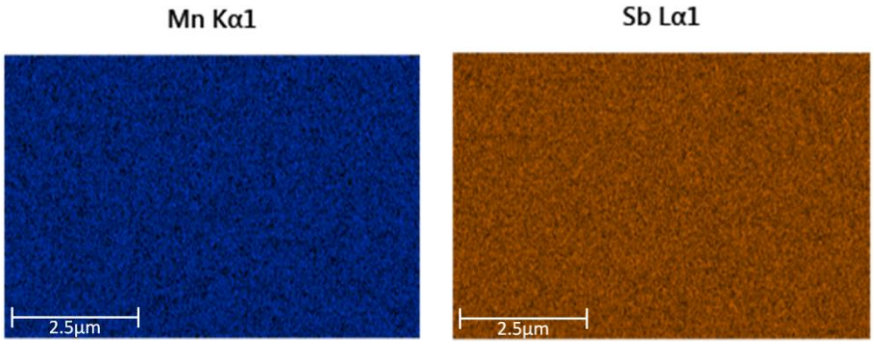

Figure 2.3: Secondary electron image collected with a 20 kV electron beam confirming the high density of the polycrystalline samples. Elemental mapping of Yb (red), Mn (blue), and Sb (orange) shows homogeneity across the whole sample.

Rietveld refinement (see **Appendix 1**, **Table A1.4**) of the synchrotron powder X-ray diffraction data indicate that the powder samples are single phase (**Figure 2.4a**). The lattice parameters obtained from Rietveld refinement (a = 17.02725(9), b = 17.04802(9), c = 16.77150(9) Å, β = 92.7936(4)°, 298 K) were observed to be larger than those obtained in the single crystal refinement (a = 16.930(3), b = 17.029(3), c = 16.693(3) Å, β = 92.61(3)°, 100 K) and attributed to the difference in data collection temperature. The positional disorder on the Yb11/12, Sb9/10, Mn2/3/5, and Sb3/Sb11 sites proved difficult to refine from powder X-ray diffraction and gave inconsistent results, likely due to the large overlap of peaks in the powder pattern leading to large displacement factors. These sites could not be reliably determined to exist from powder diffraction and were therefore removed from the Rietveld refinement. The Yb11 site did not show any appreciable deficiency and was assumed to be fully occupied. The Mn2 and Mn3 sites refined best being deficient and were constrained to have equal occupancies which refined to be 94(1)%.

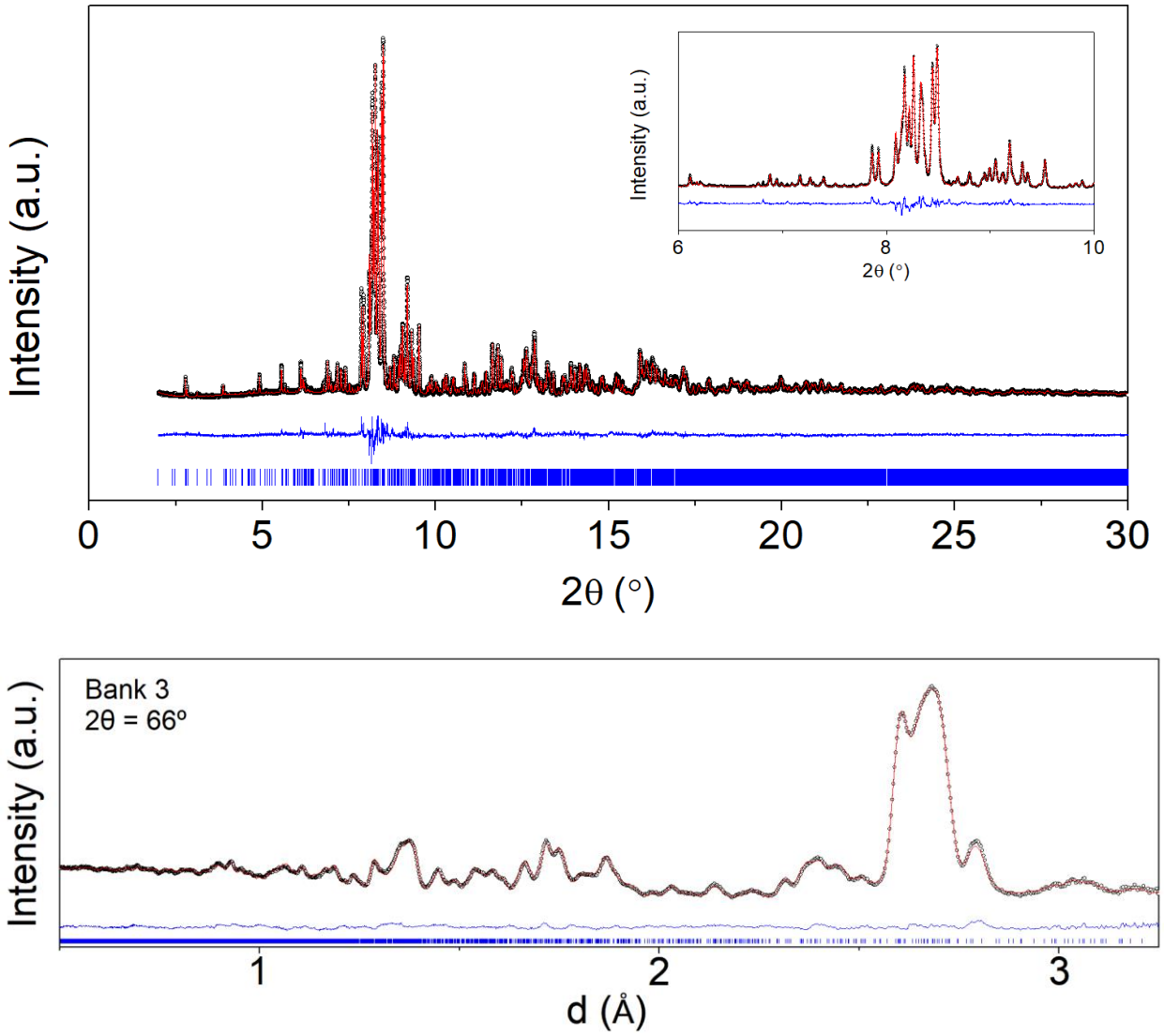

Figure 2.4: Rietveld refinement of synchrotron X-ray diffraction (λ = 0.412736 Å) data at room temperature for $Yb_{21}Mn_4Sb_{18}$ (top) and time-of-flight neutron diffraction (bottom). Refined model is shown in red, experimental data are shown as black dots, and the difference curve is shown in blue. The expected peak positions are shown by the blue tick marks.

The structural disorder was further characterized through total neutron scattering studies. Time-of-flight neutron diffraction data (**Figure 2.4b**) were collected using a high Q range for pair distribution function analysis; refer to the **Appendix 1**, **Figure A1.5** for the S(Q) − 1 function. The converted G(r) function shows distinct features out to large distances (>150 Å), indicating a high degree of crystallinity in the sample.

The total intensity of a peak in G(r) is given by the expression $I_{tot} = \sum_{x,y} N_{x,y} b_x b_y$ where $N_{x,y}$ is the number of atom pairs that contribute to the peak and b_x and b_y are the scattering lengths of atom x and atom y. The broadness of each peak in the PDF is a result of the contribution of many different atomic pairs, where the distribution of atom pairs is exemplified in the short-r region shown in **Figure 2.5** (selected bond distance ranges obtained from crystallography studies presented in **Table 2.1**).

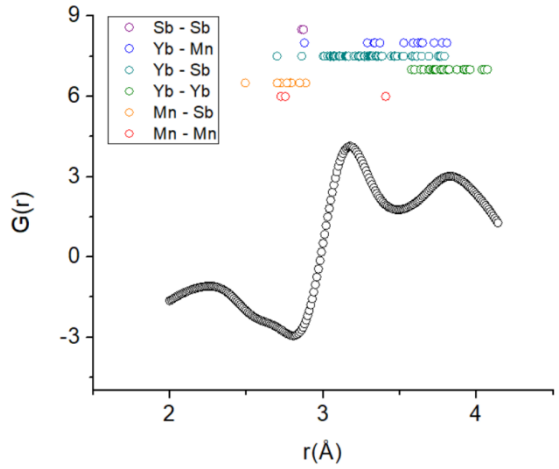

Figure 2.5: Short-r region (2 Å–4 Å) of G(r) for $Yb_{21}Mn_4Sb_{18}$ at 298 K. Peaks below 2 Å were considered to be unphysical and were not included in the analysis. Distances obtained from X-ray crystallography are plotted on here for reference.

Table 2.1: Distance Ranges for Selected Nearest Neighbor Atom Pairs Determined from Single Crystal X-ray Studies of $Yb_{21}Mn_4Sb_{18}$.

Atom Pair	**Distance Range (Å)**
Mn – Sb	2.496(1) – 2.888(1)
Mn – Mn	2.721(3) – 3.409(3)
Sb – Sb	2.860(1) – 2.872(1)
Yb – Sb	2.68(1) – 3.791(1)
Yb – Mn	2.89(3) – 3.807(1)
Yb – Yb	3.576(1) – 4.071(1)

From the 2.50 Å to 3.00 Å region, the PDF is seen to be largely made up of Mn−(Mn, Sb) pairs. The negative scattering length of Mn is apparent from the negative peak around 2.80 Å. As we progress to the higher r atom pairs, the large positive scattering lengths of Yb and Sb along with the high number of Yb−Sb atom pairs results in the upswing and peak at 3.17 Å. As the onset of the Yb−Mn pairs come into play and the number of Yb−Sb atom pairs drop, the intensity starts to decrease causing the downturn found at 3.48 Å. Finally, the appearance of the Yb−Yb pairs results in the peak at 3.83 Å.

In total, the G(r) data were fit using three different models as seen in **Figure 2.6**. The first two models assumed the fully ordered crystal structure with isotropic atomic displacement factors (ADFs) and anisotropic ADFs (**Figure 2.6a**,**b** respectively). The last model employed the disordered crystal structure, obtained from X-ray diffraction, using anisotropic ADFs (**Figure 2.6c**). The range of fitting for the G(r) function was set at a constant 20 Å.

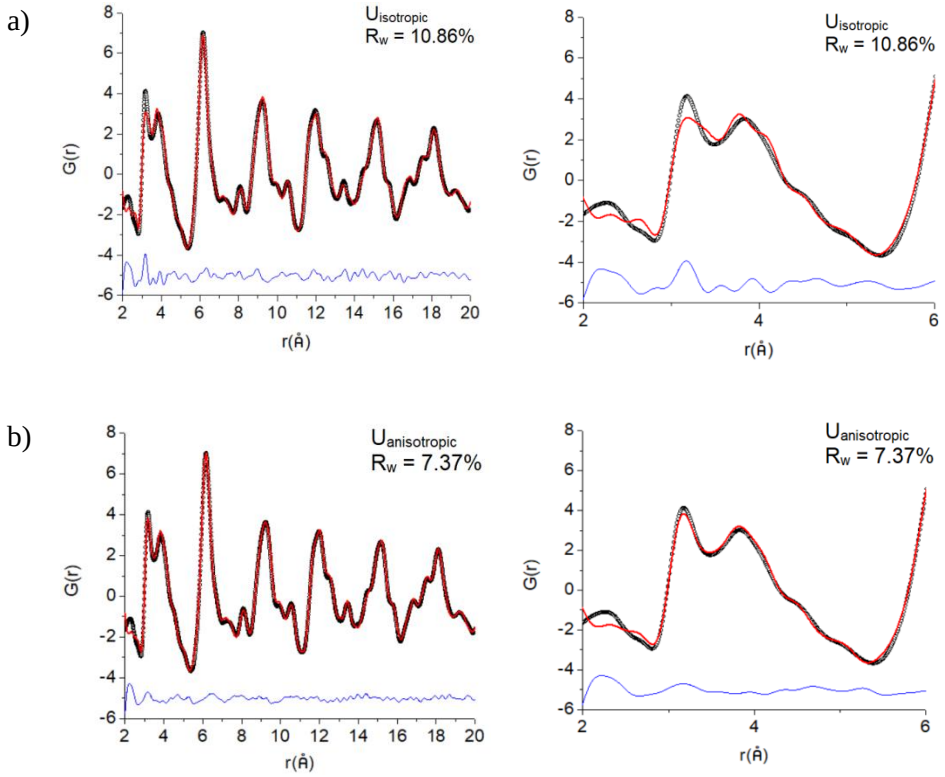

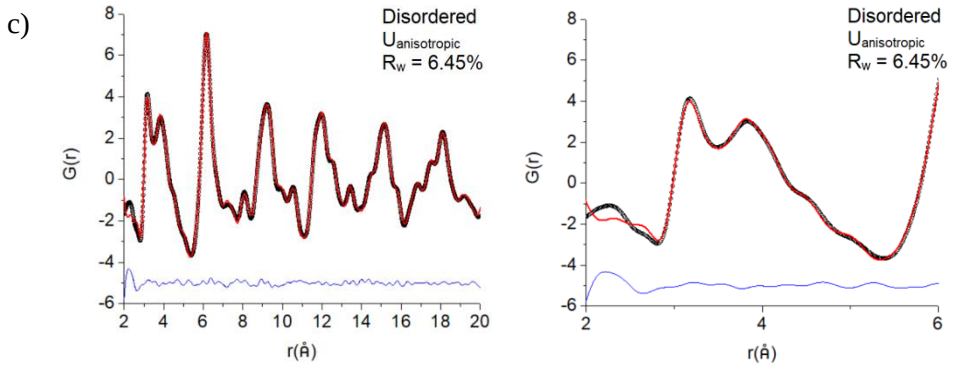

Figure 2.6: Pair distribution function (G(r)) refinement using three different models for $Yb_{21}Mn_4Sb_{18}$: (a) ordered structure isotropic ADFs, (b) ordered structure anisotropic ADFs, and (c) disordered crystal structure using anisotropic ADFs. Data were collected at 298 K.

The isotropic model fit was poor with an Rw = 10.86%. Most notably, the peak around 3.15 Å, made up from Yb−Sb pairs, is severely underestimated. The data were thus fit with anisotropic ADFs for all atoms. Significant improvements to the fit were obtained with Rw = 7.37% and gave much better descriptions of the Yb−Sb, Yb−Yb, and Yb−Mn pairs. To determine the contribution of disorder to the structure, the last structural model employed the Yb11/Yb12 and Sb9/Sb10 rattling, the Mn2/Mn3/Mn5 disorder, and Sb3/Sb11 disorder along with anisotropic ADFs. The drop in Rw value to 6.45% can be attributed to the disorder in the structure, supporting the results of the X-ray diffraction experiments. The improved fit can be observed in the short-r region of G(r) where the intensity description is seen to provide a better fit the experimental data.

2.4.4 Electronic Structure Calculations

Spin-polarized electronic structure calculations (**Figure 2.7**) show that the Fermi level lies in the top part of the spin-up valence band (see **Appendix 1**, **Figure A1.6** for a close-up view of the spin up states near the Fermi level), making the ideal system a highly doped p-type semiconductor. The conducting hole states are delocalized over all three atomic species, with a prevalent Sb character. For the spin-down polarization, the Fermi level is found in the gap between two occupied bands strongly localized on Mn

and a low-lying conduction band with the participation of Mn and Yb states. Because of the close proximity of the Mn states to the Fermi level, doping studies of the transition metal should be pursued to push these states closer to the Fermi level to increase the Seebeck coefficient. Alternatively, the Fermi level can be shifted by doping, to align with these isolated Mn states. Conversely raising the Fermi level to higher energy would place it in the spin-down conduction band, thus changing the character of transport from p-type to n-type. Overall, these calculations show that, at low temperature, $Yb_{21}Mn_4Sb_{18}$ acts as a p-type degenerate semiconducting material that can sustain spin polarized current. In general, this is a disadvantage for the thermoelectric efficiency, as only half the electrons contribute to transport: engineering the band structure to add electrons with opposite spin to contribute to transport may substantially enhance zT.

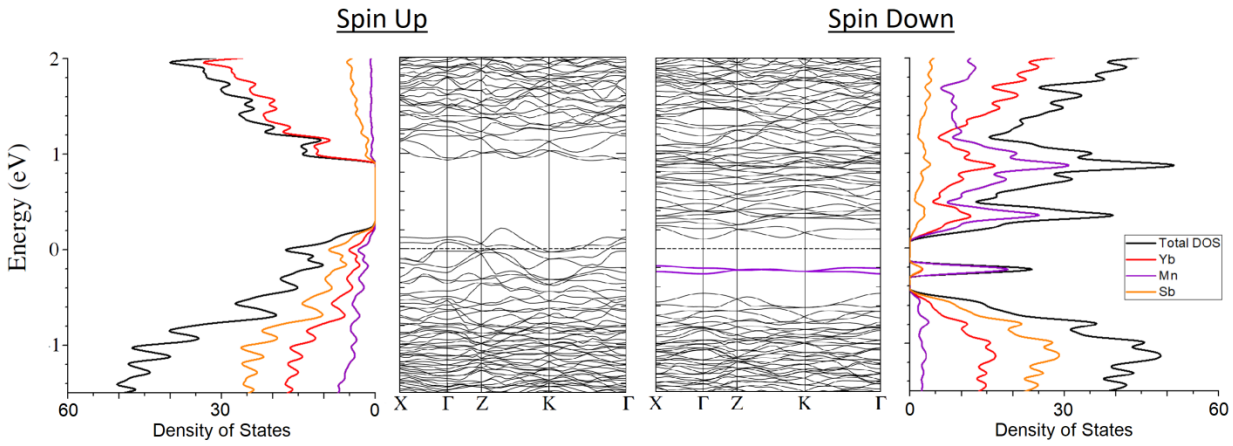

Figure 2.7: Spin-polarized band structure and density of state calculations for $Yb_{21}Mn_4Sb_{18}$. Fermi level is located at E = 0.

Furthermore, we studied the effect of Na doping by considering 21 replicas of the $Yb_{21-x}Na_xMn_4Sb_{18}$ system with x = 0.5, in which Na substitutes Yb in each symmetrically inequivalent position. This Na concentration is slightly higher than that probed in experiments. Total energy differences among the various systems are smaller than 0.17 eV, thus indicating that Na may substitute any site during high

temperature synthesis. The presence of Na reduces the cell magnetization from 36 to 35 μB/cell and produces a rigid shift of the spin-up density of states of about 0.1 eV, leaving the spindown states nearly unperturbed (see **Appendix 1**, **Figure A1.7**).

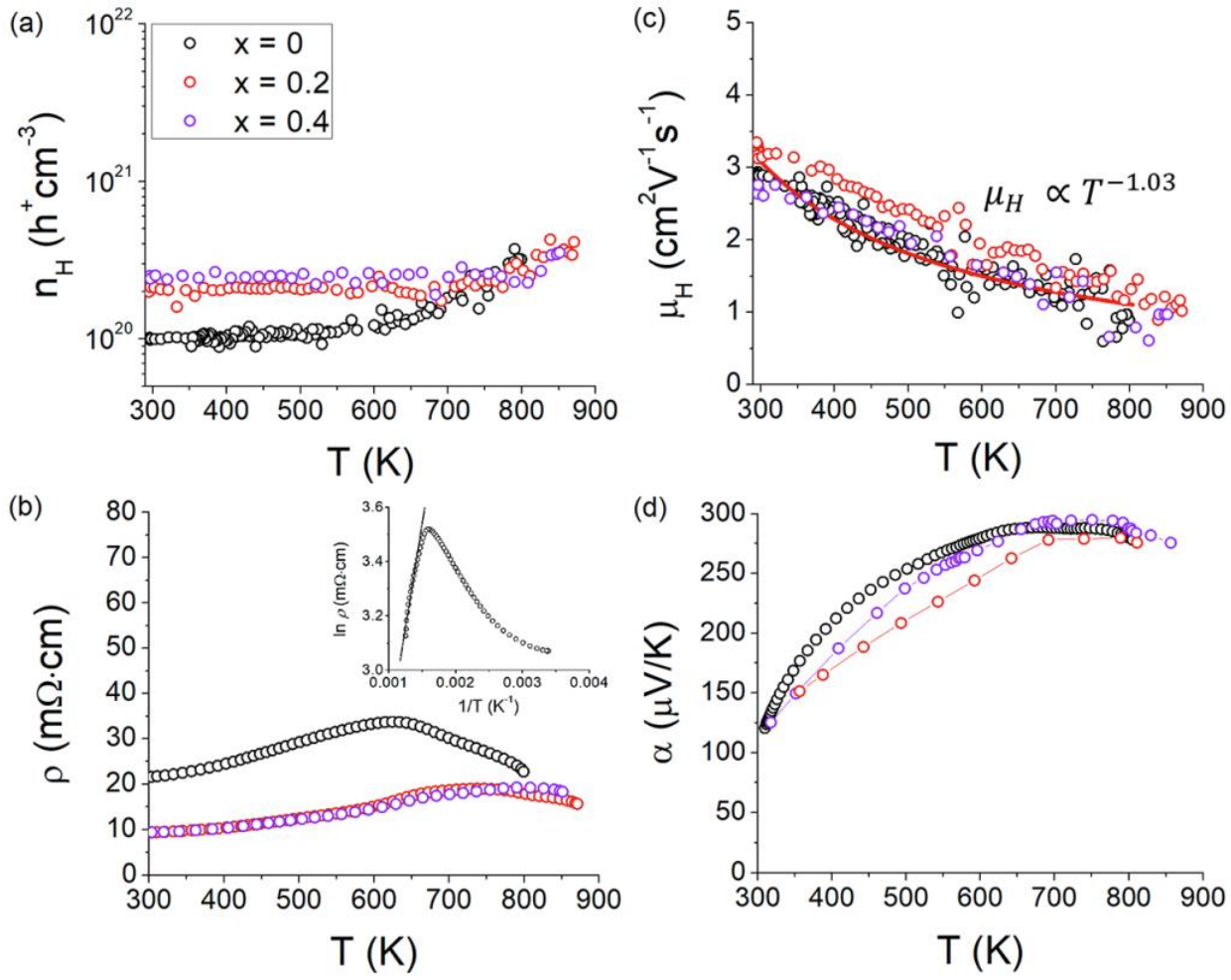

Figure 2.8: Thermoelectric transport properties of $Yb_{21-x}Na_xMn_4Sb_{18}$. (a) Temperature dependence of carrier concentration, (b) resistivity (inset shows slope of band gap determination), (c) Hall mobility (μ_H) (red line shows power law fit of $\mu_H \propto T^{-1.03}$ which is close to the expected 1/T dependence of mobility for degenerate semiconductors[53]), and (d) Seebeck coefficient.

2.4.5 Thermoelectric Transport Properties

Temperature dependent Hall measurements reveal (**Figure 2.8a**) a large carrier concentration on the order of 10^{20} cm^{-3} confirming the degenerate semiconducting nature of 21−4−18. With increasing Na content, there is a corresponding increase in carrier concentration; however, it is likely that the Na amount (x = 0.4) is slightly more than can be accommodated by the structure as there is not a complete correspondence between the x = 0.2 and x = 0.4 samples. No traces of impurities could be detected in powder X-ray diffraction or SEM for all samples. Attempts at increasing the Na doping further resulted in small impurities identified as $Yb_9Mn_{4.2}Sb_9$ and $Yb_{14}MnSb_{11}$ with Na also segregating at the grain boundaries. Once there is enough energy to thermally excite electron−hole pairs, the carrier concentration can be seen to steadily increase with temperature for all samples. As the Fermi level probes deeper into the valence band with the increasing Na content, the amount of thermal energy necessary to excite carriers across the band gap increases, making the increase in carrier concentration occur at higher temperatures. This phenomenon is carried over into the temperature dependence of resistivity (**Figure 2.8b**) where resistivity starts to bend over at the point of carrier concentration increase. The activation of electron−hole pairs increases carrier concentration and lowers the resistivity. The temperature dependence of the resistivity in the region after activation will largely be dominated by the exponential dependence of the carrier concentration[54] and should follow the relationship (**Equation 2.3**)

$$\rho = Ae^{E_g/2k_BT}$$

Equation 2.3: Arrhenius equation for electrical resistivity.

where A is a constant, E_g is the band gap, and k_B is Boltzmann's constant. From this model, a band gap of ~0.4 eV is calculated for the undoped sample.

Generally, the mobility (**Figure 2.8c**) is relatively unaffected by the Na doping and remains roughly constant over all samples. The decrease with increasing temperature is indicative of an increase in scattering interactions such as electron−phonon interactions. The temperature dependence of mobility should be given by a power law. Assuming that only acoustic phonon scattering limits the relaxation time, the mobility is expected to decrease as T^{-x} where $1 \leq x \leq 1.5$ where the limit of $x = 1$ is seen for highly degenerate samples (close to the observed $T^{-1.03}$) and $x = 1.5$ is obtained for a nondegenerate electron gas.[53]

Lastly, the temperature dependence of the Seebeck coefficient is given in **Figure 2.8d** and seems to be relatively unaffected by the increase in carrier concentration due to a corresponding increase in effective mass (see below). The presence of the maximum in the Seebeck data as a function of T agrees well with the carrier concentration data. Bipolar conduction will result in a drop of Seebeck coefficient leading to the maximum observed in all samples. Goldsmid and Sharp were able to formulate an analytical expression ($E_g = 2e|\alpha|_{max}T_{max} = 0.394$ eV) relating the band gap (E_g), the maximum Seebeck coefficient ($|\alpha|_{max}$), and the temperature of the peak (T_{max}).[55] The band gap value determined from the DFT calculations is around 0.3 eV, which is in good agreement with the experimental band gap values determined from the resistivity and the Seebeck coefficient.

From the electronic structure calculations, the Fermi level is seen to reside in an area where electrical transport is mediated by multiple bands. Some of these bands are flat, thus providing substantial contribution to the Seebeck coefficient, while a band with higher curvature at the Γ point sustains mobility (**Appendix 1, Figure A1.6**). Although the single parabolic band (SPB) model[56] would not capture the full complexity of the full electronic structure, it is a common, powerful tool for characterizing thermoelectric transport, which can provide insight into the possible ways to enhance thermoelectric efficiency such as carrier concentration optimization. The model was applied at 600 K so that the minority carrier

concentration remains negligible and acoustic phonon scattering limits the carrier mobility (λ = 0). The relationship between carrier concentration and the Seebeck coefficient was used to calculate the effective mass using the Pisarenko plot shown in the **Appendix 1**, **Figure A1.8**. According to the SPB model, the x = 0.4 sample has a higher effective mass ($m^* = 5.70\ m_e$) than the other two samples ($m^* = 3.73\ m_e$) which may be due to the Fermi level being situated in a local area of flat curvature.

The Seebeck coefficient (**Equation 2.4**) and carrier concentration (**Equation 2.5**) were calculated through evaluation of the Fermi−Dirac integral $F_j(\eta)$ (**Equation 2.6**):

$$\alpha = \frac{k}{e}\left(\frac{2F_1(\eta)}{F_0(\eta)} - \eta\right)$$

Equation 2.4: Seebeck coefficient under a single parabolic band assumption.

$$n = 4\pi\left(\frac{2m^* k_b T}{h^2}\right)^{3/2} F_{1/2}(\eta)$$

Equation 2.5: Carrier concentration under a single parabolic band assumption.

$$F_j(\eta) = \int_0^\infty \frac{\zeta^j d\zeta}{1 + \exp(\zeta - \eta)}$$

Equation 2.6: Fermi-Dirac Integral.

where η is the reduced chemical potential, ζ is the reduced carrier energy, and j is the order of the Fermi-Dirac integral. The Hall carrier concentration (n_H) can be related to the carrier concentration (n) by **Equation 2.7**:

$$n_H = \frac{n}{r_H}$$

Equation 2.7: Relation between Hall carrier concentration and carrier concentration.

where r_H is the Hall factor (**Equation 2.8**), calculated from

$$r_H = \frac{3}{2} F_{1/2}(\eta) \frac{F_{-1/2}(\eta)}{2F_0^2(\eta)}$$

Equation 2.8: Hall factor under a single parabolic band assumption.

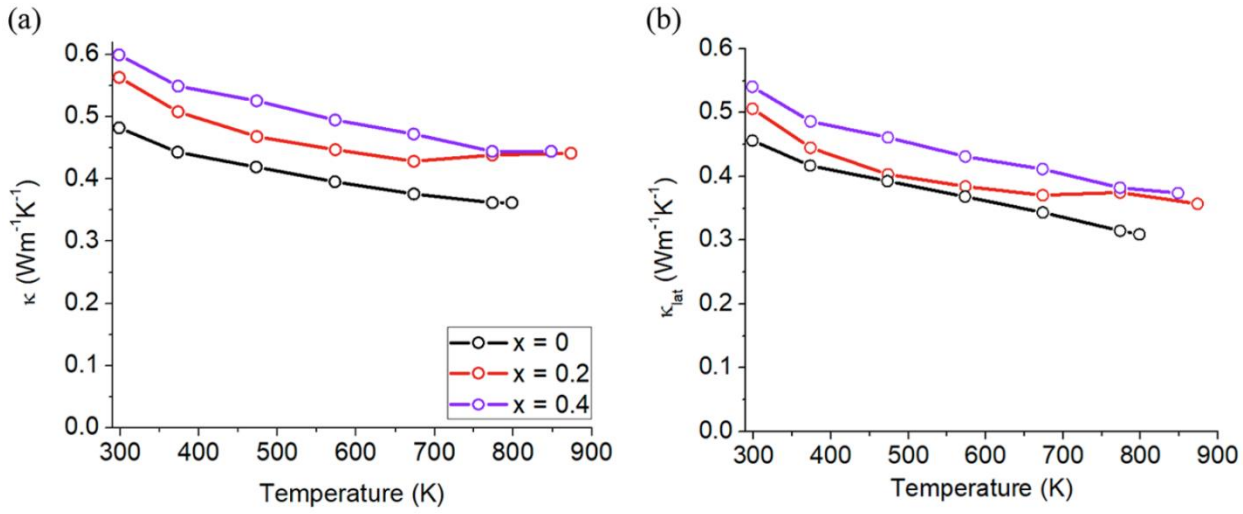

Figure 2.9: (a) Total thermal conductivity and (b) lattice thermal conductivity of $Yb_{21-x}Na_xMn_4Sb_{18}$ (x = 0, 0.2, 0.4).

Thermal conductivity (κ) data (**Figure 2.9**) were calculated from obtained measurements of thermal diffusivity (**Equation 2.9**):

$$\kappa = D\rho C_p$$

Equation 2.9: Thermal conductivity calculation from thermal diffusivity (D).

where D is the thermal diffusivity, ρ is the density of the sample, and Cp is the heat capacity. The Dulong−Petit law was used to estimate the heat capacity (C_p = 0.177 J g−1 K−1 for the undoped sample). The total thermal conductivity (**Figure 2.9a**) is primarily made up of two components: the electronic contribution (κ_e) and the lattice (κ_l). According to the Wiedemann−Franz relationship, $\kappa_e = L\sigma T$, the

electronic component can be subtracted from the total thermal conductivity to yield the lattice thermal conductivity (**Figure 2.9b**). The small increase in thermal conductivity with respect to increasing Na doping is attributed to Na atoms filling in the Yb vacancies. By filling in the vacancies (which would act as phonon scattering centers) the thermal conductivity of the system should slightly increase. In general, the low values in thermal conductivity are the result of the phonon mean free path being limited by the number of atoms in the unit cell and the large degree of structural disorder within the material.

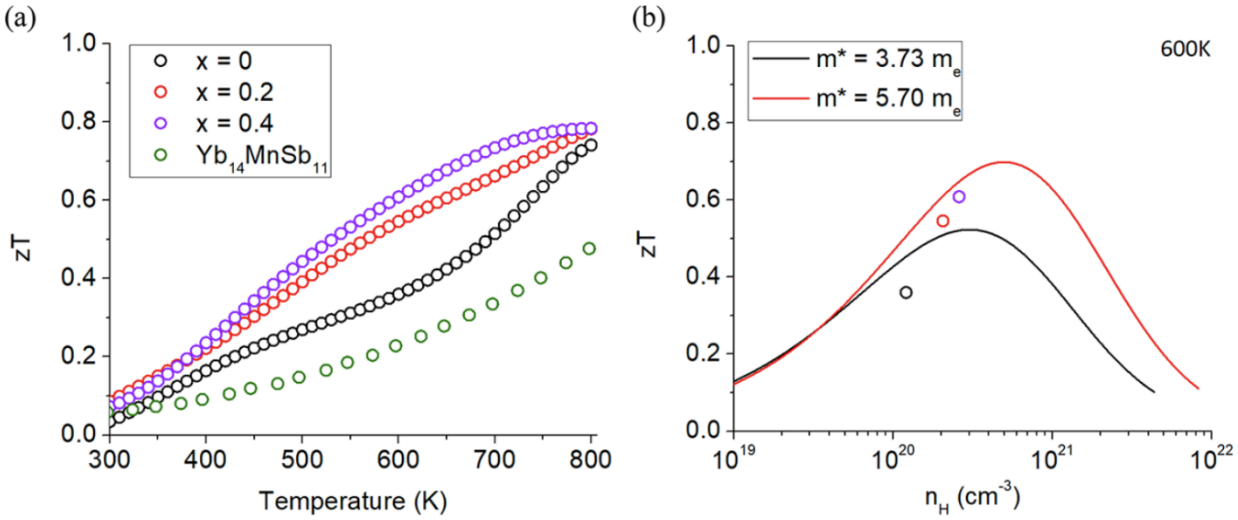

Figure 2.10: (a) Temperature dependent thermoelectric figure of merit, zT, for $Yb_{21-x}Na_xMn_4Sb_{18}$ (x = 0, 0.2, 0.4). A maximum value of 0.74 was obtained at 800 K. (b) Single parabolic band model fit (right) at 600 K using m* = 3.73 m_e, μ_0 = 2.31 $cm^2 V^{-1}s^{-1}$, and κ_l = 0.38 $Wm^{-1}K^{-1}$ in black and m* = 5.70 m_e, μ_0 = 1.97 $cm^2V^{-1}s^{-1}$, and κ_l = 0.43 $Wm^{-1}K^{-1}$ in red.

2.4.6 Figure of Merit

The thermoelectric figure of merit zT was calculated using polynomial fits to α, ρ, κ. As seen in **Figure 2.10a**, a maximum zT ≈ 0.8 was obtained at 800 K. The obtained zT was fit to the single parabolic band model (**Figure 2.10b**). The theoretical zT was calculated from **Equation 2.10–2.13**:

$$zT = \frac{\alpha^2}{L + \frac{1}{\Psi\beta}}$$

Equation 2.10: Theoretical zT calculated from a single parabolic band assumption.

$$L = \frac{k^2}{e^2}\frac{3F_0(\eta)F_2(\eta) - 4F_1^2(\eta)}{F_0^2(\eta)}$$

Equation 2.11: Lorenz number under a single parabolic band assumption.

$$\beta = \frac{\mu_0 \left(\frac{m^*}{m_e}\right)^{\frac{3}{2}} T^{\frac{5}{2}}}{\kappa_L}$$

Equation 2.12: β parameter for calculation of theoretical zT.

$$\Psi = \frac{8\pi e}{3}\left(\frac{2m_e k}{h^2}\right)^{\frac{3}{2}} F_0(\eta)$$

Equation 2.13: Ψ parameter for calculation of theoretical zT.

The values used for effective mass (m*), intrinsic mobility (μ_0), and lattice thermal conductivity (κ_L) were all obtained from the experimental data at 600 K for the SPB model. As seen from the model, the carrier concentrations obtained are close to the optimal carrier concentration predicted to give the largest zT.

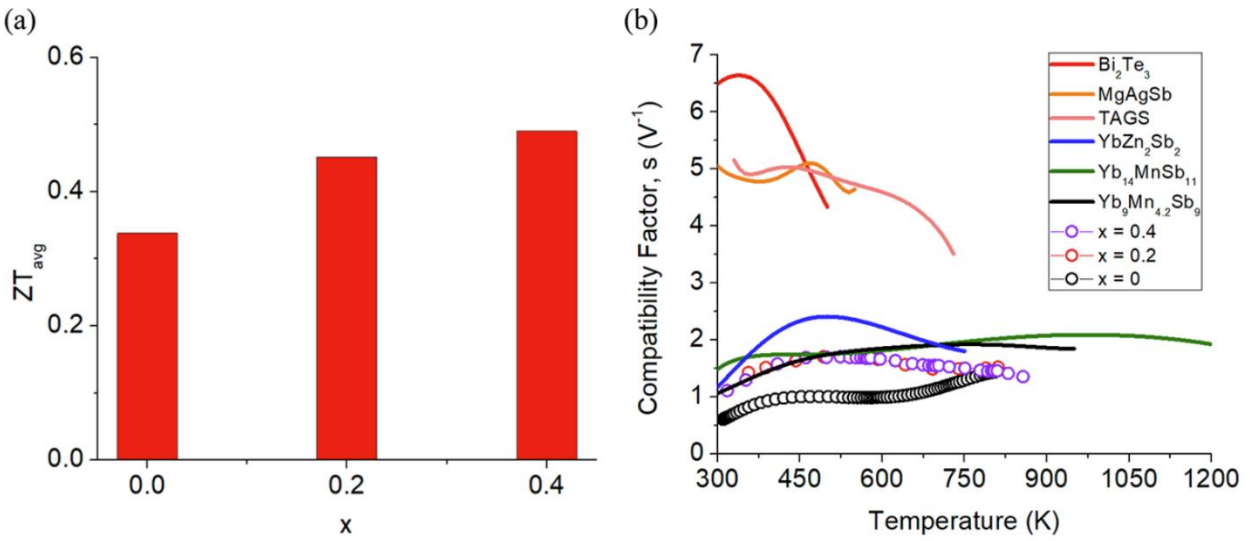

Figure 2.11: Practical considerations of $Yb_{21-x}Na_xMn_4Sb_{18}$ in device segmentation showing (a) an increase of ZT_{avg} with Na doping while (b) being compatible with other high zT materials. Compatibility factor was calculated from Seebeck coefficients and zT taken from Yu et al. (Bi_2Te_3),[57] Zhao et al. (MgAgSb),[58] Schröder et al. (TAGS),[59] Zevalkink et al. ($YbZn_2Sb_2$),[60] Brown et al. ($Yb_{14}MnSb_{11}$),[4] and Bux et al. ($Yb_9Mn_{4.2}Sb_9$).[50]

For practical applications, a high peak zT within a narrow temperature range is often not enough to realize a high efficiency. Instead, efficiency of the thermoelectric module requires a large average zT as well as similar compatibility factors (s) of the segmented materials. With increasing amounts of Na doping, $Yb_{21-x}Na_xMn_4Sb_{18}$ experiences an increase in zT across the whole temperature range, yielding a larger ZT_{avg} calculated from the integration method (**Figure 2.11a**, ZT_{avg} = 0.34 for x = 0, ZT_{avg} = 0.49 for x = 0.4). For optimum device efficiency, the compatibility factors of the segmented materials should be within a factor of 2.[61] Here, ZT_{avg} refers to the performance of a device whereas lower case zT indicates the material performance. The compatibility factor (**Figure 2.11b**) of the Na-doped samples is much greater at low temperatures compared to the intrinsic sample but ends up with a similar compatibility factor at high temperature to that of $Yb_{14}MnSb_{11}$ due to the similarity of zT and the Seebeck coefficient. With the Na doping, this material has become much more compatible with other p-type thermoelectric materials at

the lower temperatures, making it more viable for segmentation and potentially increasing the efficiency due to a better electrical and thermal impedance matching.

2.5 Summary

The complex Zintl phase, $Yb_{21}Mn_4Sb_{18}$, has been successfully synthesized through high temperature annealing followed by spark plasma sintering, resulting in phase pure powder according to synchrotron powder diffraction. Methods for single crystal growth have also been elucidated, and single crystal X-ray diffraction studies reveal the disordered nature of this phase on multiple Yb, Mn, and Sb sites and within the $[Mn_4Sb_{10}]^{22-}$ tetramer units. The structural disorder was supported with total neutron scattering experiments using pair distribution function analysis which complement and agree with the X-ray scattering experiments. The structure consists of 1 $[Mn_4Sb_{10}]^{22-}$ unit, 2 $[Sb_2]^{4-}$ dimers, 4 isolated Sb^{3-} anions, and 21 Yb^{2+} and can be described within the Zintl–Klemm electron counting scheme as a Zintl phase. Transport property measurements and DFT calculations show that $Yb_{21}Mn_4Sb_{18}$ behaves as a heavily doped p-type semiconductor with large carrier concentration (~1020 cm^{-3}), high Seebeck coefficient (~290 μVK^{-1}), and low thermal conductivity (~0.4 $Wm^{-1}K^{-1}$). The transport properties were modeled with a single parabolic band model assuming acoustic phonon scattering, and the carrier concentration was optimized according to the composition $Yb_{21-x}Na_xMn_4Sb_{18}$ (x = 0, 0.2, 0.4). The large effective mass (5.70 m_e) obtained by probing the Fermi level deeper through Na doping into the hole conduction band has shown an overall increase in zT across the whole temperature range for the x = 0.4 sample. Further optimization may be possible through doping or substitution of Yb, Mn, or Sb in this structure type to change the band structure in a favorable way. A maximum zT ≈ 0.8 at 800 K is obtained for the x = 0.4 sample, and ZT_{avg} increases from 0.34 to 0.49 compared to the intrinsic sample.

2.6 Supporting Information

The Supporting Information is available free of charge on the ACS Publications website at DOI: 10.1021/acs.chemmater.9b02671.

C2/c structure motif figures, single crystal X-ray data collection and refinement parameters, atomic coordinates and displacement parameters determined from single crystal and synchrotron X-ray diffraction, picture of a single crystal, close-up view of disordered sites, compositional analysis on pressed pellets (WDS and EDS), Rietveld refinement results, structure function (S(Q) −1) for PDF, close-up view of the spin-up band structure near Ef , DFT calculations on Na-doped $Yb_{21}Mn_4Sb_{18}$, and Pisarenko plot for SPB model (PDF)

Crystallographic information for $Yb_{21}Mn_4Sb_{18}$ (CIF)

2.7 Acknowledgements

The authors acknowledge Modern Methods in Rietveld Refinement for Structural Analysis (MMRRSA) 2018 for beamline time at ORNL-SNS and ANL and Katherine Page, Jue Liu, and Joerg Neuefeind at NOMAD for useful discussion. We thank Christopher J. Perez for his help in measuring transport properties, Elizabeth L. Kunz Wille and Dr. Jim Fettinger for useful crystallography discussions, and NSF DMR1709382 for funding. Some of this work was performed at the California Institute of Technology/Jet Propulsion Laboratory under contract with the National Aeronautics and Space Administration. JPL affiliates were supported by the NASA Science Missions Directorate's Radioisotope Power Systems program. Calculations were performed on Comet at the San Diego Supercomputer Center, using the Extreme Science and Engineering Discovery Environment (XSEDE), which is supported by National Science Foundation Grant Number ACI-1548562, allocation CHE190009.

Chapter 3

The Impact of Site Selectivity and Disorder on the Thermoelectric Properties of $Yb_{21}Mn_4Sb_{18}$ solid solutions: $Yb_{21}Mn_{4-x}Cd_xSb_{18}$ and $Yb_{21-y}Ca_yMn_4Sb_{18}$

Allan He[1], Giacomo Cerretti[2], and Susan M. Kauzlarich[1*]

[1]Department of Chemistry, One Shields Ave, University of California, Davis, California 95616, USA

[2]Jet Propulsion Laboratory, California Institute of Technology, 4800 Oak Grove Drive, MS 277-105, Pasadena, California 91125, USA

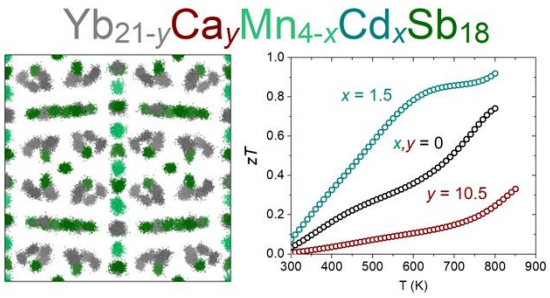

Published in *Materials Advances*, **2021**, 2, 5764 – 5776.

Allan He conducted all of the synthesis and characterization of the compounds. Giacomo Cerretti helped collect the Hall carrier concentration data and interpretation of the thermoelectric properties.

This chapter was adapted with permission from:

He, A.; Cerretti, G.; Kauzlarich, S. M. The impact of site selectivity and disorder on the thermoelectric properties of $Yb_{21}Mn_4Sb_{18}$ solid solutions: $Yb_{21}Mn_{4-x}Cd_xSb_{18}$ and $Yb_{21-y}Ca_yMn_4Sb_{18}$. *Materials Advances*, **2021**, *2*, 5764 – 5776. Reproduced with permission from the Royal Society of Chemistry.

3.1 Abstract

Thermoelectric materials can convert heat into electricity. They are used to generate electricity when other power sources are not available or to increase energy efficiency by recycling waste heat. The $Yb_{21}Mn_4Sb_{18}$ phase was previously shown to have good thermoelectric performance due to its large Seebeck coefficient (~290 μVK^{-1}) and low thermal conductivity (0.4 $Wm^{-1}K^{-1}$). These characteristics stem respectively from the unique $[Mn_4Sb_{10}]^{22-}$ subunit and the large unit cell/site disorder inherent in this phase. The solid solutions, $Yb_{21}Mn_{4-x}Cd_xSb_{18}$ (x = 0, 0.5, 1.0, 1.5) and $Yb_{21-y}Ca_yMn_4Sb_{18}$ (y = 3, 6, 9, 10.5) have been prepared, their structures characterized and thermoelectric properties from room temperature to 800 K measured. A detailed look into the structural disorder for the Cd and Ca solid solutions was performed using synchrotron powder x-ray diffraction and pair distribution function methods and shows that these are highly disordered structures. The substitution of Cd gives rise to more metallic behavior whereas Ca substitution results in high resistivity. As both Cd and Ca are isoelectronic substitutions, the changes in properties are attributed to changes in the electronic structure. Both solid solutions show that the thermal conductivities remain extremely low (~0.4 $Wm^{-1}K^{-1}$) and that the Seebeck coefficients remain high (> 200 μVK^{-1}). The temperature dependence of the carrier mobility with increased Ca substitution, changing from approximately T^{-1} to $T^{-0.5}$, suggests that another scattering mechanism is being introduced. As the bonding changes from polar covalent with Yb to ionic for Ca, polar optical phonon scattering becomes the dominant mechanism. Experimental studies of the Cd solid solutions result in a max zT of ~ 1 at 800 K and, more importantly for application purposes, a ZT_{avg} ~ 0.6 from 300K to 800K.

3.2 Introduction

Thermoelectric materials can provide a clean energy alternative when employed in a device to regenerate

electrical power from waste heat. These devices are inherently renewable and environmentally friendly making them an enticing alternative to fossil fuels. Wide-scale application of thermoelectrics and commercialization is currently being held back by modest device conversion efficiency.[62] Efficiencies can be improved by developing new and better materials[63] and/or through engineering considerations. The thermal to electrical conversion efficiency of a thermoelectric material is described by the figure of merit $zT = \frac{\alpha^2 T}{\rho\kappa}$ where α is the Seebeck coefficient, T is the temperature, ρ is the electrical resistivity, and κ is the thermal conductivity. To be an efficient thermoelectric material, low thermal conductivity, low resistivity, and high Seebeck coefficient are required to maximize the figure of merit, *zT*. The simultaneous optimization of these parameters (α, ρ, κ) is a naturally conflicting goal because of their interconnected relationship with the charge carrier concentration (n) of the material. This has led to many different strategies for optimization in the thermoelectric community. One common avenue is to first start from intrinsically low thermal conductivity materials (those with large unit cells) to provide a good starting point for optimization. One class of low thermal conductivity materials can be identified as charge-balanced and semiconducting Zintl compounds. The type of bonding in Zintl compounds can fall anywhere in between ionic, covalent, or metallic and because of this flexibility, one may imagine that a large number of unique and undiscovered compounds are possible. The subset of Zintl phases with complex unit cells gives rise to more phonon modes leading to increased phonon scattering and lower thermal conductivity. Examples of such materials include $Yb_{14}MnSb_{11}$,[4,64] Zn-Sb phases,[34,36,65] and $Tl_2Ag_{12}Te_{7+\delta}$.[66] Other optimization strategies include: electronic structure modification (e.g. increasing the density of states (DOS) near the Fermi level) either through substitutional doping demonstrated in PbTe,[67] defect control,[60] and nanostructuring/compositing for decreased thermal conductivity[68] or improved electronic and mechanical properties.[69]

Our previous study on the parent $Yb_{21}Mn_4Sb_{18}$ (referred to as 21-4-18) compound showed that extremely low values of thermal conductivity (~0.4 $Wm^{-1}K^{-1}$)[16] can be achieved due to the complex structural disorder inherent within the system.[16,17] Paired with a high Seebeck coefficient (~290 μVK^{-1}) given largely from the unique $[Mn_4Sb_{10}]^{22-}$ anion substructure, the intrinsic phase without any optimization shows a peak *zT* of ~0.75 at 800 K. Optimization of this compound was achieved through carrier concentration manipulation with the doping of sodium into the structure, increasing the maximum *zT* to ~0.8 and ZT_{avg} from 0.34 to 0.49 over the entire temperature range (300 – 800K).[16] Here, the term ZT_{avg} refers to the average *zT* across the specified temperature range calculated from the integration method.[70] Sodium doping improves the ZT_{avg} and brings the thermoelectric compatibility factor (s) of the 21-4-18 phase closer to other top performing thermoelectric materials making it more desirable for practical applications.[16] Since thermoelectric devices depend on segmentation of different materials, maximal efficiencies are only achieved if the compatibility factors of said materials are similar.

$Yb_{21}Mn_4Sb_{18}$ can be understood using a Zintl formalism of electron counting. The unit cell (Z = 4) (**Figure 3.1**) contains 1 linear $[Mn_4Sb_{10}]^{22-}$ anion, 2 dumbbell $[Sb_2]^{4-}$ anions, 4 isolated Sb^{3-} anions, and 21 Yb^{2+} cations making it charge-balanced.

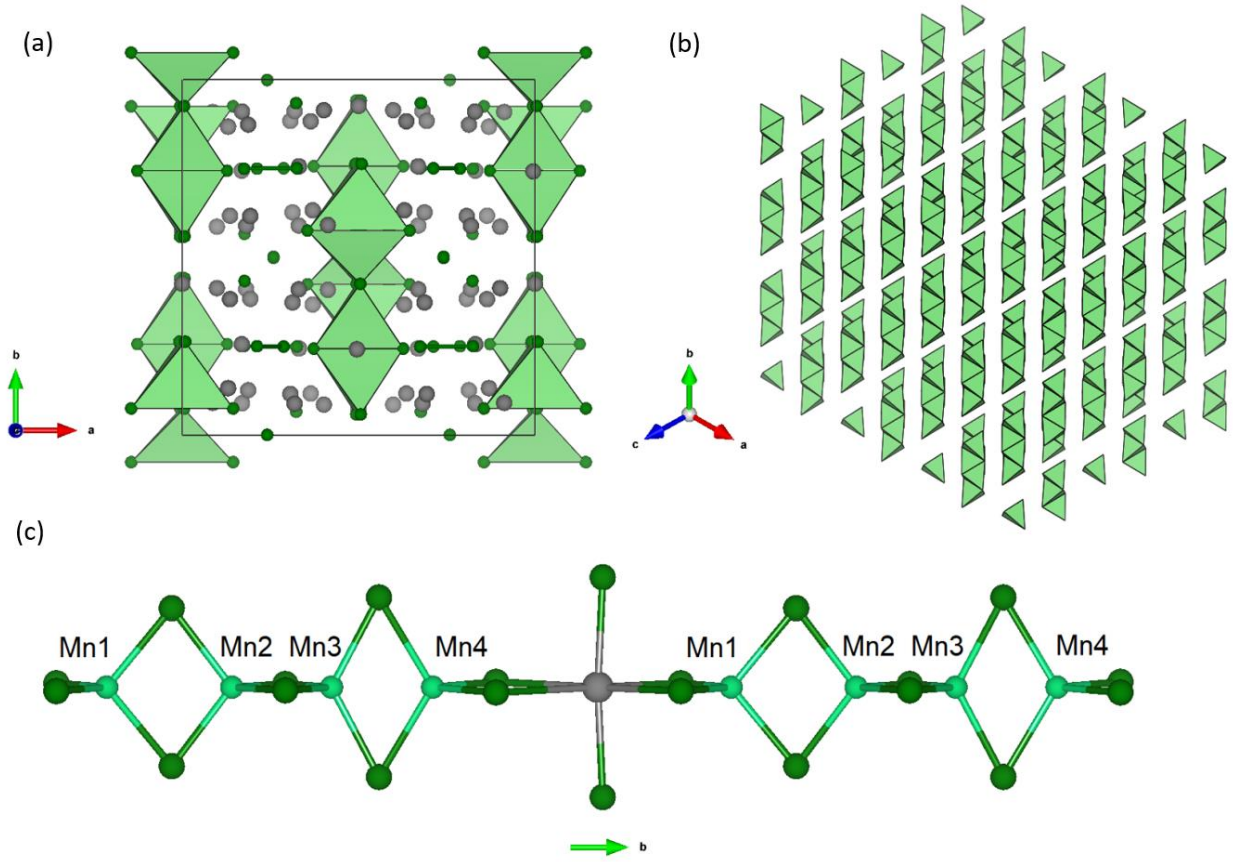

Figure 3.1: (a) Unit cell of the $Yb_{21}Mn_4Sb_{18}$ structure (a = 16.930(3) Å, b = 17.029(3) Å, c = 16.693(3) Å, β = 92.61(3)°, C2/c) viewed down the c-axis.[16] Yb atoms represented in grey, Mn atoms in light green, and Sb atoms in dark green. (b) Polyhedral view of the $[Mn_4Sb_{10}]^{22-}$ tetramer stacking shown along the (111) direction, without atoms for clarity. (c) Inter-tetramer coordination shown parallel to the b-axis.

Building on our previous work, herein we present the structure and thermoelectric properties of the $Yb_{21}Mn_{4-x}Cd_xSb_{18}$ (x = 0, 0.5, 1.0, 1.5) and $Yb_{21-y}Ca_yMn_4Sb_{18}$ (y = 3, 6, 9, 10.5) solid solutions. Although both Cd and Ca can be considered to be 2+ and therefore substitute isoelectronically for Mn^{2+} and Yb^{2+} respectively, the physical properties change drastically and cannot be explained using electron counting rules. Instead, it is necessary to consider how each solid solution changes the electronic structure to rationalize the physical properties that emerge for each solid solution. $Yb_{21}Mn_4Sb_{18}$ is a half metallic compound with Mn^{2+} having a half filled *d* band.[16] Cd was chosen as it has a filled *d* orbital and as such was expected to remove the half metallicity to improve the electrical transport. Ca substitution was

expected to increase electron donation to the clusters and thereby increase the Seebeck coefficients further. The Cd substitution in general makes the 21-4-18 phase more metallic while Ca has the opposite effect. In particular, introduction of the ionic Ca species reveals that the dominant carrier scattering mechanism can be tuned in Zintl phases and thereby providing a new avenue for thermoelectric properties optimization. The introduction of Cd and Ca into the 21-4-18 system shows the high flexibility and tunability of this structure type. This study focuses on isovalent substitutions on the A and M site in the $A_{21}M_4Pn_{18}$ system (where A is usually a rare-earth metal or alkali-earth element, M is usually a transition metal, and Pn is a pnictogen). The observed change in the physical properties for each solid solution is therefore only due to changes in the electronic band structure topology and not a combination of changes in band structure and carrier concentration from aliovalent doping studies.

3.3 Experimental Section

3.3.1 Synthesis

The polycrystalline $Yb_{21}Mn_{4-x}Cd_xSb_{18}$ (x = 0.5, 1.0, 1.5) and $Yb_{21-y}Ca_yMn_4Sb_{18}$ (y = 3, 6, 9, 10.5) samples were successfully synthesized using ball-milling and sintering processes, similar to that described previously.[16] Attempts to synthesize the x = 2.0 sample resulted in presence of $Yb_{11}Sb_{10}$ impurity. The Yb filings (Metall Rare Earth Limited, 99.99%), Ca pieces (Sigma Aldrich, 99.99%) Mn pieces (Alfa Aesar, 99.95%), Cd shots (Alfa Aesar, 99.95%) and Sb shots (Alfa Aesar, 99.999%) were loaded into a stainless steel ball-mill (50 mL vial using 3 stainless steel 0.5'' balls) under Ar atmosphere (< 1 ppm H_2O) in their appropriate stoichiometries (10 g total mass), and sealed inside a Mylar bag. The contents were milled for 1 h in a SPEX 8000 M High-Energy ball mill. For additional homogeneity, the resulting powder was ground thoroughly under Ar atmosphere, resealed in a Mylar bag, and subsequently milled for an additional hour. The mixture was then placed into 8 cm long Nb tubes, crimped and welded in an arc welder under partial

Ar pressure, and jacketed in a fused silica tube under vacuum. The reaction was heated to 650 °C (100 °C/h), sintered for 7 days, and allowed to slowly cool down to room temperature.

Densification of the powders for physical property measurements was done using spark plasma sintering (SPS) using a Dr. Sinter SPS-2050 system. Approximately 2-3g of material was sieved through a 200 mesh filter and loaded into a 12.7 mm graphite die. The SPS chamber was evacuated until <12 Pa and an initial pressure of 6 kN was applied to the die. The mixture was heated to 535 °C in 6 minutes, heated to 585 °C in 1 minute, followed by 45 minutes of dwell time. The pressure was adjusted monotonically to 11 kN upon compression of the mixture. All pellets obtained were > 95% dense (Archimedes' method) from this method.

3.3.2 Synchrotron Powder X-ray Diffraction

Synchrotron powder X-ray diffraction data were collected at the Argonne National Laboratory using the 11-BM beamline of the Advanced Photon Source (APS), Argonne National Laboratory. The samples were placed into Kapton capillaries, sealed with epoxy and the scattering data collected in transmission mode. Because of the highly absorbing nature of the samples, the powders were diluted with SiO_2 until $\mu R \approx 1$. A wavelength of $\lambda = 0.457884$ Å was used and the data were measured at room temperature. A brief comparison was completed with Rietveld refinement using the 11-BM data with our previously reported structure[16] and a more recently reported disordered structural model of 21-4-18.[17] The recently published model[17] yielded a slightly lower R_{wp} value of ~5.9 after refinement and needed more independent parameters to refine compared to our previous model which obtained a R_{wp} value of ~6.1. The atomic positions of both models and atomic displacement parameters were refined accordingly.

3.3.3 Pair Distribution Function

Synchrotron X-ray total scattering measurements on the $Yb_{21}Mn_{4-x}Cd_xSb_{18}$ (x = 0, 0.5, 1.0, 1.5) and $Yb_{21-y}Ca_yMn_4Sb_{18}$ (y = 3, 6, 9, 10.5) samples were carried out at 11-ID-B beamline ($\lambda = 0.2115$ Å) at the Advanced

Photon Source, Argonne National Laboratory using a 2D plate detector. The powders were sealed inside polyimide capillaries using epoxy and the data were collected at room temperature. The data images were analyzed using General Structure Analysis System-II (GSAS-II) program[71] where they were azimuthally integrated, resulting in a 1D pattern. The experimental parameters were calibrated using CeO_2 as the standard material. The pair distribution functions (PDFs) were obtained through the PDFgetX3 software[72] using a Q_{max} of 23.47 $Å^{-1}$ and were corrected for background diffraction from the air/capillary. The G(r) functions were modelled with the PDFgui software[43] using the results from Rietveld refinement of the powder X-ray synchrotron data as starting parameters. Overall, the lattice parameters, atomic displacement parameters (ADPs) and atomic positions were refined. Reverse Monte Carlo (RMC) fitting of the PDFs was done using RMCprofile software[73] using a 8 x 8 x 8 supercell (88064 atoms). The simulations were constrained with bond valence sum rules in order to keep the model chemically sound. A minimum distance restraint was applied to prevent any unreasonably short atomic pairs. Convergence was achieved after approximately 100 h on a standard PC. The resultant structural model from RMC was tested on 11-BM powder data using Rietveld refinement and resulted in a slightly higher R value (5.908 vs. 5.833 originally), as expected since the RMC model captures local structural features.

3.3.4 Thermoelectric Property Measurements

A Linseis LSR-3 instrument was used for resistivity and Seebeck coefficient measurements using the 4-probe method from 350 K to 800 K under He atmosphere. Samples were cut into bars (~10 mm x 2 mm x 2 mm) and measured using 8 mm probes. Many samples were measured to ensure reproducibility of the data and were cross-checked by measurements at the Jet Propulsion Laboratory (JPL). The Seebeck coefficient measured at JPL employed a light pulse technique with W/Nb thermocouples.[44] A custom system (4-point probe) was used to measure the electrical resistivity and Hall voltage simultaneously under dynamic vacuum, from which, the carrier density and mobility were derived.[45]

Thermal diffusivity (D) was measured using a Netzsch LFA 457 instrument under vacuum up to 800 K. The sample disks were polished flat and an even graphite coating was applied. The heat capacity (C_p) was estimated using the Dulong-Petit method, and the density (d) was measured by Archimedes' method. The thermal conductivity (κ) was then calculated using the formula $\kappa = DdC_p$.

3.3.5 Compositional Analysis

The samples were mounted in epoxy and polished to a smooth, flat surface. Elemental analysis was carried out using energy dispersive spectroscopy (EDS) using a FEI Scios DualBeam SEM/FIB with a window-less Oxford Instruments X-max50, 50 mm^2 silicon drift detector. Backscattered electron images were collected with an accelerating voltage of 20 kV and a current of 1.6 nA.

3.4 Results and Discussion

3.4.1 Crystal Structure

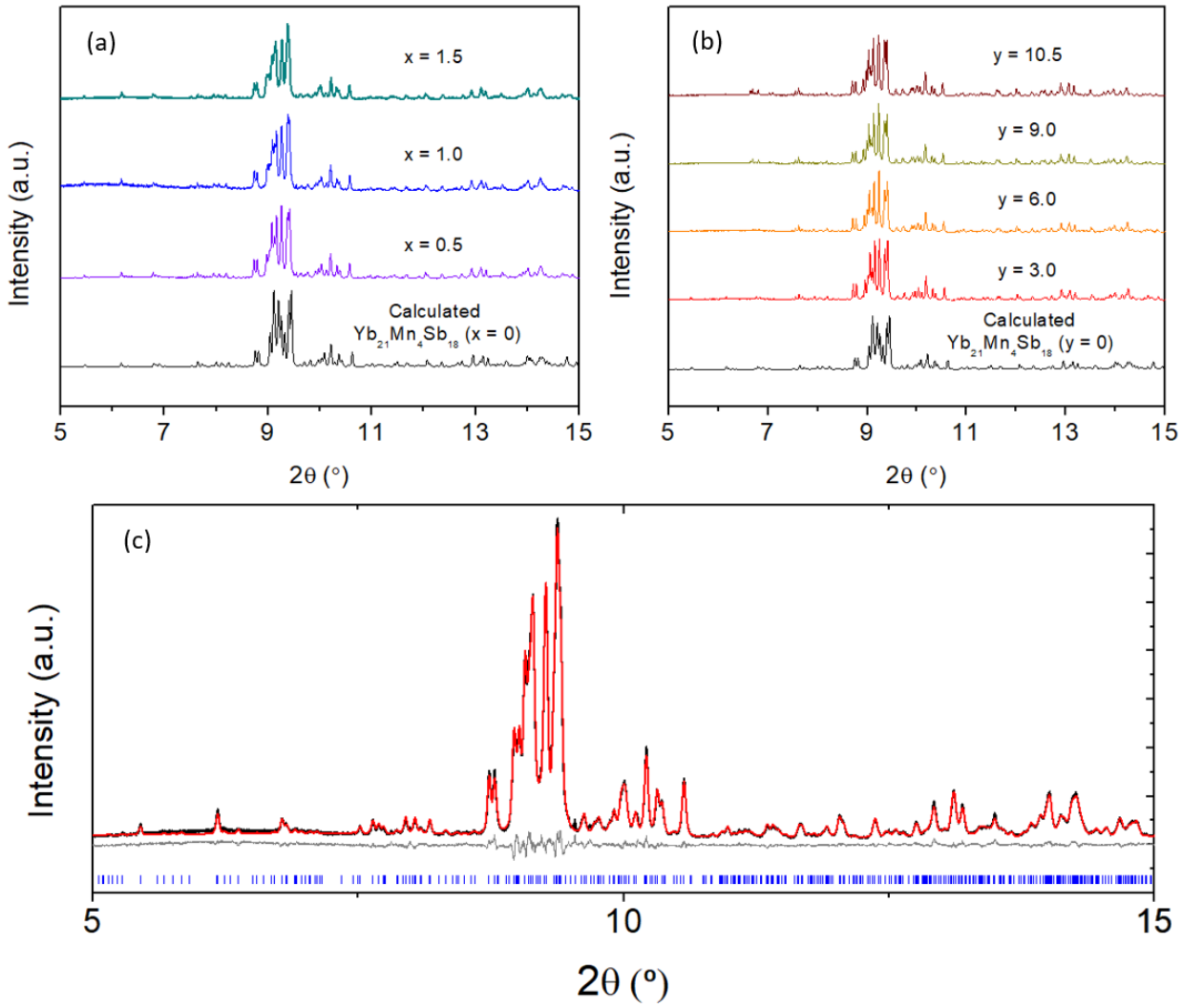

Figure 3.2: Synchrotron powder X-ray diffraction data collected at room temperature for (a) $Yb_{21}Mn_{4-x}Cd_xSb_{18}$ (x = 0, 0.5, 1.0, 1.5) and (b) $Yb_{21-y}Ca_yMn_4Sb_{18}$ (y = 3.0, 6.0, 9.0, 10.5) with λ = 0.457884 Å. (c) A representative Rietveld refinement for sample $Yb_{21}Mn_{2.5}Cd_{1.5}Sb_{18}$ where data are shown in black, calculated fit in red, difference in grey, and Bragg reflections in blue. Rietveld refinement parameters and results can be found in **Appendix 2 (Table A2.1, Table A2.2)**.

The synchrotron powder X-ray diffraction patterns (**Figure 3.2**) of all the prepared polycrystalline samples (x = 0, 0.5, 1.0, 1.5) and y = 3.0, 6.0, 9.0, 10.5) remain in the monoclinic *C2/c*, α-$Ca_{21}Mn_4Sb_{18}$ structure

type. No impurity phases were apparent in either the Cd or Ca solid solution series. During Rietveld refinement, the relative Mn/Cd and Yb/Ca occupancies were allowed to refine freely on each of the 4 Mn/Cd sites and the 11 Yb/Ca sites that converged to values close to nominal loading composition (see **Appendix 2 (Table A2.1, Table A2.2)**). Subsequent refinements constrained the total Mn/Cd and Yb/Ca occupancies to the nominal composition, with little to no change in R_{wp} (see **Appendix 2 (Table A2.1, Table A2.2)**). Substitution of the transition metal site (Mn) with Cd was found to exhibit site preference within the $[Mn_4Sb_{10}]^{22-}$ tetramer chain, where the Cd atoms prefer to reside on the terminal sites (Mn1/Cd1 and Mn4/Cd4) of the tetramer unit and the Mn atoms prefer to occupy the central two sites (Mn2/Cd2 and Mn3/Cd3) within the tetramer (see **Figure 3.3a**). In fact, the Mn2 site is completely devoid of Cd for the compositions investigated. We believe that the Cd site preference for the terminal sites of the tetramer unit arise from their intrinsically softer, longer bonds. The terminal sites are directly next to an octahedrally coordinated Yb atom (Yb11) which has previously been shown to exhibit rattling and disorder[16] and the softer bonds of the Cd atoms would be more accommodating of any local distortions on the octahedral site. Additionally, a comparison of the (Mn, Cd)-(Mn, Cd) distances within the tetramer chain reveal that the Mn2 – Mn3/Cd3 bond distance is the shortest among all the TM-TM bonds in the tetramer unit. It is reasonable to expect that the Mn atoms would prefer to sit on the two sites that are closest to each other to give rise to the strongest exchange coupling. With additional Cd doping, the tetramer structure evolves such that the Mn1/Cd1 atom begins to segregate away from the other atoms (i.e. Mn1/Cd1 – Mn2 distance increases from 3.64(3) Å to 4.004(2) Å for $x = 0$ and $x = 1.5$, respectively) while the total length of the tetramer chain remains relatively constant (i.e. Mn1/Cd1 – Mn4/Cd4 distance ranges from 8.74(3) Å to 8.724(2) Å for $x = 0$ and $x = 1.5$, respectively).

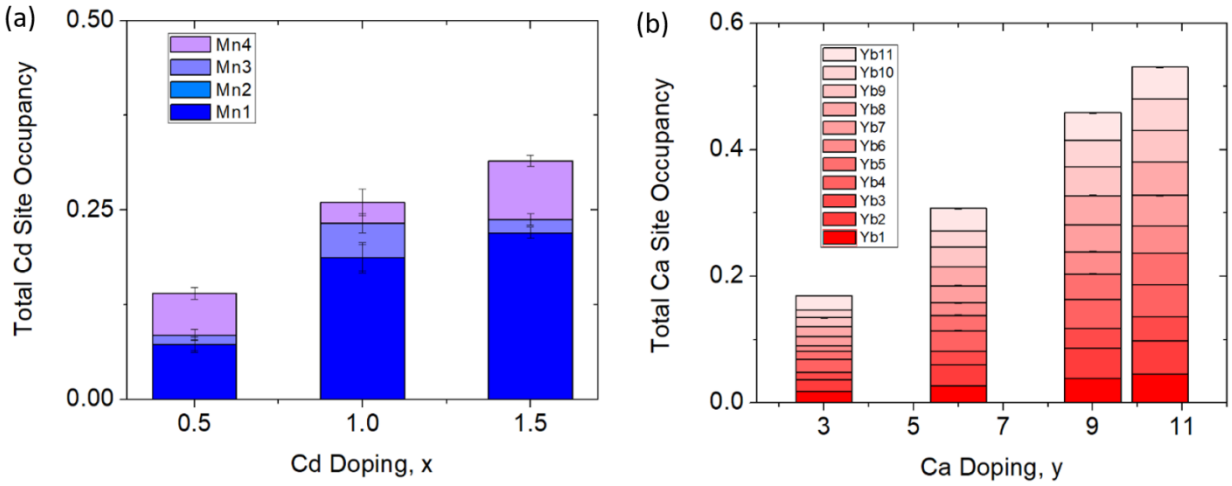

Figure 3.3: Percent site occupancies of the (a) Cd series ($Yb_{21}Mn_{4-x}Cd_xSb_{18}$, x = 0.5, 1.0, 1.5) and (b) Ca series ($Yb_{21-y}Ca_yMn_4Sb_{18}$, y = 3.0, 6.0, 9.0, 10.5) determined from Rietveld refinement of synchrotron X-ray powder diffraction data.

Substituting Ca on the rare earth site (Yb) did not result in any site preference (see **Figure 3.3b**). Overall, the Ca atoms are spread fairly evenly on all of the 11 sites which is probably due to the similarity in their 6-coordinate ionic radii (Ca: 1.00 Å vs. Yb: 1.02 Å) and bonding. The lack of site preference for the Ca atoms has been previously observed in the $Yb_{14-x}Ca_xMnSb_{11}$ system.[74]

3.4.2 Pair Distribution Function

Small Box Modelling

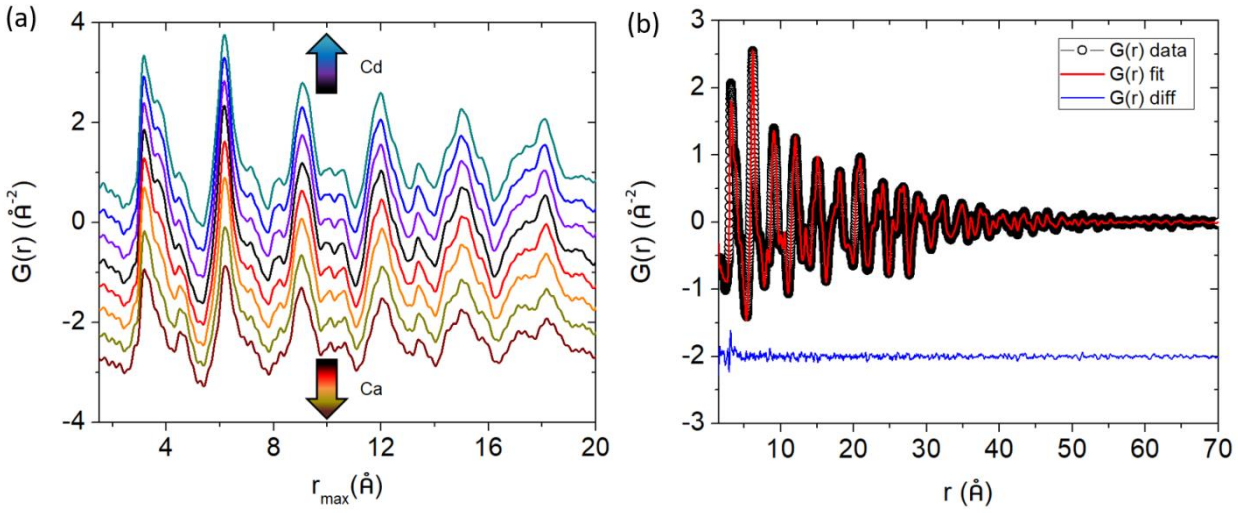

Figure 3.4: (a) Pair distribution functions (G(r)) of $Yb_{21}Mn_{4-x}Cd_xSb_{18}$ (x = 0, 0.5, 1.0, 1.5, black, purple, blue, teal respectively) and $Yb_{21-y}Ca_yMn_4Sb_{18}$ (y = 3.0, 6.0, 9.0, 10.5, red, orange, gold, brown respectively) within an r range of 1.5 – 20 Å. (b) The G(r) fit for $Yb_{21}Mn_4Sb_{18}$ up to r = 70 Å. Data are given by black dots, fit is provided in red, and the difference in blue.

Figure 3.4a shows the experimental pair distribution functions for the Cd and Ca solid solution series. The peaks that show up in the G(r) are broad, indicative of the large number of atoms (and atom pairs) in the unit cell. The model obtained from Rietveld refinement of the X-ray synchrotron data was used as a starting point in the PDF refinements. Analysis was completed up to a r_{max} = 70 Å, a range of approximately 4 unit cell lengths from the origin, and thus this study is focused on the local to intermediate structural regime (**Figure 3.4b** shows a representative fit for $Yb_{21}Mn_4Sb_{18}$ with r_{min} = 1.5 Å and r_{max} = 70 Å). Any peaks in the G(r) less than 1.5 Å were considered to be unphysical and was chosen as the lower bound (i.e. r_{min}) for analysis. The lattice constants, atomic displacement parameters (ADP), and atomic positions were refined. Refinements of site occupancy did not converge and led to unphysical values. For the ADP refinement, each individual element (i.e. Yb, Mn, Sb) was assigned one ADP to avoid over

parameterization regardless of their different crystallographic sites. The results from fitting the G(r) with r_{min} = 1.5 Å to an incrementally increasing r_{max} up to r_{max} = 70 Å, is shown in the **Appendix 2 (Figure A2.1, Figure A2.2)**. The results obtained from Rietveld refinement were used as a starting model for the PDF refinement. The unit cell parameters and ADP start to converge close to the values obtained from Rietveld refinement after approximately 35 Å (see **Appendix 2, Figure A2.1, Figure A2.2**), corresponding to a length of approximately two unit cells. The converged values from the small box PDF refinement are extremely close to that obtained from Rietveld refinement (see **Figure 3.5**).

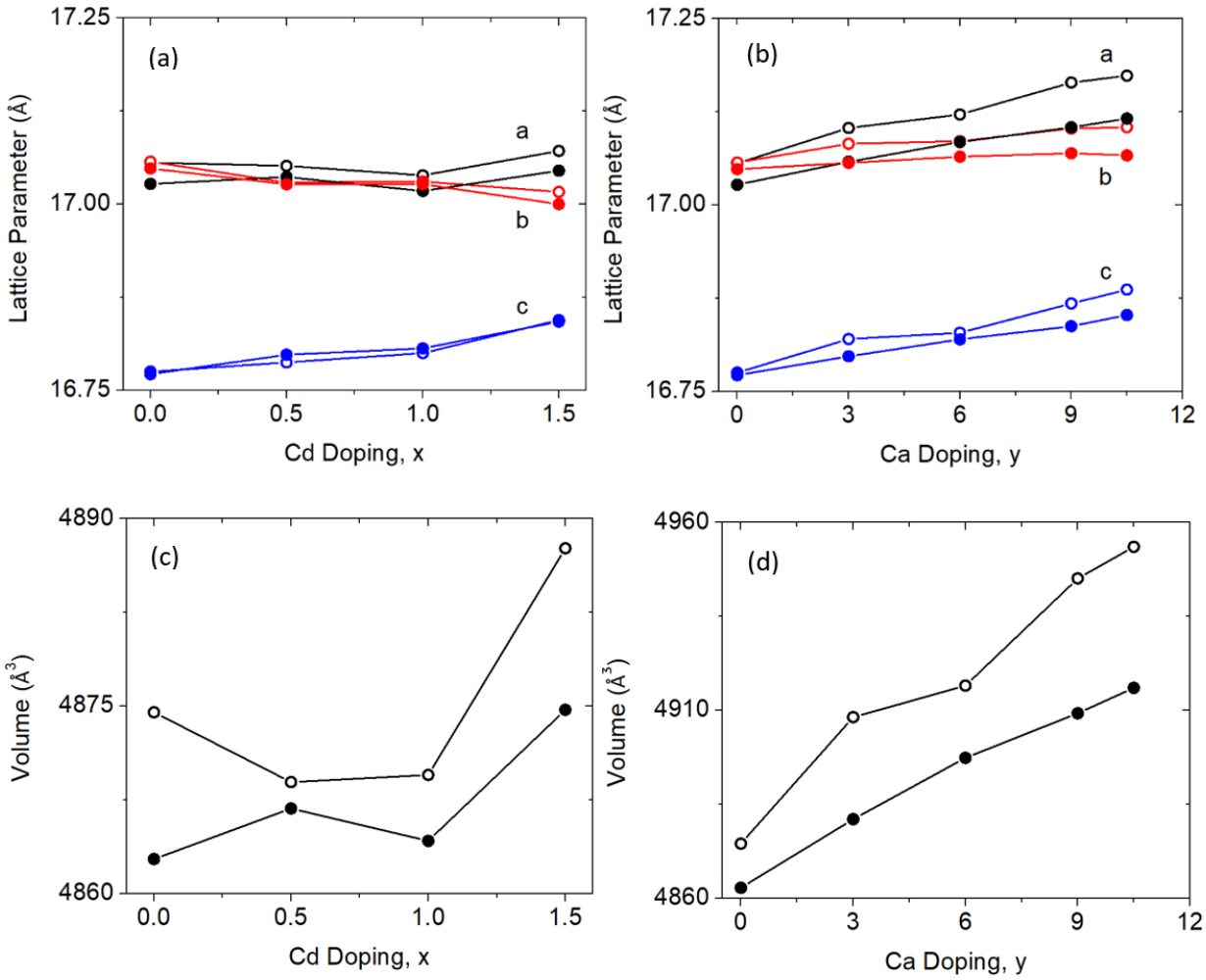

Figure 3.5: Lattice parameters and unit cell volume obtained from Rietveld refinement (filled circles) of the X-ray synchrotron data and the small box modelling (open circles) of total scattering X-ray

synchrotron data (G(r) with an r_{max} = 70 Å, see **Appendix 2** (**Table A2.3, Table A2.4**)) (a,c) Lattice parameters and unit cell volume of Cd solid solution. (b,d) Lattice parameters and unit cell volume of the Ca solid solution.

Both the lattice parameter and unit cell volume obtained from the Rietveld refinements and PDF refinements follow the same trend. With increasing Cd substitution, lattice parameters *a* and *c* both increase while *b* decreases, resulting in an overall increase in unit cell volume from *x* = 0 to *x* = 1.5. For the Ca solid solution series, there is a similar trend. Lattice parameters *a* and *c* both increase, while *b* stays relatively the same resulting in the unit cell volume increase across the series.

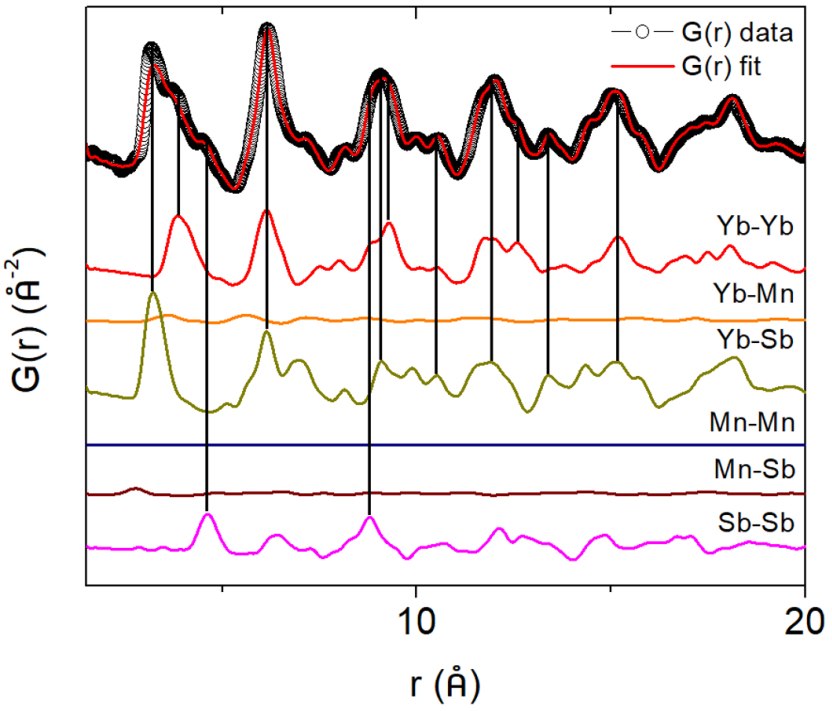

Figure 3.6: Partial pair distribution functions for $Yb_{21}Mn_4Sb_{18}$ (*x* = 0) to deconvolute the contribution of each atom-atom pair to the total pair distribution function.

To directly see the contribution of individual atom-atom pairs to the pair distribution function, the partial pair distribution function curves were plotted in **Figure 3.6** for the parent (*x* = 0) $Yb_{21}Mn_4Sb_{18}$ sample. The overall PDF (G(r)) is obtained by summing all the partial PDFs (g(r)) with appropriate weighting

coefficients, i.e. $G(r) = \sum_{i,j} c_i c_j b_i b_j (g_{ij}(r) - 1)$. The contribution of a particular atom pair depends upon the concentration of the particular atom (c_i,c_j) and the scattering factor (b_i,b_j). Because Yb and Sb make up most of the formula unit in this system (large c), and since Yb and Sb have larger scattering factors in comparison to Mn, the largest atom-atom pair contributions to G(r) are from the Yb – Yb, Yb – Sb, Sb – Sb pairs.

Reverse Monte Carlo (RMC) Modelling

After the small box modelling, we turned to RMC or "big box" modelling, because it is not restricted by symmetry and hence can better capture any short-range order present in the samples. In the RMC simulations, an initial configuration of atoms is modified through successive steps until the obtained model is in agreement with the experimental data using a Monte Carlo algorithm. The changes to the structure are proposed as random and then tested to see if there is an improvement in the fitting. If the change results in a better fit, it is accepted. If the change results in a worse fit, the change is accepted according to a probability algorithm. By accepting "bad" changes, this method of fitting prevents getting stuck in local minimum states. Bond valence sum restrictions were set in order to keep the model chemically sound and to avoid any unphysical bond lengths.

The G(r) function was modelled according to an 8 x 8 x 8 supercell for all the different compositions (**Figure 3.7a**). For the solid solutions, the Cd and Ca atoms were randomly distributed among their respective sites for the initial configuration prior to refinement. During the refinement, the Mn and Cd atoms were allowed to swap places with equal probability for the Cd solid solutions, and similarly, the Yb and Ca atoms were allowed to swap with equal probability for the Ca solid solutions.

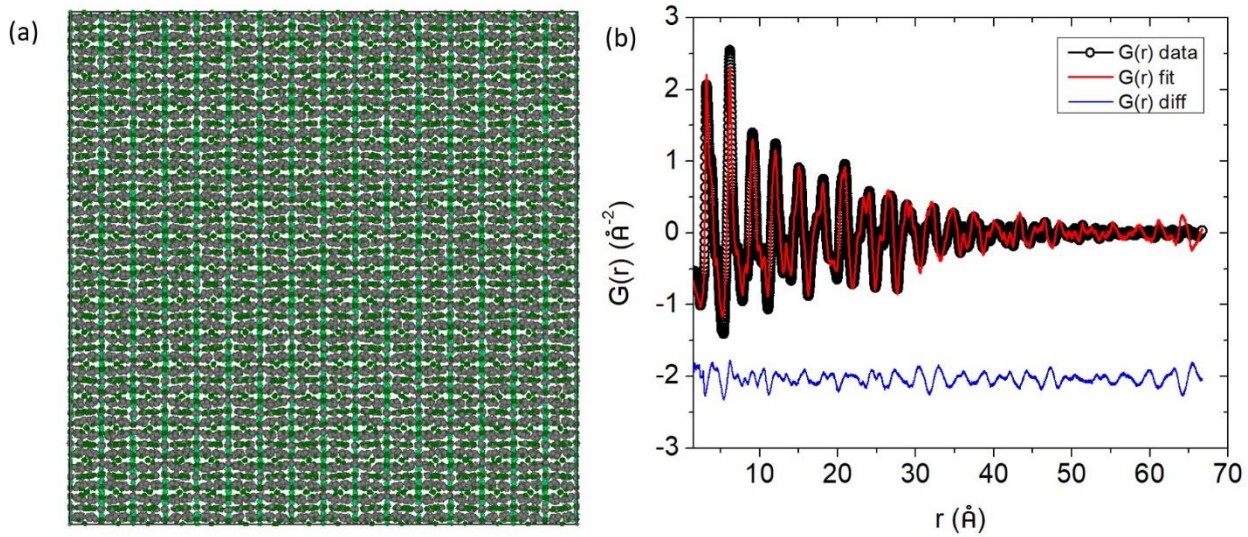

Figure 3.7: (a) Refined supercell (8 x 8 x 8) for $Yb_{21}Mn_4Sb_{18}$ after RMC simulations (b) The G(r) fit obtained from RMC modelling. The finite size of the supercell is apparent from the $r_{max} \approx 67$ Å. Data are shown by black dots, fit curve is the red solid line, and the difference is shown by the blue solid line.

An excellent fit over the whole r range of the PDF is obtained (**Figure 3.7b**) given the small supercell that was used. For visualization, the distribution of the atomic positions in the 8 x 8 x 8 supercell were superimposed onto a single unit cell (i.e. point cloud distributions, **Figure 3.8a**) for $Yb_{21}Mn_4Sb_{18}$ and the two most highly substituted samples of Cd and Ca (**Figure 3.8b**, **Figure 3.8c**). There are two structural models for $Yb_{21}Mn_4Sb_{18}$ based on single crystal data[16,17] and both give rise to similar Rietveld refinements of the data, as noted above. The RMC model cannot support or discard either of these models because the aforementioned models are based on long range ordering in single crystal samples while the current analysis is looking at local ordering in powder samples.

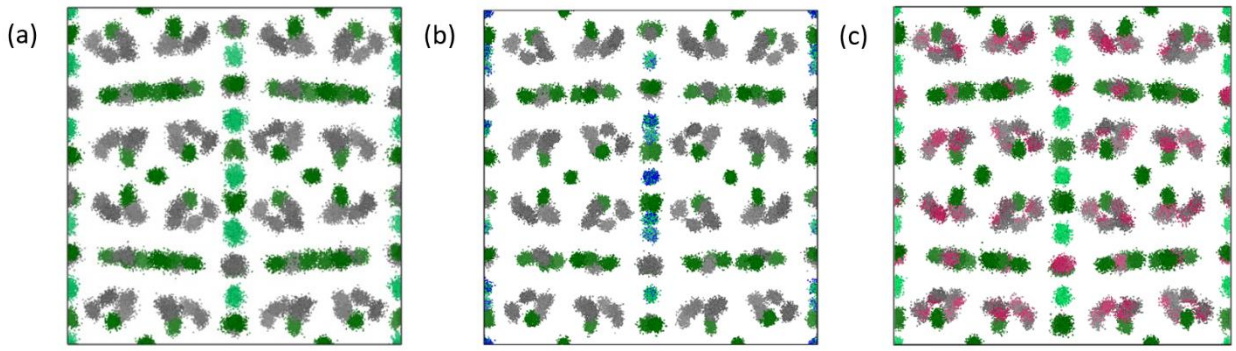

Figure 3.8: Point cloud distributions of (a) $Yb_{21}Mn_4Sb_{18}$ (b) $Yb_{21}Mn_{2.5}Cd_{1.5}Sb_{18}$ (c) $Yb_{10.5}Ca_{10.5}Mn_4Sb_{18}$ showing cation site and transition metal site occupations from RMC simulations. Yb atoms are in gray, Mn atoms in light green, Sb atoms in dark green, Cd atoms in blue, and Ca atoms in red. Other point cloud distributions can be found in **Appendix 2, Figure A2.3**.

The results from the RMC modeling suggest a highly disordered structure that is unique and separate from the average model obtained through Rietveld refinement. **Figure 3.9** shows the site occupations of Cd and Ca substituted samples obtained from the RMC simulations. The simulations show that there is some degree of site preference for both the Ca and Cd atoms in the local structure that is distinct from the average structure.

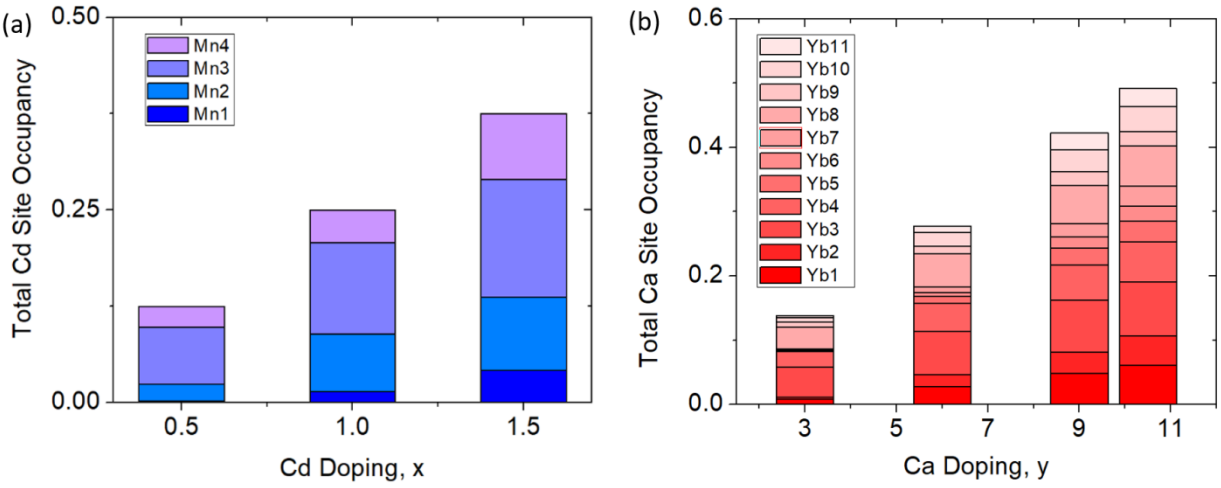

Figure 3.9: Percent site occupancies of the (a) Cd series ($Yb_{21}Mn_{4-x}Cd_xSb_{18}$, x = 0.5, 1.0, 1.5) and (b) Ca series ($Yb_{21-y}Ca_yMn_4Sb_{18}$, y = 3.0, 6.0, 9.0, 10.5) determined from RMC simulations of synchrotron total X-ray scattering data.

For example, in the *x* = 1.5 sample, the Cd atoms populate the Mn2/Cd2 site and Mn3/Cd3 site the most, whereas in the Rietveld refinement, Cd atoms reside on the terminal Mn1/Cd1 and Mn4/Cd4 sites the most (refer back to **Figure 3.3**). Additionally, in the Ca solid solutions, Rietveld refinement showed that the Ca atoms were roughly evenly distributed across all 11 Yb sites while the RMC simulations show some degree of site preference. To verify whether or not these results are local structural features, further simulations were performed. The final structural model for *y* = 10.5 was chosen as a representative sample and was allowed to randomly swap the Yb and Ca atoms with absolute probability for more than 12 h. The resultant structure (and fit) was compared to the model prior to swapping which resulted in a substantially worse agreement with the experimental data (see **Appendix 2, Figure A2.4**) providing additional evidence of the local ordering. From the total scattering experiments, it is clear that there are local structural features on the nanoscale domain that are missed by the Rietveld refinement. These domains are approximately ~70 Å long with no obvious signs of long range order that could be observed within the 8 x 8 x 8 supercell model.

3.4.3 Compositional Analysis

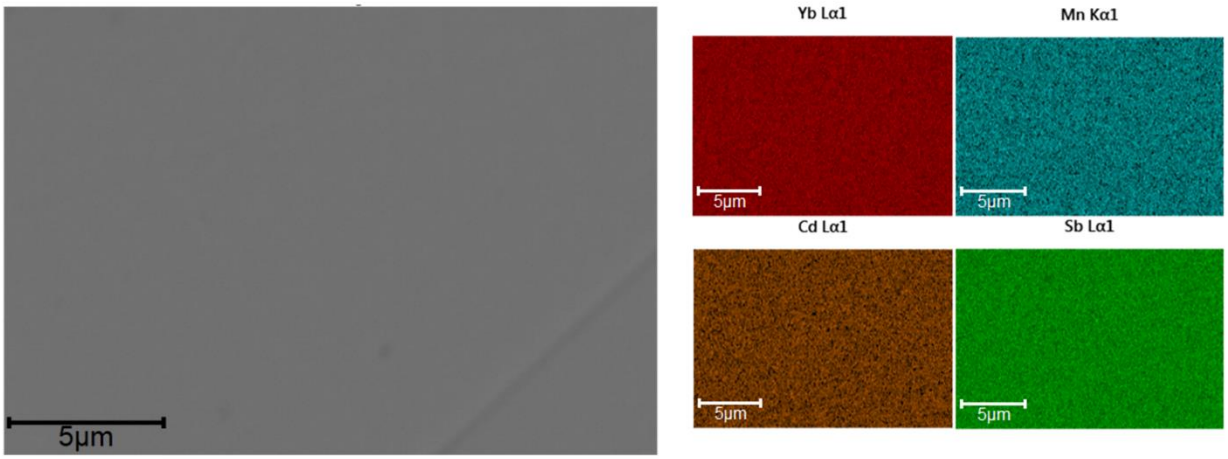

Figure 3.10: Representative backscattered electron images from a dense pellet of $Yb_{21}Mn_{4-x}Cd_xSb_{18}$ (x = 0.5) collected with 20 kV electron beam (left) and elemental mapping (right). Images of other Cd solid solutions can be found in **Appendix 2 (Figure A2.5, Figure A2.6)**.

All the samples after the SPS process were >95% dense. Backscattered electron images of a representative polished pellet surface of x = 0.5 is shown in **Figure 3.10**. The compositions of all the samples were found to be within approximately 1 at. % of the nominal stoichiometry (see **Appendix 2, Table A2.5**) according to EDS. Since the Ca K-edge (4.0381 keV) overlaps heavily with the Sb L-edges (L-I edge: 4.6983 keV, L-II edge: 4.3804 keV, L-III edge: 4.1322 keV), quantification of the Ca amount in the Ca solid solution samples was not reliable using EDS. Instead, we refer the reader to the refined compositions obtained via synchrotron powder X-ray diffraction data (see **Appendix 2, Table A2.2**).

3.4.4 Electronic Transport Properties

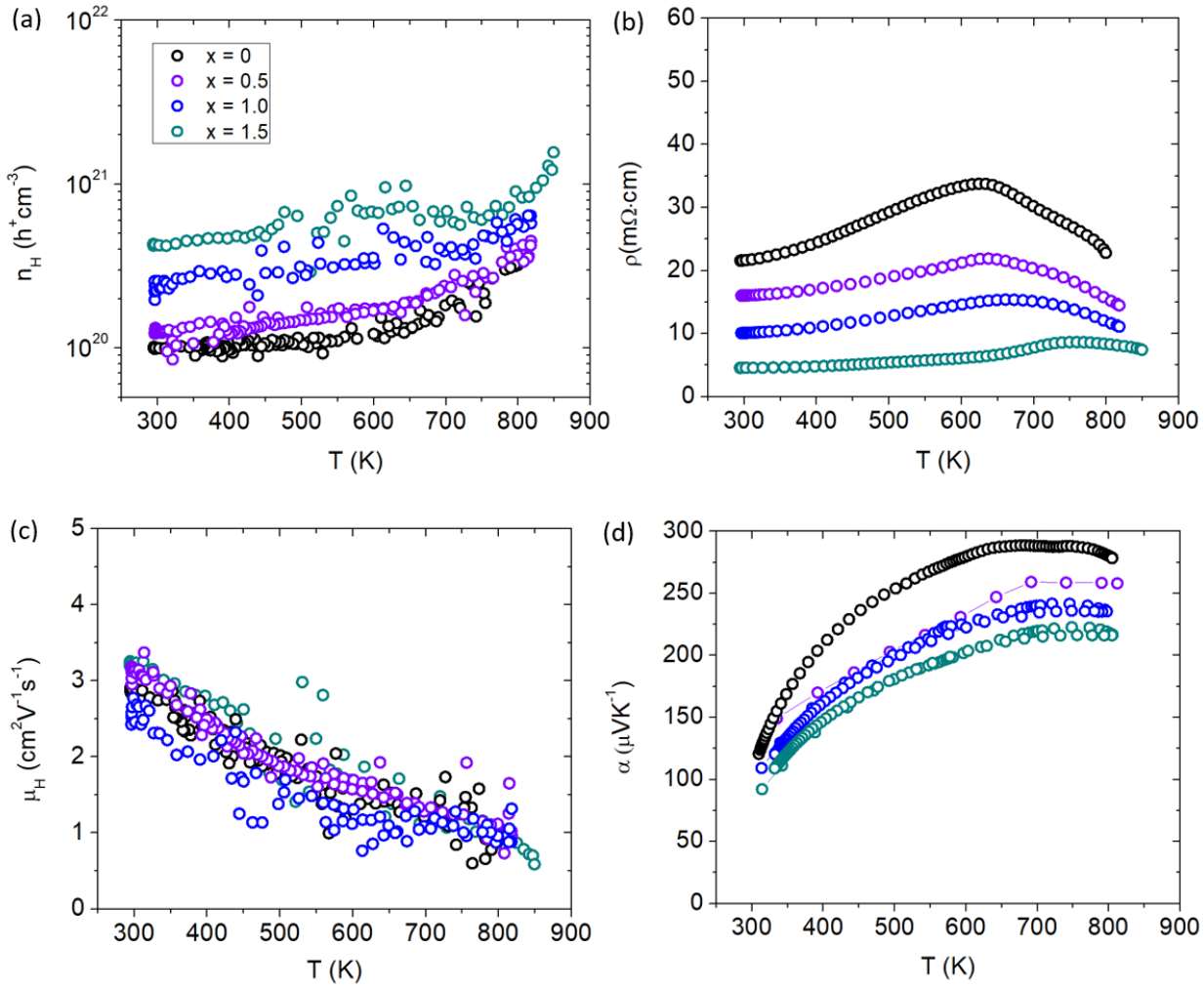

Figure 3.11: Transport properties of $Yb_{21}Mn_{4-x}Cd_xSb_{18}$ (x = 0, 0.5, 1.0, 1.5). (a) Hall carrier concentration (n_H), (b) resistivity (ρ), (c) Hall mobility (μ_H), (d) Seebeck coefficient (α). See **Appendix 2** for Pisarenko plot (**Figure A2.7**).

Figure 3.11a shows the temperature dependent Hall measurements for the Cd-substituted series yielding a large carrier concentration (cc) of $n_H > 1 \times 10^{20}$ h+ cm^{-3} for all samples. Although the isoelectronic substitution of Cd^{2+} with Mn^{2+} is not expected to change the carrier concentration from basic electron counting, the cc can be seen to steadily increase with Cd substitution. Since Cd is more electronegative than Mn, it will provide a more incomplete electron transfer to the anions to yield a higher p-type cc for

the solid solutions. Stated another way, the larger electronegativity of Cd will result in lower energy atomic orbitals compared to Mn (Koopmans' Theorem)[75] providing more states for the holes to occupy, leading to a larger cc. The increase in cc with Cd content is reflected in the electrical resistivity data (**Figure 3.11b**). All samples show metallic behavior with increasing temperature before transitioning into semiconducting behavior above 600 K. There is a peak in resistivity at about 600 K that shifts to higher temperatures with additional Cd content signaling an increase in the band gap. The Hall mobility is shown in **Figure 3.11c** and stays relatively constant with the additional Cd doping. The Seebeck coefficient (**Figure 3.11d**) steadily decreases with Cd content because of the increase in cc and is consistent with the temperature dependence of the electrical transport data.

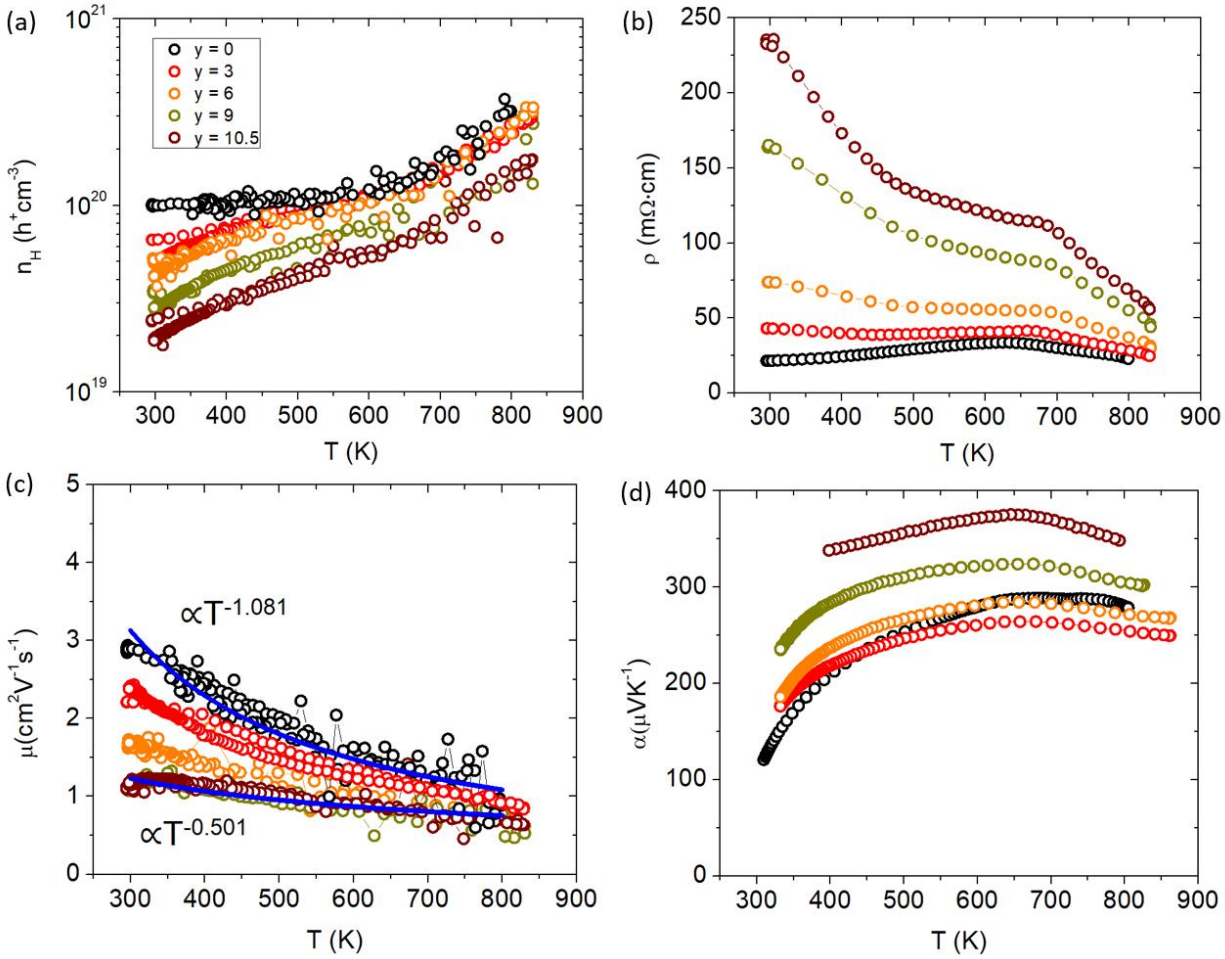

Figure 3.12: Transport properties of $Yb_{21-y}Ca_yMn_4Sb_{18}$ (a) Hall carrier concentration (n_H), (b) resistivity (ρ), (c) Hall mobility (μ_H), (d) Seebeck coefficient (α). See **Appendix 2** for Pisarenko plot (**Figure A2.7**).

The thermoelectric transport properties for the Ca solid solution series are shown in **Figure 3.12**. With additional Ca substitution, the carrier density decreases accordingly, dropping an order of magnitude from ~1 x 10^{20} h^+cm^{-3} (y = 0) to ~2 x 10^{19} h^+cm^{-3} (y = 10.5) at room temperature. Since Ca^{2+} is more ionic than Yb^{2+} and less electronegative, samples with more Ca will donate more e^- density into the system lowering the hole carrier concentration. As Ca is incorporated, Yb *f* states near the Fermi level are removed. The loss of these Yb states results in the observed decrease in carrier concentration as there are less places for the holes to populate the valence band. In addition to the drop in cc, the cc slope is also increased for

the Ca-substituted samples compared to the parent ($x = 0$) sample. The electrical resistivity increases with Ca content and shows an exponential increase in the room temperature value. The high temperature slope-change of the electrical resistivity (similar to the Cd series) shifts to higher temperature with Ca content and marks the point of minority carrier activation or bipolar conduction, consistent with the temperature dependence of the cc. The carrier mobility decreases steadily with additional Ca content and decreases its temperature dependence from approximately T^{-1} to $T^{-0.5}$. The temperature dependence of mobility is a combination of all the different scattering mechanisms at play, but is usually dominated by acoustic phonon scattering at high T which will yield $T^{-1.5}$ for nondegenerate semiconductors and T^{-1} for degenerate systems.[53] The gradual shift in temperature dependence to $T^{-0.5}$ with increased Ca substitution suggests that another scattering mechanism is being introduced. As the material becomes more polar with Ca substitution, the lattice becomes more polarizable, increasing the degree of electron-phonon interaction (i.e. Fröhlich constant (α)) to make polar optical phonon scattering the dominant mechanism[76] and suggests polaron formation. Compared to $Yb_{21}Mn_4Sb_{18}$, the $y = 3$ sample experiences an initial drop in Seebeck which may be due to the loss in Yb *f* states, before increasing with additional Ca content.

3.4.5 Thermal Transport Properties

Thermal conductivities were calculated from measurements of thermal diffusivity using **Equation 3.1**:

$$\kappa = \mathrm{D}\mathrm{d}C_p$$

Equation 3.1: Thermal conductivity calculated from thermal diffusivity.

where D is thermal diffusivity, d is the sample density, and C_p is the heat capacity. The Dulong-Petit law was used to estimate the heat capacity. The total thermal conductivity (κ) can be expressed as the sum of the lattice (κ_{lat}) and electronic (κ_e) contributions ($\kappa = \kappa_{lat} + \kappa_e$).

With increasing Cd and Ca content, the total thermal conductivity increases slightly (see **Figure 3.13a, Figure 3.13b**). In general, on a large scale the thermal conductivity of all the samples are not changed drastically from $Yb_{21}Mn_4Sb_{18}$, with the maximal changes amounting to approximately ~0.2 $Wm^{-1}K^{-1}$. From the Wiedemann-Franz law, the electronic part of the thermal conductivity is given by $\kappa_e = L\sigma T$, where L was approximated with an accuracy within 0.5% of a single parabolic band model calculation.[77] The electronic contribution was subtracted from the total thermal conductivity to yield the lattice thermal conductivity (see **Appendix 2, Figure A2.8**). The lattice thermal conductivity can be seen to slightly increase for both solid solutions and may be due to the difference in defect formation energies of the substituted elements where previously Yb defects were calculated to be more energetically favorable than Ca defects.[78]

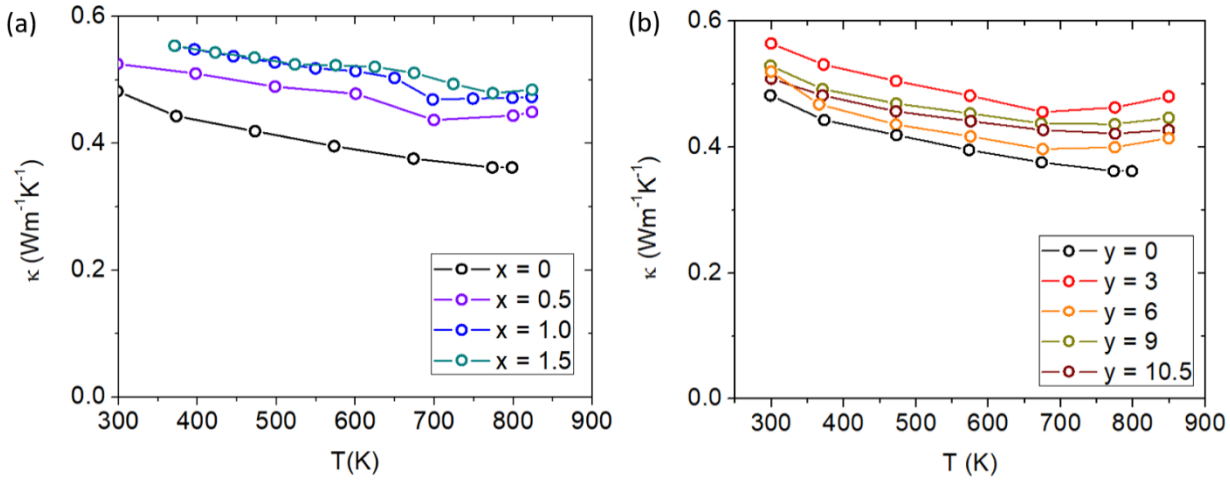

Figure 3.13: (a) Total thermal conductivity of Cd-substituted series ($Yb_{21}Mn_{4-x}Cd_xSb_{18}$) and (b) total thermal conductivity of Ca-substituted series ($Yb_{21-y}Ca_yMn_4Sb_{18}$).

Room temperature measurements of speed of sound yield a transverse and longitudinal value of $v_t =$ 1774 m/s and 3006 m/s respectively for the pristine sample of $Yb_{21}Mn_4Sb_{18}$. A corresponding Debye temperature of $\Theta_D \approx 192$ K for x = 0 sample was calculated from **Equation 3.2** and **3.3** where v_m is the mean speed of sound, v_l and v_t are the longitudinal and transverse speeds of sound respectively.

$$\theta_D = \frac{v_m \hbar}{k_b}\left(\frac{6\pi^2}{V}\right)^{1/3}$$

Equation 3.2: Debye temperature calculation.

$$v_m^3 = \frac{3}{v_l^{-3} + 2v_t^{-3}}$$

Equation 3.3: Mean speed of sound calculation.

From Cahill et al.,[79] an estimate of the lower limit of thermal conductivity (κ_{min}) can be calculated from **Equation 4**.

$$\kappa_{min} = \left(\frac{\pi}{6}\right)^{1/3} \frac{k_b}{V^{2/3}} \sum_i v_i \left(\frac{T}{\theta_i}\right)^2 \int_0^{\theta_i/T} \frac{x^3 e^x}{(e^x - 1)^2}\, dx$$

Equation 3.4: Minimum thermal conductivity calculation.

where V is the average atomic volume, v_i is the i[th] sound mode (three in total - two transverse, one longitudinal), and $\theta_i = \frac{v_i \hbar}{k_b}\left(\frac{6\pi^2}{V}\right)^{1/3}$ is the frequency cutoff for the i[th] polarization in units of K. The lattice thermal conductivity of the samples can be seen to drop below κ_{min} which may be due to shortcomings of the Lorenz number calculation and the assumptions of the single parabolic band model.[80]

3.4.6 Figure of Merit

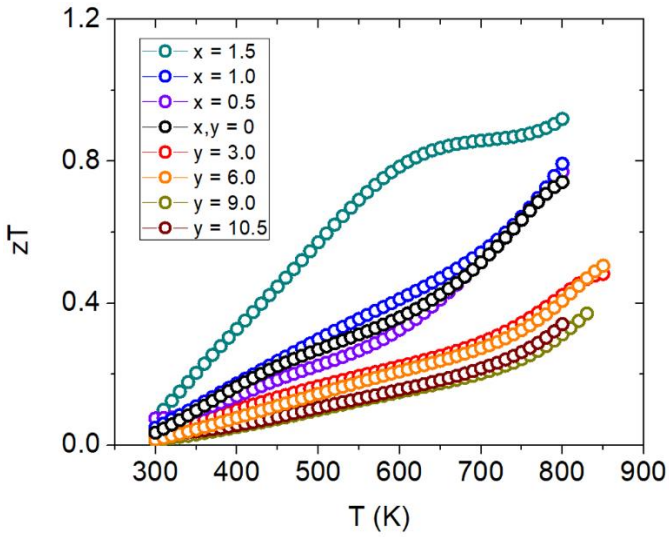

Figure 3.14: Figure of merit (zT) plots for Cd-substituted samples ($Yb_{21}Mn_{4-x}Cd_xSb_{18}$) and Ca-substituted samples ($Yb_{21-y}Ca_yMn_4Sb_{18}$).

The figure of merit, *zT*, plots are shown in **Figure 3.14** where we see a max *zT* ~ 0.92 is achieved for the x = 1.5 ($Yb_{21}Mn_{2.5}Cd_{1.5}Sb_{18}$) sample. The ZT_{avg} of this sample is 0.61 from 300K to 800K, calculated from the integration method, making it the highest for the 21-4-18 compositions reported to date. There is a large improvement over the whole temperature range at this Cd concentration and this result is important for practical thermoelectric device implementation. For the Ca-substituted series, the figure of merit ultimately decreases with increasing amounts of Ca mainly due to the large increase in resistivity. However, the change in scattering mechanism and the possibility of keeping the low thermal conductivity while tuning the carrier concentration *via* aliovalent substitution provides a new avenue towards additional *zT* improvements.

3.5 Conclusion

The two solid solutions of $Yb_{21}Mn_{4-x}Cd_xSb_{18}$ (x = 0, 0.5, 1.0, 1.5) and $Yb_{21-y}Ca_yMn_4Sb_{18}$ (y = 3, 6, 9, 10.5) have been successfully synthesized using high temperature annealing of the elements followed by spark plasma

sintering for densification. Building upon our previous work, this study continues to show the highly disordered nature of the 21-4-18 system from total X-ray synchrotron diffraction studies (pair distribution function) and from synchrotron powder X-ray diffraction. The average structure obtained from Rietveld refinement has been observed to differ from the local structure determined from reverse Monte Carlo simulations of PDF data in terms of the site occupation of the Cd and Ca to give rise to nanodomains within the material. In general, the 21-4-18 phase becomes more metallic with Cd substitution and more insulating with Ca substitution. The highest zT~1 is achieved at 800 K by the material with stoichiometry $Yb_{21}Mn_{2.5}Cd_{1.5}Sb_{18}$. Even though these substitutions are in principle, isoelectronic substitutions, the systematic change in the physical properties show that one cannot solely rely on electron counting rules to rationalize these results. These studies show that the carrier scattering mechanism can be tuned through ionic substitutions to make the material more polar and in particular for the 21-4-18 system, that the correct optimization strategy is to increase the carrier concentration. Given that there are many possibilities within the 21-4-18 structures, even higher zTs are possible with further optimization and expansion of the possible solid solutions.

3.6 Supporting Information

The Supporting Information is available free of charge on the ACS Publications website at DOI:

Pisarenko plot of Cd and Ca substituted samples, Lattice thermal conductivities, EDS elemental mapping data for Cd substituted samples, Rietveld refinement data for Cd and Ca substituted samples, total X-ray scattering refinement data using PDFgui for Cd and Ca substituted samples, point cloud distributions for Cd and Ca substituted samples, reverse Monte Carlo fit after 12h of random atom swapping

3.7 Acknowledgements

The authors would like to acknowledge Dr. Leighanne Gallington at Argonne National Laboratory for her help with collection of the total X-ray synchrotron diffraction data and Dr. Yuanpeng Zhang from Oak Ridge National Laboratory for his helpful suggestions with the Monte Carlo simulations. This work was supported by NSF DMR-1709382, DMR-2001156. Part of this work was conducted at the Jet Propulsion Laboratory California Institute of Technology under contract with the National Aeronautics and Space Administration with funding from the Science Mission Directorate's Radioisotope Power Systems program. G. Cerretti's research at the Jet Propulsion Laboratory was supported by an appointment to the NASA Postdoctoral Program, administered by Universities Space Research Association under contract with NASA.

Chapter 4

Investigating the Effects of Anion Substitution in the $Yb_{21}Mn_4Sb_{18-x}Bi_x$ System

Allan He[1] and Susan M. Kauzlarich[1*]

[1]Department of Chemistry, One Shields Ave, University of California, Davis, California 95616, USA

4.1 Abstract

The $Yb_{21}Mn_4Sb_{18-x}Bi_x$ solid solution is of interest as a possible high efficiency thermoelectric phase. The synthesis has been investigated employing high temperature annealing and spark plasma sintering. The crystal structure was analyzed through powder X-ray diffraction and the solid solution is revealed to stay in the C2/*c* space group following Vegard's Law. The phase becomes more metallic with increasing amounts of Bi substitution leading to the lowering of the electrical resistivity by an order of magnitude. This study confirms previous single parabolic band predictions that for this system, a larger carrier concentration is necessary for higher efficiency (figure of merit, *zT*) where it is observed that a higher *zT* is achieved for the *x* = 9 sample.

4.2 Introduction

In the U.S., a large percentage of energy produced is lost as waste heat (over 60%).[81] Generators based on thermoelectric materials can turn this waste heat into electricity through the Seebeck effect. This conversion process is very reliable and is free of any moving parts making it an eco-friendly and robust solution for this problem. Conversion of even a small fraction of this waste heat would lead to immense economic and environmental benefits. The efficiency of a thermoelectric material is based on the figure of merit (*zT*), $zT = \frac{\alpha^2 T}{\rho\kappa}$, where α is the Seebeck coefficient, T is the temperature, ρ is the electrical resistivity, and κ is the thermal conductivity.

The *zT* values of several different materials have been improved dramatically through many different optimization considerations. Some representative thermoelectric systems include the lead chalcogenides,[82,83] SnSe,[84,85] skutterudites,[86] and in particular $Yb_{14}MnSb_{11}$ (14-1-11).[4] The $Yb_{14}MnSb_{11}$ Zintl phase is currently the best p-type material at high temperatures. The complicated crystal structure of this

material leads to a very low thermal conductivity and has inspired the discovery and optimization of other related Zintl phases in the Yb-Mn-Sb family such as $Yb_9Mn_4Sb_9$[50,52] and $Yb_{21}Mn_4Sb_{18}$ (21-4-18).[16,18]

Prior to any optimization, the intrinsic 21-4-18 phase has shown a peak *zT* of ~0.75 at 800 K.[16] Previous work on the $Yb_{21}Mn_4Sb_{18}$ phase has focused on both aliovalent[16] and isovalent[18] cation substitution to tune the carrier concentration. These studies showed that despite the various substitutions, the lattice thermal conductivity of this system remains extremely robust and low at around ~0.5 $Wm^{-1}K^{-1}$ while the electrical properties can be tuned over an order of magnitude. The disordered crystal structure has been studied through single crystal X-ray diffraction, synchrotron powder X-ray diffraction, and pair distribution function studies leading to a consistently low thermal conductivity.[16,18]

The two aforementioned studies have focused on the change of structure and properties through substitutions on the A and M site in the $A_{21}M_4Pn_{18}$. This work focuses on substitution of the anion (Pn) site and will provide a complete picture on the substitutional effects within the 21-4-18 system. The anion sites have been shown to contribute to the majority of states in the valence band of this material.[16] Making substitutions on these sites provide an additional pathway for tuning the properties of this system due to their proximity to the Fermi level.

Herein, we report the structure and properties of the $Yb_{21}Mn_4Sb_{18-x}Bi_x$ solid solution.

4.3 Experimental

4.3.1 Synthesis of $Yb_{21}Mn_4Sb_{18-x}Bi_x$

Polycrystalline samples were synthesized similarly to that described previously.[16,18] Stoichiometric amounts Yb filings (Metall Rare Earth Limited, 99.99%), Mn pieces (Alfa Aesar, 99.95%), Sb shots (Alfa Aesar, 99.999%) and Bi needles (Alfa Aesar, 99.99%) for the $Yb_{21}Mn_4Sb_{18-x}Bi_x$ (x = 0, 4.5, 9, 18) samples were loaded into a stainless steel ball-mill (50 mL vial, 3 stainless steel 0.5'' balls) for homogenization

under Ar atmosphere. The ball-mill was heat sealed inside a Mylar bag followed by one hour mixing in a SPEX 8000 M High-Energy ball-mill. The contents were scraped off the sides of the ball-mill, resealed in Mylar and milled for an additional hour. The powder was transferred and sealed into 8 cm long Nb tubes using an arc welder under partial Ar pressure and further encapsulated in fused silica tube under vacuum. Ampoules were heated to 650°C at 100°C/h, sintered for 4 days, and allowed to slowly cool to room temperature in the furnace.

Consolidation of the sintered powder samples was completed using spark plasma sintering using a Dr. Sinter SPS-2050. The samples were first ground in a mortar and pestle and passed through a 200 mesh sieve and were loaded into a 12.7 mm diameter graphite die between multiple graphite foil spacers. The SPS chamber was evacuated until <100 mTorr and backfilled with Ar prior to sintering. The die was set to an initial pressure of 6 kN and heated to 535°C in 6 minutes, 585°C in 1 minute to prevent overshooting, and allowed to dwell at the maximum temperature for 30 minutes. The applied pressure was adjusted monotonically to 10.8 kN upon observing a positive displacement of the die. All of the pellets obtained were ~95% dense according to the Archimedes' method.

4.3.2 Powder X-ray Diffraction

Powder X-ray Diffraction (PXRD) data was collected on a Bruker D8 Advance Eco Diffractometer using Cu Kα radiation from 2θ = 20° - 80° at room temperature. Rietveld refinement was completed using the TOPAS5 software.

4.3.3 Thermoelectric Property Measurements

A Linseis LSR-3 instrument was used to measure both the resistivity and Seebeck coefficient using the four-probe method (8mm probes) from 300K to 800K under He atmosphere. For the measurements, the sample was shaped into a bar with dimensions approximately 10 mm x 2 mm x 2 mm and polished.

A Netzsch LFA 457 instrument was used to measure the thermal diffusivity under vacuum up to 800 K. Samples measured were polished flat and coated with a thin layer of graphite. The heat capacity was estimated using the Dulong-Petit method for thermal conductivity calculation.

4.4 Results and Discussion

4.4.1 Crystal Structure

Rietveld refinement of the PXRD data shows that throughout the whole solid solution, the crystal structure of the $Yb_{21}Mn_4Sb_{18-x}Bi_x$ system remains in the C2/*c* space group like the parent compound (*x* = 0). A representative sample is shown in **Figure 4.1**. The lattice parameters obtained from the refinement are listed in **Table 4.1**.

Table 4.1: Summary of Lattice Parameters for the $Yb_{21}Mn_4Sb_{18-x}Bi_x$ Solid Solution and Weight % of the Impurity $Yb_{11}Sb_{10}$

Sample	**a (Å)**	**b (Å)**	**c (Å)**	**β (°)**	**Vol. (Å^3)**	**$Yb_{11}Sb_{10}$ wt. %**
x = 0*	17.02725(9)	17.04802(9)	16.77150(9)	92.7936(4)	4862.66(4)	-
x = 4.5	17.121(1)	17.133(1)	16.857(1)	92.862(2)	4938.5(5)	1.91
x = 9.0	17.196(1)	17.226(1)	16.936(1)	92.893(3)	5010.3(6)	9.02
x = 18.0	17.368(1)	17.393(1)	17.117(1)	92.938(3)	5164.3(5)	11.36

*Ref. [16]

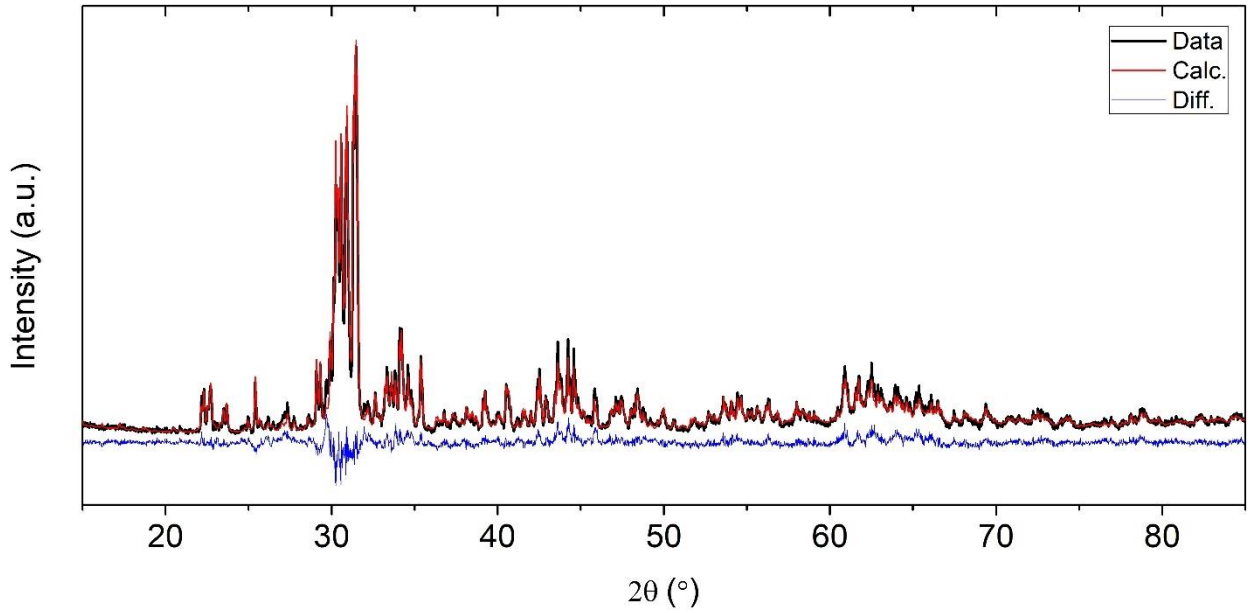

Figure 4.1: Representative X-ray powder diffraction pattern for the $Yb_{21}Mn_4Sb_{18-x}Bi_x$ (x = 18) sample.

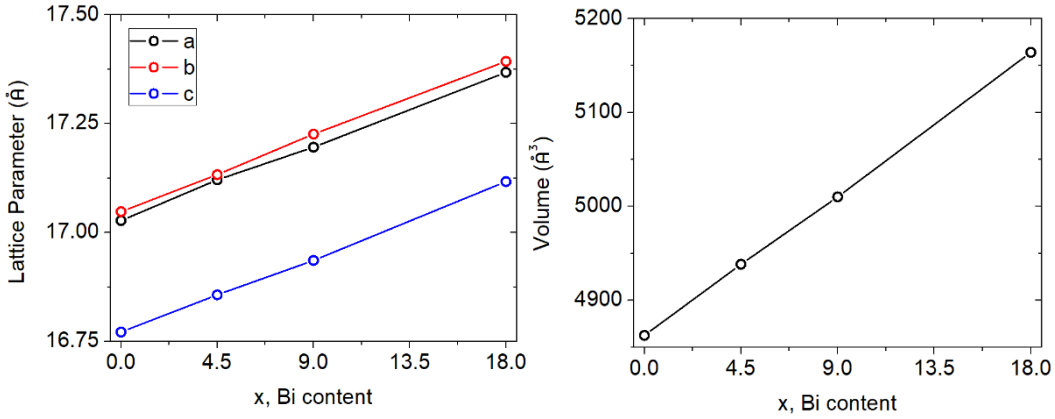

Figure 4.2: Lattice parameter progression and unit cell volume with additional Bi substitution in the $Yb_{21}Mn_4Sb_{18-x}Bi_x$ system following Vegard's Law.

The monotonic increase in unit cell volume (**Figure 4.2**) is expected (Vegard's Law) since the Shannon crystal radius of Sb in the current coordination environment is 0.9 Å while Bi has a crystal radius of 1.17 Å.[87] Precise site occupation factors for the Bi atoms on the Sb sites could not be determined from lack of

single crystal samples. Instead, the Rietveld refinements were completed assuming an even distribution of Bi atoms among the Sb sites to account for the changes in scattering factor between Sb and Bi.

As the system goes toward the pure Bi phase, the impurity phase of $Yb_{11}Sb_{10}$ (11-10) was identified in the XRD patterns in increasing amounts (**Table 4.1**). This is strong evidence that as we go toward the full Bi phase, the phase stability of the 11-10 phase increases and signals a change in the phase equilibrium between 21-4-18 and 11-10. The temperature space was surveyed through annealing experiments at 600 °C and 700 °C but did not yield a decrease in 11-10 concentration suggesting that perhaps a new synthetic route is necessary to achieve phase purity in this system (e.g. through binary starting materials) or through careful, systematic experiments exploring the phase space to understand the proper loading composition.

4.4.2 Thermoelectric Properties

Complementary to our previous study on isoelectronic substitutions,[18] the solid solution with Bi completes a survey within this structure type on the influences of isoelectronic site selective substitution. With the additional Bi substitution, it is expected that the carrier mobility will increase due to the more diffuse orbitals of Bi. Previous DFT calculations on the electronic band structure of the 21-4-18 system have shown that the majority of the valence band states are made up from the anionic states in the compound.[16] By replacing the Sb with Bi, it is expected that the states will shift higher in energy on the basis of electronegativity arguments. This would make the compound more metallic as states move closer to the Fermi level. The electrical resistivity in the solid solution can be seen to steadily decrease with an increase in Bi content (**Figure 4.3**).

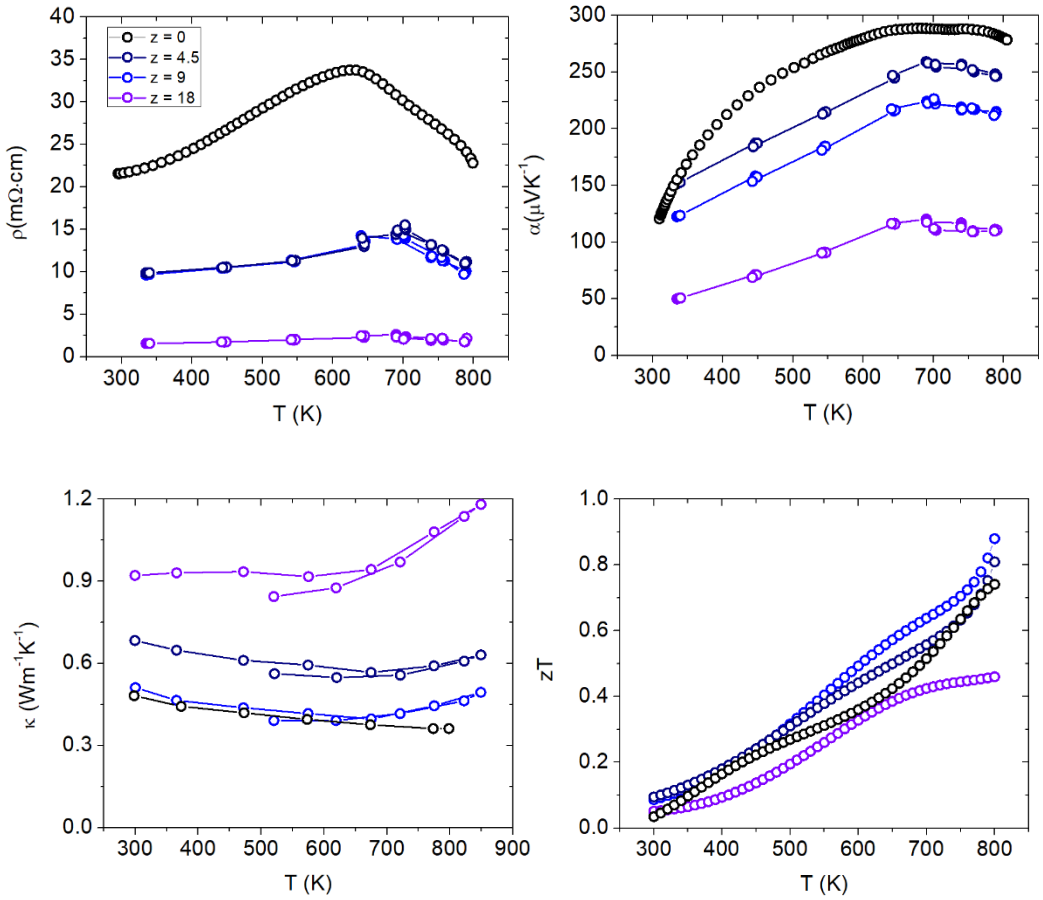

Figure 4.3: Thermoelectric transport properties of the $Yb_{21}Mn_4Sb_{18-x}Bi_x$ showing the temperature dependence of a) electrical resistivity, b) Seebeck coefficient, c) Thermal conductivity, d) Figure of merit *zT*.

Additionally, the Seebeck coefficient can also be seen to decrease with additional Bi content (**Figure 4.3**). This may be due to a decrease in effective mass due to the higher mobility and/or from higher carrier concentrations with the Bi substitution. The thermal conductivity of this system was calculated according to $\kappa = \mathrm{D}\mathrm{d}C_p$ where D is thermal diffusivity, d is the sample density, and C_p is the heat capacity. The Dulong-Petit law was used to estimate the heat capacity. Overall, an increase in the total thermal conductivity was observed with additional Bi doping due to the increasing electronic component to the thermal conductivity (**Figure 4.3**). This is in part due to the increasing fraction of 11-10 within the samples, where $Yb_{11}Sb_{10}$ is observed to have a larger thermal conductivity than the 21-4-18 phase.[88] Since the

resistivity decreases by an order of magnitude at maximum Bi substitution, the increase in the electronic portion to the thermal conductivity will also contribute to the increase of total thermal conductivity (Wiedemann-Franz relationship) where the total thermal conductivity can be approximated as the sum between electronic and lattice contributions $\kappa = \kappa_{lat} + \kappa_e$. At *x* = 9, the total thermal conductivity is seen to drop due to the solid solution being at the minimum in lattice thermal conductivity from mass disorder/alloy scattering.[89]

The figure of merit *zT* was calculated according to polynomial fits to α, ρ, κ. Overall despite the 11-10 impurity, a slight increase in the figure of merit was observed for the z = 9 sample reaching a maximum *zT* value of 0.9 (**Figure 4.3**). If the synthetic scheme is optimized and the compounds can be made pure phase, the thermal conductivity of the 0.9 sample is expected to decrease even further, leading to an increased figure of merit. As even more Bi is put into the system, the material becomes too metallic resulting in heightened thermal conductivity and lower Seebeck coefficient resulting in a lower overall zT compared to the intrinsic phase.

4.5 Conclusion

The Bi solid solution ($Yb_{21}Mn_4Sb_{18-x}Bi_x$) for the 21-4-18 system has been investigated through high temperature annealing and spark plasma sintering. As *x* increases, the amount of side phase impurity, $Yb_{11}(Sb, Bi)_{10}$ increases. The crystal structure remains in the C2/*c* space group throughout and exhibits a linear increase in unit cell volume as expected from Vegard's Law. There is a clear trend in the physical properties where the phase becomes more metallic with increased Bi substitution leading to an increased figure of merit for the *x* = 9 sample. As even more Bi is introduced, the system becomes too metallic ultimately resulting in a decreased figure of merit.

Chapter 5 $Eu_5Al_3Sb_6$: Dual Al_4 tetrahedra discovered in rock salt-like structure

Allan He[1], Zihao Shen[2], Valentin Taufour[2], Weiwei Xie[3], Zhen Wang,[4] Yimei Zhu,[4] Luis Garay,[1] James C. Fettinger[1], Raphaël P. Hermann[5], and Susan M. Kauzlarich[1*]

[1]Department of Chemistry, One Shields Ave, University of California, Davis, California 95616, USA

[2]Department of Physics and Astronomy, University of California, Davis, California 95616, USA

[3]Department of Chemistry and Chemical Biology, Rutgers University, Piscataway, New Jersey 08854, USA

[4]Condensed Matter Physics and Materials Science Department, Brookhaven National Laboratory, Upton, New York 11973, USA

[5]Materials Science and Technology Division, Oak Ridge National Laboratory, Oak Ridge, Tennessee 37831, USA

Allan He conducted the synthesis and characterization. Zihao Shen and Valentin Taufour helped with the magnetic, resistivity and heat capacity measurements and interpretation of the data. Weiwei Xie contributed the electronic structure calculations and helped with data interpretation. Zhen Wang and Yimei Zhu contributed the TEM analysis and interpretation. Luis Garay helped to grow some single crystal samples. Jim Fettinger helped with the single crystal solution. Raphaël Hermann collected the Mössbauer spectroscopic data and provided interpretation.

5.1 Abstract

The $Eu_5Al_3Sb_6$ phase has been successfully synthesized as a pure phase through Sn flux methods yielding large, high-quality crystals. This new structure type features disordered Al clusters that appear in the form of dual tetrahedra. It crystallizes in the monoclinic *C2/m* space group exhibiting a rock-salt like Eu-Sb framework with two interpenetrating [Al_4] tetrahedra replacing some of the cationic Eu atoms (Space group: *C2/m*, a = 8.151(1) Å, b = 14.181(2) Å, c = 8.145(1) Å, β = 109.577(2)). The presence of the Al_4 cluster is further supported by HRTEM. Electronic structure calculations show that this material has the potential to realize topological behavior with proper defect concentration tuning. Magnetic susceptibility measurements can be described well with a Curie-Weiss law where an effective moment of 7.80 μ_B/mol Eu is obtained, consistent with Eu^{2+} and shows canted AFM behavior. Temperature dependent resistivity shows metallic behavior with a residual resistance ratio of 1.142 suggesting a highly disordered compound.

5.2 Introduction

Zintl phases have been shown to be a promising field for material discovery. These are charge balanced compounds where the combination of ionic and covalent bonding can lead to the formation of extremely complex structure types such as $Yb_{14}MnSb_{11}$[4] and $Yb_{21}Mn_4Sb_{18}$[16,18] and can exhibit a whole range of interesting physical phenomena. This includes high thermoelectric performance,[67] intermediate valent behavior,[90] Kondo type magnetism,[91] superconductivity,[92] topological behavior[93] and more. The variety in physical phenomena stems from the large number of possible structures that fall within the Zintl formalism. A new structure type and compound with the nominal stoichiometry of $Eu_5Al_3Sb_6$ has been discovered. The structure features disordered Al clusters in an otherwise ordered rock-salt type Eu-Sb framework where the Al-clusters replace some of the Eu atoms.

These kinds of triel clusters are rarely seen in the solid-state with only a few examples known in the literature such as the $Sr_{14}Al_8Ge_3$ phase[94] and $Ni_{20}Al_3B_6$.[95] Understanding the nature of triel clusters has been a subject of intense investigation in the organometallic community where work has been done on large Al clusters such as the iodized Al_{13} and Al_{14} clusters,[96,97,98] as well as characterization of triel tetrahedra (including Al_4 tetrahedra).[99,100] These clusters have exhibited unique behavior with electronic properties that are fundamentally different from bulk metals. For example, the Al_{13} cluster has been found to act as a superhalogen whereas Al_{14} can behave like an alkaline earth metal.[96] Although these clusters have been shown to exist in the gas phase, it is unclear what interesting properties could emerge in solid state.

The inherent defects present in this structure type make it ideal for property tuning. The idea of using defect chemistry for electrical property tuning has been used in the thermoelectric community for carrier concentration tuning where, depending on what type of vacancy is present, the vacancy can shift the carrier concentration higher or lower.[60] Vacancies have been shown to control the electronic properties of oxides[101] and clathrates[38] and play an important role in property optimization making this structure type very tunable. This new phase has the potential for realizing topological behavior through careful defect concentration tuning where band crossing has been observed in electronic structure calculations.

Herein, we report the synthesis, crystal structure, electronic structure calculations, electrical resistivity, magnetic susceptibility, and heat capacity studies for the $Eu_5Al_3Sb_6$ compound.

5.3 Experimental

5.3.1 Synthesis

Single crystal growth was completed using Sn flux. Large single crystals of this phase were grown where elemental Eu pieces (Ames Laboratory, 99.999%), Al shots (Alfa Aesar, 99.999%, size of shots), Sb shots

(Alfa Aesar, 99.999%, size of shots), and Sn shots (Alfa Aesar, 99.99%, size of shots) were loaded into Canfield Al_2O_3 crucibles[40] with loading composition of $Eu_3Al_5Sb_3Sn_{15}$. Quartz wool was placed on both the top and bottom of the crucible and the reaction was sealed into evacuated quartz tubes. The sample was heated to 1050°C at 100°C/h, dwelled for 12h, and then cooled slowly to 750 °C at 2 °C/h to yield the crystals shown in **Figure 5.1** after which the crucible was inverted and centrifuged to remove the molten tin.

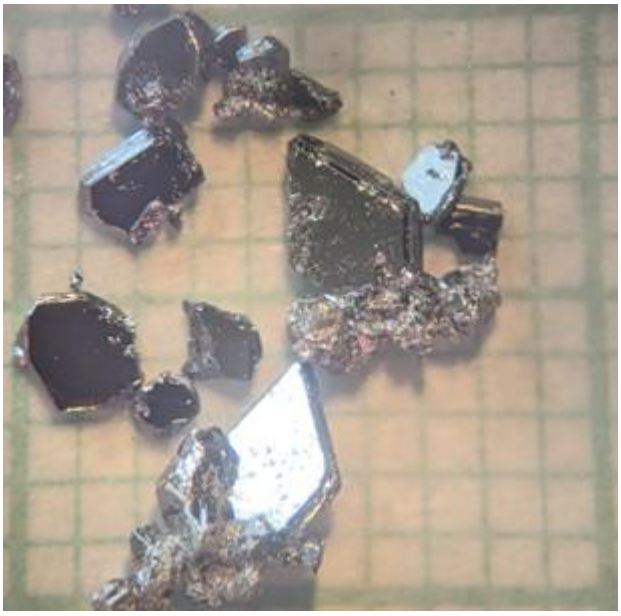

Figure 5.1: Representative single crystals obtained from flux experiments. One grid square is 1 mm x 1 mm.

5.3.2 Single Crystal X-ray Diffraction

Single crystal diffraction data were collected at 100 K using a Bruker Apex Duo diffractometer with Mo Kα (λ = 0.71073 Å) radiation. Crystals were selected under Paratone oil, mounted on a MiTeGen MicroLoop and then placed in the cold nitrogen stream. Crystals are mildly air-sensitive and tarnish over time. The crystals had plate morphology and were highly black and reflective (see **Figure 5.1**). Absorption

corrections were applied using SADABS. Space group determination was done using XPREP and structural solutions were completed through direct methods with SHELXS and refined using the SHELXL software. Initial structural solutions assumed a Cm space group that yielded a Flack parameter closer to 0.5 which suggested twinning. Solutions were then pursued with the addition of the two-fold axis in the C2/m space group that no longer had a problem with the Flack parameter and yielded a slightly lower R_1 value. All aluminum atoms were allowed to freely refined and converged close to the ideal 37.5% occupancy and was restricted as such. The partially occupied Eu1 site was allowed to freely refine. Data collection parameters, atomic coordinates and selected bond distances are provided in **Table 5.1**, **Table 5.2** and **Table 5.3,** respectively.

Table 5.1: Selected Crystal Data and Data Collection Parameters for $Eu_5Al_3Sb_6$.

Wavelength	0.71073 Å
Space Group	C2/m
Unit cell dimensions	a = 8.151(1) Å b = 14.181(2) Å c = 8.145(1) Å β = 109.577(2)
Volume	887.1(2) $Å^3$
Z	2
Θ-range for data collection	2.654° – 27.546°
Reflections collected	4066
Completeness to Θ = 25.242°	100.0%
Density	3.405 g/cm^3
Absorption coefficient	12.479 mm^{-1}
Goodness-of-fit	1.116
Final R indices [I>2σ(I)]	R_1 = 0.0320, wR_2 = 0.0571
Final R indices [all data]	R_1 = 0.0370, wR_2 = 0.0788

Table 5.2: Atomic Coordinates, Isotropic Displacement Parameters and Occupancy for $Eu_5Al_3Sb_6$.

Atom	Wyckoff Position	x	y	z	U_{eq} ($Å^2$)	Occupancy
Eu1	2a	0	0	0	0.017(4)	0.08(5)
Eu2	4g	0	0.33434(4)	0	0.0222(3)	1
Eu3	2d	0	0.5	0.5	0.0199(3)	1
Eu4	4h	0	0.16967(4)	0.5	0.0180(3)	1

Al1	8j	0.4332(8)	0.4065(5)	0.0700(8)	0.023(2)	0.375
Al2	4i	0.211(1)	0	0.069(1)	0.032(3)	0.375
Al3	4i	0.066(1)	0	0.214(1)	0.027(2)	0.375
Sb1	8j	0.24739(6)	0.16496(3)	0.24832(6)	0.0175(2)	1
Sb2	4i	0.24586(9)	0	0.75024(9)	0.0207(2)	1

Table 5.3: Selected Bond Distances for $Eu_5Al_3Sb_6$.

Eu Atom Pairs		Distance (Å)	Al Atom Pairs		Distance (Å)	Sb Atom Pairs		Distance (Å)
Eu2	– Sb1 x 2	3.3349(5)	Al1	– Al1	2.65(1)	Sb1	– Al1	2.684(7)
	Sb1 x 2	3.3457(7)		Al2	2.63(1)		Al1	2.713(6)
	Sb2 x 2	3.3353(7)		Al3	2.67(1)		Al2	2.720(5)
	Al2 x 2	3.501(8)					Al3	2.730(5)
	Al1 x 2	3.535(7)					Eu1	3.3009(6)
Eu3	– Sb1 x 4	3.3294(5)	Al2	– Al3	2.64(1)	Sb2	– Al1 x 2	2.732(6)
	Sb2 x 2	3.3578(8)					Al2	2.70(1)
	Al2 x 2	3.51(1)					Al3	2.656(9)
	Al3 x 2	3.52(1)					Eu1	3.3009(6)
Eu4	– Sb1 x 2	3.3231(5)						
	Sb1 x 2	3.3337(6)						
	Sb2 x 2	3.3500(7)						
	Al3 x 2	3.513(7)						
	Al1 x 2	3.529(6)						

5.3.3 Transmission Electron Microscopy

Samples for TEM analysis were crushed in an agate mortar and deposited directly onto a holey carbon copper grid. The Scanning Transmission Electron Microscopy (STEM) imaging and electron diffraction were performed on a 200kV JEOL ARM electron microscope at Brookhaven National Library equipped with double aberration correctors and a cold field emission source. The high-angle annular dark-field image (HAADF) STEM image were collected with a 21 mrad convergent angle (30 µm condenser aperture) and a collection angle of 67 – 275 mrad.

5.3.4 Powder X-ray Diffraction

Powder X-ray Diffraction (PXRD) data were collected on a Bruker D8 Advance Eco Diffractometer using Cu Kα radiation from 2θ = 20° - 80° at room temperature in air. The crystals were ground in air and plated on a zero-background holder. Rietveld refinements were completed using the TOPAS5 software.

5.3.5 Compositional Analysis

Single crystal samples were placed flat on carbon tape for elemental analysis. Energy dispersive X-ray spectroscopy data was done with a FEI Scios DualBeam SEM/FIB with a window-less Oxford Instruments X-max50, 50 mm^2 silicon drift detector. Secondary electron images were collected using 20 kV and 1.6 nA electron beam.

5.3.6 Electronic Structure Calculations

The hypothetical "$Eu_5Al_4Sb_6$" with fully occupied tetrahedral Al_4 cluster instead of partially occupied Al_4 cluster was employed to perform the electronic structure calculations. The experimental structural parameters were employed. The Wien2k program which implements the full-potential linearized augmented plane wave method (FP-LAPW) was used. On-site U = 6 eV was used for Eu *f*-orbitals.[102] The spin−orbit coupling (SOC) was included on Eu and Sb atoms self-consistently in the calculations of electronic structures with a Monkhorst–Pack *k*-point mesh 8 × 4 × 8 with the cut-off energy 500 eV.

5.3.7 Magnetic Susceptibility

Magnetization measurements were performed in a Quantum Design Magnetic Properties Measurement System (MPMS) from 2 – 300 K and up to 5T. The crystals chosen for magnetic measurements had their unit cells confirmed through single crystal XRD prior to measurement. The crystals were aligned with the c-axis perpendicular to the applied field.

5.3.8 Electronic Transport and Magnetoresistance

D.C. resistivity and magnetoresistance were measured in a Quantum Design Physical Property Measurement System (PPMS) from 0 – 0.5 T using the four-lead method from 2 – 300 K. Contacts were made with platinum wire held in pace by silver epoxy. The electrical resistivity was measured in the ab-plane (see **Figure 5.2**).

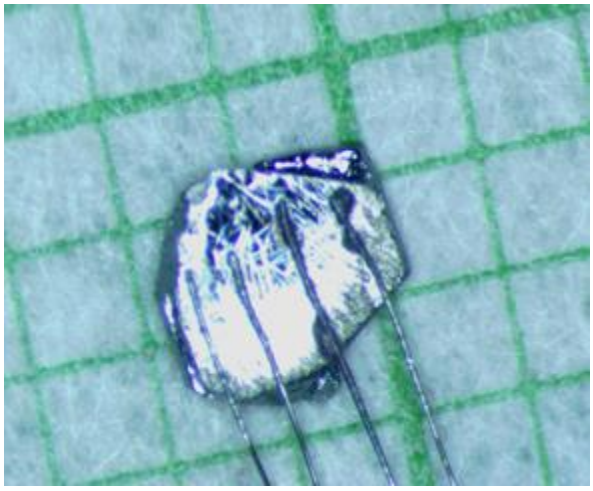

Figure 5.2: Four-lead setup on the $Eu_5Al_3Sb_6$ crystals. Grid square is 1 mm x 1 mm.

5.3.9 Heat Capacity

Heat capacity measurements were done in a Quantum Design PPMS from 2 K – 300 K.

5.3.10 Mössbauer spectroscopy

Europium-151 and antimony-121 Mössbauer spectra were measured at room temperature using a constant acceleration Mössbauer drive (Wissel GmbH) in constant acceleration mode, with the velocity in the -20 to +20 mm/s range, calibrated using a cobalt-57 source and alpha-iron foil; the sources, $^{151}SmF_3$

amd $Ca^{121}SnO_3$, respectively, were kept at room temperature. Data and isomer shifts are reported relative to the respective source. The sample was prepared by mixing 75 mg/cm^2 of powder with boron nitride.

5.4 Results and Discussion

5.4.1 Crystal Structure

$Eu_5Al_3Sb_6$ crystallizes in the monoclinic *C2/m* space group and the structure features a rock-salt like Eu-Sb framework with two interpenetrating [Al_4] tetrahedra replacing some of the cationic Eu atoms (**Figure 5.3**). The [Al_4] tetrahedra have an average bond length of around 2.65 Å and a polyhedral volume of 2.185 Å^3.

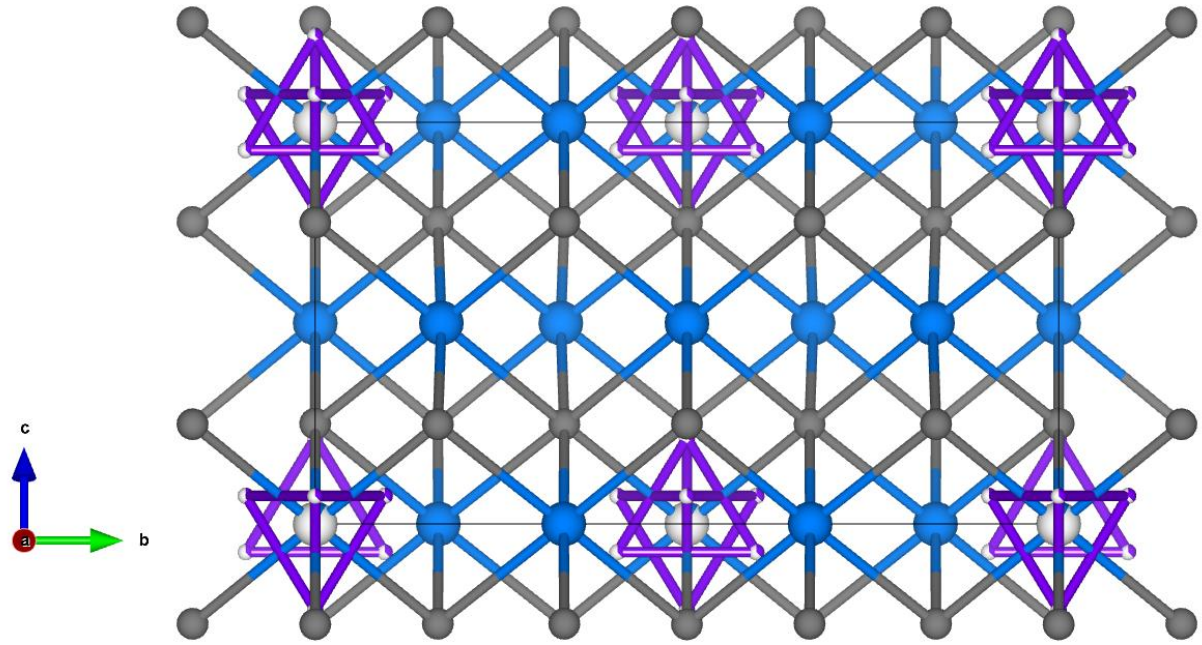

Figure 5.3: The $Eu_5Al_3Sb_6$ structure type where Eu atoms are in blue, Sb atoms in gray, and Al atoms in purple (Space group: C2/m, a = 8.151(1) Å, b = 14.181(2) Å, c = 8.145(1) Å, β = 109.58(1)°) projected down the a-axis.

A close-up of the Al moiety is provided in **Figure 5.4a** where all Al (Al1, Al2, Al3) atoms are partially occupied 37.5% of the time and the central Eu1 atom is present 8% of the time. The Eu1 and Al atoms cannot exist simultaneously as the bond distance is too small (~1.64 Å). The presence of the partially occupied Eu atom changes the nominal stoichiometry of $Eu_5Al_3Sb_6$ to $Eu_{5.08}Al_3Sb_6$. In **Figure 5.4b**, the two interpenetrating tetrahedra are colored purple and pink for clarity. Note that the vertices of the two tetrahedra in conjunction form a cube, however the Al-Al distance of adjacent Al atoms in the cube are too small for all Al atoms to be present at the same time (~1.8 Å). Therefore, the presented structural model is such that the tetrahedra exist only in one orientation at a time, and only when the central Eu atom is not present. Since the tetrahedra reside within a Sb_6 octahedra, there is no structural restrictions for one orientation of Al_4 over the other and therefore the best model provides a dual tetrahedra in the center.

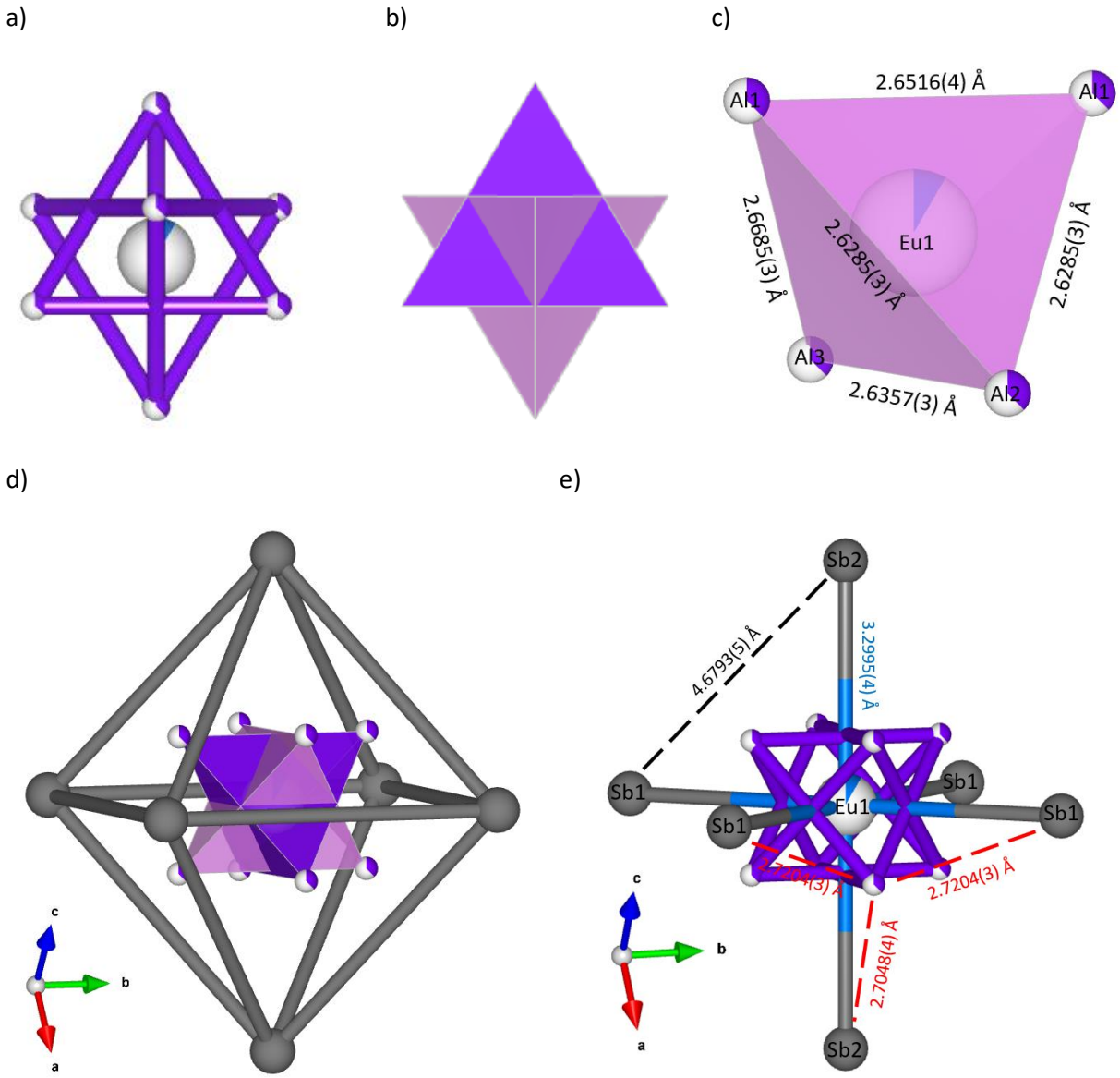

Figure 5.4: Close-up view of the a) two interpenetrating [Al_4] tetrahedra and the central deficient Eu atom (Eu1), b) dual tetrahedra color schemed for clarity, c) single tetrahedra, d) Eu1 coordination showing arrangement of the dual tetrahedra inside the Sb octahedral cage, e) Eu1 coordination environment.

In **Figure 5.4c**, a close-up of one orientation of the tetrahedra is showed with select Al-Al distances. **Figure 5.4d** shows the coordination environment of the Eu1/Al_4 dual tetrahedra in a polyhedral view emphasizing that the Al tetrahedra are positioned within the Sb octahedra such that each vertex of the Al tetrahedra point toward the center of a unique octahedral face. This is the most sensible configuration to minimize

Coulombic repulsion within the structure and provides stabilization. The coordination environment of Eu1 with select bond distances is shown in **Figure 5.4e** where we note that the Al atom does not sit precisely in the center of the octahedral face but is slightly below the plane of the octahedral face.

DFT calculations have been done on free aluminum clusters that have found that the ground state structural isomer of an Al_4 cluster is a planar rhombus in a triplet spin state while the Al_4 tetrahedral clusters are the least energetically favorable form.[103,104,105] The ab initio calculations predict a bond length of 2.74 Å for the tetrahedral cluster (multiplicity of 5)[104] or a bond length of 2.692 Å in a triplet state[105]. The bond length found experimentally for the Al tetrahedra is around 2.65 Å, slightly smaller than either of the calculations but may be a requirement of the Sb octahedron in which it is centered. When hydrogen is attached to the tetrahedral Al atom vertices, the bond lengths of the Al cluster decrease so that the Al-Al distance for an Al_4H_2, Al_4H_4 cluster is 2.66 Å, 2.60 Å, respectively, and the overall stability of the cluster increased.[104] Since the bond length observed in the $Eu_5Al_3Sb_6$ compound (2.65 Å) is less than that observed for the calculated, free Al_4 tetrahedra in any spin configuration, and because the Al cluster is not observed in the ground state structure (planar rhombus), there must be a source of stabilization. It is presumed that like the hydrogenation case, each face of the Sb octahedral cage could provide charge stabilization to the Al cluster, allowing it to adopt the observed tetrahedral geometry and therefore the cluster results in the shorter than expected bond distance. As mentioned previously, it is expected that the Al tetrahedra can only exist in high spin states.

Given that other Eu-Al-Sb phases such as $Eu_5Al_2Sb_6$[2] and $Eu_{14}AlSb_{11}$[106] and similar compounds are all Zintl phases, it may be reasonable to approach the structure using Zintl electron counting and assume a charge balanced phase. In the unit cell, there are a total of 16 Al atoms (Al1 site: 8j, Al2 site: 4i, Al3 site: 4i), each at 0.375 occupation. Since Z = 2 for this structure, then per formula unit there are 8 aluminum atoms (2 tetrahedra), where 8 x 0.375 = 3, the molar ratio of aluminum in the formula unit. Assuming that the Sb

atoms are 3- and that the Eu atoms are 2+, then in the nominal $Eu_5Al_3Sb_6$ compound, there is an excess of 8 electrons that must be accounted for the two tetrahedra, meaning that each tetrahedra must be 4+ making each 0.375Al atom formally 1+. In summary, the compound can be written as $(Eu^{2+})_5([0.375Al_4]^{4+})_2(Sb^{3-})_6$. However, it is also possible to think of this compound simply as the Al atoms being 3+ each with one of the electrons being itinerant in the material. The interaction of this itinerant electron with the local 4f states of Eu would result in heightened carrier scattering that is apparent only at low T where quantum phenomenon dominate. This corresponds well to the observed increase in resistivity at low T. Under the itinerant electron framework, the Al_4 cluster would have an S = 0 and a multiplicity of 1 (singlet) with all electrons paired, necessitating the existence of a stabilization source (i.e. the Sb octahedra) in order for this structure to be realized since it has been shown that the singlet spin configuration of the Al tetrahedra is the least energetically stable isomer.[105]

In either structural framework, there would be deviation from the Zintl precise structure as there exists a partially occupied Eu site (Eu1) when the Al clusters are not present. This would result in more electrons being donated into the structure to push it more n-type which is what we observe in Hall carrier concentration measurements.

5.4.2 Transmission Electron Microscopy

a) b)

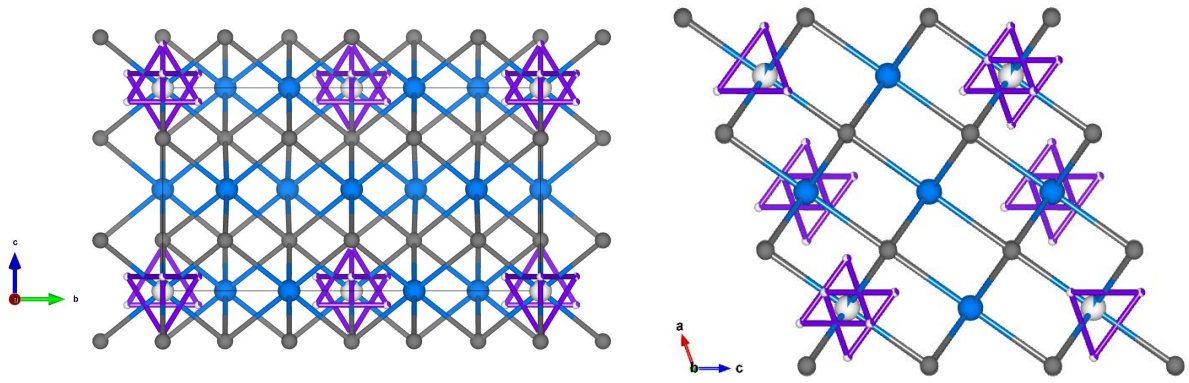

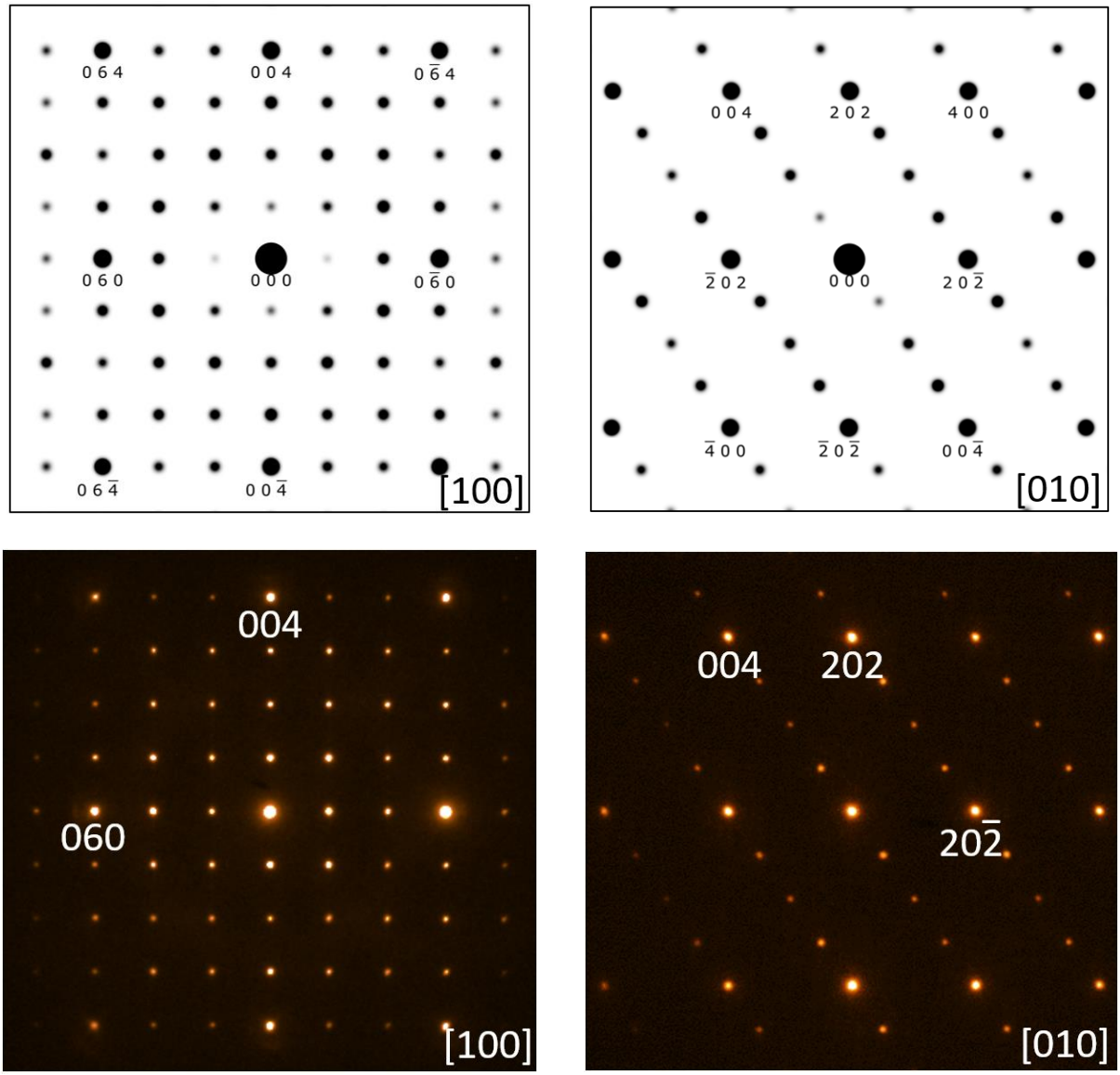

Figure 5.5: Selected area electron diffraction (SAED) taken along the a) [100] and b) [010] direction, respectively. Top: Projected crystal structures in real space, Middle: Simulated electron diffraction patterns, Bottom: Experimental SAED patterns.

Selected area electron diffraction (**Figure 5.5**) and HAADF-STEM imaging (**Figure 5.6**) were performed to further confirm the structure obtained from X-ray crystallography. The simulated and experimental electron diffraction data show good agreement. In the Z-contrast HAADF image shown in **Figure 5.6**, the Eu (Z = 63) layers are brighter than the Sb ones, which is good agreement with the superimposed unit cell.

Since Al (Z = 13) is much lighter than Eu and Sb, the Al clusters cannot be directly seen in the Z-contrast image.

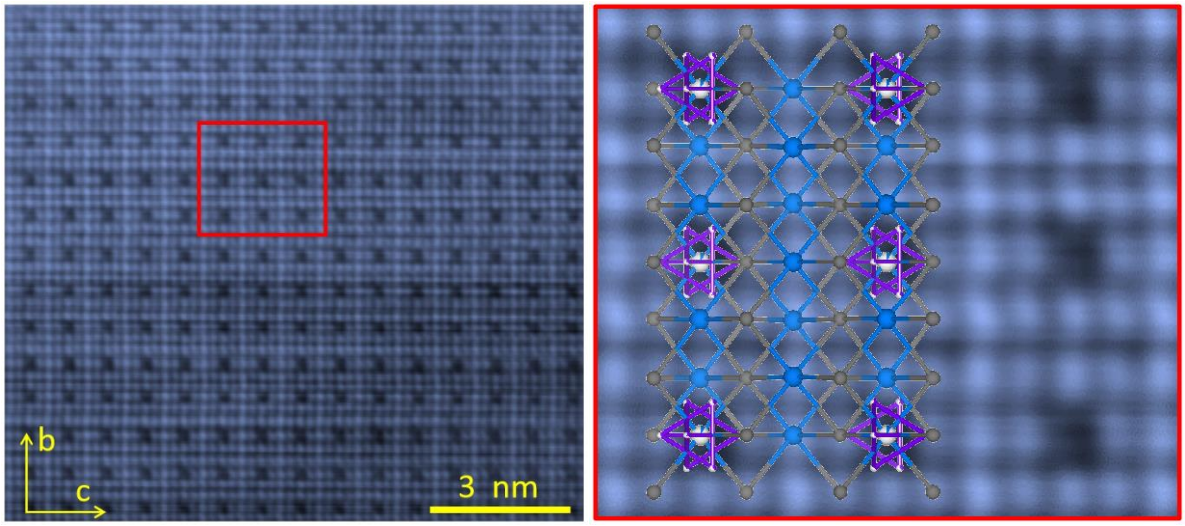

Figure 5.6: False-colored HAADF-STEM image of $Eu_5Al_3Sb_6$ single crystals taken along the [100] direction. The crystal model is superimposed on the enlarged image showing the same structure.

5.4.3 Powder X-ray Diffraction

Entire batches of crystals isolated from the Sn flux experiments were ground up and analyzed through powder X-ray diffraction (PXRD). Rietveld refinement of the PXRD data (**Figure 5.7**) show that the single crystal synthetic scheme presented here yields samples that are pure phase. The obtained lattice parameters from the refinement (a = 8.1642(4) Å, b = 14.2129(5) Å, c = 8.1716(4) Å, β = 109.61(1)°) are slightly larger than those obtained from the single crystal refinement due to the difference in data collection temperature. In the single crystal analysis, presence of weak reflections seem to indicate that the unit cell could be multiple times larger. The larger unit cell should have higher level ordering of the vacancies, the two tetrahedral orientations, and the deficient Eu atomic site but is the subject of future

investigation. It should be noted that despite this, the current average structural model has an R_1 value of 0.0320 and is sufficient for the current study.

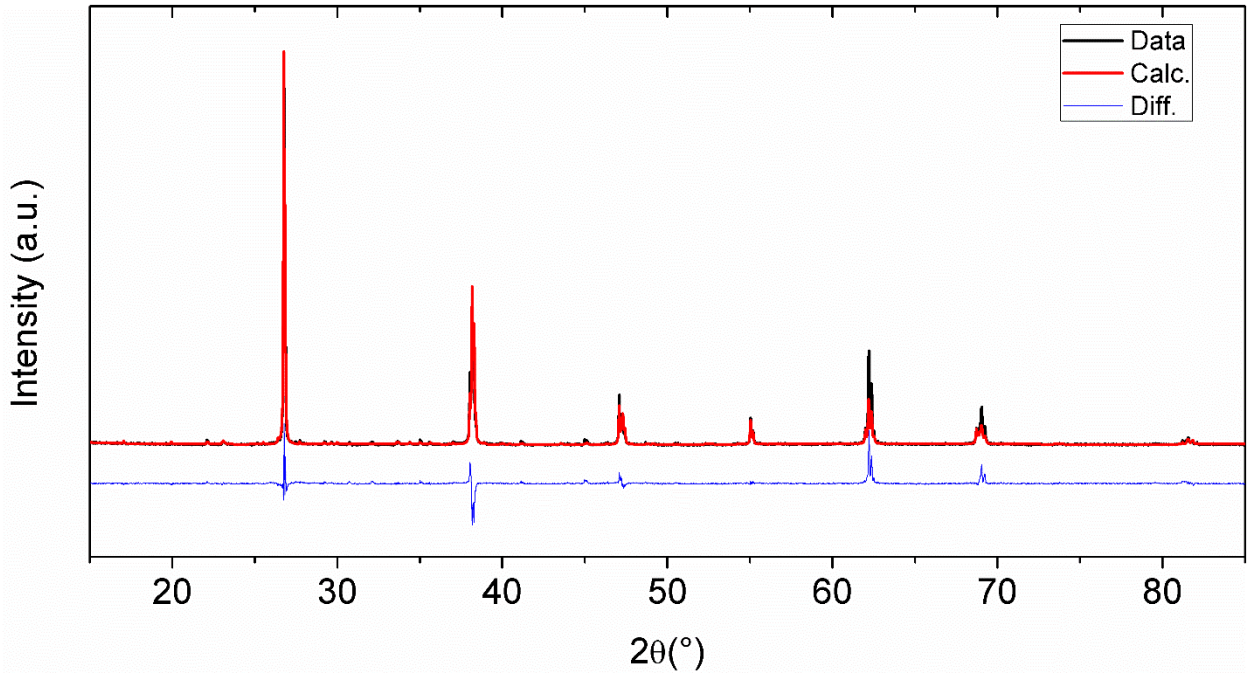

Figure 5.7: Powder X-ray diffraction pattern for $Eu_5Al_3Sb_6$ single crystals grown from Sn flux ground into powder showing Rietveld refinement with the obtained cif file. The data are presented in black, calculated spectrum in red, and difference in blue.

5.4.4 Compositional Analysis

a) b)

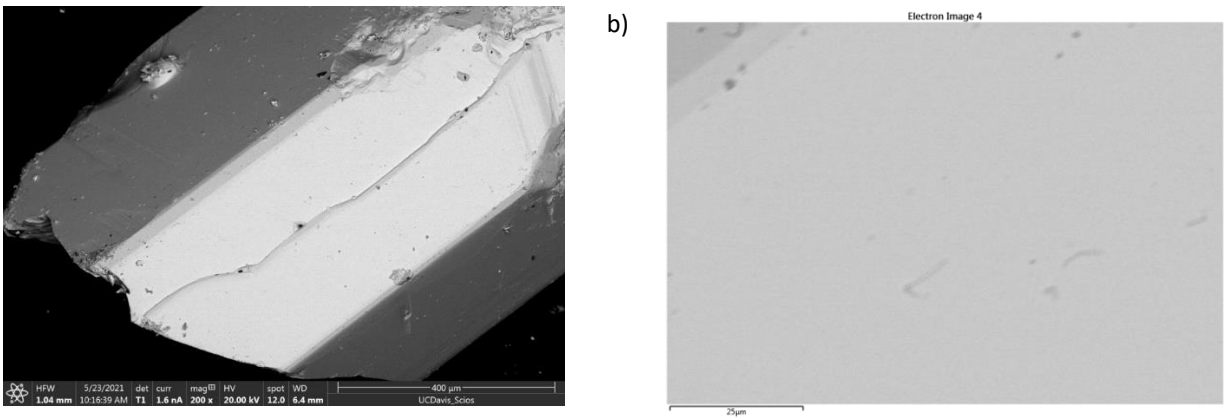

Figure 5.8: Secondary electron image collected with a 20 kV electron beam on the single crystals showing a) an overall view of the crystal and b) an enlarged view of the surface.

Single crystals were analyzed using SEM-EDS (**Figure 5.8**). Compositions of the crystals were experimentally found to be 34.8% Eu, 22.9% Al, 42.3% Sb which are within error of the nominal composition for this phase (nominally 36.0% Eu, 21.3% Al, 42.6% Sb).

5.4.5 Magnetic Susceptibility

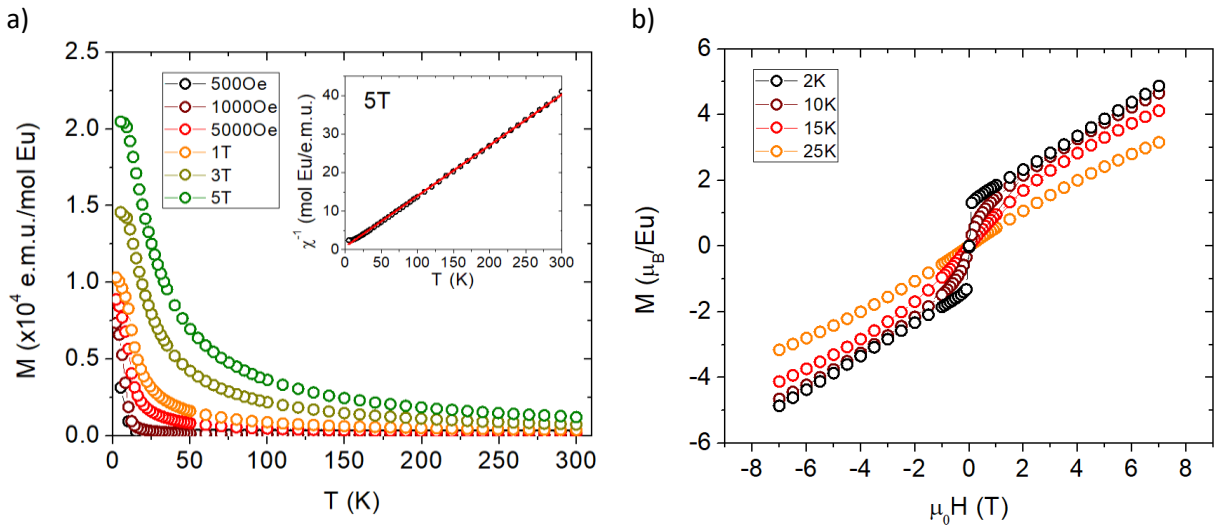

Figure 5.9: a) Magnetization measurements as a function of field (H = 0.05 T, 0.1 T, 0.5 T, 1 T, 3 T, 5 T). Inset shows the Curie-Weiss fit to the inverse susceptibility yielding a moment of 7.80 μ_B/mol Eu for the 5T data. b) Magnetization as a function of field up to 7T.

The magnetic susceptibility measurements are shown in **Figure 5.9a**. Magnetic susceptibility at 5 T was fit with a Curie-Weiss law, $\chi(T) = \frac{C}{T-\theta}$, to yield C = 7.604 and θ = -5.95 K. The Curie constant (C) leads to an effective magnetic moment of μ_{eff} = 7.80 μ_B/mol Eu. Given that the theoretical moment of Eu^{2+} is 7.94 μ_B, there is good agreement with the obtained effective magnetic moment. With larger applied field, the magnetic phase transition may shift to higher temperatures. From **Figure 5.9b**, the compound shows signs of magnetic ordering up to 25 K. The broad transition may suggest a canted antiferromagnetic

ordering and the compound does not reach saturation up to a field of 7 T at 2 K where a maximum value of 4.87 μ_B/Eu is obtained.

5.4.6 Electrical Resistivity

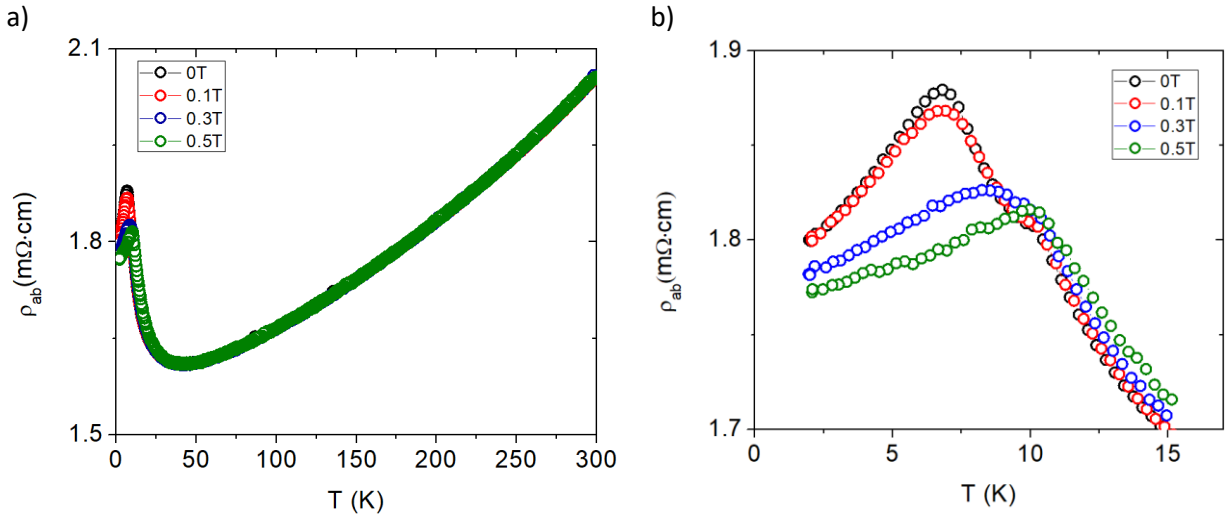

Figure 5.10: a) In-plane electrical resistivity as a function of temperature and field for the $Eu_5Al_3Sb_6$ single crystal samples. b) Close-up of the region between 2 – 15K that shows the AFM transition shifting to higher temperatures.

The electrical resistivity as a function of temperature and field is shown in **Figure 5.10**. The compound exhibits metallic behavior (increasing resistivity with temperature) with a low resistivity value (~2 mΩ·cm) at room temperature indicating that the intrinsic carrier concentration is very high. A residual resistance ratio of 1.142 is observed that suggests the structure is highly disordered and is consistent with the presented structural model. There is a clear phase transition at low T that is concurrent to the magnetic phase transition. With higher field, the AFM transition can be seen to shift to higher temperatures (**Figure 5.10b**). The increase in resistivity at 50 K may arise from a Kondo effect or interaction of the itinerant Al 3s electron with the localized 4*f* electrons of Eu leading to enhanced scattering. Room temperature Hall measurements show that the carriers are electrons with a carrier density of 2.5×10^{20} cm^{-3}. The resistance

is not strongly affected by field up to 0.5 T where a small magnetoresistance response is observed near the phase transition.

5.4.7 Heat Capacity

a) b)

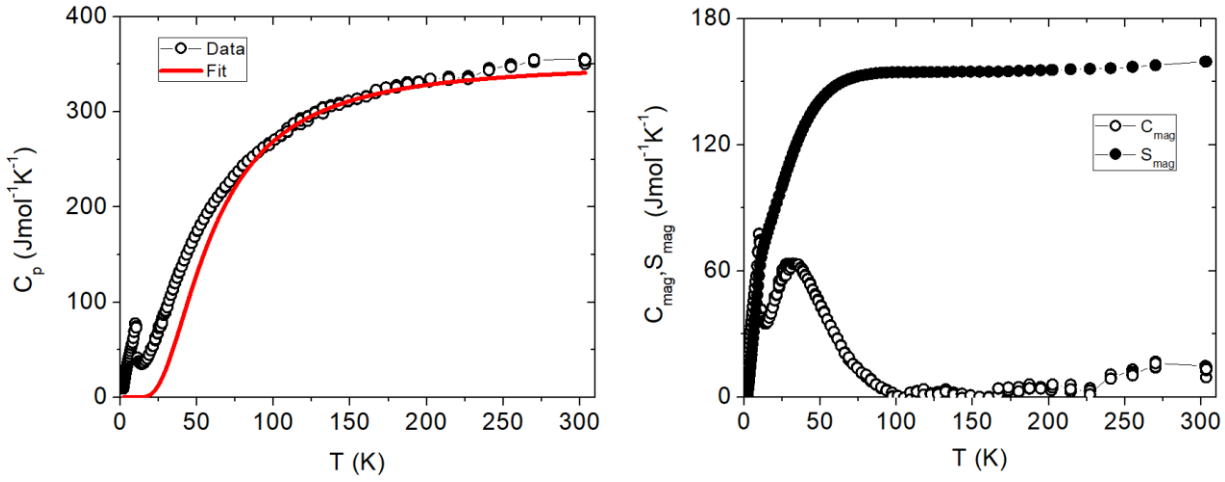

Figure 5.11: a) Temperature dependence of the heat capacity $C_p(T)$ of $Eu_5Al_3Sb_6$ and the Einstein model fit in red ($\theta_E = 181K$) b) Temperature dependence of the magnetic heat capacity (C_{mag}) and magnetic entropy (S_{mag}).

The temperature dependence of the heat capacity is shown in **Figure 5.11**. The $C_p(T)$ value at room temperature of approximately 354.36 Jmol^{-1}K^{-1} is close to the predicted high-T Dulong-Petit limit $C_V = 3nR$ = 351.18 Jmol^{-1}K^{-1} where n = 14.08 is the number of atoms per formula unit and R is the gas constant. The $C_p(T)$ data were fit (**Figure 5.11a**) using an Einstein model according to the following equation:

$$C_{Einstein} = 3R\left(\frac{\theta_E}{T}\right)^2 \frac{e^{\frac{\theta_E}{T}}}{\left(e^{\frac{\theta_E}{T}} - 1\right)^2}$$

Equation 5.1: Einstein model for heat capacity fitting.

where R is the gas constant and θ_E is the Einstein temperature (fit yields 181K). The magnetic heat capacity (C_{mag}) is estimated by subtracting the fit from the total heat capacity (**Figure 5.11b**) and subsequently integrated to yield S_{mag} according to the equation:

$$S_{mag} = \int_0^T \frac{C_{mag}}{T} dT$$

Equation 5.2: Magnetic entropy calculated from the magnetic heat capacity.

The measurements show a well-defined peak at 10 K from the magnetic phase transition and a much broader peak around 45K that arises from the shortcomings of the Einstein model in describing the phonon contribution to the heat capacity. This leads to a greater than expected magnetic entropy. The heat capacity was fit with alternative models (i.e. Debye model, weighted Debye and Einstein) however all models yielded similar fits. In the interest of restricting the number of free parameters and keeping the model physically sound, the Einstein model fit is chosen because most of the phonon branches are optical in nature for this compound. These models are in general, huge approximations that assume simplistic phonon dispersion relations and do not always model the heat capacity properly. Proper subtraction of the lattice heat capacity require detailed DFT phonon calculations or a non-magnetic analog of the compound should be measured and subtracted. The high temperature theoretical limit is given by $S_{mag} = 5.08*Rln(2S+1) = 87.8$ $Jmol^{-1}K^{-1}$ which is much smaller than the observed value of magnetic entropy at room temperature (159.61 $Jmol^{-1}K^{-1}$).

5.4.8 Electronic Structure Calculations

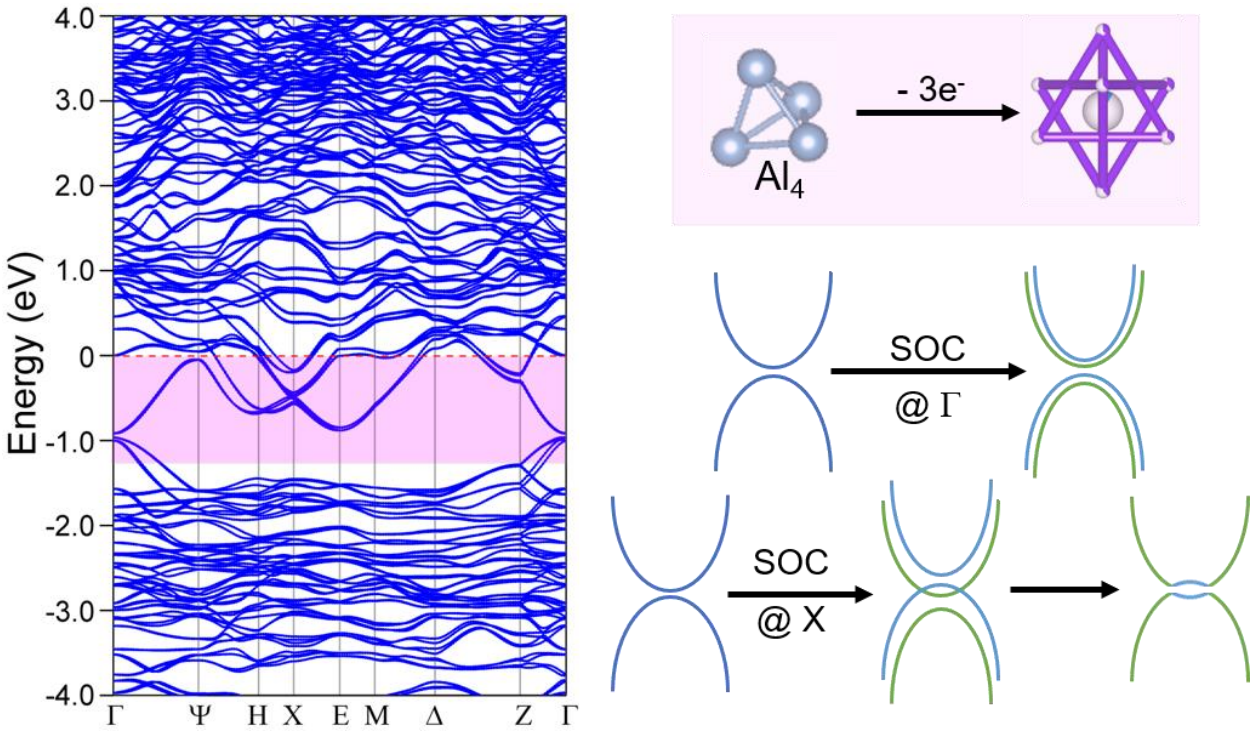

Figure 5.12: a) Band structure of hypothetical "$Eu_5Al_4Sb_6$" with spin-orbit coupling (SOC) effects on Eu and Sb atoms, spin polarization (AFM), and on-site U = 6 eV on Eu 4f. The red dashed line is the Fermi level (0 eV) for 52 valence electrons. The shaded pink area from -1.2 eV to 0 eV covers from 49 e^- to 52 e^- where the 49 e^- compound would correspond to being a semiconductor or semimetal. b) Schematic for the structure-valence relationship in the shaded pink area in a). c) Illustration of spin-orbit coupling (SOC) effects on the band structure at Γ (~1 eV below E_F) and X (~0.5 eV below E_F) points.

To further understand the structural stability, Al cluster occupancies, and electronic properties of $Eu_{5.08}Al_3Sb_6$, we performed first-principles calculations on the bulk band structure of hypothetical model "$Eu_5Al_4Sb_6$" with fully occupied Al_4 tetrahedral cluster based on the generalized gradient approximation (GGA) and GGA with SOC (GGA+SOC) methods, as shown in **Figure 5.12**. Most of the bands between −2 and +1 eV (0 eV = Fermi level for 52 valence electrons) are contributed from the hybridization of Sb 5*s* and 5*p* bands and Al 3*s* and 3*p* bands. Below −2 eV is ~2 eV bands comprising mainly Eu 4*f* orbital contributions that is on-site U dependent. A noticeable bandgap at approximately −1.0 eV (49.5 valence electrons)

below 0 eV, which is only ~0.03 eV wide, was observed. According to band analysis, the wave functions contributing to this area (Fermi level to 1 eV below Fermi level) are mainly from Sb atoms. When SOC effects on Eu and Sb atoms are turned on, Eu-4*f* and Sb-*s, p* bands are split due to the Rashba effects.[107] Moreover, when electronic interactions via LDA plus correlation parameter U (LDA+U) was considered into the calculations, Eu-4*f* bands (split into the $j = 7/2$ states and $j = 5/2$ states by SOC) are shifted to 2.0 ~ 4.0 eV below E_F. In addition, strong SOC effect gap out the band crossing points between Sb-5*s, p* and Al-3*s, p* orbitals around X point around 0.5 eV below the Fermi level, and further enhance the band splitting of crossing states and flattening at H, X, E, and M points around E_F. Targeting this energy space where the band crossings occur through defect control on the disordered Eu/Al sites could induce topological behavior within this compound.

The Fermi level for $Eu_{5.08}Al_3Sb_6$ (~49.5 valence electrons) compound would be located exactly at the bandgap around -1 eV, which would make it a semiconductor or semimetal. The presence of the Eu atoms however, increase the valence electron count and would shift the Fermi level into the conduction band. This observation is consistent with the experimental observations from resistivity measurements and Hall carrier concentration.

5.4.9 Mössbauer spectroscopy

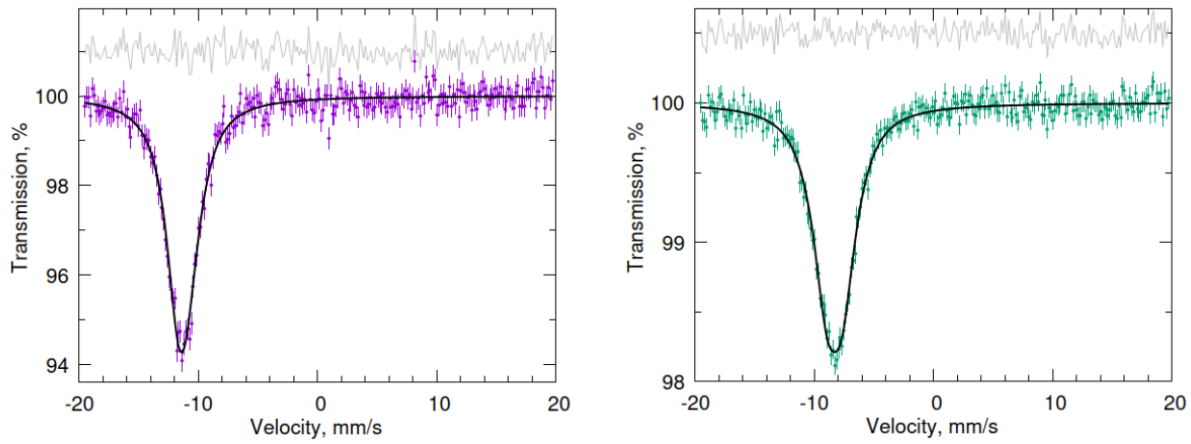

Figure 5.13: Europium-151 (left) and antimony-121 (right) Mössbauer spectra of $Eu_{5.08}Al_3Sb_6$ obtained at room temperature. Data with error bars are shown as points, fits as black line, and differences as offset grey line.

The Europium-151 and Sb-antimony-121 Mössbauer spectra (**Figure 5.13**) show that all Eu ions have 2+ (isomer shift δ = -11.31(2) mm/s, similar to Eu in $Eu_{14}AlSb_{11}$[106]) and all Sb ions have 3- oxidation state (δ = -8.30(2) mm/s , similar to Sb in AlSb[108]) as suspected from the Zintl formalism. A fit of both spectra with a single Eu or Sb site reveals that the line shape is not a simple Lorentzian. For Eu, a small quadrupople splitting (ΔE_Q = -2.2(3) mm/s) suffices to obtain a good fit; for Sb using an asymmetry parameter, η, is required (ΔE_Q =-3.7(3) mm/s; η=1). The obtained fit parameters are certainly not unique and correspond to an average over the different sites. Because both fits account for the residuals (χ^2_{red}=1), it is unwarranted to use additional sites. Because the line width (Γ_{Eu} = 2.6(1) mm/s; Γ_{Sb} = 2.6(1) mm/s) is rather narrow, we can infer that there is little variation in the local coordination environment for Eu and Sb. This makes sense when comparing to the structure visually, where the Eu and Sb atoms adopt a rock-salt like framework.

5.5 Conclusion

In conclusion, the $Eu_5Al_3Sb_6$ phase has been successfully synthesized through Sn flux. The crystal structure has been characterized through x-ray diffraction that reveals disordered Al_4 tetrahedral clusters. Magnetoresistance measurements show weak dependence with field and reveal metallic behavior up to room temperature. Magnetic susceptibility measurements show good agreement with a Curie-Weiss model to yield an effective moment of 7.80 μ_B/mol Eu and suggest antiferromagnetic ordering. Heat capacity fitting with a weighted Debye and Einstein model suggest the possibility of a supercell in this material. Electronic structure calculations on hypothetical $Eu_5Al_4Sb_6$ structure shows the potential for topological behavior in this compound.

5.6 Acknowledgements

This work was supported by NSF DMR-2001156. Mössbauer spectral work by RPH supported by the US Department of Energy (DOE), Office of Science, Office of Basic Energy Sciences (BES), Materials Sciences and Engineering Division. W.X. at Rutgers was supported by NSF- DMR-2053287. The electron microscopy work at BNL was supported by U.S. DOE-BES, Materials Sciences and Engineering Division under Contract No. DESC0012704.

Chapter 6 Intermediate Yb Valence in the Zintl Phases $Yb_{14}MSb_{11}$ (M = Zn, Mn, Mg): XANES, Magnetism, and Heat Capacity

Allan He,[1] Elizabeth L. Kunz Wille,[1] Liane M. Moreau,[2] Sean M. Thomas,[3] Jon M. Lawrence,[3] Eric D. Bauer,[3] Corwin H. Booth,[2*] Susan M. Kauzlarich[2*]

[1]Department of Chemistry, One Shields Ave, University of California, Davis, California 95616, USA

[2]Chemical Sciences Division, Lawrence Berkeley National Laboratory, Berkeley, California 94720, USA

[3]Materials, Physics and Applications Division, Los Alamos National Laboratory, Los Alamos, New Mexico 87545, USA

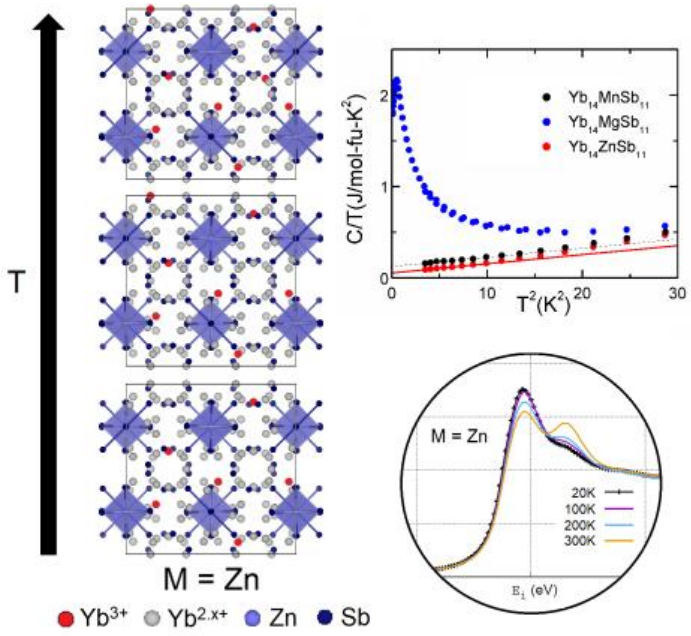

Published in *Phys. Rev. Mater.*, **2020**, *4*, 114407.

Allan He and Elizabeth L. Kunz Wille did the synthesis of single crystals and overall data interpretation, Liane M. Moreau and Corwin H. Booth conducted XANES measurements, analysis, and overall data interpretation, Sean M. Thomas and Jon M. Lawrence and Eric D. Bauer conducted the low temperature heat capacity and provided interpretation of the intermediate valence/Kondo physics.

This chapter was adapted with permission from:

He, A.; Wille, E. L. K.; Moreau, L. M.; Thomas, S. M.; Lawrence, J. M.; Bauer, E. D.; Booth, C. H.; Kauzlarich, S. M. Intermediate Yb Valence in the Zintl Phases $Yb_{14}MSb_{11}$ (M = Zn, Mn, Mg): XANES, Magnetism, Heat Capacity. *Phys. Rev. Mater.,* **2020**, *4*, 114407.

6.1 Abstract

$Yb_{14}MnSb_{11}$ is a magnetic Zintl compound as well as being one of the best high temperature p-type thermoelectric materials. According to the Zintl formalism, which defines intermetallic phases where cations and anions are valence satisfied, this structure type is nominally made up of 14 Yb^{2+}, 1 $MnSb_4^{9-}$, 1 Sb_3^{7-}, and 4 Sb^{3-} atoms. When Mn is replaced by Mg or Zn, the Zintl defined motifs become 13 Yb^{2+}, 1 Yb^{3+}, 1 (Mg, Zn)Sb_4^{10-}, 1 Sb_3^{7-}, and 4 Sb^{3-}. The predicted existence of Yb^{3+} based on simple electron counting rules of the Zintl formalism calls the Yb valence of these compounds into question. XANES, magnetic susceptibility, and specific heat measurements on single crystals of the three analogs show signatures of intermediate valence Yb behavior and in particular, reveal the heavy fermion nature of $Yb_{14}MgSb_{11}$. In these isostructural compounds, Yb can exhibit a variety of electronic configurations from intermediate (M = Zn), mostly 2+ (M = Mn), to 3+ (M = Mg). In all cases, there is a small amount of intermediate valency at the lowest temperatures. The amount of intermediate valency is constant for M = Mn, Mg and temperature dependent for M = Zn. The evolution of the Yb valence correlated to the transport properties of these phases is highlighted. The presence of Yb in this structure type allows for fine tuning of the carrier concentration and thereby the possibility of optimized thermoelectric properties along with unique magnetic phenomena.

6.2 Introduction

The broad class of materials known as Zintl phases are considered charge balanced intermetallic compounds that are composed of cations and polyatomic anions where the oxidation states can be clearly calculated and electrons are considered to be completely transferred from the cations to the anionic units.[29] Among Zintl compounds, many unique and interesting physical properties have been discovered and continue to be uncovered.[28,64,109–111] In terms of electronics, Zintl phases are generally

semiconducting; however, they can be tuned to be insulating or metallic. Control of electronic behavior for a particular phase is possible because of the large number of possible substitutions that can be accommodated into the structure, in addition to effects stemming from non-stoichiometry and defects. These factors will inherently change density of states near the Fermi level to have a direct effect on the physical properties. The flexibility of electronic tuning in Zintl phases has been utilized among the thermoelectric community where carrier concentrations can be tailored based on Boltzmann transport models to maximize thermoelectric performance.[27] This approach has yielded tremendous success across all temperature regions in such compounds as $Yb_{14}Mn_{1-x}Al_xSb_{11}$,[33] $Ca_{3-x}Na_xAlSb_3$,[112] $Yb_{21-x}Na_xMn_4Sb_{18}$,[16] and $Pb_{1-x}Tl_xTe$.[67] In particular, $Yb_{14}MSb_{11}$ (M = Mn, Mg) are among the best p-type high temperature thermoelectrics.[4,113,114] This is attributed to their stability at high temperature (>1273 K), along with a reasonable Seebeck coefficient, electrical resistivity and very low thermal conductivity.

The $A_{14}MPn_{11}$ (14-1-11) structure type[115] (tetragonal $I4_1/acd$) is comprised of an alkaline earth or rare earth atom on the A sites, a transition metal, alkaline earth, or triel on the M site, and pnictogen on the Pn sites. Aside from the high thermoelectric performance, this structure type exhibits a whole range of magnetic and electronic behavior: ferromagnetism,[116] antiferromagnetism,[117] CMR,[116,117] being close to half-metallic,[118] as well as being a rare underscreened Kondo system.[91] According to the Zintl formalism for $Yb_{14}MnSb_{11}$ (**Figure 6.1**), this structure type is nominally made up of 14 Yb^{2+}, 1 $MnSb_4^{9-}$, 1 Sb_3^{7-}, and 4 Sb^{3-} atoms with 8 formula units per unit cell.

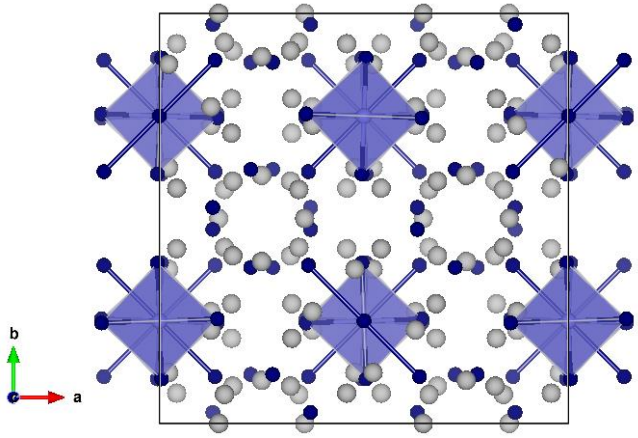

Figure 6.1: Crystal structure of $Yb_{14}MnSb_{11}$ viewed down the c-axis (a = 16.578 Å, c = 21.897 Å, tetragonal space group, $I4_1/acd$). Yb atoms are shown in light gray, Mn atoms in light blue, and Sb atoms in navy.

The magnetic behavior of $Yb_{14}MnSb_{11}$ was initially investigated by Fisher et al.,[119] and described as consistent with Mn^{3+} (d^4), showing no evidence of Yb^{3+} (f^{13}) from Curie-Weiss law fitting and therefore Yb oxidation state was assigned as Yb^{2+} (f^{14}, nonmagnetic). Subsequent X-ray magnetic circular dichroism (XMCD) studies[120] on single crystals revealed a strong dichroism signal at the Mn $L_{2,3}$–edge that is better described as Mn^{2+} (d^5) than the Mn^{3+} (d^4) determined from magnetism. Additionally, a dichroism signal anti-aligned with the Mn was observed at the Sb $M_{4,5}$–edge with no evidence of any moment on Yb at the Yb $N_{4,5}$–edge (oxidation state of Yb^{2+} in $Yb_{14}MnSb_{11}$ also confirmed through XPS[121]). These results, taken together with the magnetic data, provide a model where the configuration of the $MnSb_4^{9-}$ cluster is more accurately considered as Mn^{2+} (d^5) + h^+ (a polarized hole carrier (h^+) decentralized over the 4 Sb atoms in the cluster and a moment anti-aligned with the Mn moment), instead of simply Mn^{3+} (d^4). Detailed LSDA calculations on isostructural $(Ca,Ba)_{14}MnBi_{11}$ support this configuration hypothesis[118] where the Mn was calculated to be 2+ with an anti-aligned moment located on the pnictogen *p* states that participate within the tetrahedra, consistent with the XMCD study[120] and reported magnetism.[119] A recent polarized neutron diffraction study has shown that the picture is more complicated, with the compensating moments not localized on the Sb atoms bonded to Mn in the $MnSb_4^{9-}$ tetrahedra but are distributed fairly uniformly

across the unit cell on both Sb and Yb sites.[122] This work provides evidence for the Kondo screening cloud that has been proposed for this compound.[91,122]

In contrast to the Mn analog, the Zn and Mg phases of 14-1-11 require from the Zintl formalism the following structural motifs: 13 Yb^{2+}, 1 Yb^{3+}, 1 $(Zn,Mg)Sb_4^{10-}$, 1 Sb_3^{7-}, and 4 Sb^{3-}. The predicted existence of Yb^{3+} based on these simple electron counting rules is confirmed through magnetization measurements on single crystal samples. An effective magnetic moment of μ_{eff} = 3.8 μ_B/fu (fu = formula unit) for T > 150 K is observed for the Zn analog[123] and a μ_{eff} = 3.4 μ_B/fu for the Mg analog[124] suggesting intermediate Yb valence states (Yb^{3+} (f^{13}, J = 7/2) has μ_{eff} = 4.54 μ_B). This hypothesis has been supported through X-ray photoemission spectroscopy (XPS) where both Yb^{2+} and Yb^{3+} have been observed for the Zn analog.[121] Note that a single Yb^{3+} atom per formula unit is not allowed in the 14-1-11 structure since the minimum multiplicity of equivalent sites is two for the A element.[115] Therefore, as a Zintl phase, it is possible that there is an intermediate valency or mixed valency, especially as the *f* level of Yb is expected to be close to the Fermi level and there is covalent/metallic bonding.[118,125] Intermediate valence states generally arise from hybridization of localized d or f electrons with the conduction electrons. The f electrons in systems containing for example, Yb, Eu, or Ce, often fluctuate between two electronic configurations that compete for stability and this is referred to as intermediate valency, whereas mixed valency is a term used when the atom can be assigned a specific integral valence such as 2+ or 3+. While intermediate valency is known in intermetallic compounds,[20,126–130] such behavior in Zintl phases which are typically semiconductors is rare. In particular, the Yb compounds studied in this work compete between the magnetic $4f^{13}$ state and the non-magnetic $4f^{14}$ state.

Studies of RE^{3+} substitutions into this structure type, $A_{14-x}RE_xMSb_{11}$ show x = 1 when A = Ca^{2+} and $x \leq 0.5$ when A = Yb, regardless of the identify of M.[131–135] In all cases, the RE^{3+} is found on more than 1 of the 4 possible crystallographic sites, correlated with size. Overall, in the series of compounds, $Yb_{14}MSb_{11}$ (M =

Zn, Mn, Mg), the unit cell increases in the order Zn < Mn < Mg concurrent with the room temperature carrier concentration decreasing with Zn > 1 x 10^{21} cm^{-3}, Mn ≈ 1 x 10^{21} cm^{-3}, and Mg ≈ 5 x 10^{20} cm^{-3}.[4,113,136,137] For these compounds, the Zn analog is too metallic for good thermoelectric properties but both the M = Mn, Mg phases are excellent high temperature p-type thermoelectrics.[4,113,114] A recent paper showed that adding a small amount of RE^{3+} to $Yb_{14}ZnSb_{11}$ dramatically increased the thermoelectric efficiency.[135] Because of the important role of Yb valence in these compounds and the possibility of a localized Yb^{3+} (J = 7/2) heavy fermion state for $Yb_{14}MgSb_{11}$, XANES, magnetic susceptibility, and heat capacity measurements on single crystals of the three analogs were performed. The contribution of Yb to properties of these systems is elucidated providing insight that may be also applied to other Yb containing Zintl phases with an aim towards optimized thermoelectric properties along with new and unique physics.

6.2 Experimental

6.2.1 Synthesis

The single crystals of $Yb_{14}MSb_{11}$ were synthesized through previously reported flux methods.[119,123,138] The crystals were approximately 2 x 2 x 2 mm^3 in dimensions with highly reflective facets (see **Appendix 3**, **Figure A3.1**).

6.2.2 XANES Measurements

X-ray absorption near-edge structure (XANES) data were collected on beamline 11-2 at the Stanford Synchrotron Radiation Lightsource using a half-tuned Si(220) double-crystal monochromator ($\phi = 0°$). Single crystal samples were placed into a slotted aluminum sample holder which was then put into a liquid helium flow cryostat. Yb L_{III}-edge data were collected in fluorescence mode at 4 different temperatures: 20 K, 100 K, 200 K and 300 K. Data were corrected for the dead time of the 100-element germanium detector and a constant background was fit to the lowest-energy data in each scan and subtracted from

the data. The incident energy was calibrated by setting the peak in the first derivative of the absorption spectrum of a Yb_2O_3 sample to 8943.0 eV. The data were corrected for self-absorption using the FLUO program,[139] and the results were also normalized to the data above the edge.

6.2.3 Magnetic Susceptibility and Specific Heat Measurements

The magnetic susceptibility measurements were performed in a SQUID magnetometer from 2 – 300 K in a magnetic field (0.01 T for M = Mn, 1 T for M = Mg, 0.1 T for M = Zn). The data for M = Mn, Zn, Mg were collected as previously described and in the case of M = Mn, Zn, with the easy axis (*c* axis) aligned parallel to the field.[123,124,140] Since M = Mg showed paramagnetic behavior regardless of orientation, no efforts were made to align the crystal with regards to the applied magnetic field. The specific heat for M = Mg was measured from 0.4 – 300 K using a thermal relaxation method (0 T – 1 T).

6.3 Results and Discussion

Figure 6.2a compares XANES spectra collected at 20 K for the three compounds $Yb_{14}MSb_{11}$ (M = Mn, Mg, Zn), together with the spectrum from a Yb_2O_3 standard as a benchmark for the Yb^{3+} peak. All three compounds have a dominant peak at about 8939 eV (8 eV below that of Yb_2O_3), indicative of a predominantly Yb(II) configuration. A shoulder at 8947 eV, consistent with the main peak energy of Yb_2O_3 indicates a relatively small amount of 3+ character that is somewhat more pronounced in $Yb_{14}MgSb_{11}$. $Yb_{14}MnSb_{11}$ has the lowest fraction of 3+, as is also visually observed in having the lowest shoulder. Still, there appears to be an unexpectedly high 3+ fraction even for this sample. A FEFF[141] calculation confirms that this shoulder is not due to an EXAFS oscillation. **Figure 6.2b** displays temperature-dependent behavior of the $Yb_{14}ZnSb_{11}$ XANES data. At 20 K, the Zn sample spectrum appears similar to that of the Mn and Mg samples; however, increasing temperature results in a decrease in the 2+ peak amplitude at lower energy and an increase in the 3+ peak at higher energy. Spectra collected at other temperatures for

$Yb_{14}MnSb_{11}$ and $Yb_{14}MgSb_{11}$ (see **Appendix 3**, **Figure A3.2**) are nearly identical and indicate no significant temperature dependence with regards to the Yb valence.

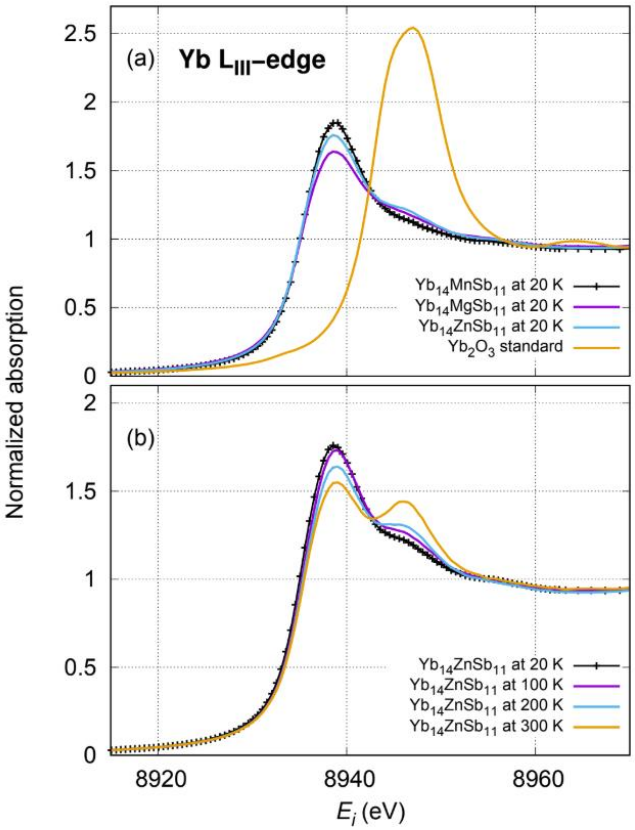

Figure 6.2: (a) XANES spectra of the three analogs of $Yb_{14}MSb_{11}$ (M = Zn, Mn, Mg,) collected at 20 K at the Yb L_{III} edge along with a Yb_2O_3 standard. (b) Temperature dependence of $Yb_{14}ZnSb_{11}$ showing the increase of the Yb^{3+} peak with increasing T.

Figure 6.3a shows the fit to the XANES spectrum of the $Yb_{14}ZnSb_{11}$ compound at 20 K. Fits for $Yb_{14}ZnSb_{11}$ at other temperatures and 20 K fits for M = Mn, Mg can be found in **Appendix 3** (**Figure A3.3**). The relative 2+/3+ character of Yb is based on the relative peak ratios at the Yb-L_{III} absorption edge. In order to extract an estimate of the Yb valence, we fit the spectra using a previous method[142,143] that utilizes a broadened arctan-like function[144] (actually an integrated Gaussian) to account for transitions to the continuum

(dashed, purple). A Gaussian profile is used to describe the main peak associated with the Yb(II) configuration, another to describe the Yb(III) configuration, and another to model the first structural oscillation. Note that Gaussians are used rather than Lorentzian or pseudo-Voigt profiles since all of these profiles are to represent a collection of discrete transitions, e.g. the two continuum functions associated with the Yb(II) and Yb(III) configurations, or the crystal field-split 5d manifold that accounts for part of the width of the individual configuration peaks. The widths of the individual configuration peaks are held equal, and the position of the arctan-like function is set to the weighted mean position of the configuration peaks. The structural oscillation is due to the Extended X-ray Absorption Fine Structure (EXAFS), which occurs from backscattering of the photoelectron off neighboring atoms[141] and is only included to account for any overlap with the Yb(III) peak. This weighted sum of the peak areas of the individual configuration peaks gives an f-hole occupancy, $n_{f,avg} = A_{Yb(III)}/(A_{Yb(II)}+A_{Yb(III)})$, where a given $n_{f,avg}$ = 0 denotes a full-shell, divalent, f^{14} configuration, and $n_{f,avg}$ = 1 denotes a trivalent, f^{13} configuration (J = 7/2). The overall resulting fits (red) overlay well with the experimental data (black).

At 20 K, the $Yb_{14}MSb_{11}$ compounds each have a similar valence state for the Yb, with $n_{f,avg}$ = 0.27(2), 0.23(2), and 0.28(3) for M = Zn, Mn, and Mg, respectively. The temperature dependence of $n_{f,avg}$ for M = Zn is shown in **Figure 6.3b**, increasing monotonically from about 0.27(2) to 0.39(1).

Fisher et al.[123] make the point that it is simplistic to treat $Yb_{14}ZnSb_{11}$ as having integral valence on each Yb site because covalent or metallic bonding is undoubtedly present. Based on the susceptibility and specific heat, they conclude that for $Yb_{14}ZnSb_{11}$ a small fraction of the Yb atoms are intermediate valent. The results reported here show that the Yb atoms are not all divalent in any of the three analogs. The measurements provide the average valence of Yb and the specific valence on the four inequivalent Yb sites in the crystal structure cannot be deconvoluted. It is clear, however, that for all three compounds, the Yb atoms are on the whole strongly intermediate-valent with a mean occupation number of

approximately $n_{f,avg} \approx 0.25$ at T = 20 K from XANES. It is therefore more accurate to consider the bonding in this structure type to be covalent/metallic in character with some contribution or hybridization from the Yb 4f electrons with the Sb p states. It is also likely that the availability (or lack thereof) of *d* orbitals on M (Zn, d^{10}, Mn, d^5, Mg, d^0) contribute to the hybridization. The situation is reminiscent of that for CeO_2, which formally would have tetravalent cerium; in reality the cerium atoms have strong intermediate valence.[145,146] Previous studies of XMCD[120] and XPS[121] could not definitively determine the bulk Yb^{3+} contribution to these systems because of the difference in energy between the techniques.

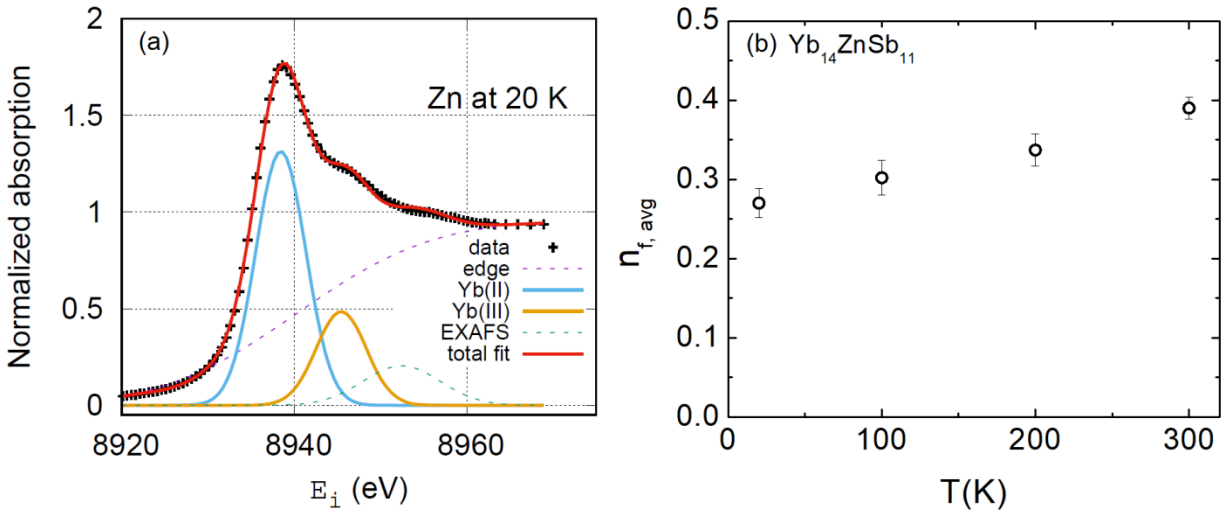

Figure 6.3: (a) XANES fitting and extraction of the 3+ fraction in the $Yb_{14}ZnSb_{11}$ sample at 20K. (b) Temperature dependence of $n_{f,avg}$ for the $Yb_{14}ZnSb_{11}$ sample.

Magnetic susceptibility of the three compounds are shown in **Figure 6.4** and specific heat in **Figure 6.5**. The units are given in terms of mole-formula-units (mol-fu) so that each plot represents the contribution of the 14 Yb atoms. Strongly intermediate valent compounds occur when there is substantial hybridization between the 4f electrons and the ligand electrons. The characteristic (Kondo) energy for 4f excitations in these compounds is typically very large ($T_K >> 1000$ K) which leads to a small contribution to the linear coefficient of specific heat ($\gamma \approx 1/T_K < 10$ mJ/mol-K^2) and small Pauli susceptibility ($\chi_p \approx 1/T_K <$ 10^{-}

^{3} emu/mol). The susceptibility and 4f occupation number vary on the scale of the Kondo temperature so for such a large T_K, both n_f and χ will exhibit very little change below room temperature.[147,148]

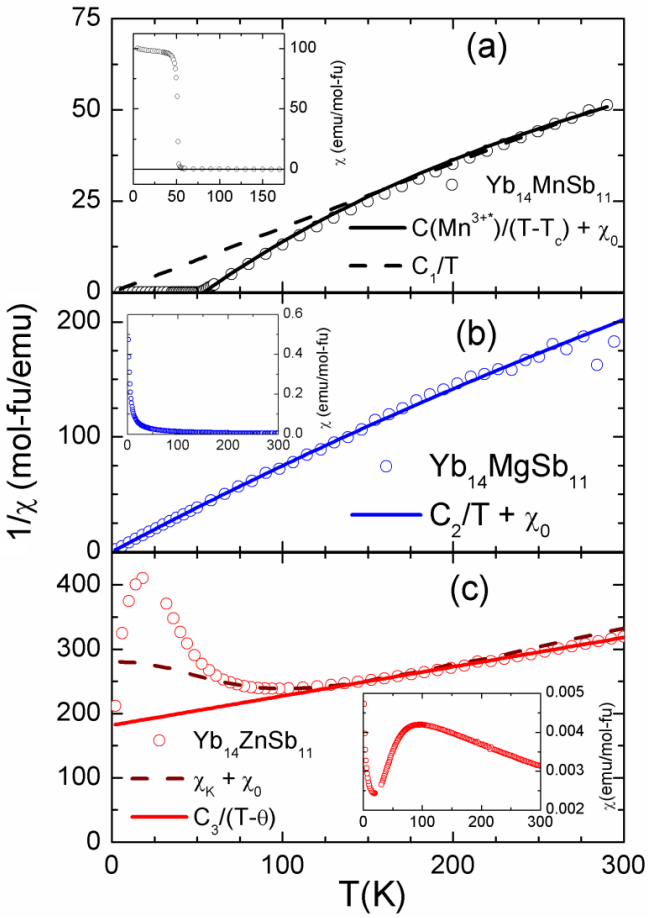

Figure 6.4: The inverse susceptibility $\chi(T)^{-1}$ of the three $Yb_{14}MSb_{11}$ (M = Mn, Mg, Zn) compounds (the formulae given for the dashed and solid lines are direct susceptibility $\chi(T)$ which are also included as insets) between 2 and 300 K. (a) $Yb_{14}MnSb_{11}$ (b) $Yb_{14}MgSb_{11}$ (c) $Yb_{14}ZnSb_{11}$. The dashed and solid lines are not least squares fits but give comparisons of the data to the formulae. These serve the purpose of showing how our data favorably compares to other groups and allow us to make reasonable estimates of the Mn and Yb moments, as well as the fraction of Yb^{3+} involved.

Consider first the case of $Yb_{14}MnSb_{11}$. The ferromagnetic transition at $T_c \approx 54$ K is clearly observed in the magnetic susceptibility as displayed in the inset to **Figure 6.4a**. The Curie constant associated with the

$\chi(T) = C/(T - T_c) + \chi_0$ fit in **Figure 6.4a** is associated with a Mn^{3+*} (d^4) (where $Mn^{3+*} = Mn^{2+}$ (d^5) + h^+, S = 4/2) configuration. These results are in excellent agreement with those reported in Ref. [119], albeit that the constant term χ_0 = 7.0x10^{-3}emu/mol-fu is slightly larger than the value 4.9x10^{-3} emu/mol-fu reported there. Above 200 K, the data can be approximated by a simple Curie law $\chi(T) = C_1/T$ where C_1 = 5.65 emu-K/mol-fu (μ_{eff} = 6.72 μ_B/fu). This is considerably larger than the value C = 3.00 emu-K/mol-fu (μ_{eff} = 4.90 μ_B/fu) expected for a Mn^{3+*} configuration with L = 0 and g = 2 or even Mn^{2+} (C = 4.38 emu-K/mol-fu; μ_{eff} = 5.92 μ_B/fu). Assuming that the Mn stays 2+ to high T, the difference between the high T Curie constant (C = 5.65 emu-K/mol-fu, μ_{eff} = 6.72 μ_B/fu) and the Mn^{2+} moment is C = 1.27 emu-K/mol-fu (μ_{eff} = 3.19 μ_B/fu) which is half the value of $C_{7/2}$ = 2.58 emu-K/mol-Yb (μ_{eff} = 4.54 μ_B/Yb) expected for the single Yb^{3+} (J = 7/2) local moment. This analysis ignores any potential constant term, which would reduce the Curie constant. Given the downward curvature in the inverse susceptibility of this compound, the high T Curie constant is potentially even larger. Despite these caveats, it makes sense that in the paramagnetic region the Yb might contribute to the high temperature Curie constant with a magnitude similar to that seen in the M = Mg compound, see below.

The susceptibility of $Yb_{14}MgSb_{11}$ (**Figure 6.4b**) is well described by a Curie law with a small constant term $\chi(T) = C_2/T + \chi_0$ where C_2 = 1.26 emu-K/mol-fu (μ_{eff} = 3.17 μ_B/fu) is again about half the value expected for a single Yb^{3+} (J = 7/2, $C_{7/2}$ = 2.58 emu-K/mol-Yb, μ_{eff} = 4.54 μ_B/fu) local moment in the formula unit and χ_0 is an order of magnitude smaller (χ_0 = 7.5x10^{-4} emu/mol-fu) than the constant contribution used in fitting the Mn compound. The fitting of the Mg analog is essentially identical to that reported in Ref. 124, where the data from 50 – 250 K was fit to a Curie-Weiss law $\chi = C_2/(T - \theta)$ and obtained C_2 = 1.46 emu-K/mol-fu and θ = 3.6 K.[124] Wille et al.[124] have shown via X-ray diffraction that there are Mg atoms on the Yb(1) and/or Yb(3) sites in the single crystal sample. The appropriate stoichiometry was found to be $(Yb_{13.8}Mg_{0.2})MgSb_{11}$ which was confirmed by electron microprobe measurements. The Curie-law

susceptibility seen in this compound is attributed to approximately a single Yb^{3+} atom in the formula unit. As indicated above in the Introduction, the existence of one trivalent Yb atom per formula unit cannot be explained if the material possesses perfect structural order, but it could arise from site disorder. Yb atoms in a disordered environment can experience a weaker-than-average *4f*/conduction hybridization, and hence can be trivalent. An active (trivalent) Yb site number of precisely one could also occur if there were a modification of the $Ca_{14}AlSb_{11}$-structure type removing the equivalency of the atoms on one of the Yb sites; however, such a modified structure has not been observed to date.

Under the assumption that there are 13 Yb_A atoms, all with identical strong intermediate valence, and one active Yb_B atom per formula unit, we can use **Equation 6.1**:

$$\frac{13n_{f,A}(Yb_A) + n_{f,B}(Yb_B)}{14} = n_{f,avg}$$

Equation 6.1: Fractional valence calculation assuming 13 identical intermediate valent Yb atoms and 1 Yb^{3+}.

For a $n_{f,avg} = 0.28$ and $n_{f,B} = 1$, we obtain $n_{f,A} = 0.224$ for $Yb_{14}MgSb_{11}$. Hence the existence of one trivalent Yb atom has only a small effect on the average valence of the other sites, but also leads to no temperature dependence for n_f, as observed, since the atom will remain trivalent to high temperature.

The fact that the Curie constant (**Figure 6.4b**) is only half that expected for a Yb^{3+} ($J = 7/2$) moment could arise from crystal field (CF) splitting. The small constant contribution $\chi_0 = 7.5\text{x}10^{-4}$ emu/mol-fu could easily arise from the other 13 strongly intermediate valent Yb's, each contributing $\chi_p \approx 6\text{x}10^{-5}$ emu/mol-fu. The CF splitting, however, would have to be much greater than 30 meV in order to give a Curie law behavior below 300 K in a pure doublet CF ground state. For smaller CF energies, the contributions from the gradual excitation of higher-lying crystal field multiplets would lead to deviations from the Curie law below room

temperature. We note that such a large CF splitting is unusual for Yb where simple Curie behavior is rarely observed over the whole interval 2 – 300 K.

The high temperature susceptibility of $Yb_{14}ZnSb_{11}$ approximately follows a Curie-Weiss law with a value C_3 = 2.2 emu-K/mol-fu (μ_{eff} = 4.19 μ_B/fu) that is slightly smaller than $C_{7/2}$; the value of θ is -400 K (solid line in **Figure 6.4c**). This behavior is typical of Yb intermediate valence compounds[147,148] whose susceptibility often can be described by that calculated for a Kondo impurity. The dashed line in **Figure 6.4c** gives the result of such a calculation[149] with T_K = 450 K, put on an absolute basis by utilizing the formula $\chi_K(0) = (2J+1)/2\pi)*C_J/T_K$ for the zero temperature susceptibility; the Curie constant is that of a single Yb^{3+} (J = 7/2) local moment in the formula unit. The Kondo curves given here are strictly valid only in the Kondo limit $n_f \rightarrow 1$, i.e when the Yb is close to trivalent. Inclusion of a small constant term, identical to that of $Yb_{14}MgSb_{11}$, brings the theory curve into excellent alignment with the data. These data are again in good agreement with those reported earlier.[123] Although there has been no report for this compound of the kind of site disorder seen in $Yb_{14}MgSb_{11}$, we assume that such disorder is present and leads to a moderately weak hybridization on the approximately one active Yb site per formula unit than on the other 13 sites. Such a moderate hybridization would then cause the Kondo effect with the value $T_K \approx 450$ K observed for this compound.

It can be seen in **Figure 6.5a** that the total specific heats C(T) of all three compounds are nearly equal over the interval 2 – 300 K. This implies that the phonons, which make the major contribution to the total specific heat, are essentially identical in all three materials.[150] In **Figure 6.5b** we compare the low temperature behavior of C/T for the Mn and Zn compounds to the form $C/T = \gamma + AT^2$. The coefficient of the phonon term is indeed identical for both materials, and the Sommerfeld coefficients (γ) are in reasonable agreement with those reported earlier. For the Mn compound, Ref. 91 found γ = 160 mJ/mol-fu-K^2, Ref. 119 found γ = 70 mJ/mol-fu-K^2, and Ref. 151 found γ = 145 mJ/mol-fu-K^2, which compare to our

value 125 mJ/mol-fu-K^2. Our XANES results show that the Yb atoms are on average strongly intermediate valent with $n_{f,avg}$ = 0.23(2) and no detectable temperature dependence of $n_{f,avg}$. The small constant term in the susceptibility and the linear coefficient of specific heat may be properties of the ordered phase,[119] and possibly include a contribution from the 14 strongly intermediate valent Yb atoms. For the Zn compound, Ref. 123 found a value 80 mJ/mol-fu-K^2, close to our value γ = 55 mJ/mol-fu-K^2. While the linear coefficient of specific heat is affected by the ferromagnetism for M = Mn, that for the M = Zn compound is typical of moderately intermediate valent materials. For the Mg analog, the low temperature data show a peak in C/T near T_{max} = 0.7 K with a magnitude 2.17 J/mol-fu-K^2 (**Figure 6.5b**). Such a large value of C/T is characteristic of extremely heavy fermion and/or magnetic order. The origin of the maximum is discussed below.

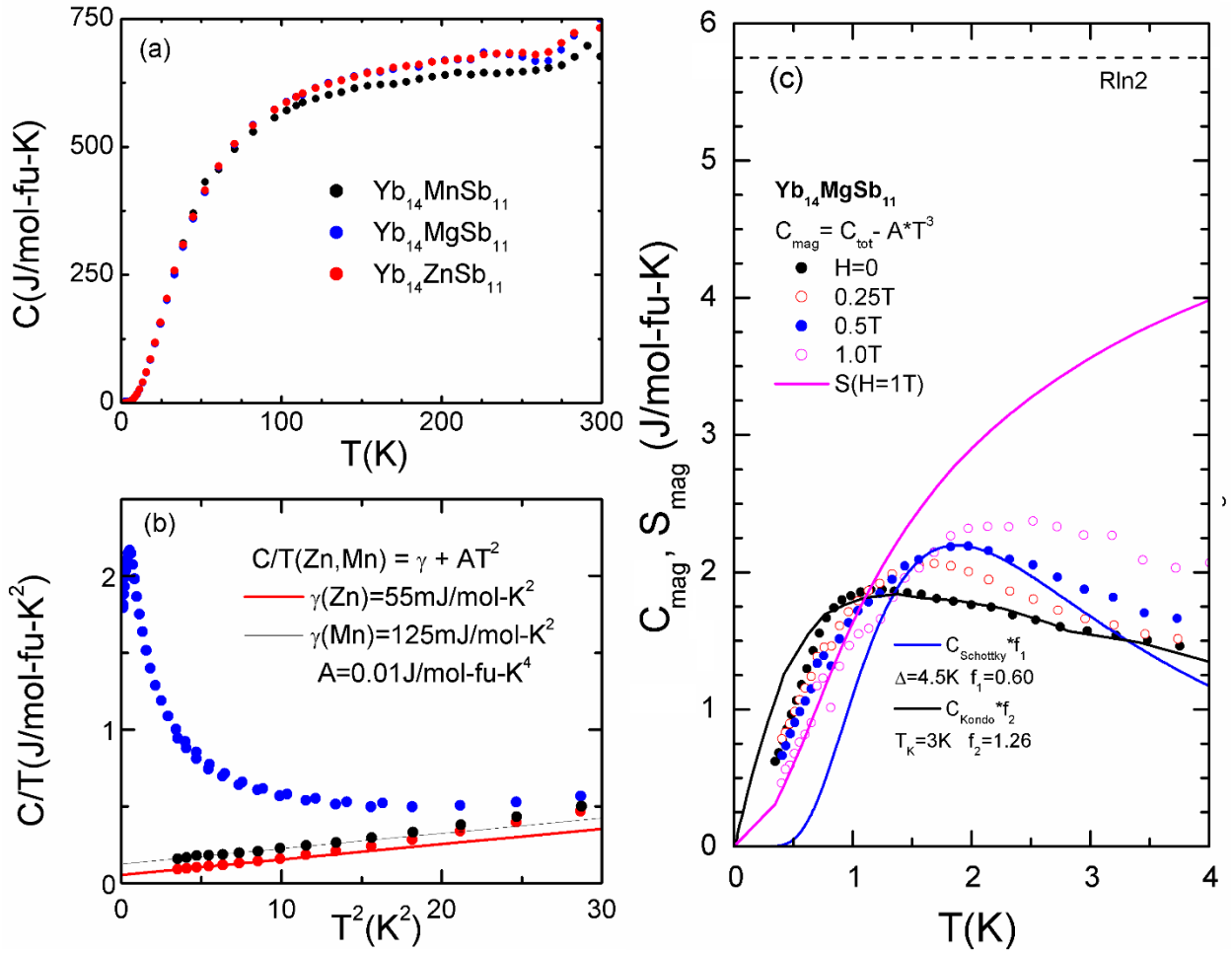

Figure 6.5: The specific heat C(T) of all three $Yb_{14}MSb_{11}$ (M = Mn, Mg, Zn) compounds. **(a)** C(T) plotted over the temperature range 2 - 300K. **(b)** The low temperature specific heat with the same legend for the data as in **(a)** divided by the temperature, C(T)/T. The maximum at T = 0.7K for M = Mg is typical of very heavy fermion behavior and/or magnetic order. **(c)** The specific heat of $Yb_{14}MgSb_{11}$ for four magnetic fields in the range 0 - 1T and temperature in the range 0.3 – 4 K. The black line is the theoretical Kondo curve[149] for J = 1/2, T_K = 3 K, and for 1.26 Yb^{3+} atoms per fu. The blue line is the Schottky specific heat for a two-level (J = 1/2) system with splitting Δ = 4.5K and for 0.6 Yb^{3+} per fu. The magenta line is the magnetic entropy for H = 1T.

Figure 6.5c shows the specific heat for $Yb_{14}MgSb_{11}$ in the range 0.3 – 4 K and for 0 < *H* < 1T. Subtracting the phonon term AT^3 with the same value of A as observed in the Mn and Zn compounds, we determine the magnetic contribution to the specific heat of $Yb_{14}MgSb_{11}$, which is peaked at temperatures that increase with *H*. The data follow closely the predictions[149] for 1.26 Kondo doublets in the formula unit

with T_K = 3 K (black line, **Figure 6.5c**). Kondo doublet ground states typically occur in heavy fermion compounds where the crystal field splitting of the Yb J = 7/2 multiplet is much larger than the Kondo temperature, and such low-T_K compounds are always very close to trivalent. The small-T_K Kondo behavior for this compound would then arise from weaker-than-average hybridization of the Yb^{3+} *4f* doublets with the conduction electrons. Also, as can be seen for the H = 0.5 T data with the blue line **Figure 6.5c**, the peaks in C(T) are broader than expected for a two-level (J = 1/2) Schottky doublet. The entropy (which we show for H = 1 T) appears to be approaching the value Rln2 as the temperature is raised to 9 K (not shown), suggesting that the peak represents the contribution of a ground state Yb crystal field doublet.

It is possible that the peaks in C(T) seen for $Yb_{14}MgSb_{11}$ in the range $0 < H < 1$T arise from magnetic order, where the disorder in the system creates a broadening beyond that expected for a clean system. If this is the case, then the peak near 0.7 K at H = 0 would arise from a broadened phase transition, and the peaks at higher temperature as the field is raised would reflect Zeeman splitting of the ground state doublets. We note, however, that entropy at the peak in C/T for H = 0 is less than 1 J/mol-fu-K. This entropy is such a small fraction of Rln2 that it casts doubt on the interpretation that there is a magnetic phase transition at 0.7 K. In any case, given the disorder, it is not possible at present to distinguish the Kondo mechanism from one of magnetic order. Quite possibly, both the Kondo effect and magnetic correlations are present.

The susceptibility and specific heat of $Yb_{14}ZnSb_{11}$ are typical of moderately intermediate valent compounds, where a maximum in the susceptibility occurs at a temperature $T_{max} = T_K/\alpha$ ($\alpha \approx 3$-5) and the specific heat coefficient is in the range 40 - 100 mJ/mol-fu-K^2. The behavior of $Yb_{14}ZnSb_{11}$ is similar to that of the intermediate valent compound $YbAl_3$,[152] which has a Kondo temperature of nearly 600 K, a maximum in the susceptibility at T_{max} = 125 K, and a coefficient of specific heat $\gamma \approx 40$ mJ/mol-K^2. The ground state valence of $YbAl_3$ is of order 2.75 ($n_{f,avg}$ = 0.75). It is very likely that the occupation number of the active Yb site in $Yb_{14}ZnSb_{11}$ is similar to this value. The overall behavior of these intermediate valent

14-1-11 compounds is close to that of a trivalent Kondo theory at high T, but with some differences, especially at low temperature. The deviation of the measured susceptibility from the Kondo curve below 50 K (**Figure 6.4c**) can be explained from the ratio $\chi(T=0)/\chi(T_{max})$, which is smaller for moderate intermediate valence systems than for trivalent Kondo behavior. The universal (Wilson) ratio between $\chi(0)$ and γ is also altered. For the Zn compound, with T_K = 450 K, the specific heat coefficient in the Kondo limit[149] would be $\gamma = J\pi R/3T_K$ (where R is the gas constant) which for J = 7/2 and T_K = 450 K would give γ = 67 mJ/mol-Yb-K^2 (i.e., one active Yb site), somewhat larger than the value 55 mJ/mol-fu-K^2 (equivalent mJ/mol-Yb-K^2 for 1 Yb) to that we report here.

The occupation numbers of intermediate valent compounds such as $YbAl_3$ increase as the temperature is raised, by an amount $n_{f,avg}(300K) - n_{f,avg}(0K) \approx 0.1 - 0.2$. If in $Yb_{14}ZnSb_{11}$ we assume that the ground state valence of the one active site per fu is $n_f(B) = 0.75$, as for $YbAl_3$, then using **Equation 6.1** with $n_{f,avg} = 0.27$, we find that $n_f(A) = 0.233$. (We note in passing that the A-site occupations derived in this manner appear to be very similar – of order 0.22-0.23 in all three $Yb_{14}MSb_{11}$ compounds). If the valence of the active site then increases to $n_f(B) = 1$ at 300 K, while the occupation of the other sites stay the same, the resulting average valence at 300 K would be only $n_{f,avg} = 0.288$, not the 0.390 observed for $Yb_{14}ZnSb_{11}$ (**Figure 6.3b**). This implies that there must be a change in occupation number on the other Yb sites. For example, if the active site occupation number increased to 1 while that of all the other 13 sites increased to 0.343, then an average occupation 0.390 would be observed at 300 K. In other words, the change in $n_{f,avg}$ observed in $Yb_{14}ZnSb_{11}$ is too large to be attributed to merely the one active Yb site per fu, suggesting that some of the other 13 Yb sites exhibit an appreciable increase with temperature. If this involvement of other Yb sites is the case, it is not clear why such an increase is not also observed in $Yb_{14}MnSb_{11}$ and $Yb_{14}MgSb_{11}$, which have comparable average valence at low temperature. However, it has been noted that $Yb_{14}ZnSb_{11}$ has both the smallest unit cell and highest metallic character.[119,123,124] Perhaps the change of valence on

the active Yb site feeds back to increase the f-hole content on the inactive sites. Chemical pressure arising from the change in volume associated with the change in valence on the active site is one possible way the observed valence change with temperature might happen.

The hybridization of the Yb *4f* states with the *p* states of the Sb in the valence band is crucial for the intermediate valent nature of the Yb atoms in this system. The relatively low values of $n_{f,avg}$ for all analogs show that the Yb atoms naturally favor the divalent state where the electron is localized on the site, rather than being in the conduction band. The intermediate valency of these systems lends itself to the flexibility of doping for this structure. Substitutions that increase the unit cell volume are expected to decrease the average Yb valence since Yb^{2+} is larger than Yb^{3+}. It is also possible to introduce chemical pressure in the system by formation of a solid solution, which will in turn cause a shift in the average valence state for the Yb. Control of the valence can, in theory, be exploited to enhance the Seebeck coefficient especially since the *4f* Yb energy levels fall very close to the Fermi level and increase the figure of merit, *zT*. Any substitutions or doping into the system will change the degree of intermediate valency on the Yb atoms (as exemplified by the difference between the M = Zn, Mn, Mg) and will simultaneously change the density of states near the Fermi level, as well as the carrier concentration within the system. The difference in the local environment of the Yb atoms due to the valence fluctuations also helps to explain the low thermal conductivity in the 14-1-11 system, where the different environments lead to increased phonon scattering. The idea of exploiting the intermediate valent nature of the rare earth element has been visited in some skutterudite systems.[25,26] One can expect that there will be an optimal average Yb valence for 14-1-11 to yield the best thermoelectric properties.

6.4 Conclusion

The Yb atoms of the three analogs of $Yb_{14}MSb_{11}$ (M = Zn, Mn, Mg) have been found to exhibit intermediate valence. XANES measurements reveal that while the $Yb_{14}MnSb_{11}$ and $Yb_{14}MgSb_{11}$ analogs have a nearly

constant average Yb^{3+} fraction (n_f), $Yb_{14}ZnSb_{11}$ has a $n_{f,avg}$ that is strongly temperature dependent. Using field dependent specific heat measurements, the Mg analog is confirmed to exhibit a Schottky-like anomaly with a peak at T = 0.7 K, consistent with this compound being a heavy fermion. A $n_{f,avg} \approx 0.25$ ($4f^{13.75}$) may be a criterion for the requirements of the Yb containing 14-1-11 structure type.

If we bring these conclusions back to the ideas of employing Zintl formalism for these compounds, it is clear that Yb is close to 2+ in all cases. Since the transport properties of all three are those of a heavily degenerate semiconductor or metal, it suggests that the Yb may be hybridized to give rise to a f electron-count a little less than 14. Since one Yb^{3+} is not allowed given the 2-fold or 4-fold equivalency of the Yb sites, but because the Zintl formulism requires one (for M = Mg, Zn), the compound can accommodate this in one of two ways: (1) create disorder and allow Yb^{3+} on some random sites or (2) undergo a small distortion which allows a one-fold Yb site. Therefore, as the carriers are decreased according to Zn > Mn > Mg, the Zintl formalism is best fulfilled with Mg. These results are consistent with the limited amount of RE^{3+} substitution, $x \leq 0.5$, observed in $Yb_{14-x}RE_xMSb_{11}$, presumably because of the presence of intermediate valence of Yb that also exists in these compounds. Systematic substitution of RE in M = Zn, Mg would provide additional verification of electronic vs size restrictions in this structure type. Systematic synthesis of solid solutions compositions with Yb-Eu and Yb-A (A = alkaline earth) may uncover quantum behavior in these narrow bandgap semiconductors. Because of the heavy fermion characteristics in $Yb_{14}MgSb_{11}$, replacing Ge for Sb or an alkali metal for Yb, for example, to obtain higher carrier concentrations along with substitution of M with *4d* or *5d* metals, may result in anomalous behavior induced through hybridization of the Yb *4f* orbitals with Sb *p* and M *d* orbitals.[128] These results and suggestions for further investigation are relevant to many of the Yb containing Zintl phases with magnetic and thermoelectric properties to consider and may provide a pathway towards quantum behavior and thermoelectric optimization.

6.5 Acknowledgements

We thank NSF for funding, DMR-1709382. Work at Lawrence Berkeley National Laboratory was supported by the Director, Office of Science, Office of Basic Energy Sciences, Division of Chemical Sciences, Geosciences, and Biosciences Heavy Element Chemistry Program of the U.S. Department of Energy (DOE) under Contract No. DE-AC02-05CH11231. X-ray absorption measurements were performed at beamline 11-2 at the Stanford Synchrotron Radiation Lightsource, which is supported by the U.S. Department of Energy, Office of Science, Office of Basic Energy Sciences under contract no. DE-AC02-76SF00515. Work at Los Alamos was performed under the auspices of the U.S. DOE, Office of BES, Division of Materials Sciences and Engineering.

Appendix 1.
Supporting Information for Structural Complexity and High Thermoelectric Performance of the Zintl Phase: $Yb_{21}Mn_4Sb_{18}$ (Chapter 1)

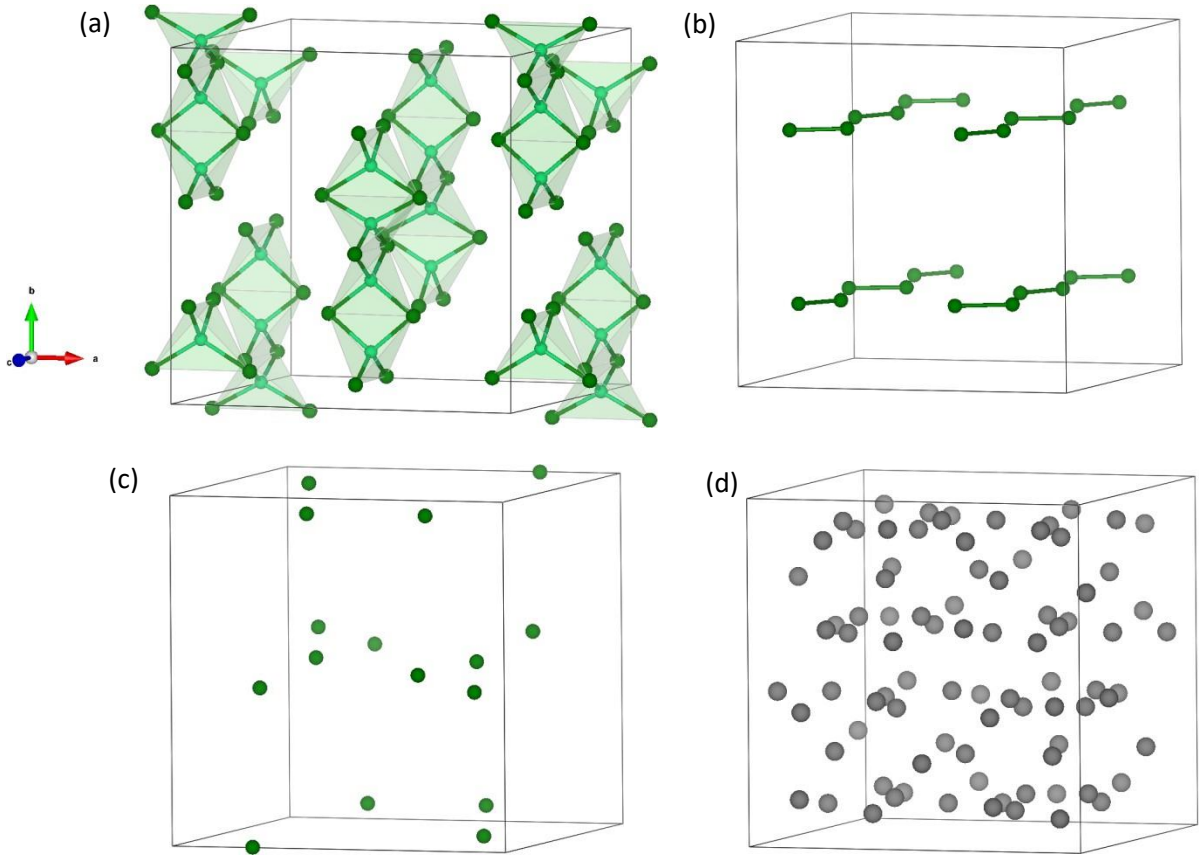

Figure A1.1: The C2/c structure type is made up of: a) linear $[Mn_4Sb_{10}]^{22-}$ tetramer anion units, b) dumbbell $[Sb_2]^{4-}$ anion units, c) individual Sb^{3-} anions and d) individual Yb^{2+} cations to satisfy the Zintl formalism of being charge balanced.

Table A1.1: Single Crystal X-ray Data Collection Parameters and Refinement Results for $Yb_{21}Mn_4Sb_{18}$.

Temperature	100 K	
Wavelength	0.71073 Å	
Crystal system	Monoclinic	
Space group	C2/c	
Unit Cell Dimensions	a = 16.930(3) Å b = 17.029(3) Å c = 16.693(3) Å	α = 90° β = 92.61(3)° γ = 90°
Volume	4807.7(17) $Å^3$	
Z	4	
Density (calculated)	8.352 g/cm^3	
Absorption coefficient	51.279 mm^{-1}	
Crystal size	0.118 x 0.089 x 0.079 mm^3	
Θ range for data collection	2.123° to 30.567°	
Reflections collected	51508	
Goodness-of-fit on F^2	1.142	
Independent reflections	7370 [R(int) = 0.0388]	
Final R indices [I > 2σ(I)]	R1 = 0.0224, wR2 = 0.0394	
Extinction coefficient	0.0000471(10)	
Largest diff. peak and hole	1.942 and -1.518 $e^-/Å^3$	

Table A1.2: Sites of Atomic Coordinates, Occupation and Isotropic Displacement Parameters from Single Crystal X-ray Diffraction and Synchrotron X-ray Powder Data for $Yb_{21}Mn_4Sb_{18}$.

Atom	Site	x	y	z	Occ.[a]	U_{eq}[a]	Occ.[b]	U_{eq}[b]
Yb1	8f	0.33127(2)	-0.24397(2)	0.75786(2)	1	0.01129(5)	1	0.90(4)
Yb2	8f	0.40160(2)	-0.08637(2)	0.93465(2)	1	0.00983(5)	1	0.20(4)
Yb3	8f	0.00463(2)	-0.25826(2)	0.57742(2)	1	0.01160(5)	1	0.70(4)
Yb4	8f	0.31876(2)	0.08877(2)	0.84455(2)	1	0.00985(5)	1	0.60(5)
Yb5	8f	0.30672(2)	0.11622(2)	0.62343(2)	1	0.01245(6)	1	1.05(5)
Yb6	8f	0.16959(2)	-0.08981(2)	0.65824(2)	1	0.01076(5)	1	0.51(5)
Yb7	8f	0.18707(2)	0.12681(2)	0.38076(2)	1	0.01095(5)	1	0.81(6)
Yb8	8f	0.36440(2)	-0.11728(2)	0.56608(2)	1	0.01175(5)	1	0.42(5)
Yb9	8f	0.13017(2)	-0.13264(2)	0.43751(2)	1	0.01138(5)	1	1.16(5)
Yb10	8f	0.08687(2)	0.09116(2)	0.57150(2)	1	0.01009(5)	1	0.61(5)
Yb11	4e	0.50000	-0.07414(3)	0.75000	0.916(2)	0.0110(1)	1	1.18(7)
Yb12	4e	0.50000	-0.030(1)	0.75000	0.025(1)	0.0110(1)	-	-
Sb1	8f	-0.00627(2)	-0.44113(2)	0.60403(2)	1	0.00964(7)	1	1.7(1)
Sb2	8f	0.12711(2)	-0.25639(2)	0.75836(2)	1	0.00978(7)	1	1.79(7)
Sb3	8f	-0.00541(4)	-0.07468(4)	0.60163(5)	0.923(3)	0.0103(1)	1	1.48(8)
Sb4	8f	0.14444(2)	0.07552(2)	0.75324(2)	1	0.01033(8)	1	1.09(7)
Sb5	8f	-0.00844(2)	0.26294(2)	0.62365(2)	1	0.00974(7)	1	1.4(7)
Sb6	8f	0.32487(2)	-0.24938(2)	0.96365(2)	1	0.00924(7)	1	1.54(7)
Sb7	8f	0.21202(2)	-0.25043(2)	0.57517(2)	1	0.00927(7)	1	2.26(7)
Sb8	8f	0.24110(2)	-0.00131(2)	0.49991(2)	1	0.00900(7)	1	0.93(6)
Sb9	8f	0.67745(4)	-0.06628(4)	0.74678(4)	0.942(2)	0.0097(1)	1	1.18(8)
Sb10	8f	0.6552(7)	-0.0642(7)	0.7509(7)	0.058(2)	0.0097(1)	-	-
Sb11	8f	0.0007(7)	-0.0711(6)	0.5819(6)	0.077(3)	0.0103(1)	-	-
Mn1	4e	0.00000	-0.36052(8)	0.75000	1	0.0106(2)	1	0.9(2)
Mn2	4e	0.00000	-0.16025(9)	0.75000	0.923(3)	0.0124(3)	0.94(1)	0.1(2)
Mn3	4e	0.00000	-0.00048(9)	0.75000	0.923(3)	0.0111(3)	0.94(1)	0.5(2)
Mn4	4e	0.00000	0.16132(8)	0.75000	1	0.0110(3)	1	0.1(2)
Mn5	4e	0.00000	-0.066(1)	0.75000	0.077(3)	0.0111(3)	-	-

[a]Single crystal refinement results, 100 K

[b]Rietveld refinement results, 298 K

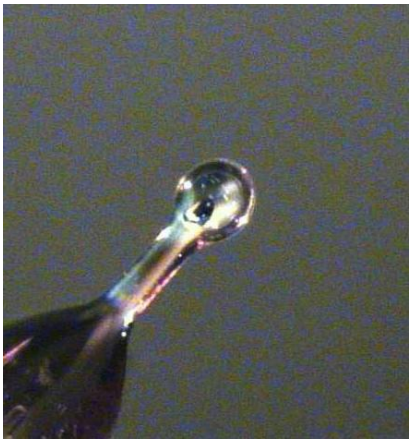

Figure A1.2: Single crystal of $Yb_{21}Mn_4Sb_{18}$ mounted on a MiTeGen loop under paratone oil. Approximate dimensions are 0.118 mm x 0.089 mm x 0.079 mm.

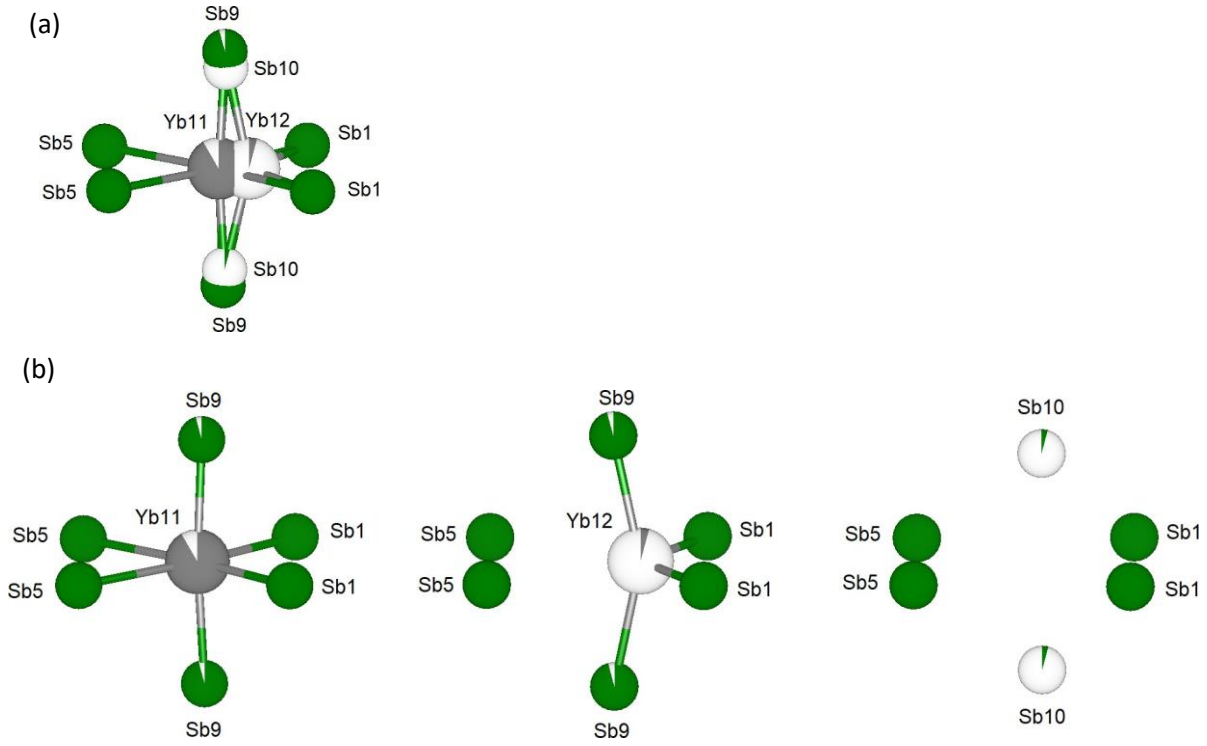

Figure A1.3: Close-up views of the Yb11/Yb12 and Sb9/Sb10 site disorder. (a) shows the superposition of the Yb/Sb atoms and (b) shows the different possible coordination environments.

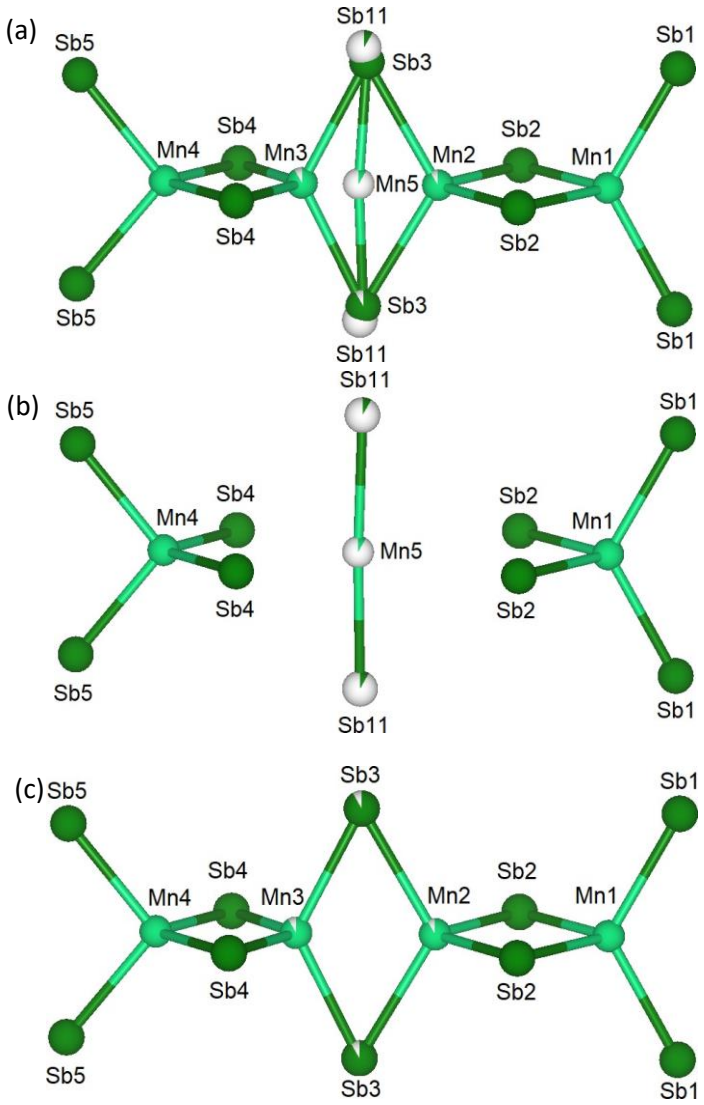

Figure A1.4: Close-up views of the Mn disorder in the tetramer chain. (a) shows the superposition of the Mn/Sb atom disorder, and (b) and (c) show the two possible coordination environments.

Table A1.3: Results of compositional analysis using WDS and EDS for dense pellets of $Yb_{21}Mn_4Sb_{18}$.

$Yb_{21-x}Na_xMn_4Sb_{18}$	Yb (at. %)	Na (at. %)	Mn (at. %)	Sb (at. %)
$Yb_{21}Mn_4Sb_{18}$ (nominal) (x = 0)	48.84	-	9.30	41.86
$Yb_{21}Mn_4Sb_{18}$ (WDS) (x = 0)	49.1(3)	-	9.09(9)	41.8(3)
$Yb_{21}Mn_4Sb_{18}$ (EDS) (x = 0)	47(2)	-	9.4(5)	43(2)
$Yb_{20.8}Na_{0.2}Mn_4Sb_{18}$ (nominal) (x = 0.2)	48.37	0.47	9.30	41.86
$Yb_{20.8}Na_{0.2}Mn_4Sb_{18}$ (WDS) (x = 0.2)	48.5(2)	0.4(1)	9.1(2)	41.9(2)
$Yb_{20.6}Na_{0.4}Mn_4Sb_{18}$ (nominal) (x = 0.4)	47.91	0.93	9.30	41.86
$Yb_{20.6}Na_{0.4}Mn_4Sb_{18}$ (WDS) (x = 0.4)	48.0(2)	0.8(2)	9.1(2)	42.2(2)

Table A1.4: Rietveld Refinement Results for $Yb_{21}Mn_4Sb_{18}$ from Refinement with $2\theta = 2° - 34°$.

Wavelength	0.412736 Å	
Crystal system	Monoclinic	
Space group	C2/c	
Unit Cell Dimensions	a = 17.02725(9) Å b = 17.04802(9) Å c = 16.77150(9) Å	α = 90° β = 92.7936(4)° γ = 90°
Volume	4862.66(5) $Å^3$	
R_{wp}	6.139	

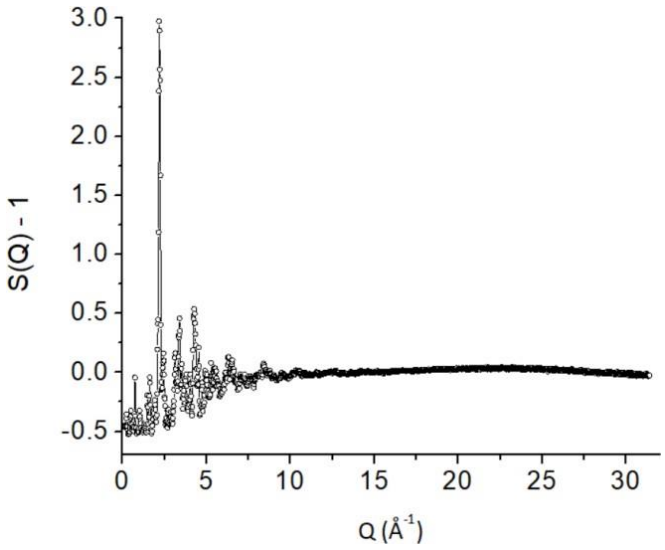

Figure A1.5: Structure function S(Q) – 1.

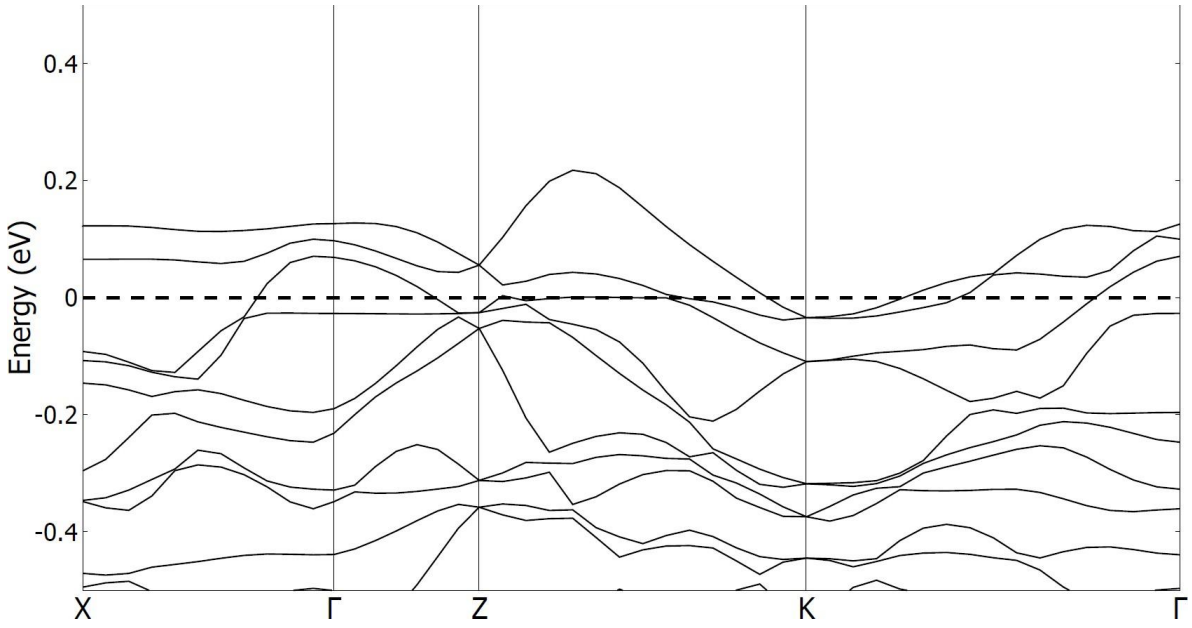

Figure A1.6: Detail of the spin-up band structure for $Yb_{21}Mn_4Sb_{18}$ near the Fermi level. Within a few k_BT of the Fermi level there are mostly rather flat bands, contributing to enhance the Seebeck coefficient, but there are also bands with larger curvature at the Γ point, which sustain higher mobility. This mixed character of the bands involved in hole transport contributes to enhance the thermoelectric figure of merit.

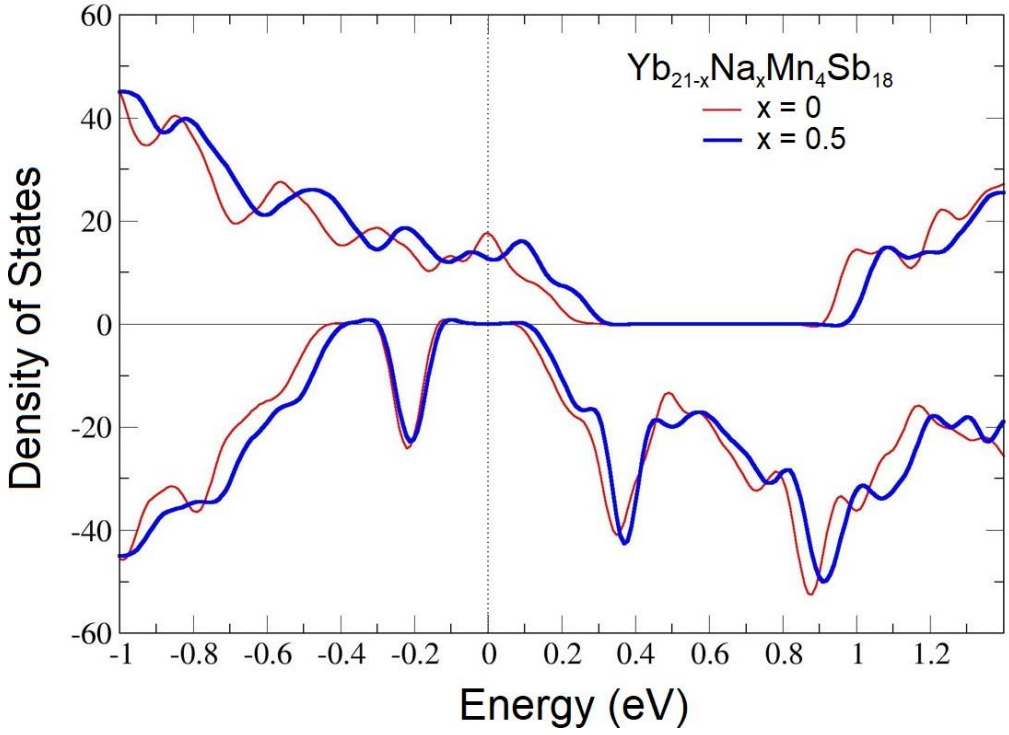

Figure A1.7: Spin-polarized total density of states for $Yb_{21-x}Na_xMn_4Sb_{18}$ (x = 0.5).

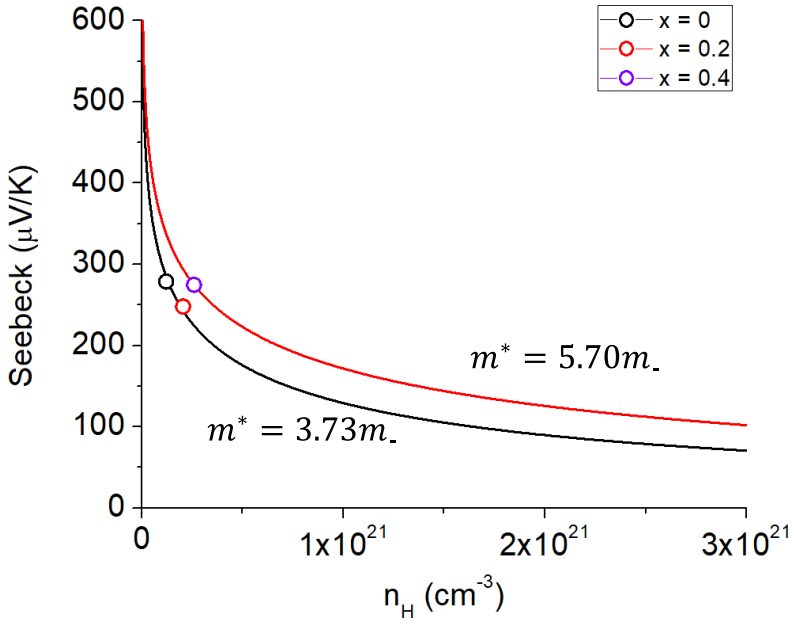

Figure A1.8: The Seebeck coefficient dependence of $Yb_{21-x}Na_xMn_4Sb_{18}$ (x = 0, 0.2, 0.4) is plotted against Hall carrier concentration (n_H) and is modeled by a single parabolic band (Pisarenko plot at 600 K) using two different effective masses.

Appendix 2.

Supporting Information for The Impact of Site Selectivity and Disorder on the Thermoelectric Properties of the solid solutions: $Yb_{21}Mn_{4-x}Cd_xSb_{18}$ and $Yb_{21-y}Ca_yMn_4Sb_{18}$ (Chapter 2)

Table A2.1: Rietveld Refinement Results for $Yb_{21}Mn_{4-x}Cd_xSb_{18}$ with 2θ = 2° - 35° from Synchrotron Powder X-ray Diffraction (11-BM).

Composition	$x = 0.5$	$x = 1.0$	$x = 1.5$
Wavelength	0.457844 Å		
Crystal System	Monoclinic		
Space Group	C2/c		
Unit Cell Dimensions	a = 17.0365(2) Å b = 17.0266(2) Å c = 16.7977(2) Å β = 92.7775(5)°	a = 17.0176(4) Å b = 17.0267(4) Å c = 16.8062(3) Å β = 92.718(1)°	a = 17.0449(2) Å b = 17.0000(2) Å c = 16.8422(2) Å β = 92.7222(6)°
Volume ($Å^3$)	4866.8(1)	4864.2(2)	4874.7(1)
Cd Site Occupation (free)	Mn1 = 0.29(4) Mn2 = 0.00(3) Mn3 = 0.05(3) Mn4 = 0.22(3) Total Cd = 0.57(7) R_{wp} = 6.906	Mn1 = 0.75(7) Mn2 = 0.00(8) Mn3 = 0.18(5) Mn4 = 0.11(7) Total Cd = 1.0(1) R_{wp} = 8.552	Mn1 = 0.88(3) Mn2 = 0.00(3) Mn3 = 0.07(3) Mn4 = 0.31(3) Total Cd = 1.3(1) R_{wp} = 5.831
Refined Composition (free)	$Yb_{21}Mn_{3.43(7)}Cd_{0.57(7)}Sb_{18}$	$Yb_{21}Mn_{3.0(1)}Cd_{1.0(1)}Sb_{18}$	$Yb_{21}Mn_{2.7(1)}Cd_{1.3(1)}Sb_{18}$
Cd Site Occupation (constrained occ.)	Mn1 = 0.25(5) Mn2 = 0.00(3) Mn3 = 0.00(3) Mn4 = 0.25(3) Total Cd = 0.500 R_{wp} = 6.907	Mn1 = 0.65(11) Mn2 = 0.00(3) Mn3 = 0.35(5) Mn4 = 0.00(6) Total Mn = 1.000 R_{wp} = 8.532	Mn1 = 0.96(5) Mn2 = 0.00(3) Mn3 = 0.20(3) Mn4 = 0.34(2) Total Mn = 1.500 R_{wp} = 5.834
Mn1 – Mn2	3.64(3) Å	3.74(5) Å	4.004(2) Å
Mn2 – Mn3	2.35(3) Å	2.40(5) Å	2.07(3) Å
Mn3 – Mn4	2.75(2) Å	2.63(3) Å	2.65(3) Å

Table A2.2: Rietveld Refinement Results for $Yb_{21-y}Ca_yMn_4Sb_{18}$ with 2θ = 2° - 35° from Synchrotron Powder X-ray Diffraction (11-BM).

Composition	y = 3.0	y = 6.0	y = 9.0	y = 10.5
Wavelength	0.457844 Å			
Crystal System	Monoclinic			
Space Group	*C*2/*c*			
Unit Cell Dimensions	a = 17.0580(2) Å b = 17.0566(2) Å c = 16.7969(2) Å β = 92.8587(4)°	a = 17.0845(2) Å b = 17.0649(2) Å c = 16.8196(2) Å β = 92.9170(4)°	a = 17.1042(2) Å b = 17.0694(2) Å c = 16.8373(2) Å β = 92.9772(4)°	a = 17.1160(2) Å b = 17.0665(2) Å c = 16.8523(2) Å β = 93.0095(4)°
Volume ($Å^3$)	4880.99(8)	4897.32(8)	4909.2(1)	4915.96(9)
Ca Site Occupation (free)	Yb1: 0.202(6) Yb2: 0.204(7) Yb3: 0.126(6) Yb4: 0.224(7) Yb5: 0.140(7) Yb6: 0.096(7) Yb7: 0.157(7) Yb8: 0.173(7) Yb9: 0.159(8) Yb10: 0.137(7) Yb11: 0.242(9) Total Ca: 1.86(2) R_{wp}: 6.945	Yb1: 0.290(6) Yb2: 0.370(7) Yb3: 0.237(6) Yb4: 0.357(7) Yb5: 0.267(8) Yb6: 0.218(7) Yb7: 0.297(8) Yb8: 0.327(8) Yb9: 0.343(8) Yb10: 0.281(7) Yb11: 0.392(9) Total Ca: 3.38(2) R_{wp}: 6.187	Yb1: 0.427(6) Yb2: 0.519(7) Yb3: 0.345(6) Yb4: 0.502(7) Yb5: 0.447(8) Yb6: 0.386(6) Yb7: 0.467(7) Yb8: 0.508(8) Yb9: 0.501(8) Yb10: 0.462(7) Yb11: 0.479(9) Total Ca: 5.04(2) R_{wp}: 6.374	Yb1: 0.498(5) Yb2: 0.581(5) Yb3: 0.421(5) Yb4: 0.554(5) Yb5: 0.542(6) Yb6: 0.475(5) Yb7: 0.532(6) Yb8: 0.584(6) Yb9: 0.542(6) Yb10: 0.553(5) Yb11: 0.552(7) Total Ca: 5.83(2) R_{wp}: 5.834
Refined Composition (free)	$Yb_{17.45(2)}Ca_{3.55(2)}Mn_4Sb_{18}$	$Yb_{14.55(2)}Ca_{6.45(2)}Mn_4Sb_{18}$	$Yb_{11.38(2)}Ca_{9.62(2)}Mn_4Sb_{18}$	$Yb_{9.86(2)}Ca_{11.13(2)}Mn_4Sb_{18}$
Ca Site Occupation (constrained Occ)	Yb1: 0.167(6) Yb2: 0.188(7) Yb3: 0.103(6) Yb4: 0.198(7) Yb5: 0.133(8) Yb6: 0.068(7) Yb7: 0.110(8) Yb8: 0.157(8) Yb9: 0.121(8) Yb10: 0.115(7) Yb11: 0.212(8) Total Ca: 1.57143 R_{wp}: 6.853	Yb1: 0.276(6) Yb2: 0.358(7) Yb3: 0.215(6) Yb4: 0.337(7) Yb5: 0.240(8) Yb6: 0.199(7) Yb7: 0.291(8) Yb8: 0.299(8) Yb9: 0.324(8) Yb10: 0.256(7) Yb11: 0.349(9) Total Ca: 3.14286 R_{wp}: 6.177	Yb1: 0.395(6) Yb2: 0.496(7) Yb3: 0.327(6) Yb4: 0.470(6) Yb5: 0.425(8) Yb6: 0.358(6) Yb7: 0.443(8) Yb8: 0.486(8) Yb9: 0.465(8) Yb10: 0.434(7) Yb11: 0.415(8) Total Ca: 4.71429 R_{wp}: 6.385	Yb1: 0.467(5) Yb2: 0.559(5) Yb3: 0.400(5) Yb4: 0.522(5) Yb5: 0.524(6) Yb6: 0.448(5) Yb7: 0.506(6) Yb8: 0.563(6) Yb9: 0.503(7) Yb10: 0.528(5) Yb11: 0.480(7) Total Ca: 5.5 R_{wp}: 5.409

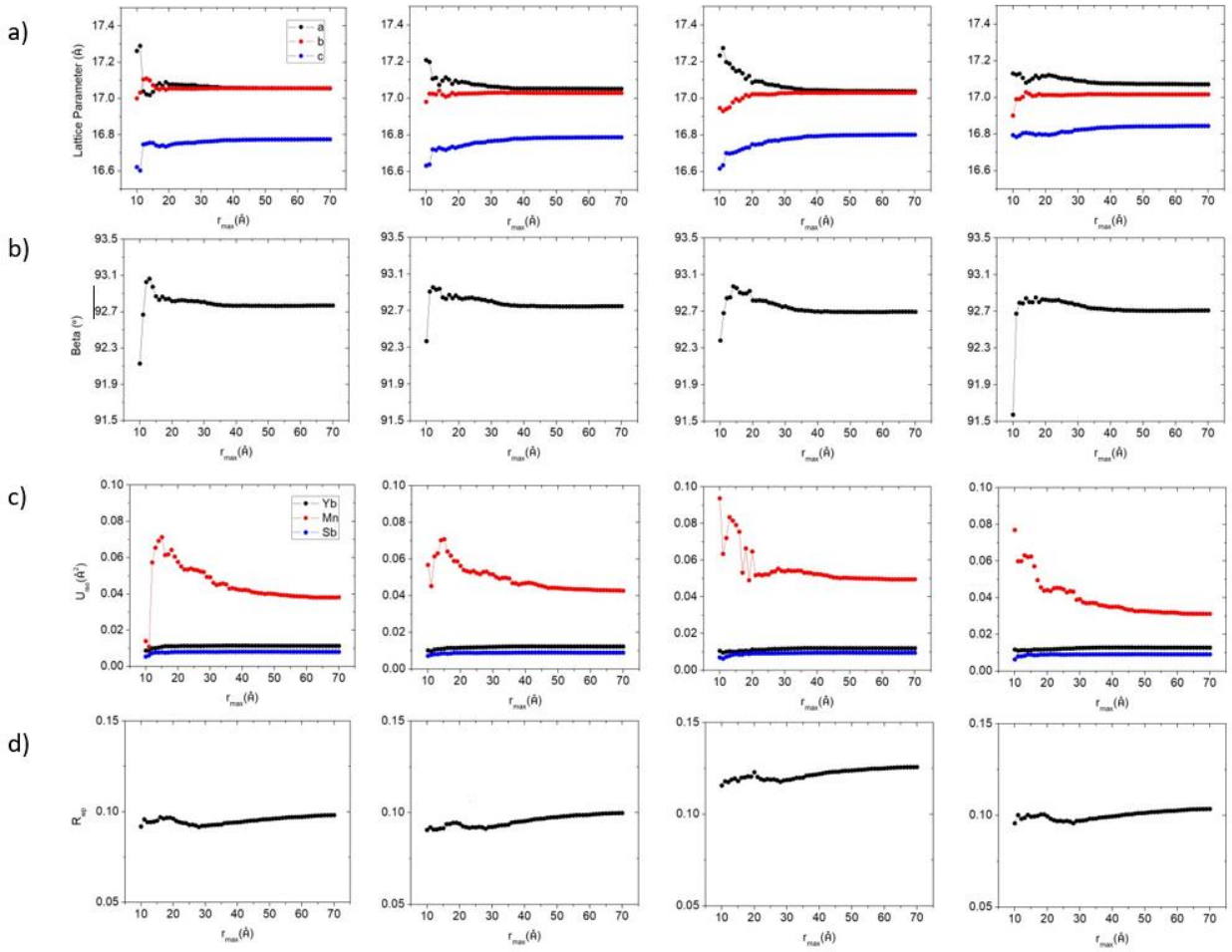

Figure A2.1: Total X-ray Scattering Refinement Results for $Yb_{21}Mn_{4-x}Cd_xSb_{18}$ (x = 0, 0.5, 1.0, 1.5) showing (a) Lattice parameters, (b) beta angle, (c) atomic displacement parameters, (d) R_{wp} value.

Table A2.3: Total X-ray Scattering Refinement Results for $Yb_{21}Mn_{4-x}Cd_xSb_{18}$ (x = 0, 0.5, 1.0, 1.5) with a restricted r_{max} = 70 Å.

Composition	x = 0	x = 0.5	x = 1.0	x =1.5
Wavelength	0.2115 Å			
Crystal System	Monoclinic			
Space Group	C2/c			
Unit Cell Dimensions	a = 17.0558 Å b = 17.057 Å c = 16.775 Å β = 92.7695°	a = 17.0514 Å b = 17.0291 Å c = 16.7873 Å β = 92.7507°	a = 17.0386 Å b = 17.0305 Å c = 16.7998 Å β = 92.6999°	a = 17.0715 Å b = 17.0163 Å c = 16.8441 Å β = 92.7107°
U_{iso}	Yb = 0.011356 Å^2	Yb = 0.012259 Å^2	Yb = 0.011992 Å^2	Yb = 0.012778 Å^2

	Mn = 0.038174 Å^2 Sb = 0.008016 Å^2	Mn = 0.04267 Å^2 Sb =0.0089 Å^2	Mn = 0.05343 Å^2 Sb = 0.009549 Å^2	Mn = 0.031206 Å^2 Sb = 0.009141 Å^2
R_{wp}	0.09816	0.099837	0.125745	0.103506

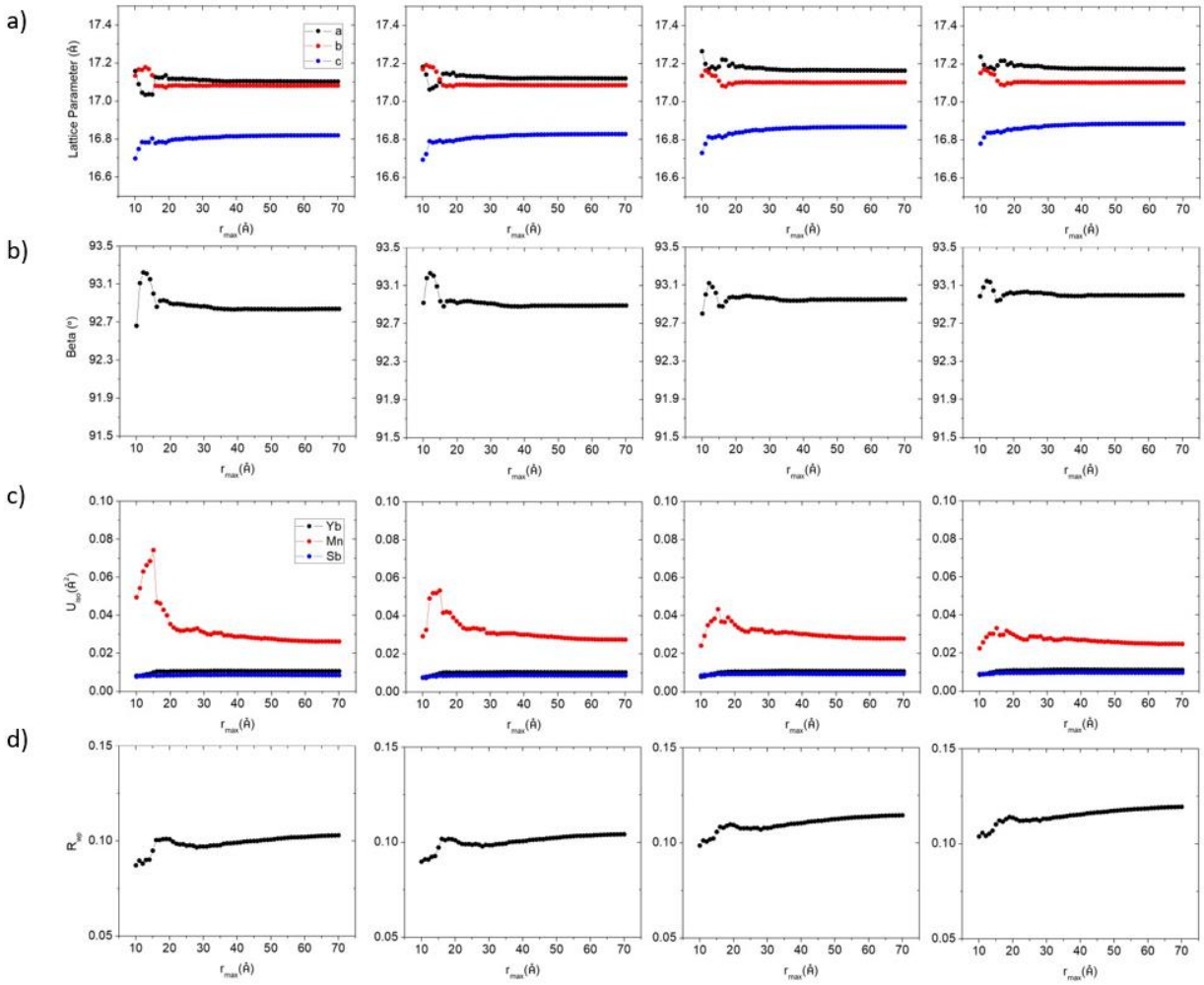

Figure A2.2: Total X-ray Scattering Refinement Results for $Yb_{21-y}Ca_yMn_4Sb_{18}$ (y = 3, 6, 9, 10.5) showing (a) Lattice parameters, (b) beta angle, (c) atomic displacement parameters, (d) R_{wp} value.

Table A2.4: Total X-ray Scattering Refinement Results for $Yb_{21-y}Ca_yMn_4Sb_{18}$ (y = 3, 6, 9, 10.5) with a restricted r_{max} = 70 Å.

Composition	y = 3.0	y = 6.0	y = 9.0	y = 10.5
Wavelength	0.2115 Å			
Crystal System	Monoclinic			
Space Group	C2/c			
Unit Cell Dimensions	a = 17.1034 Å b = 17.0821 Å	a = 17.1214 Å b = 17.0857 Å	a = 17.1643 Å b = 17.1026 Å	a = 17.1736 Å b = 17.1044 Å

	c = 16.8201 Å β = 92.8404°	c = 16.8284 Å β = 92.8918°	c = 16.8679 Å β = 92.95°	c = 16.8864 Å β = 92.9974°
U_{iso}	Yb = 0.01063 Å^2 Mn = 0.026261 Å^2 Sb = 0.008568 Å^2	Yb = 0.010348 Å^2 Mn = 0.027556 Å^2 Sb =0.008664 Å^2	Yb = 0.010761 Å^2 Mn = 0.027916 Å^2 Sb = 0.009294 Å^2	Yb = 0.011148 Å^2 Mn = 0.024777 Å^2 Sb = 0.009637 Å^2
R_{wp}	0.103003	0.104197	0.114528	0.119490

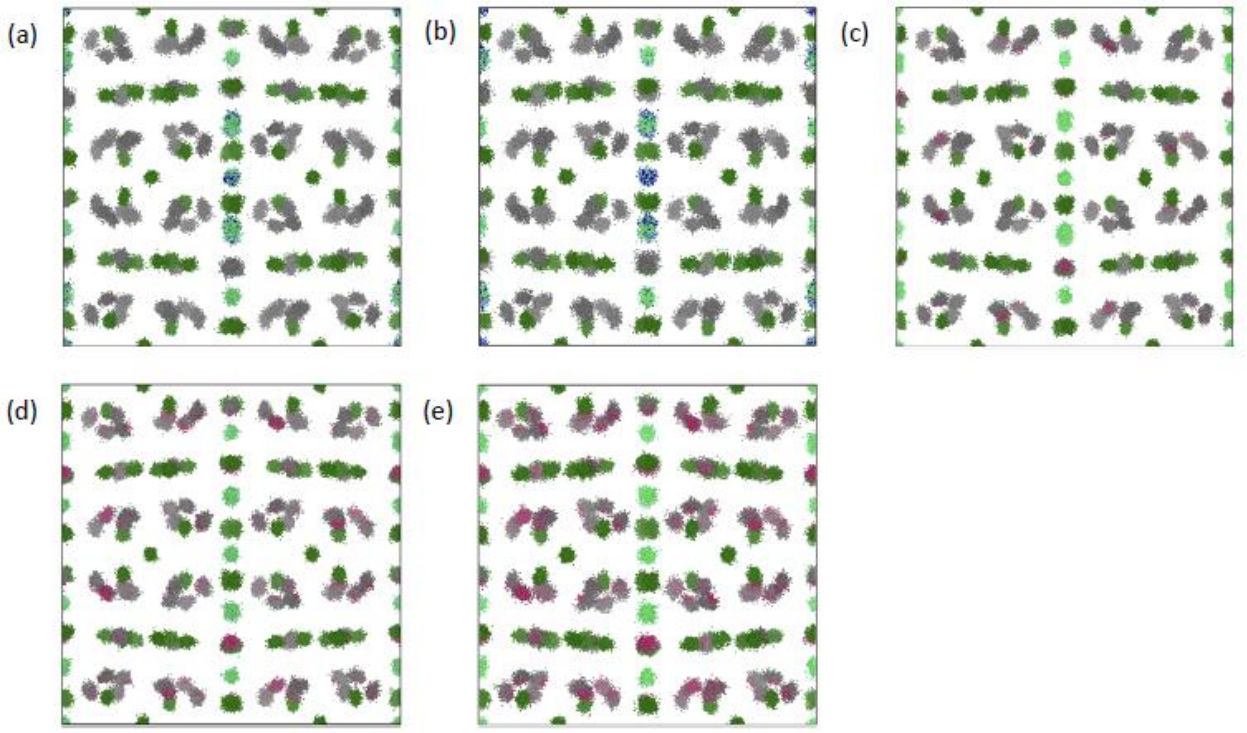

Figure A2.3: Point-cloud distributions for $Yb_{21}Mn_{4-x}Cd_xSb_{18}$ and $Yb_{21-y}Ca_yMn_4Sb_{18}$ a) x = 0.5, b) x = 1.0, c) y = 3, d) y = 6, e) y = 9.

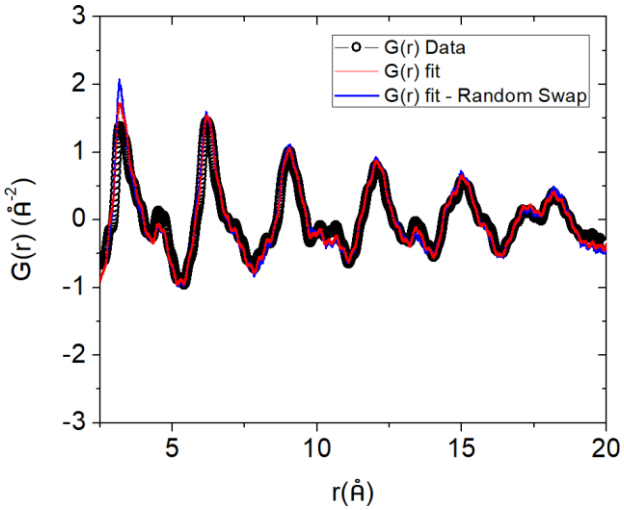

Figure A2.4: Reverse Monte Carlo fit for sample $Yb_{10.5}Ca_{10.5}Mn_4Sb_{18}$ before (red) and after (blue) 12h random swapping of Ca and Yb atoms.

Table A2.5: Experimental Energy Dispersive X-ray Spectroscopy Results for $Yb_{21}Mn_{4-x}Cd_xSb_{18}$ (x = 0.5, 1.0, 1.5) Pellets.

$Yb_{21}Mn_{4-x}Cd_xSb_{18}$	Yb (at. %)	Mn (at. %)	Cd (at. %)	Sb (at. %)
$Yb_{21}Mn_{3.5}Cd_{0.5}Sb_{18}$ (nominal) (x = 0.5)	48.84	8.14	1.16	41.86
$Yb_{21}Mn_{3.5}Cd_{0.5}Sb_{18}$ (EDS) (x = 0.5)	48(3)	8.1(4)	1.4(1)	43(2)
$Yb_{21}Mn_{3.0}Cd_{1.0}Sb_{18}$ (nominal) (x = 1.0)	48.84	6.98	2.32	41.86
$Yb_{21}Mn_{3.0}Cd_{1.0}Sb_{18}$ (EDS) (x = 1.0)	48(2)	6.9(3)	2.6(1)	43(2)
$Yb_{21}Mn_{2.5}Cd_{1.5}Sb_{18}$ (nominal) (x = 1.5)	48.84	5.81	3.49	41.86
$Yb_{21}Mn_{2.5}Cd_{1.5}Sb_{18}$ (EDS) (x = 1.5)	48(2)	6.0(2)	3.7(1)	43(1)

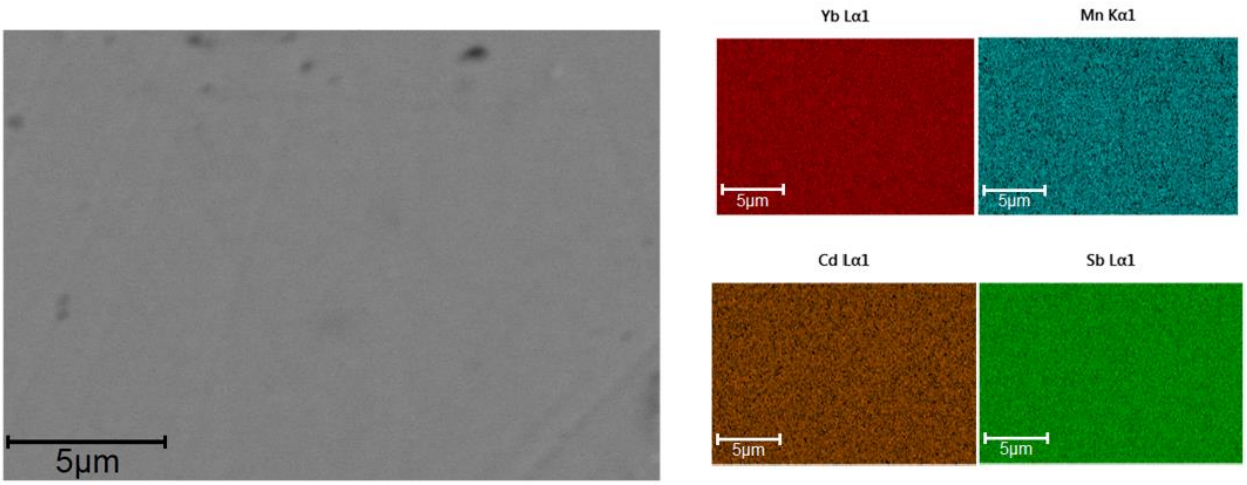

Figure A2.5: Backscattered Electron Images of x = 1.0 sample ($Yb_{21}Mn_3CdSb_{18}$) (left) after SPS along with elemental mapping (right).

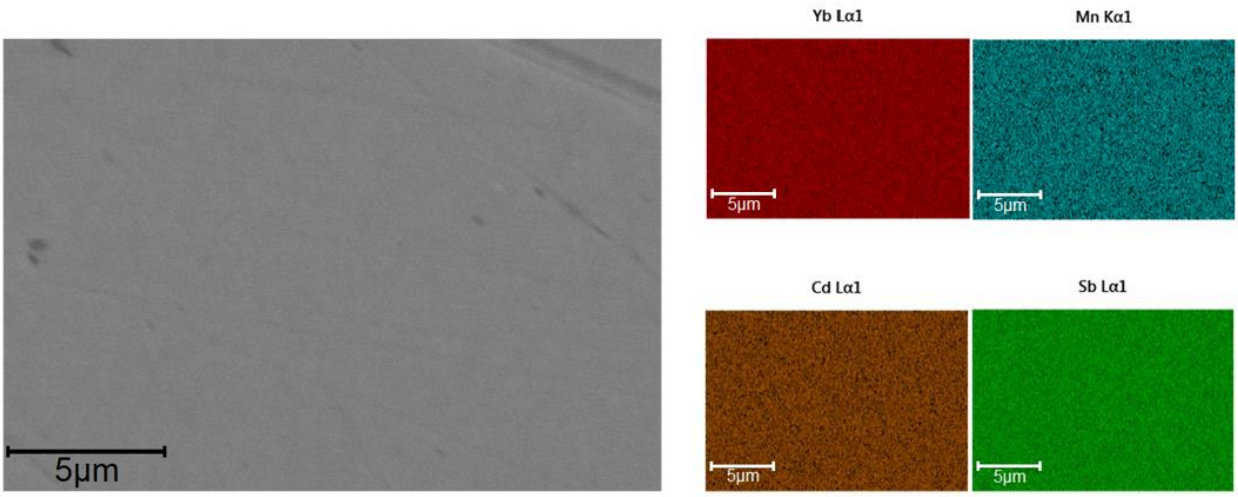

Figure A2.6: Backscattered Electron Images of x = 1.5 sample ($Yb_{21}Mn_{2.5}Cd_{1.5}Sb_{18}$) (left) after SPS along with elemental mapping (right).

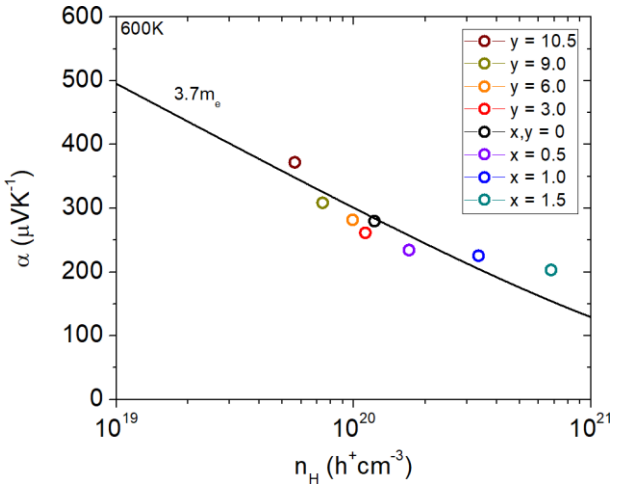

Figure A2.7: Pisarenko Plot for the Cd-substituted ($Yb_{21}Mn_{4-x}Cd_xSb_{18}$ samples and Ca-substituted ($Yb_{21-y}Ca_yMn_4Sb_{18}$) samples.

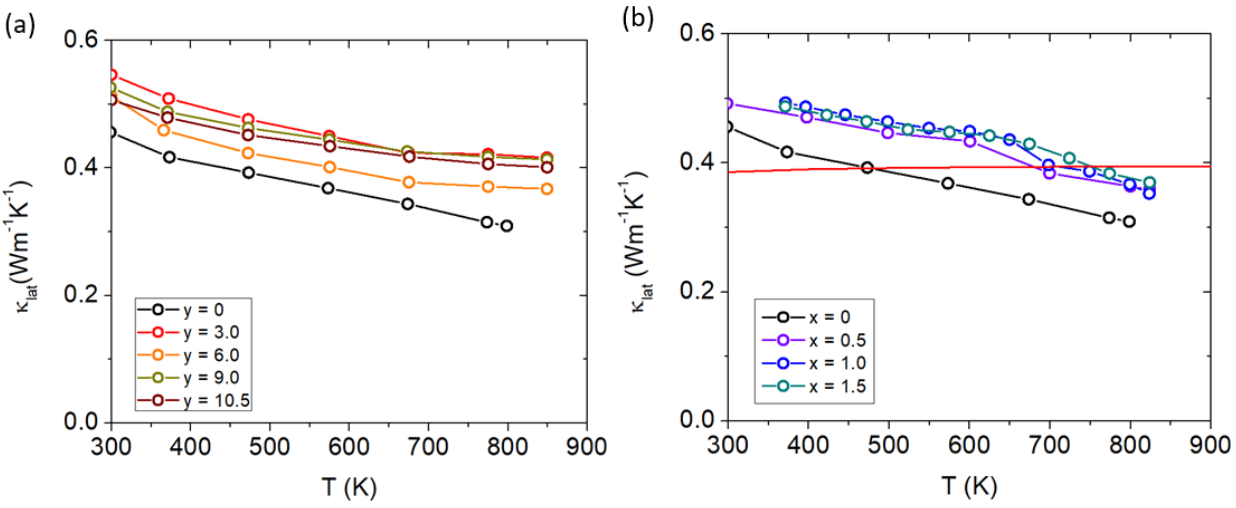

Figure A2.8: Lattice Thermal Conductivities for the a) Ca-substituted samples and b) Cd-substituted samples, plotted with κ_{lat} of the parent (x = 0) sample (red line) determined from speed of sound measurements.

Appendix 3. Supporting Information for Intermediate Yb Valence in the Zintl Phases $Yb_{14}MSb_{11}$ (M = Zn, Mn, Mg): XANES, Magnetism, and Heat Capacity (Chapter 6)

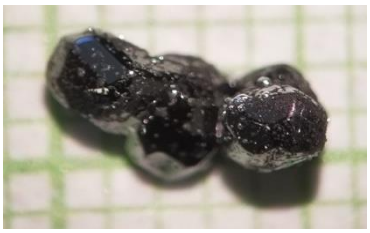

Figure A3.1: Image of typical crystals of $Yb_{14}MnSb_{11}$ grown from Sn flux and employed in this study. Droplets of Sn flux can be seen on the surface of the crystals.

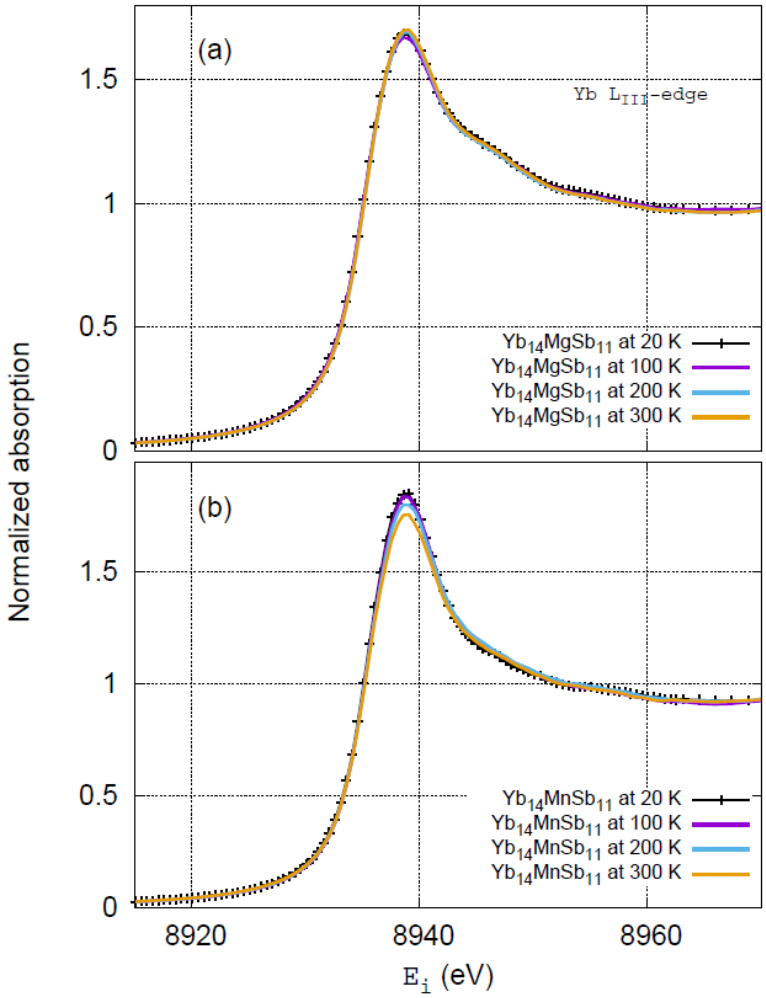

Figure A3.2: Temperature dependent XANES measurement for a) $Yb_{14}MgSb_{11}$ and b) $Yb_{14}MnSb_{11}$.

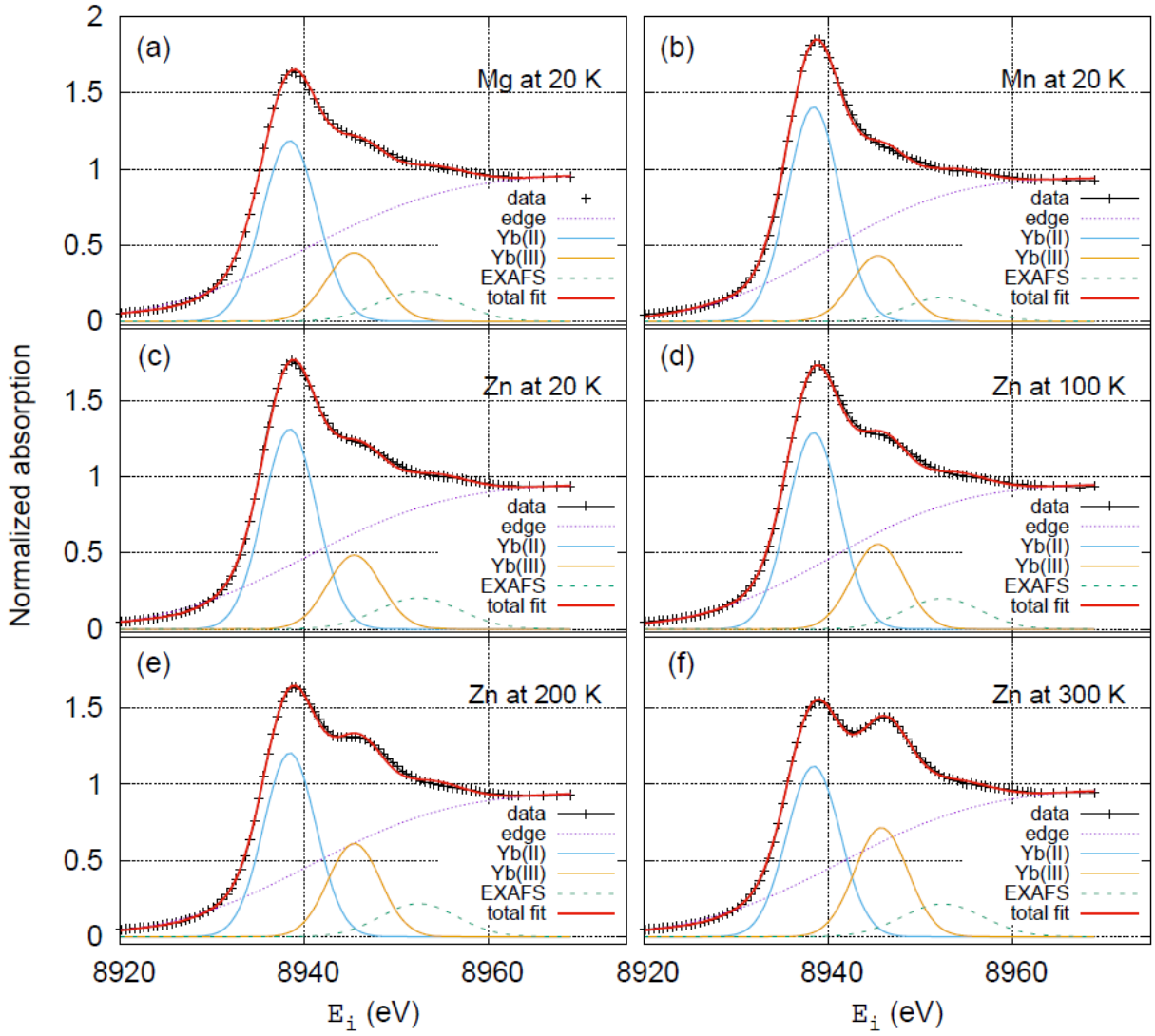

Figure A3.3: XANES measurement fittings for the three $Yb_{14}MSb_{11}$ (M = Zn, Mg, Mn) analogs.

REFERENCES

(1) May, A. F.; McGuire, M. A.; Ma, J.; Delaire, O.; Huq, A.; Custelcean, R. Properties of Single Crystalline AZn_2Sb_2 (A = Ca, Eu, Yb). *J. Appl. Phys.* **2012**, *111* (3), 1–7. https://doi.org/10.1063/1.3681817.

(2) Radzieowski, M.; Block, T.; Fickenscher, T.; Zhang, Y.; Fokwa, B. P. T.; Janka, O. Synthesis, Crystal and Electronic Structures, Physical Properties and ^{121}Sb and ^{151}Eu Mössbauer Spectroscopy of the Alumo-Antimonide Zintl-Phase $Eu_5Al_2Sb_6$. *Mater. Chem. Front.* **2017**, *1* (8), 1563–1572. https://doi.org/10.1039/c7qm00057j.

(3) Yi, T.; Cox, C. A.; Toberer, E. S.; Snyder, G. J.; Kauzlarich, S. M. High-Temperature Transport Properties of the Zintl Phases $Yb_{11}GaSb_9$ and $Yb_{11}InSb_9$. *Chem. Mater.* **2010**, *22* (3), 935–941. https://doi.org/10.1021/cm901824c.

(4) Brown, S. R.; Kauzlarich, S. M.; Gascoin, F.; Jeffrey Snyder, G. $Yb_{14}MnSb_{11}$: New High Efficiency Thermoelectric Material for Power Generation. *Chem. Mater.* **2006**, *18* (7), 1873–1877. https://doi.org/10.1021/cm060261t.

(5) Slack, G. A. *CRC Handbook of Thermoelectrics*; Rowe, D. M., Ed.; CRC Press, Boca Raton, FL, 1995.

(6) Snyder, G. J.; Toberer, E. S. Complex Thermoelectric Materials. *Nat. Mater.* **2008**, *7*, 105–114.

(7) Liu, Y.; Zhang, Y.; Ortega, S.; Ibáñez, M.; Lim, K. H.; Grau-Carbonell, A.; Martí-Sánchez, S.; Ng, K. M.; Arbiol, J.; Kovalenko, M. V.; Cadavid, D.; Cabot, A. Crystallographically Textured Nanomaterials Produced from the Liquid Phase Sintering of $Bi_xSb_{2-x}Te_3$ Nanocrystal Building Blocks. *Nano Lett.* **2018**, *18* (4), 2557–2563. https://doi.org/10.1021/acs.nanolett.8b00263.

(8) Lee, M. H.; Kim, K. R.; Rhyee, J. S.; Park, S. D.; Snyder, G. J. High Thermoelectric Figure-of-Merit in Sb_2Te_3/Ag_2Te Bulk Composites as Pb-Free p-Type Thermoelectric Materials. *J. Mater. Chem. C* **2015**, *3* (40), 10494–10499. https://doi.org/10.1039/c5tc01623a.

(9) Xia, S. Q.; Bobev, S. Zintl Phase Variations through Cation Selection. Synthesis and Structure of $A_{21}Cd_4Pn_{18}$ (A = Eu, Sr, Ba; Pn = Sb, Bi). *Inorg. Chem.* **2008**, *47* (6), 1919–1921. https://doi.org/10.1021/ic800242a.

(10) Suen, N. T.; Wang, Y.; Bobev, S. Synthesis, Crystal Structures, and Physical Properties of the New Zintl Phases $A_{21}Zn_4Pn_{18}$ (A = Ca, Eu; Pn = As, Sb) - Versatile Arrangements of $[ZnPn_4]$ Tetrahedra. *J. Solid State Chem.* **2015**, *227* (12), 204–211. https://doi.org/10.1016/j.jssc.2015.03.031.

(11) Xia, S. Q.; Bobev, S. Diverse Polyanions Based on $MnBi_4$ and $MnSb_4$ Tetrahedra: Polymorphism, Structure, and Bonding in $Ca_{21}Mn_4Bi_{18}$ and $Ca_{21}Mn_4Sb_{18}$. *Inorg. Chem.* **2007**, *46* (3), 874–883. https://doi.org/10.1021/ic061958j.

(12) Kim, H.; Condron, C. L.; Holm, A. P.; Kauzlarich, S. M. Synthesis, Structure, and Magnetic Properties of a New Ternary Zintl Phase: $Sr_{21}Mn_4Sb_{18}$. *J. Am. Chem. Soc.* **2000**, *122* (43), 10720–10721. https://doi.org/10.1021/ja002709b.

(13) Wille, E. L. K.; Cooley, J. A.; Fettinger, J. C.; Kazem, N.; Kauzlarich, S. M. A New Solid Solution Compound with the $Sr_{21}Mn_4Sb_{18}$ Structure Type: $Sr_{13}Eu_8Cd_3Mn_1Sb_{18}$. *Zeitschrift fur Krist. - Cryst.*

Mater. **2017**, *232* (7–9), 593–599. https://doi.org/10.1515/zkri-2016-2034.

(14) Wang, Y.; Darone, G. M.; Bobev, S. The New Zintl Phases $Eu_{21}Cd_4Sb_{18}$ and $Eu_{21}Mn_4Sb_{18}$. *J. Solid State Chem.* **2016**, *238* (64), 303–310. https://doi.org/10.1016/j.jssc.2016.03.044.

(15) Holm, A. P.; Olmstead, M. M.; Kauzlarich, S. M. The Crystal Structure and Magnetic Properties of a New Ferrimagnetic Semiconductor: $Ca_{21}Mn_4Sb_{18}$. *Inorg. Chem.* **2003**, *42* (6), 1973–1981. https://doi.org/10.1021/ic020530r.

(16) He, A.; Bux, S. K.; Hu, Y.; Uhl, D.; Li, L.; Donadio, D.; Kauzlarich, S. M. Structural Complexity and High Thermoelectric Performance of the Zintl Phase: $Yb_{21}Mn_4Sb_{18}$. *Chem. Mater.* **2019**, *31* (19), 8076–8086. https://doi.org/10.1021/acs.chemmater.9b02671.

(17) Baranets, S.; Ovchinnikov, A.; Bobev, S. Complex Structural Disorder in the Zintl Phases $Yb_{10}MnSb_9$ and $Yb_{21}Mn_4Sb_{18}$. *Inorg. Chem.* **2021**. https://doi.org/10.1021/acs.inorgchem.1c00519.

(18) He, A.; Cerretti, G.; Kauzlarich, S. M. The Impact of Site Selectivity and Disorder on the Thermoelectric Properties of $Yb_{21}Mn_4Sb_{18}$ Solid Solutions: $Yb_{21}Mn_{4-x}Cd_xSb_{18}$ and $Yb_{21-y}Ca_yMn_4Sb_{18}$. *Mater. Adv.* **2021**, *2* (17), 5764–5776. https://doi.org/10.1039/d1ma00497b.

(19) Havinga, E. E.; Buschow, K. H. J.; van Daal, H. J. The Ambivalence of Yb in $YbAl_2$ and $YbAl_3$. *Solid State Commun.* **1973**, *13* (5), 621–627. https://doi.org/10.1016/S0038-1098(73)80026-2.

(20) Rai, B. K.; Oswald, I. W. H.; Chan, J. Y.; Morosan, E. Intermediate Valence to Heavy Fermion through a Quantum Phase Transition in $Yb_3(Rh_{1-x}T_x)_4Ge_{13}$ (T = Co, Ir) Single Crystals. *Phys. Rev. B* **2016**, *93* (3), 1–7. https://doi.org/10.1103/PhysRevB.93.035101.

(21) Fanelli, V. R.; Lawrence, J. M.; Goremychkin, E. A.; Osborn, R.; Bauer, E. D.; McClellan, K. J.; Thompson, J. D.; Booth, C. H.; Christianson, A. D.; Riseborough, P. S. Q-Dependence of the Spin Fluctuations in the Intermediate Valence Compound $CePd_3$. *J. Phys. Condens. Matter* **2014**, *26* (22). https://doi.org/10.1088/0953-8984/26/22/225602.

(22) He, A.; Wille, E. L. K.; Moreau, L. M.; Thomas, S. M.; Lawrence, J. M.; Bauer, E. D.; Booth, C. H.; Kauzlarich, S. M. Intermediate Yb Valence in the Zintl Phases $Yb_{14}MSb_{11}$ (M = Zn, Mn, Mg): XANES, Magnetism, and Heat Capacity. *Phys. Rev. Mater.* **2020**, *4* (11), 1–12. https://doi.org/10.1103/PhysRevMaterials.4.114407.

(23) Herbst, J. F.; Lowy, D. N.; Watson, R. E. Single-Electron Energies, Many-Electron Effects, and the Renormalized-Atom Scheme as Applied to Rare-Earth Metals. *Phys. Rev. B* **1972**, *6* (5), 1913–1924. https://doi.org/10.1103/PhysRevB.6.1913.

(24) Sales, B. C.; Wohlleben, D. K. Susceptibility of Interconfiguration-Fluctuation Compounds. *Phys. Rev. Lett.* **1975**, *35* (18), 1240–1244. https://doi.org/10.1103/PhysRevLett.35.1240.

(25) Nolas, G. S.; Morelli, D. T.; Tritt, T. M. Skutterudites: A Phonon-Glass-Electron Crystal Approach to Advanced Thermoelectric Energy Conversion Applications. *Annu. Rev. Mater. Sci.* **1999**, *29*, 89–116. https://doi.org/10.1146/annurev.matsci.29.1.89.

(26) Bauer, E.; Berger, S.; Paul, C.; Michor, H.; Grytsiv, A.; Rogl, P. Effect of Ionic Valence and Electronic Correlations on the Thermoelectric Power in Some Filled Skutterudites. *Phys. B Condens. Matter* **2003**, *328* (1–2), 49–52. https://doi.org/10.1016/S0921-4526(02)01807-0.

(27) Toberer, E. S.; May, A. F.; Snyder, G. J. Zintl Chemistry for Designing High Efficiency Thermoelectric Materials. *Chem. Mater.* **2010**, *22* (3), 624–634. https://doi.org/10.1021/cm901956r.

(28) Ovchinnikov, A.; Bobev, S. Zintl Phases with Group 15 Elements and the Transition Metals: A Brief Overview of Pnictides with Diverse and Complex Structures. *J. Solid State Chem.* **2019**, *270* (August 2018), 346–359. https://doi.org/10.1016/j.jssc.2018.11.029.

(29) Kauzlarich, S. M.; Brown, S. R.; Jeffrey Snyder, G. Zintl Phases for Thermoelectric Devices. *J. Chem. Soc. Dalt. Trans.* **2007**, No. 21, 2099–2107. https://doi.org/10.1039/b702266b.

(30) Corbett, J. D. Chemistry, Structure and Bonding of Zintl Phases and Ions. *Chem. Struct. Bond. Zintl Phases Ions* **1996**, 139.

(31) Rauscher, J. F.; Cox, C. A.; Yi, T.; Beavers, C. M.; Klavins, P.; Toberer, E. S.; Snyder, G. J.; Kauzlarich, S. M. Synthesis, Structure, Magnetism, and High Temperature Thermoelectric Properties of Ge Doped $Yb_{14}MnSb_{11}$. *Dalt. Trans.* **2010**, *39* (4), 1055–1062. https://doi.org/10.1039/b920250a.

(32) Möchel, A.; Sergueev, I.; Wille, H. C.; Juranyi, F.; Schober, H.; Schweika, W.; Brown, S. R.; Kauzlarich, S. M.; Hermann, R. P. Lattice Dynamics in the Thermoelectric Zintl Compound $Yb_{14}MnSb_{11}$. *Phys. Rev. B - Condens. Matter Mater. Phys.* **2011**, *84* (18), 1–10. https://doi.org/10.1103/PhysRevB.84.184303.

(33) Toberer, E. S.; Cox, C. A.; Brown, S. R.; Ikeda, T.; May, A. F.; Kauzlarich, S. M.; Jeffrey Snyder, G. Traversing the Metal-Insulator Transition in a Zintl Phase: Rational Enhancement of Thermoelectric Efficiency in $Yb_{14}Mn_{1-x}Al_xSb_{11}$. *Adv. Funct. Mater.* **2008**, *18* (18), 2795–2800. https://doi.org/10.1002/adfm.200800298.

(34) Snyder, G. J.; Christensen, M.; Nishibori, E.; Caillat, T.; Iversen, B. B. Disordered Zinc in Zn_4Sb_3 with Phonon-Glass and Electron-Crystal Thermoelectric Properties. *Nat. Mater.* **2004**, *3* (7), 458–463. https://doi.org/10.1038/nmat1154.

(35) Mozharivskyj, Y.; Janssen, Y.; Harringa, J. L.; Kracher, A.; Tsokol, A. O.; Miller, G. J. $Zn_{13}Sb_{10}$: A Structural and Landau Theoretical Analysis of Its Phase Transitions. *Chem. Mater.* **2006**, *18* (3), 822–831. https://doi.org/10.1021/cm0515505.

(36) Lo, C. W. T.; Ortiz, B. R.; Toberer, E. S.; He, A.; Svitlyk, V.; Chernyshov, D.; Kolodiazhnyi, T.; Lidin, S.; Mozharivskyj, Y. Synthesis, Structure, and Thermoelectric Properties of α-Zn_3Sb_2 and Comparison to β-$Zn_{13}Sb_{10}$. *Chem. Mater.* **2017**, *29* (12), 5249–5258. https://doi.org/10.1021/acs.chemmater.7b01214.

(37) Christensen, M.; Lock, N.; Overgaard, J.; Iversen, B. B. Crystal Structures of Thermoelectric n- and p-Type $Ba_8Ga_{16}Ge_{30}$ Studied by Single Crystal, Multitemperature, Neutron Diffraction, Conventional X-Ray Diffraction and Resonant Synchrotron X-Ray Diffraction. *J. Am. Chem. Soc.* **2006**, *128* (49), 15657–15665. https://doi.org/10.1021/ja063695y.

(38) May, A. F.; Toberer, E. S.; Saramat, A.; Snyder, G. J. Characterization and Analysis of Thermoelectric Transport in n -Type $Ba_8Ga_{16-x}Ge_{30+x}$. *Phys. Rev. B - Condens. Matter Mater. Phys.* **2009**, *80* (12), 1–12. https://doi.org/10.1103/PhysRevB.80.125205.

(39) Chen, B.; Xu, J. H.; Uher, C.; Morelli, D. T.; Meisner, G. P. Low-Temperature Transport Properties of the Filled Skutteruditess. *Phys. Rev. B - Condens. Matter Mater. Phys.* **1997**, *55* (3), 1476–1480.

https://doi.org/10.1103/PhysRevB.55.1476.

(40) Canfield, P. C.; Kong, T.; Kaluarachchi, U. S.; Jo, N. H. Use of Frit-Disc Crucibles for Routine and Exploratory Solution Growth of Single Crystalline Samples. *Philos. Mag.* **2016**, *96* (1), 84–92. https://doi.org/10.1080/14786435.2015.1122248.

(41) Sheldrick, G. M. A Short History of SHELX. *Acta Crystallogr. Sect. A Found. Crystallogr.* **2008**, *64* (1), 112–122. https://doi.org/10.1107/S0108767307043930.

(42) Neuefeind, J.; Feygenson, M.; Carruth, J.; Hoffmann, R.; Chipley, K. K. The Nanoscale Ordered MAterials Diffractometer NOMAD at the Spallation Neutron Source SNS. *Nucl. Instruments Methods Phys. Res. Sect. B Beam Interact. with Mater. Atoms* **2012**, *287*, 68–75. https://doi.org/10.1016/j.nimb.2012.05.037.

(43) Farrow, C. L.; Juhas, P.; Liu, J. W.; Bryndin, D.; Boin, E. S.; Bloch, J.; Proffen, T.; Billinge, S. J. L. PDFfit2 and PDFgui: Computer Programs for Studying Nanostructure in Crystals. *J. Phys. Condens. Matter* **2007**, *19* (33). https://doi.org/10.1088/0953-8984/19/33/335219.

(44) Wood, C.; Zoltan, D.; Stapfer, G. Measurement of Seebeck Coefficient Using a Light Pulse. *Rev. Sci. Instrum.* **1985**, *56* (5), 719–722. https://doi.org/10.1063/1.1138213.

(45) Borup, K. A.; Toberer, E. S.; Zoltan, L. D.; Nakatsukasa, G.; Errico, M.; Fleurial, J. P.; Iversen, B. B.; Snyder, G. J. Measurement of the Electrical Resistivity and Hall Coefficient at High Temperatures. *Rev. Sci. Instrum.* **2012**, *83* (12). https://doi.org/10.1063/1.4770124.

(46) Perdew, J. P.; Burke, K.; Ernzerhof, M. Generalized Gradient Approximation Made Simple. *Phys. Rev. Lett.* **1996**, *77* (18), 3865–3868. https://doi.org/10.1103/PhysRevLett.77.3865.

(47) Monkhorst, H. J.; Pack, J. D. Special Points for Brillouin-Zone Integrations. *Phys. Rev. B* **1976**, *13* (12), 5188–5192. https://doi.org/https://doi.org/10.1103/PhysRevB.13.5188.

(48) Giannozzi, P.; Baroni, S.; Bonini, N.; Calandra, M.; Car, R.; Cavazzoni, C.; Ceresoli, D.; Chiarotti, G. L.; Cococcioni, M.; Dabo, I.; Dal Corso, A.; De Gironcoli, S.; Fabris, S.; Fratesi, G.; Gebauer, R.; Gerstmann, U.; Gougoussis, C.; Kokalj, A.; Lazzeri, M.; Martin-Samos, L.; Marzari, N.; Mauri, F.; Mazzarello, R.; Paolini, S.; Pasquarello, A.; Paulatto, L.; Sbraccia, C.; Scandolo, S.; Sclauzero, G.; Seitsonen, A. P.; Smogunov, A.; Umari, P.; Wentzcovitch, R. M. QUANTUM ESPRESSO: A Modular and Open-Source Software Project for Quantum Simulations of Materials. *J. Phys. Condens. Matter* **2009**, *21* (39). https://doi.org/10.1088/0953-8984/21/39/395502.

(49) Rühl, R.; Jeitschko, W. New Pnictides with Ce_2O_2S-Type Structure. *Mat. Res. Bull.* **1979**, *14* (c), 513–517.

(50) Bux, S. K.; Zevalkink, A.; Janka, O.; Uhl, D.; Kauzlarich, S.; Snyder, J. G.; Fleurial, J. P. Glass-like Lattice Thermal Conductivity and High Thermoelectric Efficiency in $Yb_9Mn_{4.2}Sb_9$. *J. Mater. Chem. A* **2014**, *2* (1), 215–220. https://doi.org/10.1039/c3ta14021k.

(51) Xia, S. Q.; Bobev, S. New Manganese-Bearing Antimonides and Bismuthides with Complex Structures. Synthesis, Structural Characterization, and Electronic Properties of $Yb_9Mn_{4+x}Pn_9$ (Pn = Sb or Bi). *Chem. Mater.* **2010**, *22* (3), 840–850. https://doi.org/10.1021/cm901633r.

(52) Ohno, S.; Zevalkink, A.; Takagiwa, Y.; Bux, S. K.; Snyder, G. J. Thermoelectric Properties of the $Yb_9Mn_{4.2-x}Zn_xSb_9$ Solid Solutions. *J. Mater. Chem. A* **2014**, *2* (20), 7478–7483.

https://doi.org/10.1039/c4ta00539b.

(53) Ravich, Y. I.; Efimova, B. A.; Smirnov, I. A. Semiconducting Lead Chalcogenides. *Semicond. Lead Chalcogenides* **1970**. https://doi.org/10.1007/978-1-4684-8607-0.

(54) Kittel, C. *Introduction to Solid State Physics*, 8th ed.; John Wiley & Sons, Inc., 2005; Vol. 2.

(55) Goldsmid, H. J.; Sharp, J. W. Estimation of the Thermal Band Gap of a Semiconductor from Seebeck Measurements. *J. Electron. Mater.* **1999**, *28* (7), 869–872. https://doi.org/10.1007/s11664-999-0211-y.

(56) Rowe, D. M. *Materials, Preparation, and Characterization in Thermoelectrics*; CRC Press, 2012.

(57) Yu, F.; Zhang, J.; Yu, D.; He, J.; Liu, Z.; Xu, B.; Tian, Y. Enhanced Thermoelectric Figure of Merit in Nanocrystalline Bi_2Te_3 Bulk. *J. Appl. Phys.* **2009**, *105* (9). https://doi.org/10.1063/1.3120865.

(58) Zhao, H.; Sui, J.; Tang, Z.; Lan, Y.; Jie, Q.; Kraemer, D.; McEnaney, K.; Guloy, A.; Chen, G.; Ren, Z. High Thermoelectric Performance of MgAgSb-Based Materials. *Nano Energy* **2014**, *7*, 97–103. https://doi.org/10.1016/j.nanoen.2014.04.012.

(59) Schröder, T.; Rosenthal, T.; Giesbrecht, N.; Nentwig, M.; Maier, S.; Wang, H.; Snyder, G. J.; Oeckler, O. Nanostructures in Te/Sb/Ge/Ag (TAGS) Thermoelectric Materials Induced by Phase Transitions Associated with Vacancy Ordering. *Inorg. Chem.* **2014**, *53* (14), 7722–7729. https://doi.org/10.1021/ic5010243.

(60) Zevalkink, A.; Zeier, W. G.; Cheng, E.; Snyder, J.; Fleurial, J. P.; Bux, S. Nonstoichiometry in the Zintl Phase $Yb_{1-\delta}Zn_2Sb_2$ as a Route to Thermoelectric Optimization. *Chem. Mater.* **2014**, *26* (19), 5710–5717. https://doi.org/10.1021/cm502588r.

(61) Snyder, G. J.; Ursell, T. S. Thermoelectric Efficiency and Compatibility. *Phys. Rev. Lett.* **2003**, *91* (14), 148301/1-148301/4. https://doi.org/10.1103/PhysRevLett.91.148301.

(62) Fernández-Yáñez, P.; Romero, V.; Armas, O.; Cerretti, G. Thermal Management of Thermoelectric Generators for Waste Energy Recovery. *Appl. Therm. Eng.* **2021**, *196*. https://doi.org/10.1016/j.applthermaleng.2021.117291.

(63) Beretta, D.; Neophytou, N.; Hodges, J. M.; Kanatzidis, M. G.; Narducci, D.; Martin-Gonzalez, M.; Beekman, M.; Balke, B.; Cerretti, G.; Tremel, W.; Zevalkink, A.; Hofmann, A. I.; Müller, C.; Dörling, B.; Campoy-Quiles, M.; Caironi, M. Thermoelectrics: From History, a Window to the Future. *Mater. Sci. Eng. R Reports* **2019**, *138*, 210–255. https://doi.org/10.1016/j.mser.2018.09.001.

(64) Hu, Y.; Cerretti, G.; Kunz Wille, E. L.; Bux, S. K.; Kauzlarich, S. M. The Remarkable Crystal Chemistry of the $Ca_{14}AlSb_{11}$ Structure Type, Magnetic and Thermoelectric Properties. *J. Solid State Chem.* **2019**, *271*, 88–102. https://doi.org/10.1016/j.jssc.2018.12.037.

(65) He, A.; Svitlyk, V.; Chernyshov, D.; Mozharivskyj, Y. Identification, Structural Characterization and Transformations of the High-Temperature $Zn_{9-\delta}Sb_7$ Phase in the Zn-Sb System. *Dalt. Trans.* **2015**, *44* (48), 20983–20990. https://doi.org/10.1039/c5dt03509k.

(66) Shi, Y.; Assoud, A.; Ponou, S.; Lidin, S.; Kleinke, H. A New Material with a Composite Crystal Structure Causing Ultralow Thermal Conductivity and Outstanding Thermoelectric Properties: $Tl_2Ag_{12}Te_{7+\delta}$. *J. Am. Chem. Soc.* **2018**, *140* (27), 8578–8585. https://doi.org/10.1021/jacs.8b04639.

(67) Heremans, J. P.; Jovovic, V.; Toberer, E. S.; Saramat, A.; Kurosaki, K.; Charoenphakdee, A.; Yamanaka, S.; Snyder, G. J. Enhancement of Thermoelectric of the Electronic Density of States. *Science.* **2008**, *321*, 1457–1461.

(68) Girard, S. N.; Chasapis, T. C.; He, J.; Zhou, X.; Hatzikraniotis, E.; Uher, C.; Paraskevopoulos, K. M.; Dravid, V. P.; Kanatzidis, M. G. PbTe-$PbSnS_2$ Thermoelectric Composites: Low Lattice Thermal Conductivity from Large Microstructures. *Energy Environ. Sci.* **2012**, *5* (9), 8716–8725. https://doi.org/10.1039/c2ee22495j.

(69) Cerretti, G.; Villalpando, O.; Fleurial, J. P.; Bux, S. K. Improving Electronic Properties and Mechanical Stability of $Yb_{14}MnSb_{11}$ via W Compositing. *J. Appl. Phys.* **2019**, *126* (17). https://doi.org/10.1063/1.5118227.

(70) Kim, H. S.; Liu, W.; Chen, G.; Chu, C. W.; Ren, Z. Relationship between Thermoelectric Figure of Merit and Energy Conversion Efficiency. *Proc. Natl. Acad. Sci. U. S. A.* **2015**, *112* (27), 8205–8210. https://doi.org/10.1073/pnas.1510231112.

(71) Toby, B. H.; Von Dreele, R. B. GSAS-II: The Genesis of a Modern Open-Source All Purpose Crystallography Software Package. *J. Appl. Crystallogr.* **2013**, *46* (2), 544–549. https://doi.org/10.1107/S0021889813003531.

(72) Juhás, P.; Davis, T.; Farrow, C. L.; Billinge, S. J. L. PDFgetX3: A Rapid and Highly Automatable Program for Processing Powder Diffraction Data into Total Scattering Pair Distribution Functions. *J. Appl. Crystallogr.* **2013**, *46* (2), 560–566. https://doi.org/10.1107/S0021889813005190.

(73) Tucker, M. G.; Keen, D. A.; Dove, M. T.; Goodwin, A. L.; Hui, Q. RMCProfile: Reverse Monte Carlo for Polycrystalline Materials. *J. Phys. Condens. Matter* **2007**, *19* (33). https://doi.org/10.1088/0953-8984/19/33/335218.

(74) Uvarov, C. A.; Ortega-Alvarez, F.; Kauzlarich, S. M. Enhanced High-Temperature Thermoelectric Performance of $Yb_{14-x}Ca_xMnSb_{11}$. *Inorg. Chem.* **2012**, *51* (14), 7617–7624. https://doi.org/10.1021/ic300567c.

(75) Zeier, W. G.; Zevalkink, A.; Gibbs, Z. M.; Hautier, G.; Kanatzidis, M. G.; Snyder, G. J. Thinking Like a Chemist: Intuition in Thermoelectric Materials. *Angew. Chemie - Int. Ed.* **2016**, *55* (24), 6826–6841. https://doi.org/10.1002/anie.201508381.

(76) Anke Weidenkaff, Matthias Trottmann, Petr Tomeš, Clemens Suter, A. S. and A. V. *Thermoelectric Nanomaterials: Materials Design and Applications*; 2013; Vol. 182.

(77) Kim, H. S.; Gibbs, Z. M.; Tang, Y.; Wang, H.; Snyder, G. J. Characterization of Lorenz Number with Seebeck Coefficient Measurement. *APL Mater.* **2015**, *3* (4), 1–6. https://doi.org/10.1063/1.4908244.

(78) Pomrehn, G. S.; Zevalkink, A.; Zeier, W. G.; Van De Walle, A.; Snyder, G. J. Defect-Controlled Electronic Properties in AZn_2Sb_2 Zintl Phases. *Angew. Chemie - Int. Ed.* **2014**, *53* (13), 3422–3426. https://doi.org/10.1002/anie.201311125.

(79) Cahill, D. Lattice Vibrations And Heat Transport In Crystals And Glasses. *Annu. Rev. Phys. Chem.* **1988**, *39* (1), 93–121. https://doi.org/10.1146/annurev.physchem.39.1.93.

(80) Cooley, J. A.; Promkhan, P.; Gangopadhyay, S.; Donadio, D.; Pickett, W. E.; Ortiz, B. R.; Toberer, E.

S.; Kauzlarich, S. M. High Seebeck Coefficient and Unusually Low Thermal Conductivity Near Ambient Temperatures in Layered Compound $Yb_{2-x}Eu_xCdSb_2$. *Chem. Mater.* **2018**, *30* (2), 484–493. https://doi.org/10.1021/acs.chemmater.7b04517.

(81) Gingerich, D. B.; Mauter, M. S. Quantity, Quality, and Availability of Waste Heat from United States Thermal Power Generation. *Environ. Sci. Technol.* **2015**, *49* (14), 8297–8306. https://doi.org/10.1021/es5060989.

(82) Xiao, Y.; Zhao, L. D. Charge and Phonon Transport in PbTe-Based Thermoelectric Materials. *npj Quantum Mater.* **2018**, *3* (1). https://doi.org/10.1038/s41535-018-0127-y.

(83) Pei, Y.; Shi, X.; Lalonde, A.; Wang, H.; Chen, L.; Snyder, G. J. Convergence of Electronic Bands for High Performance Bulk Thermoelectrics. *Nature* **2011**, *473* (7345), 66–69. https://doi.org/10.1038/nature09996.

(84) Zhao, L. D.; Tan, G.; Hao, S.; He, J.; Pei, Y.; Chi, H.; Wang, H.; Gong, S.; Xu, H.; Dravid, V. P.; Uher, C.; Snyder, G. J.; Wolverton, C.; Kanatzidis, M. G. Ultrahigh Power Factor and Thermoelectric Performance in Hole-Doped Single-Crystal SnSe. *Science.* **2016**, *351* (6269), 141–144. https://doi.org/10.1126/science.aad3749.

(85) Zhou, C.; Lee, Y. K.; Yu, Y.; Byun, S.; Luo, Z. Z.; Lee, H.; Ge, B.; Lee, Y. L.; Chen, X.; Lee, J. Y.; Cojocaru-Mirédin, O.; Chang, H.; Im, J.; Cho, S. P.; Wuttig, M.; Dravid, V. P.; Kanatzidis, M. G.; Chung, I. Polycrystalline SnSe with a Thermoelectric Figure of Merit Greater than the Single Crystal. *Nat. Mater.* **2021**, *20* (10), 1378–1384. https://doi.org/10.1038/s41563-021-01064-6.

(86) Tang, Y.; Gibbs, Z. M.; Agapito, L. A.; Li, G.; Kim, H. S.; Nardelli, M. B.; Curtarolo, S.; Snyder, G. J. Convergence of Multi-Valley Bands as the Electronic Origin of High Thermoelectric Performance in $CoSb_3$ Skutterudites. *Nat. Mater.* **2015**, *14* (12), 1223–1228. https://doi.org/10.1038/nmat4430.

(87) Shannon, B. Y. R. D.; H, M.; Baur, N. H.; Gibbs, O. H.; Eu, M.; Cu, V. Revised Effective Ionic Radii and Systematic Studies of Interatomie Distances in Halides and Chaleogenides. *Acta Cryst.* **1976**, A32, 751-767.

(88) Brown, S. R.; Kauzlarich, S. M.; Gascoin, F.; Jeffrey Snyder, G. High-Temperature Thermoelectric Studies of $A_{11}Sb_{10}$ (A=Yb, Ca). *J. Solid State Chem.* **2007**, *180* (4), 1414–1420. https://doi.org/10.1016/j.jssc.2007.02.007.

(89) Gascoin, F.; Ottensmann, S.; Stark, D.; Haïle, S. M.; Snyder, G. J. Zintl Phases as Thermoelectric Materials: Tuned Transport Properties of the Compounds $Ca_xYb_{1-X}Zn_2Sb_2$. *Adv. Funct. Mater.* **2005**, *15* (11), 1860–1864. https://doi.org/10.1002/adfm.200500043.

(90) He, A.; Wille, E. L. K.; Moreau, L. M.; Thomas, S. M.; Lawrence, J. M.; Bauer, E. D.; Booth, C. H.; Kauzlarich, S. M. Intermediate Yb Valence in the Zintl Phases $Yb_{14}MSb_{11}$(M = Zn, Mn, Mg): XANES, Magnetism, and Heat Capacity. *Phys. Rev. Mater.* **2020**, *4* (11), 4400. https://doi.org/10.1103/PhysRevMaterials.4.114407.

(91) Sales, B. C.; Khalifah, P.; Enck, T. P.; Nagler, E. J.; Sykora, R. E.; Jin, R.; Mandrus, D. Kondo Lattice Behavior in the Ordered Dilute Magnetic Semiconductor $Yb_{14-x}La_xMnSb_{11}$. *Phys. Rev. B - Condens. Matter Mater. Phys.* **2005**, *72* (20), 1–5. https://doi.org/10.1103/PhysRevB.72.205207.

(92) Mathieu, J. L.; Latturner, S. E. Zintl Phase as Dopant Source in the Flux Synthesis of $Ba_{1-x}K_xFe_2As_2$

Type Superconductors. *Chem. Commun.* **2009**, No. 33, 4965–4967. https://doi.org/10.1039/b910749e.

(93) Zhu, Z.; Li, M.; Li, J. Topological Semimetal to Insulator Quantum Phase Transition in the Zintl Compounds BA_2X (X = Si, Ge). *Phys. Rev. B* **2016**, *94* (15), 4–7. https://doi.org/10.1103/PhysRevB.94.155121.

(94) Wendorff, M.; Röhr, C. $Sr_{14}[Al_4]_2[Ge]_3$: Eine Zintl-Phase Mit Isolierten $[Ge]^{4-}$- Und $[Al_4]^{8-}$- Anionen. *Z. Naturforsch* **2007**, *62b*, 1227–1234.

(95) Hillebrecht, H.; Ade, M. B4 Tetrahedra for Aluminum Atoms - A Surprising Substitution in T-Borides $Ni_{20}Al_3B_6$ and $Ni_{20}AlB_{14}$. *Angew. Chemie* **1998**, *37*, 935–938.

(96) Bergeron, D. E.; Roach, P. J.; Castleman, A. W.; Jones, N. O.; Khanna, S. N. Al Cluster Superatoms as Halogens in Polyhalides and as Alkaline Earths in Iodide Salts. *Science.* **2005**, *307* (5707), 231–235. https://doi.org/10.1126/science.1105820.

(97) Castleman, A. W.; Khanna, S. N. Clusters, Superatoms, and Building Blocks of New Materials. *J. Phys. Chem. C* **2009**, *113* (7), 2664–2675. https://doi.org/10.1021/jp806850h.

(98) Castleman, A. W. From Elements to Clusters: The Periodic Table Revisited. *J. Phys. Chem. Lett.* **2011**, *2* (9), 1062–1069. https://doi.org/10.1021/jz200215s.

(99) Uhl, W. Tetrahedral Homonuclear Organoelement Clusters and Subhalides of Aluminium, Gallium and Indium. *Naturwissenschaften* **2004**, *91* (7), 305–319. https://doi.org/10.1007/s00114-004-0534-8.

(100) Dohmeier, C.; Robl, C.; Tacke, M.; Schnöckel, H. The Tetrameric Aluminum(I) Compound [{Al(H_5-C_5Me_5)}$_4$]. *Angew. Chem., Int. Ed.* **1991**, *30* (5), 564–565.

(101) Ertekin, E.; Srinivasan, V.; Ravichandran, J.; Rossen, P. B.; Siemons, W.; Majumdar, A.; Ramesh, R.; Grossman, J. C. Interplay between Intrinsic Defects, Doping, and Free Carrier Concentration in $SrTiO_3$ Thin Films. *Phys. Rev. B - Condens. Matter Mater. Phys.* **2012**, *85* (19), 1–9. https://doi.org/10.1103/PhysRevB.85.195460.

(102) Marshall, M.; Pletikosić, I.; Yahyavi, M.; Tien, H. J.; Chang, T. R.; Cao, H.; Xie, W. Magnetic and Electronic Structures of Antiferromagnetic Topological Material Candidate $EuMg_2Bi_2$. *J. Appl. Phys.* **2021**, *129* (3). https://doi.org/10.1063/5.0035703.

(103) Kawamura, H.; Kumar, V.; Sun, Q.; Kawazoe, Y. Magic Behavior and Bonding Nature in Hydrogenated Aluminum Clusters. *Phys. Rev. B - Condens. Matter Mater. Phys.* **2002**, *65* (4), 454061–4540611. https://doi.org/10.1103/PhysRevB.65.045406.

(104) Ichikawa, K.; Ikeda, Y.; Wagatsuma, A.; Watanabe, K.; Szarek, P.; Tachibana, A. Theoretical Study of Hydrogenated Tetrahedral Aluminum Clusters. *Int. J. Quantum Chem.* **2011**, *111* (14), 3548–3555. https://doi.org/10.1002/qua.22848.

(105) Bacalis, N. C.; Metropoulos, A.; Gross, A. Theoretical Study of the O_2 Interaction with a Tetrahedral Al_4 Cluster. *J. Phys. Chem. A* **2010**, *114* (43), 11746–11750. https://doi.org/10.1021/jp1052198.

(106) Radzieowski, M.; Block, T.; Klenner, S.; Zhang, Y.; Fokwa, B. P. T.; Janka, O. Synthesis, Crystal and Electronic Structure, Physical Properties and ^{121}Sb and ^{151}Eu Mössbauer Spectroscopy of the

$Eu_{14}AlPn_{11}$ Series (Pn = As, Sb). *Inorg. Chem. Front.* **2019**, *6* (1), 137–147. https://doi.org/10.1039/c8qi01099d.

(107) Manchon, A.; Koo, H. C.; Nitta, J.; Frolov, S. M.; Duine, R. A. New Perspectives for Rashba Spin-Orbit Coupling. *Nat. Mater.* **2015**, *14* (9), 871–882. https://doi.org/10.1038/nmat4360.

(108) Pruitt, R. A.; Marshall, S. W.; O'Donnell, C. M. Mössbauer Spectroscopy in Group-III Antimonides. *Phys. Rev. B* **1970**, *2* (7), 2383–2390.

(109) Luo, H.; Krizan, J. W.; Muechler, L.; Haldolaarachchige, N.; Klimczuk, T.; Xie, W.; Fuccillo, M. K.; Felser, C.; Cava, R. J. A Large Family of Filled Skutterudites Stabilized by Electron Count. *Nat. Commun.* **2015**, *6*. https://doi.org/10.1038/ncomms7489.

(110) Zeier, W. G.; Schmitt, J.; Hautier, G.; Aydemir, U.; Gibbs, Z. M.; Felser, C.; Snyder, G. J. Engineering Half-Heusler Thermoelectric Materials Using Zintl Chemistry. *Nat. Rev. Mater.* **2016**, *1* (6). https://doi.org/10.1038/natrevmats.2016.32.

(111) Wang, F.; Miller, G. J. Revisiting the Zintl-Klemm Concept: Alkali Metal Trielides. *Inorg. Chem.* **2011**, *50* (16), 7625–7636. https://doi.org/10.1021/ic200643f.

(112) Zevalkink, A.; Toberer, E. S.; Zeier, W. G.; Flage-Larsen, E.; Snyder, G. J. Ca_3AlSb_3: An Inexpensive, Non-Toxic Thermoelectric Material for Waste Heat Recovery. *Energy Environ. Sci.* **2011**, *4* (2), 510–518. https://doi.org/10.1039/c0ee00517g.

(113) Justl, A. P.; Cerretti, G.; Bux, S. K.; Kauzlarich, S. M. Hydride Assisted Synthesis of the High Temperature Thermoelectric Phase: $Yb_{14}MgSb_{11}$. *J. Appl. Phys.* **2019**, *126* (16). https://doi.org/10.1063/1.5117291.

(114) Hu, Y.; Wang, J.; Kawamura, A.; Kovnir, K.; Kauzlarich, S. M. $Yb_{14}MgSb_{11}$ and $Ca_{14}MgSb_{11}$-New Mg-Containing Zintl Compounds and Their Structures, Bonding, and Thermoelectric Properties. *Chem. Mater.* **2015**, *27* (1), 343–351. https://doi.org/10.1021/cm504059t.

(115) Cordier, G.; Schäfer, H.; Stelter, M. Darstellung Und Struktur Der Verbindung $Ca_{14}AlSb_{11}$. *ZAAC - J. Inorg. Gen. Chem.* **1984**, *519* (12), 183–188. https://doi.org/10.1002/zaac.19845191219.

(116) Chan, J. Y.; Kauzlarich, S. M.; Klavins, P.; Shelton, R. N.; Webb, D. J. Colossal Magnetoresistance in the Transition-Metal Zintl Compound $Eu_{14}MnSb_{11}$. *Chem. Mater.* **1997**, *9* (12), 3132–3135. https://doi.org/10.1021/cm9704241.

(117) Chan, J. Y.; Kauzlarich, S. M.; Klavins, P.; Shelton, R. N.; Webb, D. J. Colossal Negative Magnetoresistance in an Antiferromagnet. *Phys. Rev. B - Condens. Matter Mater. Phys.* **1998**, *57* (14), R8103–R8106. https://doi.org/10.1103/PhysRevB.57.R8103.

(118) Sánchez-Portal, D.; Martin, R. M.; Kauzlarich, S. M.; Pickett, W. E. Bonding, Moment Formation, and Magnetic Interactions in $Ca_{14}MnBi_{11}$ and $Ba_{14}MnBi_{11}$. *Phys. Rev. B - Condens. Matter Mater. Phys.* **2002**, *65* (14), 1–15. https://doi.org/10.1103/PhysRevB.65.144414.

(119) Fisher, I. R.; Wiener, T. A.; Bud, S. L.; Canfield, P. C. Thermodynamic and Transport Properties of Single-Crystal $Yb_{14}MnSb_{11}$. **1999**, *59* (21), 829–834.

(120) Holm, A. P.; Kauzlarich, S. M.; Morton, S. A.; Waddill, G. D.; Pickett, W. E.; Tobin, J. G. XMCD Characterization of the Ferromagnetic State of $Yb_{14}MnSb_{11}$. *J. Am. Chem. Soc.* **2002**, *124* (33), 9894–9898. https://doi.org/10.1021/ja020564y.

(121) Holm, A. P.; Ozawa, T. C.; Kauzlarich, S. M.; Morton, S. A.; Waddill, G. D.; Tobin, J. G. X-Ray Photoelectron Spectroscopy Studies of $Yb_{14}MnSb_{11}$ and $Yb_{14}ZnSb_{11}$. *J. Solid State Chem.* **2005**, *178* (1), 262–269. https://doi.org/10.1016/j.jssc.2004.07.009.

(122) Stone, M. B.; Garlea, V. O.; Gillon, B.; Cousson, A.; Christianson, A. D.; Lumsden, M. D.; Nagler, S. E.; Mandrus, D.; Sales, B. C. Excitations and Magnetization Density Distribution in the Dilute Ferromagnetic Semiconductor $Yb_{14}MnSb_{11}$. *Phys. Rev. B* **2017**, *95* (2), 1–5. https://doi.org/10.1103/PhysRevB.95.020412.

(123) Fisher, I. R.; Bud'ko, S. L.; Song, C.; Canfield, P. C.; Ozawa, T. C.; Kauzlarich, S. M. $Yb_{14}ZnSb_{11}$: Charge Balance in Zintl Compounds as a Route to Intermediate Yb Valence. *Phys. Rev. Lett.* **2000**, *85* (5), 1120–1123. https://doi.org/10.1103/PhysRevLett.85.1120.

(124) Kunz Wille, E. L.; Jo, N. H.; Fettinger, J. C.; Canfield, P. C.; Kauzlarich, S. M. Single Crystal Growth and Magnetic Properties of the Mixed Valent Yb Containing Zintl Phase, $Yb_{14}MgSb_{11}$. *Chem. Commun.* **2018**, *54* (92), 12946–12949. https://doi.org/10.1039/c8cc05471a.

(125) Kuroiwa, H.; Imai, Y.; Saso, T. Absence of Hybridization Gap in Heavy Electron Systems and Analysis of $YbAl_3$ in Terms of Nearly Free Electron Conduction Band. *J. Phys. Soc. Japan* **2007**, *76* (12), 1–8. https://doi.org/10.1143/JPSJ.76.124704.

(126) Sichevych, O.; Prots, Y.; Utsumi, Y.; Akselrud, L.; Schmidt, M.; Burkhardt, U.; Coduri, M.; Schnelle, W.; Bobnar, M.; Wang, Y. T.; Wu, Y. H.; Tsuei, K. D.; Tjeng, L. H.; Grin, Y. Intermediate-Valence Ytterbium Compound $Yb_4Ga_{24}Pt_9$: Synthesis, Crystal Structure, and Physical Properties. *Inorg. Chem.* **2017**, *56* (15), 9343–9352. https://doi.org/10.1021/acs.inorgchem.7b01530.

(127) Juckel, M.; Koželj, P.; Prots, Y.; Ormeci, A.; Burkhardt, U.; Leithe-Jasper, A.; Svanidze, E. Intermediate Valence Behavior of $Yb_2Cu_9Al_8$. *Zeitschrift fur Anorg. und Allg. Chemie* **2020**, *646* (14), 1238–1243. https://doi.org/10.1002/zaac.202000118.

(128) Gui, X.; Chang, T. R.; Wei, K.; Daum, M. J.; Graf, D. E.; Baumbach, R. E.; Mourigal, M.; Xie, W. A Novel Magnetic Material by Design: Observation of Yb^{3+} with Spin-1/2 in Yb_xPt_5P. *ACS Cent. Sci.* **2020**, *6* (11), 2023–2030. https://doi.org/10.1021/acscentsci.0c00691.

(129) Nakatsuji, S.; Kuga, K.; Machida, Y.; Tayama, T.; Sakakibara, T.; Karaki, Y.; Ishimoto, H.; Yonezawa, S.; Maeno, Y.; Pearson, E.; Lonzarich, G. G.; Balicas, L.; Lee, H.; Fisk, Z. Superconductivity and Quantum Criticality in the Heavy-Fermion System β-$YbAlB_4$. *Nat. Phys.* **2008**, *4* (8), 603–607. https://doi.org/10.1038/nphys1002.

(130) Macaluso, R. T.; Nakatsuji, S.; Kuga, K.; Thomas, E. L.; Machida, Y.; Maeno, Y.; Fisk, Z.; Chan, J. Y. Crystal Structure and Physical Properties of Polymorphs of $LnAlB_4$ (Ln = Yb, Lu). *Chem. Mater.* **2007**, *19* (8), 1918–1922. https://doi.org/10.1021/cm062244+.

(131) Ovchinnikov, A.; Prakash, J.; Bobev, S. Crystal Chemistry and Magnetic Properties of the Solid Solutions $Ca_{14-x}RE_xMnBi_{11}$ (RE = La-Nd, Sm, and Gd-Ho; X ≈ 0.6-0.8). *Dalt. Trans.* **2017**, *46* (46), 16041–16049. https://doi.org/10.1039/c7dt03715e.

(132) Prakash, J.; Stoyko, S.; Voss, L.; Bobev, S. On the Extended Series of Quaternary Zintl Phases $Ca_{13}REMnSb_{11}$ (RE = La–Nd, Sm, Gd–Dy). *Eur. J. Inorg. Chem.* **2016**, *2016* (18), 2912–2922. https://doi.org/10.1002/ejic.201600306.

(133) Hu, Y.; Chen, C. W.; Cao, H.; Makhmudov, F.; Grebenkemper, J. H.; Abdusalyamova, M. N.;

Morosan, E.; Kauzlarich, S. M. Tuning Magnetism of $[MnSb_4]^{9-}$ Cluster in $Yb_{14}MnSb_{11}$ through Chemical Substitutions on Yb Sites: Appearance and Disappearance of Spin Reorientation. *J. Am. Chem. Soc.* **2016**, *138* (38), 12422–12431. https://doi.org/10.1021/jacs.6b05636.

(134) Vasilyeva, I. G.; Nikolaev, R. E.; Abdusaljamova, M. N.; Kauzlarich, S. M. Thermochemistry Study and Improved Thermal Stability of $Yb_{14}MnSb_{11}$ Alloyed by Ln^{3+} (La-Lu). *J. Mater. Chem. C* **2016**, *4* (15), 3342–3348. https://doi.org/10.1039/c6tc00178e.

(135) Wille, E. L. K.; Grewal, N. S.; Bux, S. K.; Kauzlarich, S. M. Seebeck and Figure of Merit Enhancement by Rare Earth Doping in $Yb_{14-x}RE_xZnSb_{11}$ (x = 0.5). *Materials.* **2019**, *12* (5), 1–12. https://doi.org/10.3390/ma12050731.

(136) Grebenkemper, J. H.; Hu, Y.; Barrett, D.; Gogna, P.; Huang, C. K.; Bux, S. K.; Kauzlarich, S. M. High Temperature Thermoelectric Properties of $Yb_{14}MnSb_{11}$ Prepared from Reaction of MnSb with the Elements. *Chem. Mater.* **2015**, *27* (16), 5791–5798. https://doi.org/10.1021/acs.chemmater.5b02446.

(137) Brown, S. R.; Toberer, E. S.; Ikeda, T.; Cox, C. A.; Gascoin, F.; Kauzlarich, S. M.; Snyder, G. J. Improved Thermoelectric Performance in $Yb_{14}Mn_{1-x}Zn_xSb_{11}$ by the Reduction of Spin-Disorder Scattering. *Chem. Mater.* **2008**, *20* (10), 3412–3419. https://doi.org/10.1021/cm703616q.

(138) Kunz Wille, E. L.; Jo, N. H.; Fettinger, J. C.; Canfield, P. C.; Kauzlarich, S. M. Single Crystal Growth and Magnetic Properties of the Mixed Valent Yb Containing Zintl Phase, $Yb_{14}MgSb_{11}$. *Chem. Commun.* **2018**, *54* (92), 12946–12949. https://doi.org/10.1039/c8cc05471a.

(139) Haskel, D. FLUO: Correcting XANES for Self-Absorption in Fluorescence Measurements. **1999**, No. 206.

(140) Grebenkemper, J. H.; Kauzlaricha, S. M. Magnetic and Structural Effects of Partial Ce Substitution in $Yb_{14}MnSb_{11}$. *APL Mater.* **2015**, *3* (4). https://doi.org/10.1063/1.4908038.

(141) Rehr, J. J.; Albers, R. C. Theoretical Approaches to X-ray Absorption Fine Structure. *Rev. Mod. Phys.* **2000**, *72* (3), 621–654. https://doi.org/10.1103/RevModPhys.72.621.

(142) Booth, C. H.; Christianson, A. D.; Lawrence, J. M.; Pham, L. D.; Lashley, J. C.; Drymiotis, F. R. Ytterbium Divalency and Lattice Disorder in Near-Zero Thermal Expansion YbGaGe. *Phys. Rev. B - Condens. Matter Mater. Phys.* **2007**, *75* (1), 2–5. https://doi.org/10.1103/PhysRevB.75.012301.

(143) Booth, C. H.; Walter, M. D.; Kazhdan, D.; Hu, Y. J.; Lukens, W. W.; Bauer, E. D.; Maron, L.; Eisenstein, O.; Andersen, R. A. Decamethylytterbocene Complexes of Bipyridines and Diazabutadienes: Multiconfigurational Ground States and Open-Shell Singlet Formation. *J. Am. Chem. Soc.* **2009**, *131* (18), 6480–6491. https://doi.org/10.1021/ja809624w.

(144) Halbach, R. L.; Nocton, G.; Booth, C. H.; Maron, L.; Andersen, R. A. Cerium Tetrakis(Tropolonate) and Cerium Tetrakis(Acetylacetonate) Are Not Diamagnetic but Temperature-Independent Paramagnets. *Inorg. Chem.* **2018**, *57* (12), 7290–7298. https://doi.org/10.1021/acs.inorgchem.8b00928.

(145) Kotani, A. Core-Hole Effect in the Ce L3 X-Ray Absorption Spectra of CeO_2 and $CeFe_2$: New Examination by Using Resonant X-ray Emission Spectroscopy. *Mod. Phys. Lett. B* **2013**, *27* (16), 1–22. https://doi.org/10.1142/S0217984913300123.

(146) Minasian, S. G.; Batista, E. R.; Booth, C. H.; Clark, D. L.; Keith, J. M.; Kozimor, S. A.; Lukens, W. W.; Martin, R. L.; Shuh, D. K.; Stieber, S. C. E.; Tylisczcak, T.; Wen, X. D. Quantitative Evidence for Lanthanide-Oxygen Orbital Mixing in CeO_2, PrO_2, and TbO_2. *J. Am. Chem. Soc.* **2017**, *139* (49), 18052–18064. https://doi.org/10.1021/jacs.7b10361.

(147) Lawrence, J. Intermediate Valence Metals. *Mod. Phys. Lett. B* **2008**, *22* (13), 1273–1295.

(148) Lawrence, J. M.; Riseborough, P. S.; Parks, R. D. Valence Fluctuation Phenomena. *Reports Prog. Phys.* **1981**, *44* (1), 1–84. https://doi.org/10.1088/0034-4885/44/1/001.

(149) Rajan, V. T. Magnetic Susceptibility and Specific Heat of the Coqblin-Schrieffer Model. *Phys. Rev. Lett.* **1983**, *51* (4), 308–311. https://doi.org/10.1103/PhysRevLett.51.308.

(150) Hanus, R.; George, J.; Wood, M.; Bonkowski, A.; Cheng, Y.; Abernathy, D. L.; Manley, M. E.; Hautier, G.; Snyder, G. J.; Hermann, R. P. Uncovering Design Principles for Amorphous-like Heat Conduction Using Two-Channel Lattice Dynamics. *Mater. Today Phys.* **2021**, *18*. https://doi.org/10.1016/j.mtphys.2021.100344.

(151) Burch, K. S.; Schafgans, A.; Butch, N. P.; Sayles, T. A.; Maple, M. B.; Sales, B. C.; Mandrus, D.; Basov, D. N. Optical Study of Interactions in a D-Electron Kondo Lattice with Ferromagnetism. *Phys. Rev. Lett.* **2005**, *95* (4), 1–4. https://doi.org/10.1103/PhysRevLett.95.046401.

(152) Cornelius, A. L.; Lawrence, J. M.; Ebihara, T.; Riseborough, P. S.; Booth, C. H.; Hundley, M. F.; Pagliuso, P. G.; Sarrao, J. L.; Thompson, J. D.; Jung, M. H.; Lacerda, A. H.; Kwei, G. H. Two Energy Scales and Slow Crossover in $YbAl_3$. *Phys. Rev. Lett.* **2002**, *88* (11), 4. https://doi.org/10.1103/PhysRevLett.88.117201.